The geotectonic evolution of a portion of the Garies terrane, Kliprand, South Africa

by

GHARLIED ABRAHAMS

THESIS

Presented in fulfillment of the requirements for the degree of

Master of Science

in

APPLIED GEOLOGY

in the

FACULTY OF SCIENCE

of the

UNIVERSITY OF THE WESTERN CAPE

Supervisor: Dr. Russell Hope Bailie

Co-supervisor: Prof. Jan van Bever Donker

2016

Declaration

I hereby declare that the contents of this thesis, submitted for the degree of Masters to the Faculty of Natural Sciences at the University of the Western Cape, apart from the help and supervision of Dr. R.H. Bailie and Prof. J. van Bever Donker, represent my own work, and has not previously been submitted for academic examination towards any qualification.

Signed **Date**

Acknowledgements

First and foremost, I praise the almighty Creator for not only giving me the ability to complete this thesis successfully but for everything. This thesis appears in its current state due to the guidance and assistance of several people. I would therefore like to offer my sincere thanks and gratitude to my wonderful, efficient and patient supervisors Prof. Jan van Bever Donker and Dr. Russell Bailie to whom I will forever be grateful, for their support, enthusiasm and for supervising me during the great time we spent working on this project.

I would like to thank Mr. Peter Meyer and Ms. Janine Becorney (the technical staff of the Department of Earth Sciences at UWC), for their assistance during both thin section production and geochemical sample preparation respectively.

A special thanks go to the experts (most notably Prof. Dirk Frei and Dr. Angelique Laurie) at the Central Analytical Facility, Stellenbosch University and the experts (notably Dr. Petrus le Roux) at the UCT geological facility for their patience during my brief visits and many emails that I have sent. I am grateful for the geochemical data and CL images; thanks a lot.

I am also deeply grateful to my family, my mom (Kamielah), my dad (Zain), my brothers (Toriq and Eessaa), my sister (Ameeroh), my cousin (Umar) for his assistance, my late grandfather (Nadther) and late grandmother (Shanaaz), grandmother (Gaironesa) and all my family, for the support and encouragement during my studies and throughout the process of research and thesis write up.

Last but not least, I would like to thank all my friends and colleagues at the University of the Western Cape: Razeen Stoltenkamp, Muazzam Hashim, Msizi Cindi, Eric Saffou, Tshipeng (James) Mwenze, Reddy Bokana, Marc Ngama, Fritz Agbor, Hakundwi (Mike) Mandende, and Sedzani Nethenzheni, to mention a few, for the fun, laughter and all the good times we spent together.

Abstract

The Kliprand dome is a poorly investigated structure located in the central part of the high grade Garies Terrane of the western Namaqua Sector (NS) of the Namaqua-Natal Metamorphic Province (NNMP). This structure is host to a diverse variety of supracrustal rocks comprising predominantly metapelites and quartzites of the Kamiesberg Group, the streaky augen gneiss, an enigmatic pink gneiss (official name the Lekkerdrink Gneiss) of which the origin is obscure, the metasomatic charnockites along with the pre- to syn-tectonic two-pyroxene granulites (or gabbro-norite) of the Oorkraal Suite. Large bodies of garnet-quartz-feldspar granite, believed to be the products of dehydration melting during peak metamorphism, are referred to as the Ibequas Granite. The transformation of these sediments and volcanic rocks into gneisses and migmatitites was accomplished by intense regional metamorphism during the 1.2-1.0 Ga Namaqua Orogeny. In order to unravel the tectonic evolution of the Kliprand dome, a structural, lithogeochemical, isotopic and geochronological study was undertaken.

The streaky augen gneiss, pink gneiss and Ibequas granite have a strong crustal influence as indicated by the enrichment in the LREE (Light Rare Earth Elements) relative to the HREE (Heavy Rare Earth Elements), the enrichment in the LILE (Large Ion Lithophile Elements) relative to the HFSE (High Field Strength Elements), prominent Eu (which possibly also suggests melting of subcontinental lithospheric mantle) as well as the high initial $^{87}Sr/^{86}Sr$ ratios. The low $\varepsilon_{Nd(t)}$ and $f^{Sm/Nd}$ values for the streaky augen gneiss and pink gneiss suggests derivation from a highly fractionated, and, by implication, mildly depleted source with variable crustal signatures. The depletions of Sr, Ti, P, Nb and Ta in the streaky augen gneiss and pink gneiss reflects an arc-like signature.

Field and geochemical evidence indicates that the charnockite in the Kliprand area is a metasomatic equivalent of the streaky augen gneiss and pink gneiss and does not belong to the typical magmatic variety. The charnockite has a strong crustal influence and a continental arc tectonic signature that was likely inherited from its precursor (streaky augen gneiss and pink gneiss). The charnockite has a fairly high $(^{143}Nd/^{144}Nd)_i$ value of 0.511309 and a positive $\varepsilon_{Nd(t)}$ value of 0.91, similar to that of the gabbronorite, suggesting a depleted source, or mantle-derived component. The gabbro-norite may have brought fluids with it that fluxed through the lower crust and metasomatised upper crustal rocks such as the pink gneiss giving rise to this metasomatic charnockite.

The provenance to the metasedimentary rocks of the Kamiesberg Group is predominantly felsic to intermediate. The T_{DM} model ages of 1.617 Ga for the quartzite and 1.778 Ga (almost identical to that of the pink gneiss) for the metapelite, suggests that there was an influence of an approximate

1.80-1.65 Ga basement in this region which was reworked extensively and whose isotopic signature was retained in these rocks. Hence, the metasedimentary rocks (quartzite and metapelite) might have possibly been derived from a Paleoproterozoic-aged continental arc provenance. They were deposited in rift-type/passive margin basins at ~1.16-1.12 Ga, prior to peak deformation at ~1.11-1.08 Ga. The two pyroxene granulites of the pre- to syn-tectonic Oorkraal Suite were emplaced at the same time as the deposition of the Kamiesberg Group sediments and Lekkerdrink Gneiss, the latter interpreted to be a voluminous felsic volcanic succession. The gabbro-norite displays the chemical characteristics of a depleted mantle origin (source of MORB-like melt), generated within a continental tectonic rift environment.

During the main phase of the Namaqua orogeny (D_2), a well-developed, roughly E–W-trending, steeply N-dipping, penetrative S_2 gneissosity developed, and can be observed in all the paragneiss units and the pretectonic Little Namaqualand Suite gneisses. The age of D_2 was thus obtained by the youngest zircon in the in the Kamiesberg Group (~1.12 Ga) and the ~1.08-1.04 Ga post-tectonic unfoliated granites of the Spektakel Suite (SS) thus constraining D_2 deformation to between ~1.11 and ~1.08 Ga. D_3 deformation is constrained by the melt products (Ibequas granite) mainly found in the hinges of the F_3 fold closures. The earlier magmatic and sedimentary rocks were melted during high-T metamorphism to give rise to partial melts (Ibequas granite). The age of the Ibequas Granite is thus 1.07 Ga, which essentially dates the timing of the D_3 event and high-T metamorphism in the central Garies Terrane. Deformation was accompanied by regional metamorphism attaining granulite facies grade (700–900°C; 5–6 kbars), associated with migmitisation, dehydration melting and charnockitisation.

Table of Contents

List of Figures

List of Tables

List of Abbreviations

NNMP - Namaqua-Natal Metamorphic Province

NMC - Namaqua Metamorphic Complex

LNS - Little Namaqualand Suite

Qtz: Quartz

Bt: Biotite

Hb: Hornblende

Plg: Plagioclase

Grnt: Garnet

Opx: Orthopyroxene

Cpx: Clinopyroxene

Fsp: K-feldspar

Slm: Sillimanite

Myr: Myrmekite

Ser: Sericite

Crd: Cordierite

$D_{1, 2, etc}$: First deformational event (D_1), Second deformational event (D_2) etc.

$F_{1, 2, etc}$: Folding formed during the first deformational event (F_1), Folding formed during the second deformational event (F_2) etc.

$S_{1, 2, etc}$: Foliation formed due to first deformational event (S_1), Foliation formed due to second deformational event (S_2) etc.

$L_{1, 2, etc}$: Lineation formed due to first deformational event (L_1), lineation formed due to second deformational event (L_2) etc.

HFSE: High Field Strength Elements

REE: Rare Earth Elements

LILE: Large Ion Lithophile Elements

HREE: Heavy Rare Earth Elements

LREE: Light Rare Earth Elements

UCC: Upper continental crust

CL: Cathodoluminescence

CHUR: Chondritic Uniform Reservoir

DM: depleted mantle

T_{DM}: depleted mantle model ages

Chapter 1 : Introduction

1.1 Introduction

This study is based in a settlement referred to as Kliprand, located on the border of the northern and western Cape Provinces of South Africa, forming part of the larger Garies Terrane, a subdivision (the other subdivision being the Okiep Terrane) of the larger Bushmanland Subprovince, located in the Namaqualand area (De Beer et al., 2010; Macey et al., 2011). Together the Garies and Okiep Terranes have been interpreted as representative fragments or crustal blocks of Mesoproterozoic age, having rocks which formed or were deformed during the 1.2–1.0 Ga Namaquan (Grenvillian) Orogeny (Reid 1982; Blignault et al., 1983; Barton. 1983; Clifford et al. 1995, 2004; Colliston 2006, Colliston et al. 2014). The Namaquan Orogeny forms a small part of a worldwide network of Grenville-aged orogenic belts that were created during the assembly of the Rodinia supercontinent in the late Mesoproterozoic (ca. 1350-1050 Ma) (Lambert 2013). This research study focusses on a ring structure called the "Kliprand Dome" located in the high metamorphic grade (upper granulite-facies) Garies Terrane, southernmost tectonic terrane of the Bushmanland Subprovince (Figure 1-1).

Regional-scale dome structures are common features of many orogenic belts, particularly within high-grade metamorphic terrains (Johnson 2005). They occur in rocks of various ages, worldwide, and have intrigued geologists for many decades (Eskola, 1948; Johnson 2005). Eskola (1948) was the first person to have investigated the characteristics of gneiss domes in various major orogenic belts, whereby he concluded that pre-kinematic and syn-kinematic magmatic rocks intruded during gneiss-dome formation, resulting in the core of the dome being a metamorphic-plutonic complex overlain by supracrustal strata. The origin of these domes remains controversial, where numerous models involving vertical and/or horizontal tectonics are described for both contractional and extensional settings (Johnson, 2005). Johnson (2005) stated that some workers observed a range of mechanisms from diapirism of low-density middle crustal rocks or low-density magma (e.g. Teyssier and Whitney, 2002; Lee et al., 2004), to extensional exhumation of middle-crustal rocks below low-angle normal faults (e.g. Brun and Van Den Driessche, 1994; Holm and Lux, 1996) and cross folding (e.g. Blewett, 2002). Yin (2004) constructed a classification scheme for correlating the physical properties of domes and domal system to the mechanism of formation. This study assesses the similarities between the structural results of the Kliprand domal structure to the physical characteristics of domes and dome systems obtained by Yin (2004) with the aim of determining the possible mechanism that lead to its formation.

The Kliprand domal structure is comprised of high grade metamorphic rocks such as the strongly tectonized pre- to syn-tectonic streaky augen gneiss (LNS), late- to post-tectonic granitoids and charnockites and mafic to ultramafic rocks. The supracrustal rock consists of metapelites and quartzite, where pink quartzo-feldspathic gneisses are either part of the supracrustal successions or are magmatic in origin. These lithologies of the Kliprand sheet were originally mapped by Albat (1984) as part of a regional mapping project for the UCT Precambrian Research Unit. That project focussed on the petrology and metamorphic geology of the area.

In comparison to the neighbouring district of Okiep, the Garies terrane has minimal mining activity often associated with small base-metal deposits hosting nickel, copper, cobalt and zinc (Mclver et al., 1983; Clifford et al., 1995; Macey et al., 2011). As opposed to the mining activity in the Okiep terrane to the north resulting in numerous scientific studies, the lack thereof in the Garies terrane has resulted in the only whole rock geochemical studies being that of Moore (1983, 1989) and Baars (1990) who used geochemistry to identify the provenance and protolith lithologies of the supracrustal rocks of western Namaqualand. Raith et al. (2003) reported new data with regard to the age and protolith of the supracrustal rocks, as well as the approximate timing of magmatism and high-grade metamorphism in the central granulite and southern amphibolite zones of the Namaqua Tectonic Province. Recently Macey et al. (2011) used new and published whole-rock major and trace-element data to classify and characterise the Little Namaqualand and Spektakel Suites of the Loeriesfontein sheet. However, the geochemical analyses reported by these authors have many drawbacks, namely 1. Too few samples were analysed to be statistically significant, 2. The old datasets captured from other publications were obtained using other analytical methods and laboratories, 3. The general absence of rare earth element or isotopic data limits petrological modelling, and 4. The data only focusses on the Little Namaqualand and Spektakel Suites respectively.

The Hondekloof ore body (Ni-Cu-Co sulphide deposit), hosted by gabbro-norite, which is located along the southern boundary of the Kliprand dome on the farm Nuwefontein (Figure 3-1, 4-5), was discovered in 1979 by the Okiep Copper Company ('OCC'). The Hondekloof deposit (gabbro-norite) near Kliprand has been geochemically researched by Bekker (1980), Taylor (1990), Andreoli et al. (1991) and Hamman et al. (1996) and most recently by Maier et al. (2012)

Unlike the structural and geochemical investigations of western Namaqualand which are quite scarce, the metamorphic history of the Bushmanland Subprovince has been extensively investigated by Albat (1979, 1983, 1984), Joubert and Waters (1980), Zelt (1980), Waters (1986a, 1986b, 1988, 1989, 1990); Waters and Whales (1984), Waters and Moore (1985), Baars (1990), Norwicki *et al.*

(1995), Raith and Harley (1998) and Andreoli *et al.* (2007). Thus, the metamorphic history shall not be extensively investigated in this study.

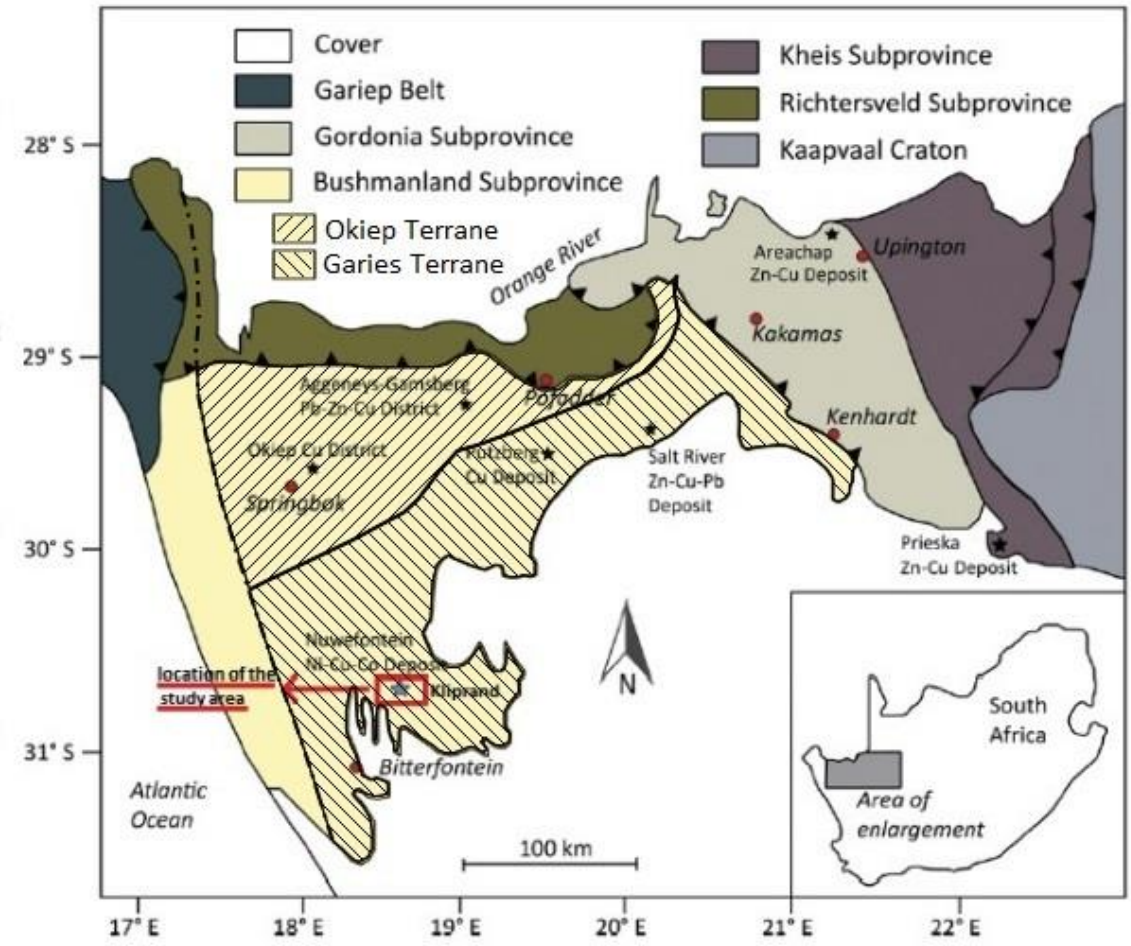

Figure 1-1. Geological map showing the extent of the Namaqua Province and the location of the Hondekloof nickel deposit on the Nuwefontein farm as well as other important base metal deposits. From Wohlgemuth-Ueberwasser et al. (2014).

1.2 Aims and objectives

The Kliprand domal structure is an important key in understanding the geologic history of the central eastern portion of the Garies Terrane as this area has been subjected to high grade metamorphism and intense deformation. The region is host to a diverse variety of igneous, sedimentary and metamorphic rock types (Macey et al., 2011). Despite having been investigated several times during the last 30 years by Albat, (1984), Macey, (2001) and Macey et al., (2011), there has been no consensus on the age, tectonic setting or protolith of the various rocks in the Kliprand area, and, as such, the Kliprand domal structure is an ideal candidate for the application of modern structural analysis, geochemical and geochronological techniques. The objectives of this study are as such:

With regards to structural geology aspects:

A. To produce a geologic map and delineate smaller subareas based on the location of unique structures observed within the study area with the overall purpose of determining the structural evolution of the dome.

B. To characterise the folds and evaluate the significance of the various deformational fabrics with the purpose of placing it into a regional structural context.

C. To provide a detailed (structural and lithological) description of the various subareas, and to analyze the various joints located in the study area.

D.To investigate the tectonic evolution of the Kliprand domal structure and evaluate its formation (e.g. by multiple folding events or diapirism, and to determine whether it might, in fact, be a sheath fold or a large scale boudin.)

With regards to the geochemistry the principal objective is to construct a well-constrained geodynamic evolution model for the Kliprand domal structure by:

A. Constraining the tectonic setting and development of the magmatic and metasedimentary succession

B. Examining the geochemistry of the magmatic and metasedimentary rocks, as well as evaluating their provenance and petrogenesis by using Sm-Nd and Rb-Sr isotope data.

C. Utilising single zircon geochronological analyses on the magmatic and metasedimentary rocks within the Kliprand domal structure with the purpose of acquiring an estimate age of both, the emplacement of the magmatic rocks, as well as the timing of deposition and relative age of source origin of these metasedimentary rocks.

1.3 Methodology

1.3.1 Sampling and structural data collection

Field work, which involved the collection of structural data and oriented samples, was conducted over the course of 1 month and 1 week during 2014. The fieldwork was completed primarily on foot, with an off-road vehicle used to travel towards the northern and southern parts of the dome, which inevitably was the starting point of a number of traverses. All locality and structural readings were recorded using the Rock logger android phone application and handheld GPS as well as a Freiberg compass. The foliation readings were recorded in dip azimuth and dip angle whereas all lineations are depicted as trend and plunge. Structural measurements (Appendix A) were mainly from the visible large scale fold closures as well as the core of the Kliprand domal structure. Oriented rock

samples collected in the field were used for petrographic and microstructural analyses, whilst the remainder were used for geochemistry.

1.3.2 Construction of geological and structural maps

A Geo-referenced topographic map and aerial photo was used to create base-maps for plotting the location of the traverses. A geological map of the Kliprand domal structure was produced through detailed field mapping (Figure 4-5). Due to the extensive distribution of metasedimentary and metavolcanic rocks in the area both Google Earth and aerial photographic imagery was used to enhance the lithological boundaries if clearly visible. The remote sensing datasets (Google Earth and aerial photographic imagery) was also used in order to identify large structures within the study area. The geologic map was scanned and georeferenced, and a database of structural information created by uploading the georeferenced map and recorded field data into the Midland Valley Move™ software. Once the database was set up, the various lithologies were digitized as the orientation of foliations, lineations and joints were automatically oriented by the software.

1.3.3 Structural analysis of the Kliprand domal structure

The foliation and lineation data were plotted on stereonets by using the Midland Valley Move™ software. In order to view structural patterns, the foliation (plotted as either a π diagram or β diagram depending on the amount of readings) and lineation data of each subarea were plotted on their own streonets where linear fabrics are illustrated using density distribution points on the same plot as the foliation. All of the cross sections were digitized via the Move™ software. Rose diagrams were constructed to display the main distribution of the various joint sets while their orientations were plotted as planes on the lower hemisphere stereonet.

1.3.4 Thin section analysis

Thin sections produced from the collected samples where cut perpendicular to foliation in order to view microstructural features. Samples used to produce thin sections had lineations both present and absent. The thin sections were analysed for compositional and structural fabrics. Compositional variations were determined and fabric analyses performed using a petrographic microscope.

1.3.5 Geochemical sampling

Of the 80 samples collected for petrographic analysis for the entire range of lithologies found in the study area, 69 of those samples (Appendix D, Table AC- 1 and 2) were used for geochemical studies. The location of these samples was recorded by the use of the Rock logger Android phone application

during field mapping. With the exception of the radioactive isotope analyses conducted at the University of Cape Town (UCT), the remainder of the geochemical analyses provided in this theses was conducted at the Central Analytical Facility (CAF) at Stellenbosch University.

Prior to these samples being sent for analysis (Appendix C), whole rock samples was crushed using a jaw crusher and milled into a fine powder using a puck mill with a chrome-steel alloy grinding set, followed by the preparation of fused discs for major and trace element analysis. Crushing of the samples using a jaw crusher was relatively fast in comparison to milling (conducted by use of a TS 250 milling machine) which took a total of 5-6 days due to the complexity of the cleansing process which included cleaning of the equipment with acetone after each sample in order to avoid cross contamination. Hand specimens where split into into two parts by using a splitter. As all of the samples were homogeneous, the larger half was used to cut blocks for petrographic thin-sections and the remaining portion was used for crushing and milling for preparation of samples for geochemical analysis.

1.3.6 Analytical methodology

The analytical methods utilized in this study include transmitted light microscopy, X-Ray Fluorescence (XRF) Spectrometry, Laser-Ablation Inductively Coupled Plasma Mass Spectrometry (LA-ICP-MS) and LA-ICP-MS U-Pb zircon dating. The main purpose of microscopy is to petrographically characterize the thin sections cut of the various lithologies, by determining modal proportions of the major, minor and accessory minerals contained in these particular rock samples. Characterization of thin sections may aid in understanding the crystallization sequence of minerals and magmatic conditions as well as the determination of metamorphic conditions and the P-T-t path sequences. XRF spectrometry was used to analyze the major element composition of the rock samples. Major elements (although highly mobile under these high grade metamorphic conditions) were used in the classification of the various rocks as well as in the production of variation diagrams. Variation diagrams are mainly used to show the interrelationship between elements in the data set so that various geochemical processes may be inferred (Rollinson, 1993). The trace elements were analyzed via LA-ICP-MS. Unlike major elements, trace element studies are capable of discriminating petrological processes. Trace elements are commonly studied in groups, and deviation from group behaviour or systematic changes in behaviour within the group are used as an indicator of a distinct petrological process (Rollinson, 1993).

1.3.6a Petrography

All samples were characterized using transmitted and reflected light microscopy. In this study microscopy was mainly used for mineral and textural identification. These characteristics would assist in identifying the various rock types and also help to constrain the type of metamorphic environment by understanding the conditions under which these samples formed. Reflected light microscopy was used to study the opaque minerals mainly found within the gabbro-norite of the Oorkraal Suite.

1.3.6b Major elements analytical procedure

Following the procedure outlined by Taylor et al. (2014):

- 1 g of rock sample was mixed with 10 g of trace element and REE free flux ($LiBO_2$ = 32.83%; $Li_2B_4O_7$ = 66.67%; LiI = 0.50%) during the preparation of Glass discs for XRF analysis. Whole-rock major element data was acquired by XRF analysis on a PANalytical Axios Wavelength Dispersive spectrometer, fitted with a Rhodium tube and LIF200, LIF220, LIF420, PE and PX1 crystals. The instrument is fitted with a gas-flow proportional counter (using a 90% Argon and 10% methane gas mixture) and a scintillation detector.
- Major elements were analysed on a fused glass disc at 50 kV and 50 mA tube operating conditions. The control standards used in the calibration for major element analyses were BE-N (basalt reference values), JB-1 (basalt (depleted) reference values), SY-3 (syenite reference values), SY-2 (syenite reference values), NIM-S (syenite reference values), BHVO-1 (basalt reference values), JG-1 (granodiorite reference values), NIM-G (granite reference values), WITS-G (granite reference values), WITS-B (basalt reference values), and DISKO-1 (basalt reference values).

1.3.6c Trace element analytical procedure

Following the procedure outlined by Taylor et al. (2014) and Matsumura (2014):

- During the preparation of the glass disks an automatic Claisse M4 Gas Fusion instrument utilising ultrapure Claisse Flux (66.67% $Li_2B_4O_7$; 32.83% $LiBO_2$; 0.50% LiI) and a sample to flux ratio of 1:10 was used.
- A New Wave 193nm laser connected to an Agilent 7500ce ICP-MS was used to analyse the trace element concentration of fused glass disks. Operating conditions for the laser were 10 Hz frequency whereby a spot size of 173µm was created during the laser ablation analysis.

- Ablation was performed in helium gas at a flow rate of 0.91.min^{-1} and mixed with argon before introduction into the ICP plasma. The laser took approximately 10 seconds to warm-up and an additional 30 seconds for each spot analysis.
- The calibration standard was run every 12 samples, with a quality control standard that was run at the beginning of the sequence as well as a calibration standard throughout. Certified reference standards BCR or BHVO, both basaltic glass was used for this purpose. At the beginning of each sequence a fusion control standard from certified basaltic reference material (BCR) was analysed to verify the effective ablation of the fused material. The data was processed using the Glitter software distributed by Access Macquarie Ltd.

1.3.6d Radiogenic Sr and Nd isotope analysis

Following the procedure outlined by Miková and Denková (2007) and Fourie (2010), radiogenic Sr and Nd isotope analysis were performed using a Nu instruments NuPlasma HR mass spectrometer in the department of Geological Sciences, at UCT, on eight whole-rock samples

- The Sr was analysed as 200 ppb 0.2% HNO_3 solutions using NIST SRM987 as a reference standard. A value of 0.710225 was used to normalize the $^{87}Sr/^{86}Sr$ data. All of the Sr isotope data were corrected for Rb interference and instrumental mass fractionation with the use of the exponential law and an $^{86}Sr/^{88}Sr$ value of 0.1194.
- Nd isotopes were analysed as 50 ppb 2 % HNO_3 solutions using the Nu Instruments DSN-100 desolvating nebuliser. The Nd-isotope values were normalized to a value of 0.512115 (JNdi-1) after Tanaka *et al*. (2000). All of the Nd-isotope data were corrected for Sm and Ce interference and instrumental mass fractionation using the exponential law and an $^{146}Nd/^{144}Nd$ value of 0.7219

1.3.6e U-Pb zircon dating

One sample of each lithology was sent to the Central Analytical Facility (CAF) University of Stellenbosch for U-Pb laser ablation-inductively coupled-mass spectrometry (LA-ICP-MS) zircon dating. The technique outlined by Lambert (2013) and Matsumura (2014), was used whereby:

- Zircons were extracted from whole rock samples at CAF by following the standard separation techniques of sieving followed by magnetic separation by means of the Frantz magnetic separator. The extracted zircon grains were then examined using a microscope and suitable grains mounted in epoxy resin.

- Photomicrographs were taken of these grains and, together with back-scatter electron (BSE) and cathodoluminescence (CL) images, used to identify the internal structures of the mounted zircon and thus isolate specific target areas for U-Pb isotope analysis.
- U–Pb Zircon age data were obtained via laser ablation single collector-magnetic sectorfield-inductively coupled plasma-mass spectrometry (LA- ICP-MS) employing a Thermo Finnigan Element2 mass spectrometer coupled to a NewWave UP213 laser ablation system (Taylor et al., 2014).
- All of the age data presented in this study were obtained by single spot analyses (spot diameter = 30µm and crater depth = ~15–20µm). The methods employed for analysis and data processing are described in detail by Gerdes & Zeh (2006) and Frei & Gerdes (2009). The calculation of Concordia ages and Concordia plots were performed using Isoplot/Ex 3.0 (Ludwig, 2003).

Chapter 2 : Geological setting

2.1 Regional geology

2.1.1 The Namaqua-Natal Metamorphic Province (NNMP)

During the 1950s minerals preserving evidence for metamorphic activity were found along the southeastern and southwestern boundaries of the Kaapvaal Craton. Radiometric dating was done on these high grade gneisses and granitoids with ages of 1 Ga obtained. Based on this discovery, it was thus proposed that a single Namaqua-Natal metamorphic belt existed (Figure 2-1) (Eglington 2006). This Namaqua Natal mobile belt is exposed in two areas of outcrop known as the “Namaqua Sector” (in the Northern Cape of South Africa and southern Namibia) and the “Natal Sector” (in Kwazulu–Natal) (Figure 2-1). De Beer and Meyer (1983) used geophysical methods in order to identify the boundaries of the Namaqua-Natal mobile belt, in which they found high resistivities within cratonic regions in comparison to that of the NNMB where lower resistivities were obtained (Powell et al. 2001).

During the later 1960s several boreholes were drilled into the Karoo Supergroup as part of regional exploration efforts for oil. These boreholes intersected granitoids and gneisses. Zircons extracted from these gneisses have been dated at ca. 1 Ga (Eglington et al. 2003). In addition, crustal xenoliths from kimberlite diatremes in Lesotho show that the two sectors of the Namaqua-Natal Belt are the exposed parts of a continuous, 1400 km × 400 km wide orogenic belt (Figure 2-1) extending beneath

the Phanerozoic Karoo Supergroup of central South Africa (Jacobs et al. 2008). The NNMB has thus been defined as a late Mesoproterozoic orogenic belt bordering the southwestern, southern and southeastern margins of the Kaapvaal Craton (Powell et al. 2001; Jacobs et al. 2008).

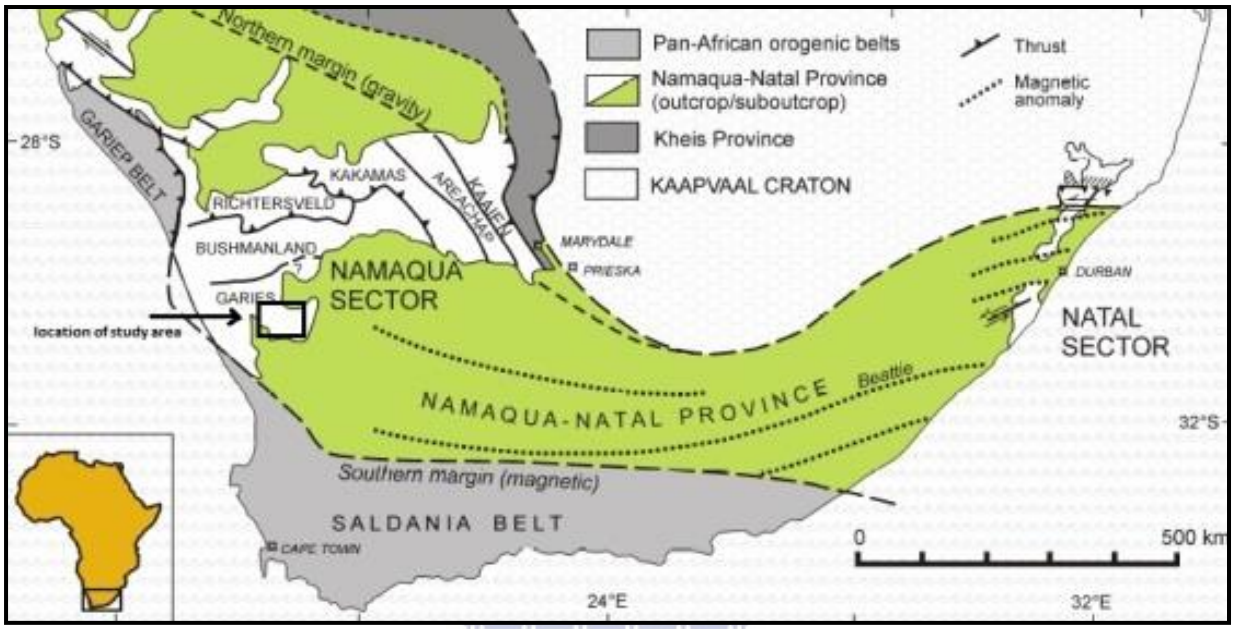

Figure 2-1. Geologic map of South Africa showing the location of the Kaapvaal craton, Khei Province, Saldania and Gariep belts and the Namaqua-Natal Province its sectors and subprovince. Map modified after Cornell et al. (2006).

2.1.2 Namaqua Sector

The orogenic domain known as the Namaqua Metamorphic Complex (NMC) or Namaqua Sector in South Africa and Namibia forms the western sector of the 100-400 km wide NNMB that spans southern Africa (Figure 2-1) (Lambert, 2013). The Namaqua mobile belt has been subjected to the 1.2–1.0 Ga Namaquan (Grenvillian) Orogeny, subsequent to the Eburnian 2.0 Ga Orange River Orogeny (Blignault et al., 1983; Colliston et al. 2014). It forms a small segment of the global network of Grenville-aged orogenic belts that were created during the assembly of the supercontinent Rodinia in the late Mesoproterozoic (ca. 1350-1050 Ma). The Namaquan Orogeny has traditionally been subdivided into two distinct tectono-metamorphic episodes at ca. 1200 and 1030 Ma (Clifford et al. 2004). Based on variation in depositional events and metamorphic grade, the NMC has been subdivided into various terranes and subprovinces (Macey et al. 2011). From west to east, the Namaqua Sector may be divided into a number of subprovinces. The Bushmanland Subprovince of southern and central Namaqual is the largest of these domains (located in the Northern Cape of South Africa and southern Namibia). The boundary between the Bushmanland Subprovince and the Richtersveld Subprovince to the north thereof is defined by the Groothoek Thrust (Schmitz and

Bowring 2004). East of the Bushmanland Subprovince, the Gordonia Subprovince is found. The boundary between the Bushmanland Subprovince and the adjacent Gordonia Subprovince is defined by the Hartbees River Thrust (Moen, 2007). The boundary between the Gordonia and eastern Kheis subprovinces has been defined by the subvertical Trooilaspan and Brakbos shear zones (Schmitz and Bowring 2004). A more detailed description of the Bushmanland Subprovince is provided below, but the remaining terranes/subprovinces are only briefly described in order to place the study area into a broader geological framework.

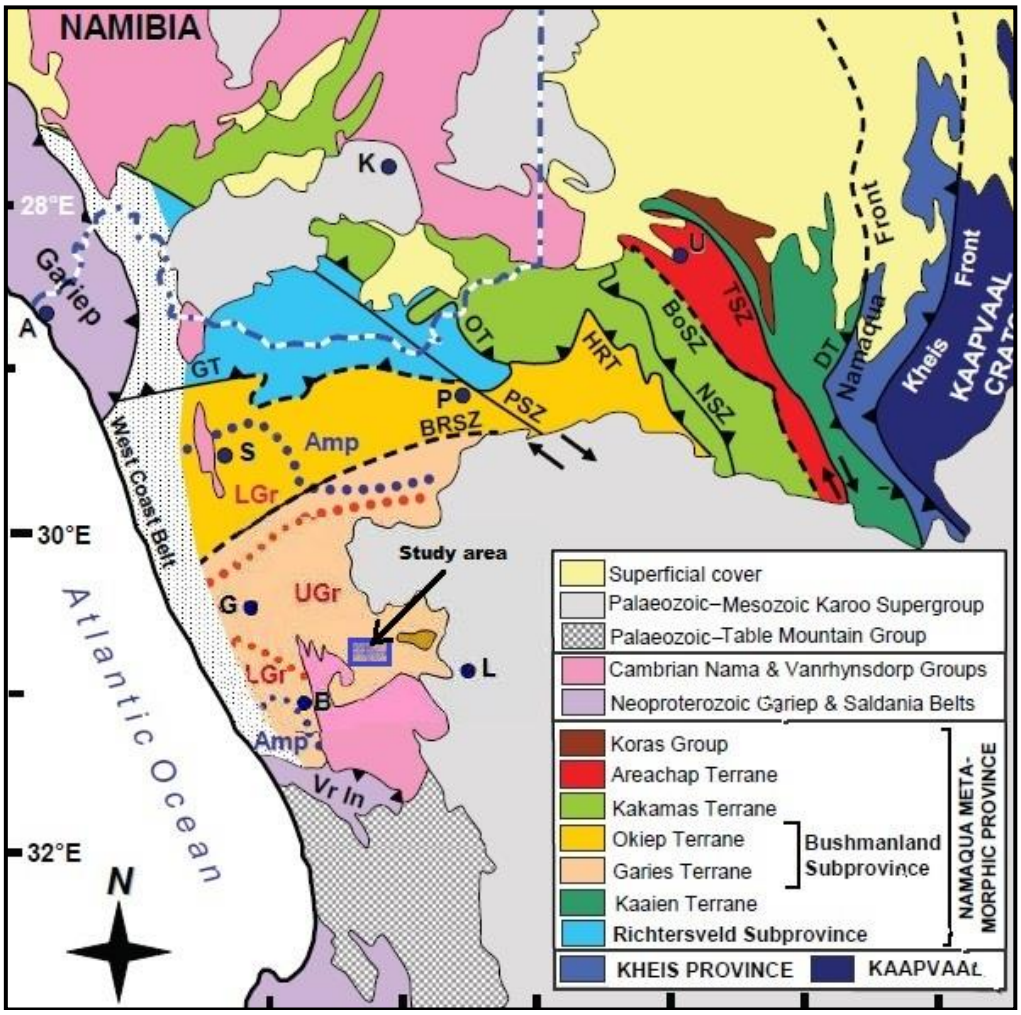

Figure 2-2. Tectonostratigraphic and metamorphic subdivision of the Namaqua Metamorphic Complex (NMC). Major crustal features and terrane boundaries of the NMC: GT= Groothoek Thrust; OT = Onseepkans Thrust; PSZ = Pofadder Shear-zone; HRT = Hartbees River Thrust; BRSZ = Buffels River Shear-zone; NSZ = Neusberg Shear-zone; BoSZ = Boven Rugzeer Shear-zone; BSZ = Brakbos Shear-zone; DT= Dabeep Thrust. Place Names are indicated as: A = Alexander Bay; B= Bitterfontein; G = Garies; K = Karasburg; L = Loeriesfontein; P = Pofadder; S = Springbok; U = Upington; Metamorphic isograds after Waters (1986): UGr = upper granulite facies; LGr = lower granulite facies; Amp = Amphibolite Facies; Gs = Greenschist Facies; The stippled region along the coast represents the Coast Belt, a zone of tectonic reworking of the NMC during the Neoproterozoic Pan African Orogeny. The blue rectangle shows the greater study area. Modified after Macey et al. (2011).

2.2 Subdivisions of the Namaqua Sector

2.2.1 Bushmanland Subprovince

The Bushmanland Subprovince is the largest crustal block in the Namaqua Sector covering an area of roughly 60000km^2. The Groothoek Thrust, a major north-dipping mylonite zone along which the Richtersveld Subprovince overthrust the Bushmanland Subprovince (Bailie et al. 2007; Schmitz and Bowring. 2004), defines the transition between the Bushmanland and neighbouring Richtersveld Subprovince. The Bushmanland Subprovince is bounded to the east by the Hartbees River Thrust against the Kakamas Terrane (Figure 2-2) (Cornell et al. 2006). To the west the rocks are overprinted in a narrow north-trending zone by thermal and deformation effects related to the Pan-African Gariep Orogeny. To the south the rocks are overlain by the younger Vanrhynsdorp Group and Karoo Supergroup sediments (Figure 2-2). There have been many subdivisions of the Bushmanland Subprovince mainly based on metamorphic zonation in which most authors agree upon the occurrence of three terranes, namely the Aggeneys terrane (upper amphibolite facies), the Okiep terrane (lower granulite facies) and the Garies terrane (upper granulite facies) found within the centre of the Bushmanland Subprovince (Figure 2-2). A terrane is defined as a portion of the crust with well-defined structural boundaries. From this definition Macey et al. (2011) subdivided the Bushmanland Subprovince into two tectono-metamorphic terranes, namely the Okiep Terrane to the north and the Garies Terrane to the south separated by the Buffels River Shear Zone (Figure 2-2). The Bushmanland Subprovince is composed of three groups of rocks, with a variation in age and composition (Cornell et al. 2006). The oldest unit is a granitic basement complex (2050-1700 Ma), with a mixed supracrustal succession of sedimentary and volcanic origin with ages of ±1900, 1600 and 1200Ma (Cornell et al., 2006). The youngest units are syn- and late-tectonic intrusive rocks of predominantly granitic and charnockitic composition. These include the LNS (±1200Ma), the Spektakel Suite (±1060Ma) and the mafic rocks of the Koperberg Suite (±1060-1030Ma) (Cornell et al., 2006).

2.2.1a Okiep Terrane

The Okiep Terrane is the northern portion of the Bushmanland Subprovince (Figure 2-2). A name commonly given to this area is the “Okiep Copper district” (Stumpfl et al. 1976). The Okiep terrane is composed of a basal suite of metasedimentary (the Khurisberg Subgroup of the Bushmanland Group) and metavolcanic rocks, a younger group of metamorphosed intrusive granites of the LNS, and a older group of intrusive granitic rocks of the Spektakel Suite (c.a. 1035±15 Ma Concordia and Rietberg granites) which were intruded by the ca. 1035Ma Koperberg Suite (Clifford et al. 1995;

Duchesne et al. 2007). The Koperberg Suite includes copper-bearing sulphide deposits that have been mined for almost 150 years, and due to its economic importance, the Okiep Terrane has been subjected to detailed studies for the past 50 years (Duchesne et al. 2007).The structure of the Okiep region has been described in terms of intrafolial folds (F_1), major recumbent folding (F_2), open folding (F_3) and steep structures (F_4), and was accompanied by a principal regional metamorphism (M_2) of granulite facies which outlasted F_2. This granulite facies metamorphism reflects P-T conditions of ±6kbar and 800-900°C respectively (Clifford et al. 1995).

2.2.1b Garies Terrane

The Garies Terrane is the southernmost tectonic terrane of the Bushmanland Subprovince, with the ENE-WSW Buffels River Shear separating the Garies Terrane in the south from the Okiep Terrane to the north (Figure 2-2) (Macey et al. 2011). Samples of the Garies Terrane point to a crustal age of less than that of the rocks which occur near Springbok, as supracrustal rocks in the Garies Terrane are derived from 1250–1200 Ma crustal material, as shown by the age data findings obtained by Raith et al. (2003). In terms of lithology the Garies terranes is dominated by supracrustal gneisses, strongly tectonized augen and streaky gneiss intruded by late tectonic granites and charnockites, and post-tectonic mafic intrusive rocks (Macey et al. 2011). In terms of deformation three major events dominated the Bushmanland Subprovince, with a weaker E-W D_4 affecting the area at a later stage (Albat, 1984; Macey et al. 2011). Metamorphism varies across the Bushmanland Subprovince, reaching upper granulite facies in the Garies Terrane (Macey et al. 2011).

2.2.2 Richtersveld Subprovince

The Richtersveld Subprovince represents a Palaeoproterozoic (1700-2000 Ma) block within the NMC that largely escaped Mesoproterozoic reworking (Cornell et al. 2006;) and is found along the border of South Africa and Namibia (Jacobs et al. 2008). The Richtersveld Subprovince comprises ca. 2000 Ma volcano-sedimentary successions that were intruded by voluminous granites and granodiorites between 1730 Ma – 1900 Ma (Reid and Barton 1983; Jacobs et al. 2008). The Richtersveld Subprovince is bounded in the west by the Gariep Front, while in the south, it is proposed to be separated from the higher grade Bushmanland Subprovince by the Groothoek Thrust. To the east, the Hartebees River Thrust (also known as the Onseepkans Thrust) separates the Richtersveld Subprovince from the Kakamas Terrane. Willner et al. (1990) and Schmitz and Bowring (2004) state that the Richtersveld Subprovince in the north overthrust the Bushmanland Subprovince to the south, with the Groothoek thrust acting as the boundary between these two subprovinces stretching from the Richtersveld in the west to beyond Pofadder in the east (Jacobs et al. 2008). Previously defined ages of basement rocks suggest that the Bushmanland and Richtersveld Subprovinces forms

part of a Paleoproterozoic micro-continent that was accreted onto the Kaapvaal craton during the Namaqua orogenesis (Schmitz and Bowring 2004).

2.2.3 Gordonia Subprovince

The Gordonia Subprovince, lying east of the Bushmanland Subprovince, comprises a central domain of volcanosedimentary rocks (Archeap Group hosting granites of the Keimoes Suite) separating the western (granitoid dominated) Kakamas terrane, from the eastern Upington terrane (Schmitz and Bowring 2004). The Gordonia Subprovince extends westwards from the Trooilapspan shear zone towards the Onseepkans and Hartbees River Thrust (Moen, 2007). Recent work, specifically in Namibia, has incorporated the Kakamas and Areachap Terranes into the Gordonia Subprovince (Eglington 2006; Bailie et al. 2011). The eastern portion of the Subprovince which contains the Areachap Terrane extends westwards up until the Boven Rugzeer and Cnydas shear zone (Moen, 2007). The Kakamas Terrane is located to the west of the Areachap Terrane, and is truncated by Hartbees River Thrust and Swartrand fault.

2.3 Local Geology

2.3.1 Structural geology

The Kliprand sheet was originally mapped by Albat (1984) as part of a regional mapping project for the Precambrian Research Unit (Macey et al., 2011). Roughly 17 years later Macey (2001) also mapped this area as part of a regional mapping program for the Council of Geoscience. Two stereonets (Figure 2-3a, b) were produced by both authors; however, due to the large areas mapped, not much attention was given to identifying the exact structural types. Macey (2001) used the stereonet (Figure 2-3b) in order to plot a large amount of recorded data. Albat (1984) defined the Kliprand fold structure as having an axial plane striking between 240 and 310 degrees dipping N-NW to NE at angles in excess of 50 degrees, with F_3 fold axes plunging W-SW to W-NW at angles of 20-60 degrees (Figure 2-3a). The stereonet produced by Macey (2001) does not focus on a specific structure, but rather on all the data of the Kliprand area (Figure 2-3b), and is thus unable to identify the structure type. Albat (1984) and Macey (2001) state that the Kliprand domal structure is possibly an F_3/F_4 interference structure. Domal structures are common throughout the Bushmanland Subprovince. Macey (2001) thus suggested that the F_3-F_4 doming is influenced by magmatic diapirism, with the late-tectonic plutonic rocks envisaged as the likely diapiric source. During the D_3 deformational event F_3 steep structures are found to have formed. These structures were interpreted by Clifford and Barton (2012) as being narrow, generally ENE trending, anticlinal folds in which the S_2 gneissosity has been rotated into a near-vertical attitude. According to Clifford and

Barton (2012) various authors interpreted these structures differently with some referring to these steep structures as “fluxion gneiss”, “diapiric” folds, and “necking” (steep structures) created by a megaboudin resulting from north–south extension. Kisters et al. (1996) did a study directly focussed on these structures, whereby they identified steep structures as localized zones of high strain and proposed that they were formed by flattening of the S_2 foliation in response to the north–south (D_3) shortening (Clifford et al., 2012).

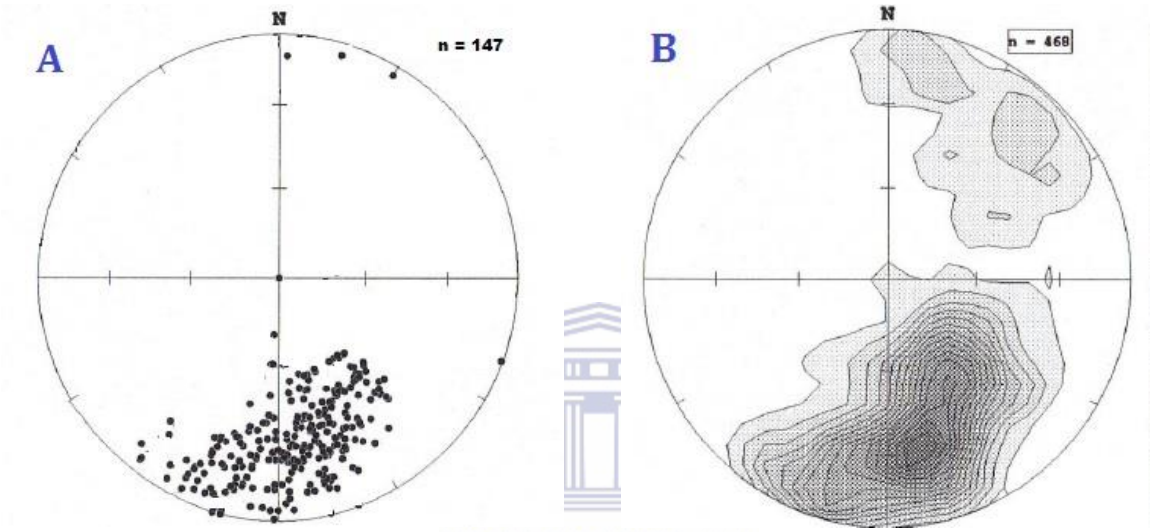

Figure 2-3. a) Poles to plane plot for the F_3 folds of the Kliprand domal structure (after Albat, 1984). b) Contoured stereoplot of poles to S_2 fabric for the entire Kliprand region (after Macey, 2001).

2.3.2 Metamorphism

Regional metamorphism in the Bushmanland Subprovince has a symmetrical zonation pattern defined by E-W trending isograds with a N-S metamorphic zonation displayed by an amphibolite facies zone enclosing a granulite facies belt (Figure 2-2), which was further subdivided by mineral parageneses within the metapelitic gneisses of the granulite-facies belt into a central upper-granulite facies zone surrounded by lower granulite facies zones (Macey, 2001). One of the very first studies to propose a variation in metamorphism was that of Joubert (1971), in which he mapped an extensive area extending from Aggeneys in the north towards Garies in the southern portion of the Bushmanland Subprovince. Across the Bushmanland Subprovince the metamorphic sequence has been subdivided into three metamorphic zones. The highest grade zone is found within the centre of the Bushmanland Subprovince (Figure 2-2), with the grade decreasing towards the north and south (Albat, 1984; Waters, 1986; Macey, 2001; Yuhara 2002). Andreoli et al. (2006) states that the higher the meatmorphic grade the higher the uranium, thorium and the Rare Earth Elements in certain rock

types. By using this understanding Andreoli et al. (2006) confirmed the presence of these zones with their analyses of radioactive isotopes across the Bushmanland Subprovince, concluding that the radioactive decay reaches its peak in the central portion of the Bushmanland Subprovince and decreases towards the north and south.

The current study area falls within the high grade upper granulite facies metamorphic zone which is defined by the mineral assemblage (quartz – hercynite) (Albat, 1984; Waters, 1986; Raith, 1995; Macey, 2001; Macey et al., 2011). The upper granulite-facies subzone attained peak metamorphic conditions of ±750–870°C and 0.45–0.6 GPa and is composed of charnockitic rocks, the Little Namaqualand and Lekkerdrink Suite gneisses as well as metasedimentary gneisses, such as pelites and semi-pelites (Albat, 1984; Waters, 1986; Raith, 1995; Macey, 2001; Macey et al., 2011). This central zone grades into lower granulite-facies garnet + cordierite + alkali feldspar zones, which to the north and south are bordered by the mineral assembledge biotite + sillimanite + quartz + muscovite belonging to the upper amphibolite zone and thus exhibit temperatures of 650-700°C and pressures of 0.35-0.45 GPa (Raith 1995; Yuhara 2002).

The absolute timing of metamorphism has been difficult to constrain (Robb et al. 1999). During the life span of a metamorphic belt more than one period of metamorphism may occur, with these periods referred to as metamorphic events, characterized by thermal highs separated by thermal troughs (Albat, 1984). However, according to Albat (1984), many studies have not considered this definition, and therefore he proposed a single continuous metamorphic event reaching a thermal climax (M_1) after which the metamorphic belt gradually cooled. Despite most authors indicating only one phase of high grade metamorphism, several features in the field suggest multiple metamorphic events (Macey, 2001). These are as follows:

D_1 must be associated with early high grades of metamorphism (M_0/M_1) seeing that the intrafolial folded S_1 foliation contains leucosomes (partial melting).

Pelitic rocks containing peak metamorphic assemblages (M_2) contain D_2 deformation fabric indicating syn D_2-growth

Late post-tectonic high-grade metamorphic textures may have formed during a metamorphic event (M_3) synchronously with the intrusion of the high-temperature magmatic rocks (Macey, 2001).

2.3.3 Lithological description

The Bushmanland Subprovince is made up of three major crustal units, a Paleoproterozoic basement consisting predominantly of granitic rocks of Kheisian age (2050 to 1700Ma) in the form of the Achab Gneiss and the Gladkop Suite, a mesoproterozoic supracrustal succession (Recent findings suggesting they were deposited at 1200Ma and younger), and various suites of syn- and late-tectonic Namaquan intrusive rocks, generally of granitic to charnockitic composition (Cornell et al. 2006; Raith et al. 2003). This last group includes the ~1200 Ma LNS, the ~1060 Ma Spektakel Suite and basic rocks of the ~1060-1030 Ma Koperberg Suite (Cornell et al. 2006; Raith et al. 2003). Despite ages of the protolith being rather obscure, the supracrustal rocks of the Bushmanland Subprovince are considered to be older than the ~1.2 Ga Namaqua igneous activity (Raith et al. 2003).

Table 1. Rocks (and ages) in the NMC resembling those found in the current study.

Suite/lithology dated	Age (Ma)	Method	Reference
Little Namaqualand Suite:			
Streaky augen gneiss	1192		Macey et al. 2011
Nababeep Gneiss	1179 ± 28	Rb-Sr whole rock	Barton 1983
Nababeep Gneiss	1223 ± 48	Rb-Sr whole rock	Clifford et al. 1995
Nababeep Gneiss	1212 ± 11	SHRIMP Pb-Pb zircon	Robb et al. 1999
Nababeep Gneiss	1192 ± 9	SHRIMP Pb-Pb zircon	Clifford et al. 2004
Aroams Gneiss	1204 ± 11	SHRIMP Pb-Pb zircon	Robb et al. 1999
Aroams Gneiss	1193 ± 6	Pb-Pb zircon	Bailie et al. 2007
Pink Gneiss:			
Hoogoor Gneiss	1149 ± 15	SHRIMP Pb-Pb zircon	Robb et al. 1999
Hoogoor Gneiss	1190 ± 6	Pb-Pb zircon	Bailie et al. 2007
Okiep Group:			
Metapelite	1111		Moore 1989
Metapelite	1157 - 1065	U-Pb zircon	Raith et al. 2003
Spektakel Suite:			
Concordia Granite	1206 ± 16	SHRIMP Pb-Pb zircon	Clifford et al. 2004
Concordia Granite	1064 ± 31	SHRIMP Pb-Pb zircon	Robb et al. 1999
Rietberg Granite	1058 ± 30	SHRIMP Pb-Pb zircon	Robb et al. 1999
Concordia Granite	1060 ± 69	Rb-Sr whole rock	Clifford et al. 1995
Rietberg Granite	1069 ± 69	Rb-Sr whole rock	Clifford et al. 1995
Koperberg Suite:			
Koperberg Suite	1022 ± 42	Sm-Nd whole rock	Clifford et al. 1995
Koperberg Suite	1029 ± 10	SHRIMP U-Pb zircon	Clifford et al. 1995
Koperberg Suite	1035 ± 33	SHRIMP Pb-Pb zircon	Robb et al. 1999

Clifford et al. (1995) showed that the ~1.2–1.0 Ga intrusive rocks have Sm-Nd crustal ages of ~2.1–1.6 Ga and have been derived by melting of Paleoproterozoic lower-crustal material (Raith et al., 2011). Reworked Paleoproterozoic basement (±1.8 Ga Gladkop Suite), is mainly preserved in the northern amphibolite facies zone and is thus not expected to be observed in the current study area.

2.3.3a Little Namaqualand Suite

a) Streaky augen gneiss (1212 ± 11Ma - 1154 ± 40Ma; Table 1)

The LNS is characterized by their granitic composition , their pre to syn-tectonic age as well as their well-developed, usually strongly flattened augen texture, which is reminiscent of the well-known Nababeep, Aroams and Grootberg gneiss (Reid and Barton 1983; Raith 1995; Cornell et al. 2006; Pettersson et al. 2009; Macey et al. 2011). The pre-tectonic granitoid orthogneisses represent the dominant lithology on the 3018 Loeriesfontein sheet (Figure 3-1). The ion probe Pb-Pb ages for zircons calculated by Robb et al. (1999) for these rocks gave an age of 1212 ± 11Ma, whereas a Rb-Sr whole rock age of 1154 ± 40Ma was determined by Reid & Barton (1983). Field relations indicate an intrusive origin for many of the granitic gneisses (Reid and Barton, 1983).

b) Lekkerdrink gneiss (1190 ± 6 - 1149 ± 15 Ma; Table 1)

The central parts of the Bushmanland Subprovince are characterized by voluminous concordant to semi-concordant bodies of red-weathered quartzofeldspathic gneisses, often referred to as the “Pink Gneiss” or “Hoogoor Suite” (Joubert, 1971; Albat, 1984). However, in the southern Garies Terrane Macey et al. (2011) refers to these “pink gneisses” as the Lekkerdrink Gneiss. According to Cornell et al. (2009) the Hoogoor Gneiss has a Pb-Pb concordia age of 1149 ± 15 Ma while Bailie et al. (2007) reported a weighted mean age of 1190 ± 6 Ma. Field exposures and the 1149 ± 15 Ma age points to an intrusive origin (Cornell et al., 2009). However, speculation still exists on whether the Lekkerdrink gneiss is meta-volcanic, meta-sedimentary or a combination of both (Macey, 2001). Hence, the Lekkerdrink gneiss was not intruded into the LNS, Spektakel Suite or even the Kamiesburg Group.
According to the geologic map produced by Albat (1984) the dominant lithology found within the Kliprand domal structure is the pink gneiss. However, more recent studies by Macey (2001) proposed that the streaky augen gneiss is the dominant lithology in the current study area. The Hoogoor Gneiss generally lies beneath the supra - crustal succession in the hills of the Bushmanland ore district and is usually included in the Bushmanland Group, implying a supracrustal origin.

2.3.3b Bushmanland Group – Kamiesberg Subgroup

Pelite (1157 – 1065 Ma; Table 1)

Lithostratigraphic information across the Bushmanland Subprovince is complex due to the discontinuous nature of the supracrustal belts, accompanied by large amounts of deformation and an increase in metamorphic grade (Macey et al., 2011). Supracrustal successions have been identified in nine geographically isolated areas within the Bushmanland Subprovince and are referred to as the Orange River Group, the Okiep Group, and the Bushmanland Groups from north to south, respectively (Raith et al., 2003). Recently, these supracrustal succesions were combined into a single Bushmanland Group (Raith et al., 2003). Good examples of mineralogical and geochemical differences between metapelites within the northern and southern portion of the Bushmanland Subprovince were noted by Moore (1989). Due to these differences the supracrustal rocks along the southern portion of the Bushmanland Subprovince were placed in the Kamiesberg Subgroup of the Bushmanland Group. The entire succession of supracrustal rocks from Pofadder southwards towards the Buffel River Shear zone have been grouped into the Bushmanland Group, whilst supracrustal rocks of the Garies Terrane including the Buffels river shear have been grouped into the Kamiesberg Group (Macey et al., 2011). In comparison to the Bushmanland Group, the Kamiesberg Group was not subdivided into subgroups or formations due to the high grades of metamorphism causing loss of facies information (Macey et al., 2011). However four lithostratigraphic units have been observed, namely metapelitic, semipelitic, calc-silicate and metaquartzitic gneiss (Macey, 2001; Macey et al., 2011).

2.3.3c Spektakel Suite

The pre-tectonic supracrustal rocks, namely the Lekkerdrink Gneiss and the Little Namaqualand Suite have all been intruded by the post-tectonic Spektakel Suite granites and charnockites (Macey et al., 2011). Although the LNS and Spektakel Suite are quite similar in terms of composition and minerology, the Spektakel Suite is clearly less deformed (Macey et al., 2011). The Spektakel Suite is represented by two distinct granitoid types, known as the “Concordia type” and “Rietberg-type” respectively (Cornell et al., 1996). The Concordia type can be described as sheet-like bodies of weakly foliated, medium-grained leucogranite and are locally garnetiferous (Macey et al., 2011). Unlike the common magmatic leucogranites of Spektakel Suite, the leucogranitic Ibiquas Granite of the Kliprand area is a late garnetiferous melt product resulting from partial melting of the supracrustal succession.

The Rietberg granites in south west Namaqualand consist of large bodies of megacrystic granite, granodiorite, charno-enderbite and charnockite, which occur extensively around Garies and Kliprand. True charnockites of the "Rietberg-type" and are well developed within the high metamorphic grade (granulite-facies) Garies Terrane, north of Bitterfontein (Cornell et al., 1996). The Rietberg-type granites occur throughout the 3018 Loeriesfontein mapped area, mostly as relatively small intrusive bodies, but some, such as the Garies megacrystic granites, occupy large areas across the mapped region.

Charnockite (1069 ± 69 - 1058 ± 30; Table 1)

Charnockites occur throughout the Okiep Terrane, but are more widespread in the Garies–Kliprand area south of the Buffels River shear zone (Andreoli et al., 2006). In the 3018 Loeriesfontein area both magmatic and metamorphic charnockites have been identified (Albat, 1984; Macey et al., 2011). A large variety of distinct charnockite bodies were recognized originally by Albat (1984), but for the sake of simplicity he grouped them all together and referred to them as the Kliprand Charnockite Suite which includes charnockite, charno-enderbite and monzonorite. Separate status has only been assigned to the dark-red weathering rock, reffered to as the Klein-Lieslap Charno-enderbite located south of Kliprand on the farm Uitkyk (Albat, 1984). Outcrops of the Klein-Lieslap Charno-enderbite and Kliprand Charnockite feature prominently along the southern limb of Kliprand domal structure (Albat, 1984; Figure 3-1). All the known outcrop localities are confined to the granulite facies terrane as defined by the presence of pyroxenes in metamorphosed mafic rocks (Albat, 1984). The charnockites are predominantly observed close to the contacts with the Koperberg Suite (Andreoli et al., 2006). The Koperberg intrusions range in size from small 100-m-wide bodies, to the 6-km-wide Klein-Lieslap pluton located 5 km south of Kliprand (Macey et al., 2011). Macey et al. (2011) noted that the metamorphic charnockites could have developed through in situ charnockitisation of the Lekkerdrink pink gneisses and the LNS augen gneisses. The charnockite plutons (e.g the Klein Lieslap charnockite) near Kliprand, probably represent granitic magmas generated by the partial melting of lower continental crustal material under water deficient conditions (Andreoli et al., 2006).

Ibequas granite (1064 ± 31 - 1060 ± 69; Table 1)

The majority of the paragneisses and orthogneissic rocks of the Kliprand area show evidence of migmatisation, with the resulting anhydrous melt material representing a major constituent of the rock (Macey et al. 2011). In the hinge zones of the fold closures where temperature and pressure are slightly higher, the melt material appears to have segregated from the host and migrated short distances to form leucogranites (Macey et al. 2011). In such instances, Macey et al. (2011) termed the anhydrous melt the Ibequas Granite.

2.3.3d Oorkraal Suite

Meta-Gabbro (1022 ± 42Ma - 1154 ± 40Ma; Table 1)

The meta-gabbro or gabbro-norite as it is more commonly known represent only a minor proportion of the 3018 Loeriesfontein mapped area, where it has been termed the "Hondekloof Cu-Ni deposit" (Macey et al., 2011). Despite differences in the nature of the Hondekloof deposit with other small mafic outcrops, all the pre-tectonic mafic rocks were grouped together in the single Oorkraal Suite. The nickel deposits occur as small lenticular gossans, with many lenses found occupying fold hinges (Maier et al., 2012). Hamman et al. (1996) interpreted these bodies to be syn-to-late tectonic and co-genetic with the cupriferous Koperberg Suite to the north in the Springbok area (Maier et al., 2012). Shallow drilling in the early 1980s defined in situ ore resources totalling 2 Mt at 0.88% Ni and 0.2% Cu (Maier et al., 2012). Data obtained by Maier et al. (2012), the Council for Geoscience and prospecting activities for nickel by Lehoma Resources (exploration company) correlate the two-pyroxene granulites of the Nuwefontein Suite to the Oorkraal Suite, and the nickeliferous gabbro-norites and related rocks (anorthosite, diorite, glimmerite) to the younger Koperberg Suite (Maier et al., 2012). Maier et al. (2012) therefore advocated discontinuing the use of the term "Nuwefontein Suite". Geochemical analysis by Maier et al. (2012) revealed that the petrogenesis of the parental magmas of the Okiep and Hondekloof deposits indicate that they are derived from a relatively differentiated mafic magma of basaltic lineage and could have formed through extreme fractionation of a magmatic sulphide liquid (Maier et al., 2012).

Chapter 3 : Lithological description

Introduction

The study area is dominated by Mesoproterozoic metamorphic and magmatic rocks. Seven distinct units have been identified for mapping purposes. As opposed to Macey (2001), which has the streaky augen gneiss dominating the Kliprand dome (Figure 3-1), this study in agreement with Albat (1984), has the biotite-rich pink gneiss making up the majority of the Klirand domal structure. The southern and the eastern boundary of the large Kliprand domal structure contain enclaves of charnockite and mafic rocks (Figure 3-1). These rock units shall be discussed from oldest to youngest based on the stratigraphic column produced by Macey et al. (2011). Metasedimentary rock units belonging to the Kamiesberg Subroup consist of the quartzite as well as the metapelitic gneiss and are exposed mainly as thin bands along the southern limb of the major Kliprand domal structure (Figure 3-1). Metasedimentary rocks are occasionally quite thin to such an extent that in certain situations it was not possible to map them as separate units. Similarly, some of the gabbro-norites and charncokites were also too small to be mapped.

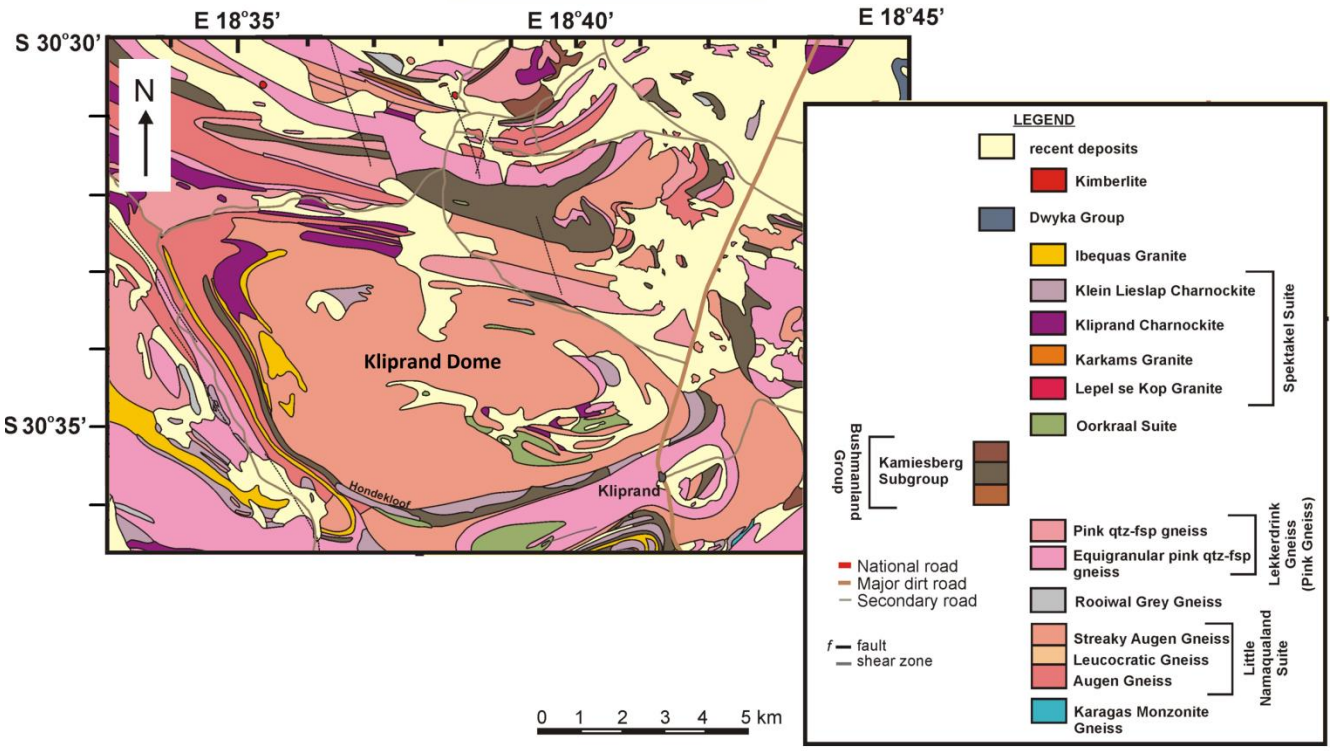

Figure 3-1. Geologic map of the Kliprand domal structure. Redrawn and Edited from Macey (2001).

3.1 Pink gneiss

3.1.1 Macroscopic description and field relations

The Kliprand domal structure is almost entirely dominated by the biotite-rich pink gneiss, the pink biotite-gneiss is generally resistant to weathering and outcrops as ridges consisting of rounded boulders (Figure 3-2) (Macey, 2001; Macey et al., 2011). Field exposures of this rock have a distinct weathered surface of a pink-to-light pink colour (Figure 3-2). The majority of outcrops display an equigranular, fine grained texture while others have very small porphyroblastic subhedral/euhedral alkali feldspar crystals, suggesting that it is related to the augen gneiss. The latter texture is commonly observed where there is a gradational contact between the pink gneisses and the augen gneiss (Figure 3-3; Figure 3-4), possibly pointing to some relationship between these two rock types (Joubert, 1971; Albat, 1984). The pink gneiss (also known as the Lekkerdrink Gneiss) has two varieties which can mainly be distinguished by their biotite content as being a biotite-rich (± 13%) variety (the dominant pink gneiss in the study area), and a biotite-poor pink gneiss variety (sporadically present), respectively.

The pink gneiss (biotite-rich unless stated as biotite-poor) contains a weak foliation that is subparallel or parallel to the axial plane of macroscopic folds in the study area. Although the pink gneiss is intruded or cross cut by leucosome bodies and the gabbro-norite lenses, the absolute age of the unit is relatively unknown in terms of age dating (Macey et al., 2011). The K-feldspar and quartz leucosomes observed in the area have been considered to be the products of the high-grade metamorphism/ partial melt products (Macey, 2001; Macey et al., 2011). The quartz content in most of the pink gneiss in the field is higher than the feldspar content thus giving it a light pink-to-cream colour. Some of the pink gneiss is slightly more feldspathic giving the. The modal abundances of quartz and alkali feldspars in the leucocratic layers are fairly uniform throughout the field area, with no significant detectable changes at the macroscopic scale. The contacts of the pink gneiss with the augen gneiss are commonly gradational with the occasional tapering of the augen gneiss into the pink gneiss (Figure 3-4).

Figure 3-2. Typical rounded boulder outcrops of the pink gneiss.

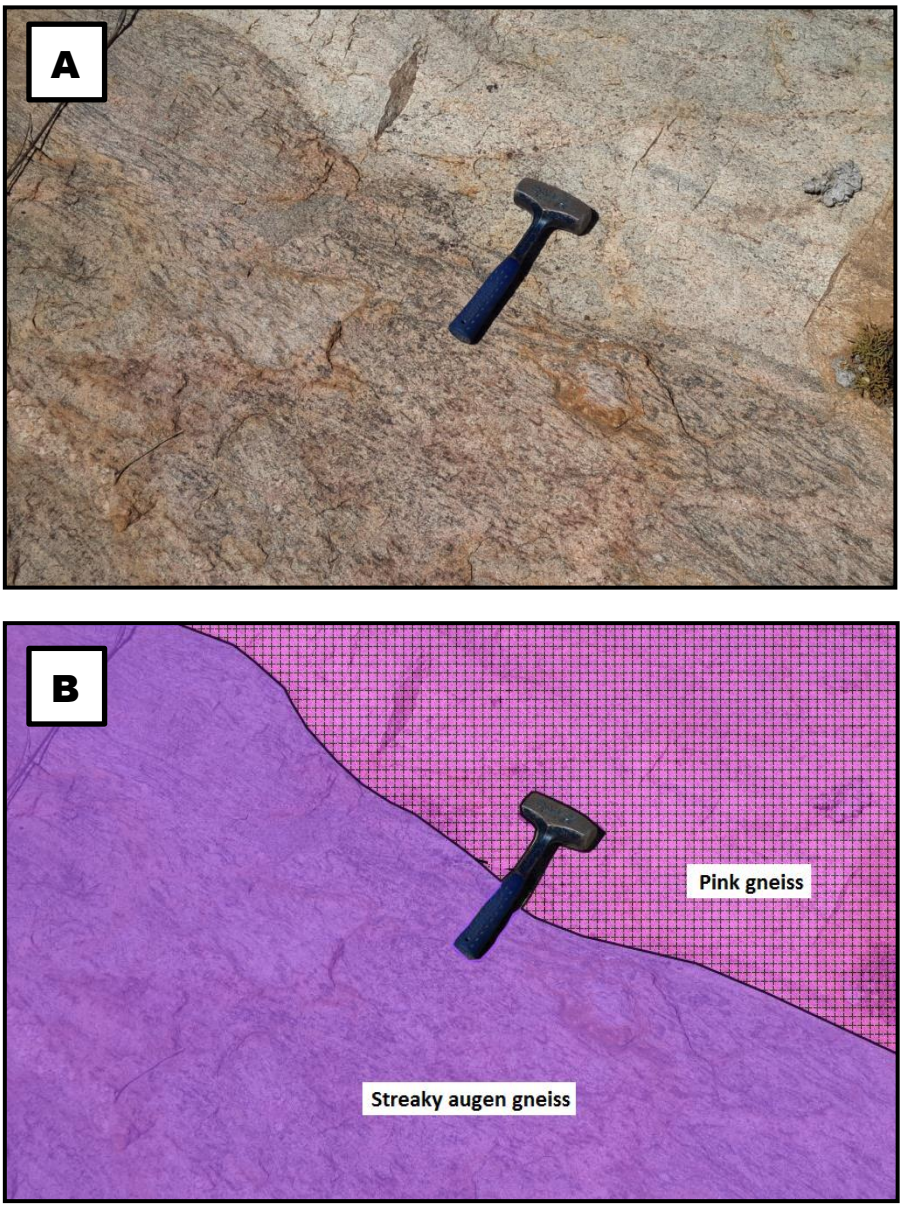

Figure 3-3*. A) Contact between streaky gneiss (bottom, dark) and pink gneiss (top, cream coloured), image by Dr Russel Bailie. B) A graphic view of the above image, outlining the contact between the two lithologies.*

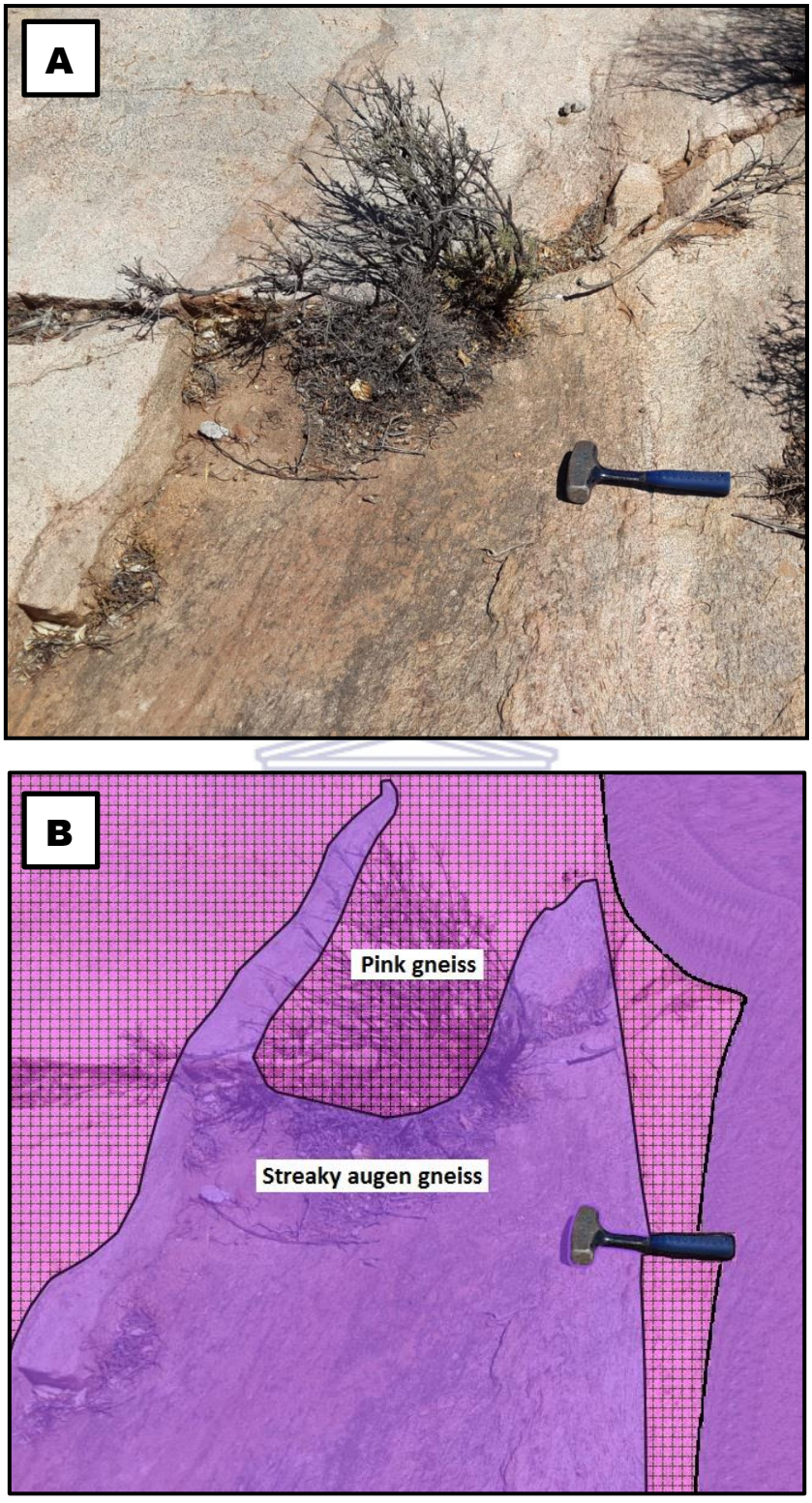

Figure 3-4. *A) Image of pink gneiss being intruded by the streaky augen gneiss. Gradational contact between the two as shown on the right side of the photo by the hammer handle. Image courtesy of Russell Bailie. B) A graphic view of the above image, outlining the contact between the two lithologies.*

3.1.2 Microscopic description

Microscopic studies of several thin sections of the pink gneiss indicate that alkali feldspar (perthite), quartz and biotite are the dominant minerals (Appendix D, Table AD-1).

Felsic minerals

Orthoclase feldspar has an average modal abundance of 32%, with grains subhedral in shape with ragged grain boundaries. About 20% of these orthoclase grains contain albite lamellae and are termed perthite (Figure 3-5A). Some perthite grains form a myrmekitic intergrowth with quartz (Figure 3-5A). This myrmekitic growth suggests some metasomatic conditions or fluid flow during deformation. Some of the alkali feldspar grains are relatively large reaching a maximum size of 2.0mm. However, the majority of the feldspars are smaller than 1mm and could, thus, not be classified as augen, as they are too small and do not display the typical eye shape. The majority of the orthoclase feldspars have been sericitized resulting in the feldspars having a cloudy, altered appearance with portions of the unaltered feldspar still present. In the more biotite-poor pink gneiss the feldspars have been altered due to oxidation giving this rock its distinct pink colour (Figure 3-5B). Quartz (average modal abundance of 38%) has a similar grain size to that of the feldspars. It has anhedral grain shapes with well-rounded grain boundaries.

Mafic minerals

The mafic minerals include biotite and garnet, with average modal abundances of 11.5% for the former and 3% for the latter (Appendix B). Biotite was commonly observed as short prismatic grains (Figure 3-5C, D). In the biotite-rich pink gneiss, most biotite grains are aligned forming a thin foliation probably due to intense deformation. Although the majority of the biotite grains have been aligned, some of the grains have been folded forming an anticline-synclinal pair (Figure 3-5E, F). Field exposures of the pink gneiss display 0.2-0.5mm crystals of garnet throughout the rock type. In the biotite-rich pink gneiss the garnet is even more dispersed than what is found in the paleosome present in the metapelites. Garnet found in the biotite-rich pink gneiss is subhedral with well-rounded quartz inclusions (Figure 3-5D).

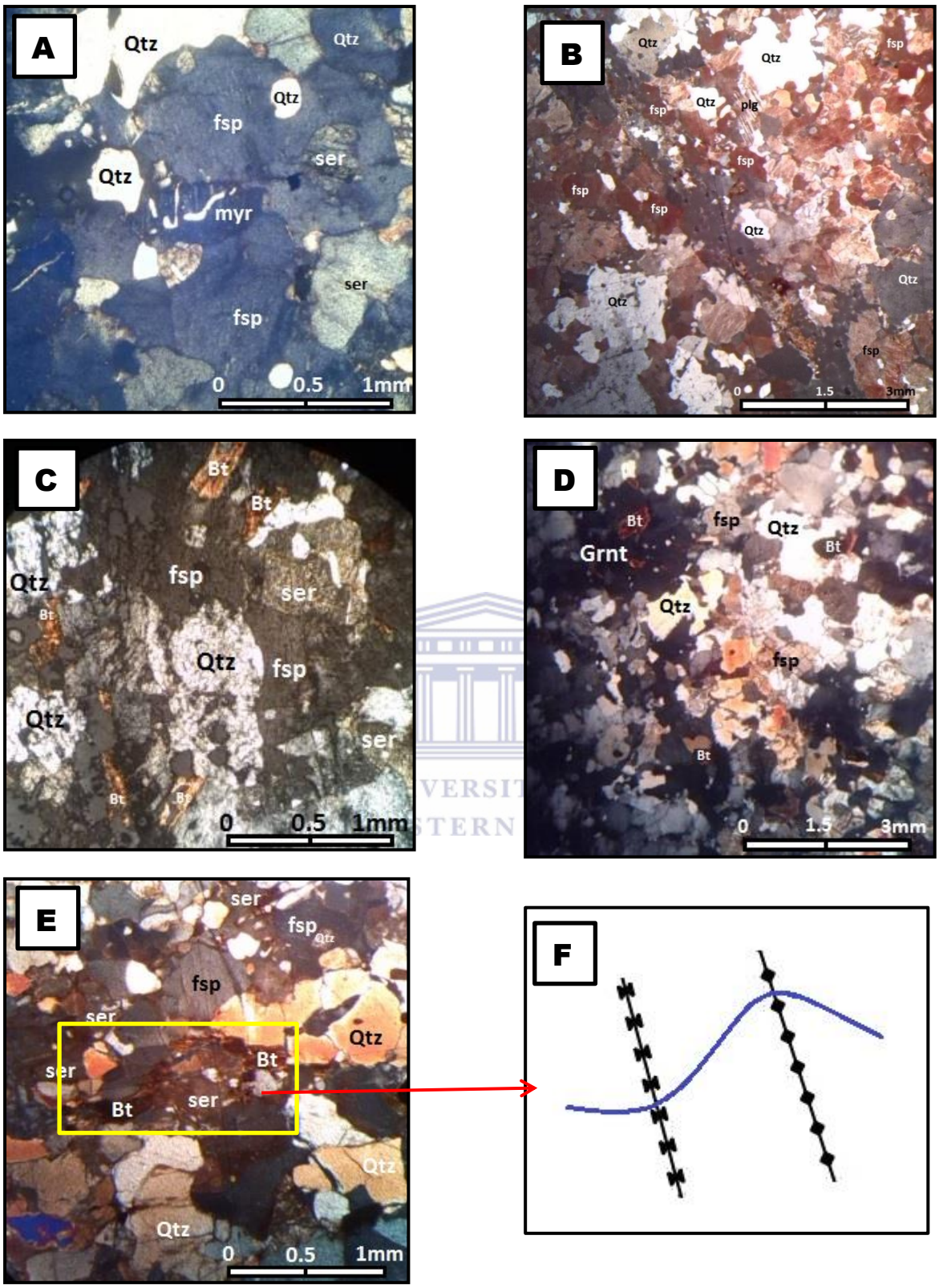

Figure 3-5. *A) Image of sample PG104 - Large perthitic feldspar with rounded quartz inclusion alongside a plagioclase showing a myrmekitic intergrowth. B) Image of sample PG169 under crossed polars displaying biotite-poor pink gneiss with feldspars that are dark red in colour due to Fe entering their lattice structure. C) Image of sample PG007 displaying subhedral platelets. D) Image of sample PG001 taken under crossed polars displaying a large subhedral garnet porphyroblasts with short stubby biotite and well-rounded quartz inclusions. E (crossed polars) –zoomed in image of sample PG001 displaying folded biotite grain. F – graphic outline of the anticline-syncline pair. Evidence of an earlier deformational event.*

3.2 Streaky augen gneiss

3.2.1 Macroscopic description and field relations

These rocks are present as exfoliated domes and well-rounded boulders produced by weathering (Macey et al., 2011). The streaky augen gneiss is a pale pink to cream coloured, medium grained rock that has a distinctive alkali feldspathic augen texture (Albat, 1984; Macey, 2001; Macey et al., 2011). In comparison to the pink gneiss that contained thin melanocratic foliation bands, the streaky augen gneiss has a morewell defined leucocratic and melanocratic banding with flattened, well developed feldspar augen defining the foliation in the streaky augen gneiss. The light coloured bands are formed by light coloured, typically felsic minerals, such as quartz and feldspars. The dark bands are composed of dark, typically mafic, minerals such as biotite.

The augen mainly consist of medium- to coarse-grained flattened crystals of alkali feldspar. The alkali feldspar augen are typically pink to milky white in colour, and can reach up to 3 cm in length in the fine-to-medium grained matrix; quartz and finer crystals of feldspar occupy the groundmass between the feldspar phenocrysts. Based on field appearance as well as the fact that the augen likely represent phenocrysts which have been deformed into augen (original sedimentary rocks would not develop such augen), the protolith of the streaky augen gneiss is regarded as having been an igneous rock and they are thus termed orthogneiss. However, further petrographic and geochemical analysis was done to confirm whether they are igneous or sedimentary in origin.

3.2.2 Microscopic descriptions

Field exposures of the streaky augen gneiss are pink, orange to cream coloured rock consisting of alternating bands of biotite (±2mm thick) and quartz-feldspar (1-1.5cm thick), together with white feldspar augen. Microscopic studies clearly display the streaky augen gneiss as having a porphyroclastic texture with large feldspars generally 2–5 mm in length with extensive recrystallization of quartz, plagioclase, alkali feldspar, and the alignment of euhedral mafic minerals (platelets) along the margins (Figure 3-6A; Appendix D, Table AD- 3).

Felsic minerals

Within the streaky augen gneiss orthoclase feldspar is a major felsic mineral with an average modal composition of 39%. These large feldspar augen are subhedral to euhedral in shape, some with embayed margins due to dissolution and enclosing smaller quartz. The larger feldspar augen grains also contain elongate quartz inclusions and commonly have embayed grain boundaries. The megacrystic feldspar augen consist of a single crystal of K-feldspar with quartz and platelets filling a

pressure shadow at the edges of the feldspar (Figure 3-6A-C). Quartz is the second most abundant mineral with an average abundance of 36%. It displays various strain features such as undulose extinction and subgrain boundaries. They are mainly found between feldspar grains as euhedral quartz crystals showing undulose extinction, granoblastic polygonal textures and 120^{o} boundaries (Figure 3-6B, C).

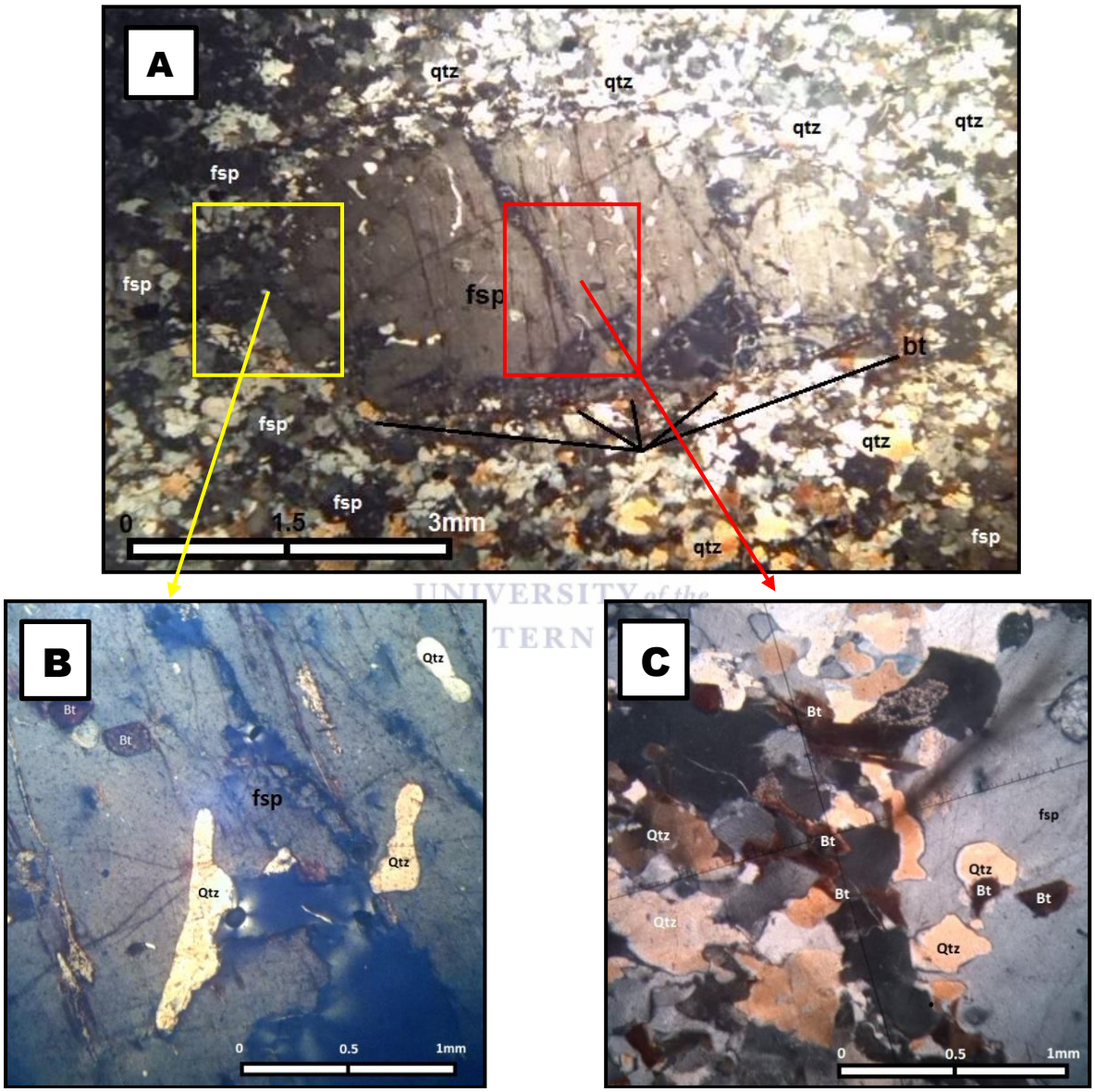

Figure 3-6 *A) Image of sample 113 displaying a subedral feldspar augen 3.5 mm in length. This feldspar porphyroclast is rounded and looks to have experienced recrystallization along its margins. B) Image of sample 113 displaying the well-rounded elongate quartz inclusions within the larger feldspar grain, these don't appear to be particularly crystallographically controlled suggesting potential inclusion during recrystallization. C) An image of the edge of the feldspar augen where there seems to be a weak pressure shadow.*

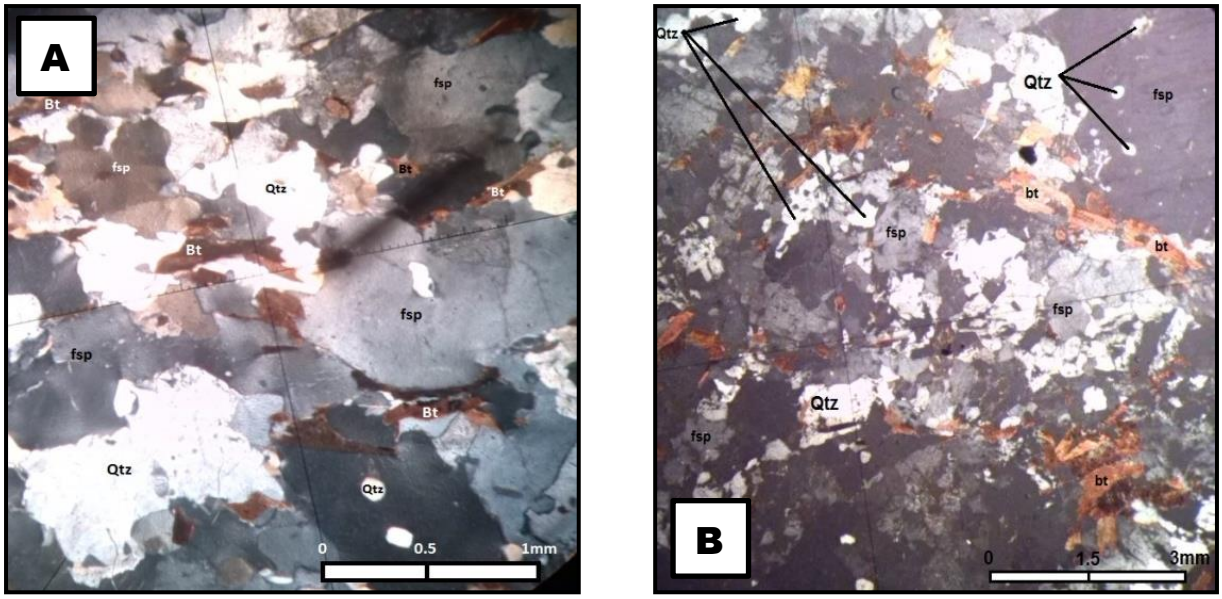

Figure 3-7. A) Image of sample 113 under crossed polars displaying subhedral biotite at the grain boundaries of the larger Orthoclase feldspar grains. B) Large scale view of sample 212 displaying the biotite as the defining foliation within the rock.

Mafic minerals

Biotite is the predominant mafic mineral and is commonly present as brown to red-coloured platelets; they are 0.2-0.7mm in size with an average whole rock abundance of 15% of total volume. These biotite grains, found mostly as small laths or coarser grained aggregates as well as disseminated grains between the boundaries of felsic minerals (Figure 3-7A), define the foliation (Figure 3-7B). Plagioclase, with an average modal abundance of 7%, occurs as subhedral grains with relatively small grain sizes of 0.2-0.5mm.

With regards to the deformation of the augen gneiss, the microstructures include suturing of grain boundaries (grain boundary recrystallization) and undulatory extinction in quartz, subgrain formation and formation of grain boundary migration. Kinked and deformation twins also occur in plagioclase. Well defined foliation comprising separate micaceous (Figure 3-7B) and quartzofeldspathic material, as well as strain separation around porphyroclasts (Figure 3-6C), are indicators of deformation that these samples have experienced.

3.3 Quartzite

3.3.1 Macroscopic description and field relations

In agreement with Albat (1984) and Macey et al., (2011) the white to creamish white quartzite (Figure 3-8A) represents the dominant quartz-rich paragneiss in the Kliprand domal structure. This rock is highly weather resistant and forms large exposures along the southern limb of the Kliprand domal structure (Figure 3-1). The rocks are medium to coarse grained and equigranular with a granoblastic texture. They occur in close association with, and are frequently sandwiched between the metapelites and the overlying streaky gneiss (biotite-rich pink gneiss). It appears that these rocks reach their maximum thickness in the hinge of the D_4 fold (Figure 3-1) and become less voluminous towards the edge of the limbs where they eventually fade out (Figure 3-1) (Albat, 1984). On the southern limb of the Kliprand domal structure, the quartzites reach a stratigraphic thickness of 3-10m where they bear a strong resemblance to a semi-pelite due to the appearance of very small (4mm) dispersed garnet grains (Figure 3-8B) within the rock type, as well as the fact that they are overlying a thick band of metapelite. Further analysis in the field shows that this rock type constitutes mainly feldspar (abundance of ~25%) and quartz (abundance of more than 50%) whilst garnet makes up the remainder of the rock, thus imparting the distinct white colour of the rock. The fact that feldspar is also so abundant suggests that the quartzite is almost a quartzofeldspathic rock, as verified by the microscopic analysis given below.

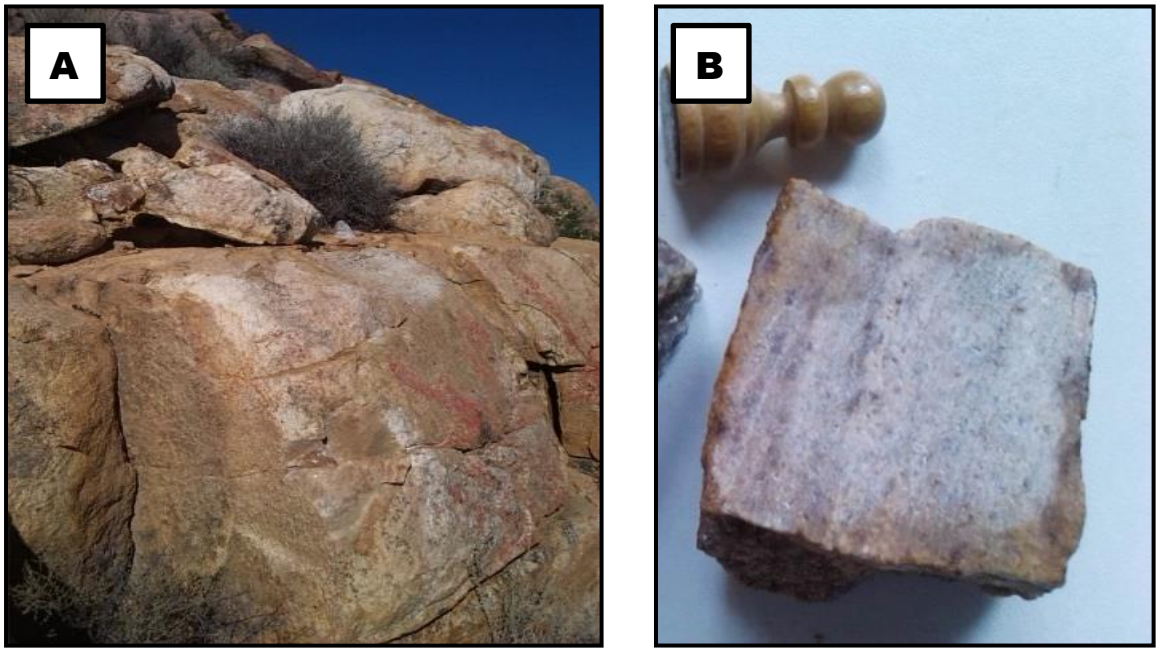

Figure 3-8*. A) Large outcrops of quartzite exposed along the southern limb of the Kliprand domal structure. B) Hand speicmen of quartzite displaying small red dots of garnet in trace amounts. Pawn piece is 6 cm in size.*

3.3.2 Microscopic descriptions

This rock consists of quartz (50%), orthoclase feldspar (31%), Plagioclase (7%), biotite (7%) and garnet (3%) with oxide and chlorite making up 2% (Appendix D, Table AD- 5). Seeing that the rock is highly quartzitic most quartz crystals are in contact with one another. Orthoclase Feldspar is the second most abundant mineral and is found adjacent to quartz creating quartz-feldspar boundaries and quartz-quartz boundaries in comparison to the streaky gneiss and augen gneiss which have interstitial biotite grains on their grain boundaries. Where present the elongated biotite minerals are randomly oriented and locally interstitial.

Felsic minerals

Quartz is by far the most dominant mineral within the quartzite with a mineral abundance of 50%. In most cases the relatively clear to smoky coloured quartz grains are anhedral in shape with interlocking grain boundaries when in contact with adjacent quartz crystals. More than 50% of these quartz grains display undulose extinction due to deformation (Figure 3-9A). The second most abundant mineral is subhedral to anhedral orthoclase feldspar which makes up 31% of the total rock volume where they range in size from 0.3-1.9mm. The orthoclase feldspars are locally perthitic and contain well rounded quartz inclusions. In addition to orthoclase, anhedral plagioclase (average modal abundance of 7%) locally occurs as small crystals ranging in size between 0.2-1.0mm.

Mafic minerals

Biotite (average modal abundance of 7%) is the dominant mafic mineral within the quartzite, with smaller amounts of garnet (average modal abundance of 3%) locally observed. Biotite occurs as interstitial grains between quartz-quartz boundaries and quartz-feldspar boundaries (Figure 3-9C). Even though light brown-green pleochroic biotite was observed, the majority of this mineral had dark red pleochroism. The garnet in the quartzite is significantly smaller (0.7-1.2mm) than that seen in both the paleosome (1.5-3mm) of the metapelite as well as in the Ibiquas granite (see latter). They are commonly subhedral to anhedral in shape and have abundant quartz inclusions (Figure 3-9B).

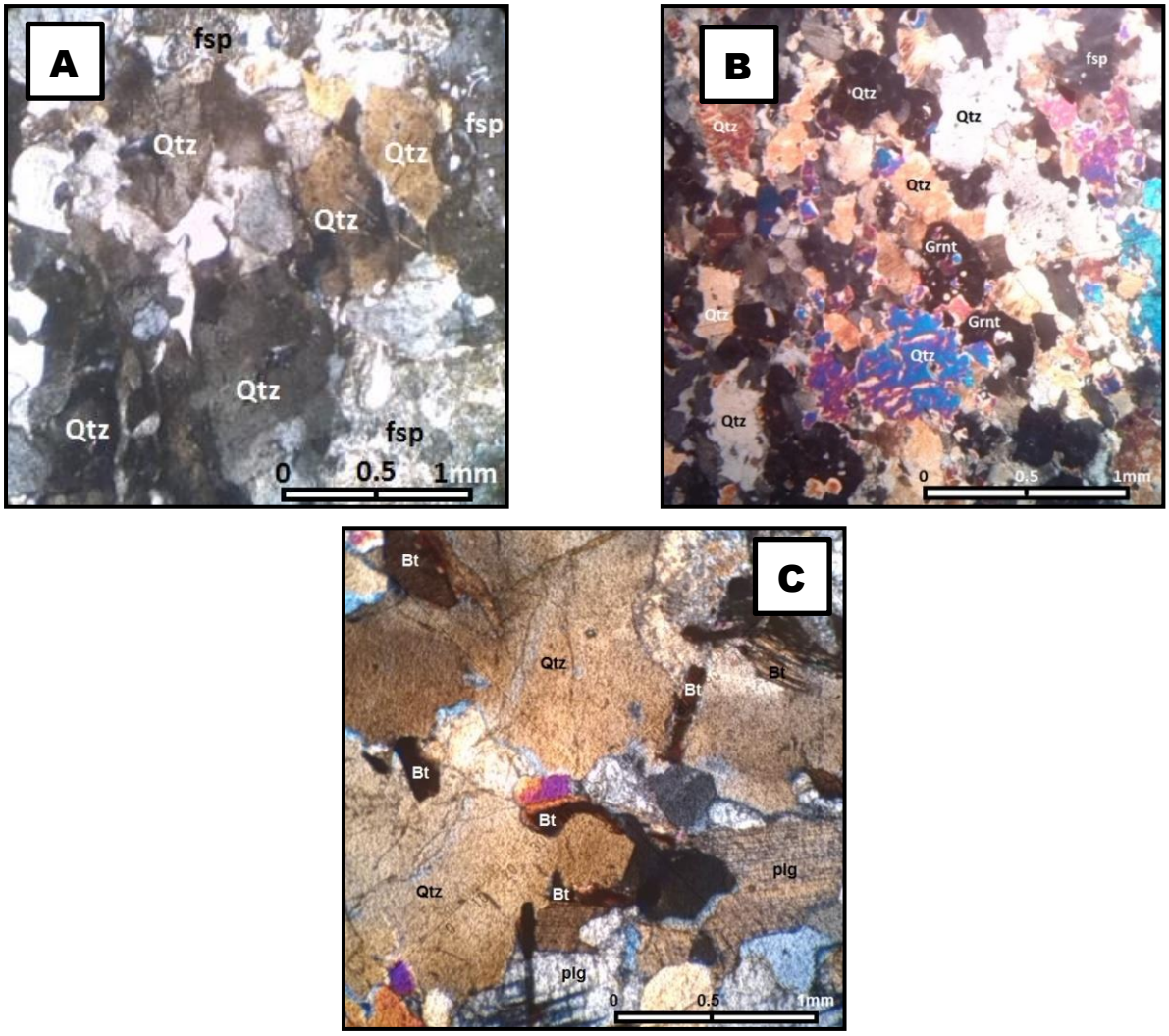

Figure 3-9. *A) Sample Q190 displays large anhedral quartz grains with sharp grain boundaries. They show undulose extinction and are in contact with sericitized feldspar grains. B) Sample Q067 also displays these quartz grains as anhedral crystals although some of their colours are 2nd order blue and purple due to this portion of the slide being slightly thicker. Sample Q067 also contains two subhedral garnet crystals with well-rounded quartz inclusions. Due to the the slight increase in garnet content the abundance of feldspar is very low in this rock in comparison to the other samples.* C) Image of Sample 068 under crossed polars displaying smoky feldspars along with quartz with undulose extinction and anhedral plagioclase with straight to curved grain boundaries.

3.4 Meta-pelitic gneisses

3.4.1 Macroscopic description and field relations

Metapelite is one of the dominant metasedimentary lithologies within the study area. The medium-coarse grained metapelites have varying appearances mainly due to their grain size and mineral textures. These rocks have a migmatitic appearance, with alternating bands of biotite-cordierite-sillimanite- rich palaeosomes interlayered with thick coarse grained garnet-rich quartzo-feldspathic leucosomes (Figure 3-10A, B). Garnet which reaches a maximum size of 4cm in hand specimen is an

almandine as they are bright red in color. The meta-pelites occupy the southern hinge of the Kliprand domal structure (Figure 3-1) and are found as lenses within the hinges of some fold closures. In comparison to the surrounding rock types they are not voluminous in outcrop extent and are found as narrow regional fabric-parallel bodies within the late-tectonic granites and are also associated with other supracrustal units (Macey, 2001; Macey et al., 2011).

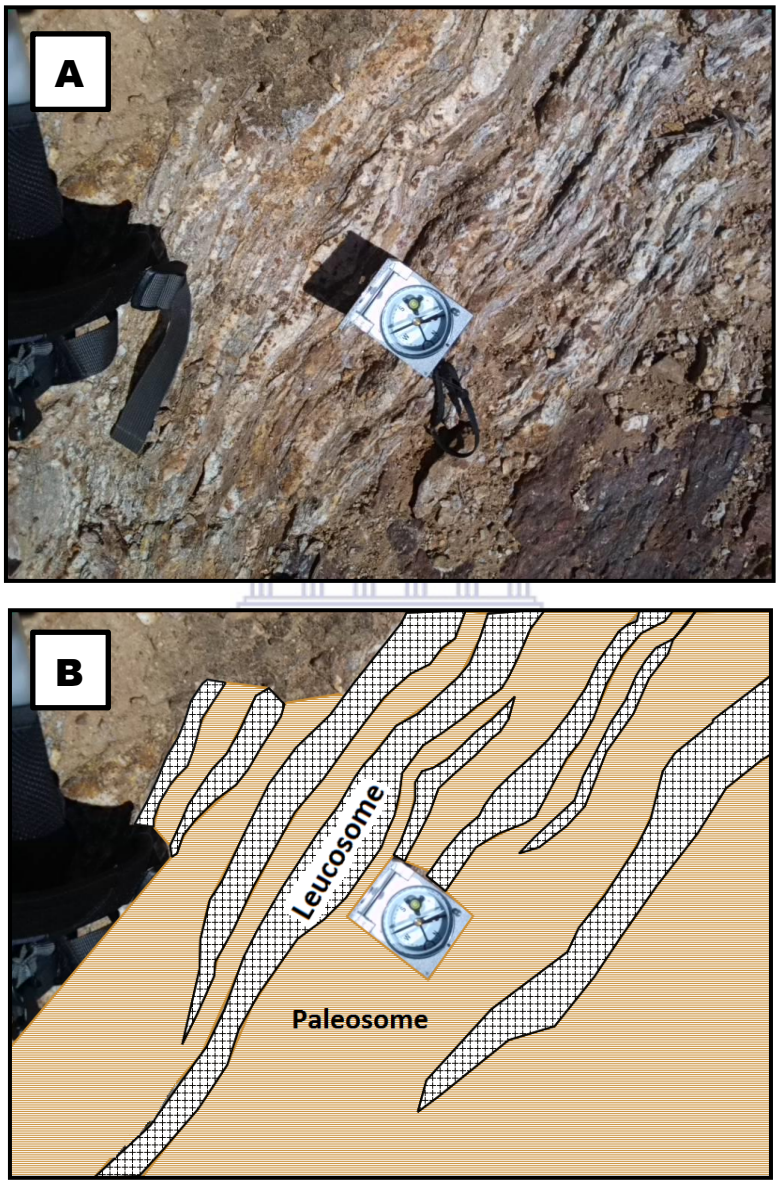

Figure 3-10 A) The flat outcrop of metapelitic gneiss outcropping in the southern closure displays a strong migmatitic texture containing a melanosome of cordierite-sillimanite-K-feldspar-rich restite and a leucosome of anhydrous quartz, K- feldspar and garnets. B) *Graphic view of the visible melanosomes and leucosome of the above image.*

The melanosome/paleosome of the metapelite is typified mainly by the mineral paragenesis K-feldspar + cordierite + plagioclase + garnet + sillimanite + biotite with a lower abundance of quartz.

The leucosome is largely composed of quartz + K-feldspar + garnet with less biotite. Moore (1989) proposed that this mineral assemblage is a prograde metamorphic reaction whereby:

Sillimanite + biotite + quartz ⟶ cordierite + garnet + K-feldspar + (either melt or H_2O)

3.4.2 Microscopic descriptions

The microscopic study focusses on the restite/paleosome, as this resembles the left over material after the reaction. The paleosome displays a streaky appearance characterized by lenticular biotite and sillimanite, with spots of garnet set in a medium grained matrix of quartz, Orthoclase feldspar and cordierite. Large sillimanite needles are generally well oriented within the gneissic banding and define a pronounced linear fabric. A microscopic view of the paleosome shows that the minerals alkali-feldspar (27%), cordierite (17%), almandine (15%), quartz (12%), sillimanite (10%), biotite (8%), plagioclase (5%) and opaque minerals (3%) make up the majority of this rock (Appendix B).

The anhedral cordierite has an average modal abundance of 17% and is commonly quite small, with grain sizes ranging between 0.2-0.8mm which is in agreement with Macey (2001). Under crossed polarized light the cordierite crystals have a dusty appearance with twinning that resembles plagioclase (Figure 3-11A). Most of the cordierite grains have not been altered; in sample M205, however, quite a few of the cordierite crystals have been completely altered to pinite (Figure 3-11B).

Sillimanite was commonly found as long prismatic grains (Figure 3-12A) except for where it occurs as inclusions within almandine (indicating that they formed before almandine). The majority of the fibrolite inclusions have been folded and are not well aligned. However, when fibrolite inclusions are aligned in garnet (Figure 3-12C) then they are also oriented parallel to the main and external foliation. In most cases the fibrolite inclusions have been folded and reoriented. Even though the fibrolite inclusions have random orientations, one garnet grain has sillimanite needles that have been folded (Figure 3-12B). The folded sillimanite needles therefore predate the regional gneissic banding in which the garnet has developed.

Biotite is moderately pleochroic as it changes from dark red to brown in colour. Surrounding garnet they are commonly found as euhedral lath shaped grains compared to where they occur as inclusions where they are mainly anhedral. The grain sizes of the inclusions and the surrounding biotite is almost identical. As there are no replacements or overgrowths of biotite by almandine and/or K-feldspar, the inclusion of biotite and sillimanite in almandine suggests that they possibly reacted to form almandine.

Alkali feldspar is the most abundant leucocratic mineral. It has an average modal abundance of 27% with grain sizes ranging between 0.2-1mm. Locally the orthoclase feldspar is found as xenoblastic microperthitic grains with thin lamellae of albite. Locally slightly larger crystals, with sizes of 1.5-1.8mm, occur; due to recrystallization during granulite facies metamorphism.

The only common characteristic between the melanosome and the leucosome was the presence of garnet; however, the garnet in the melanoosome was slightly smaller than that in the leucosome with sizes ranging between 1.5-3.0mm. Here the subhedral to anhedral almandine garnet makes up approximately 14% of the rock mass. They commonly have irregular grain boundaries with inclusions of opaque minerals, quartz, sillimanite and biotite (Figure 3-12C-D).

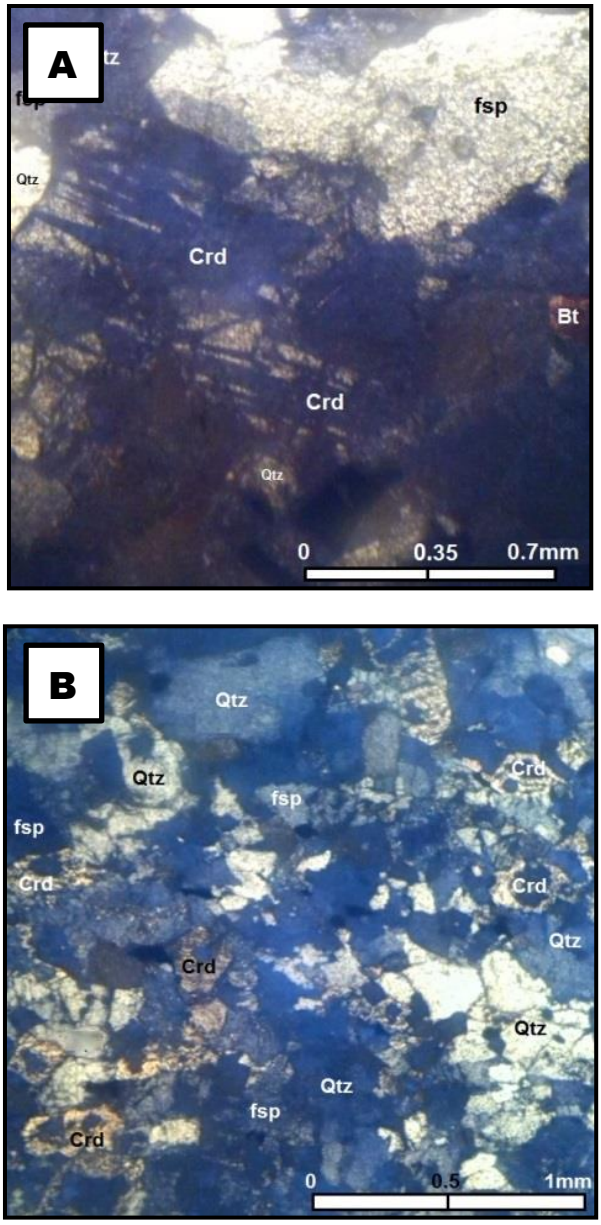

Figure 3-11. A) Sample M205 displays 0.3-1mm cordierite grains displaying twins that resemble that of plagioclase. These cordierite grains are commonly anhedral to subhedral with hardly any alteration observed. b) Sample M205 displays well-defined subhedral to euhedral cordierite crystal grains.

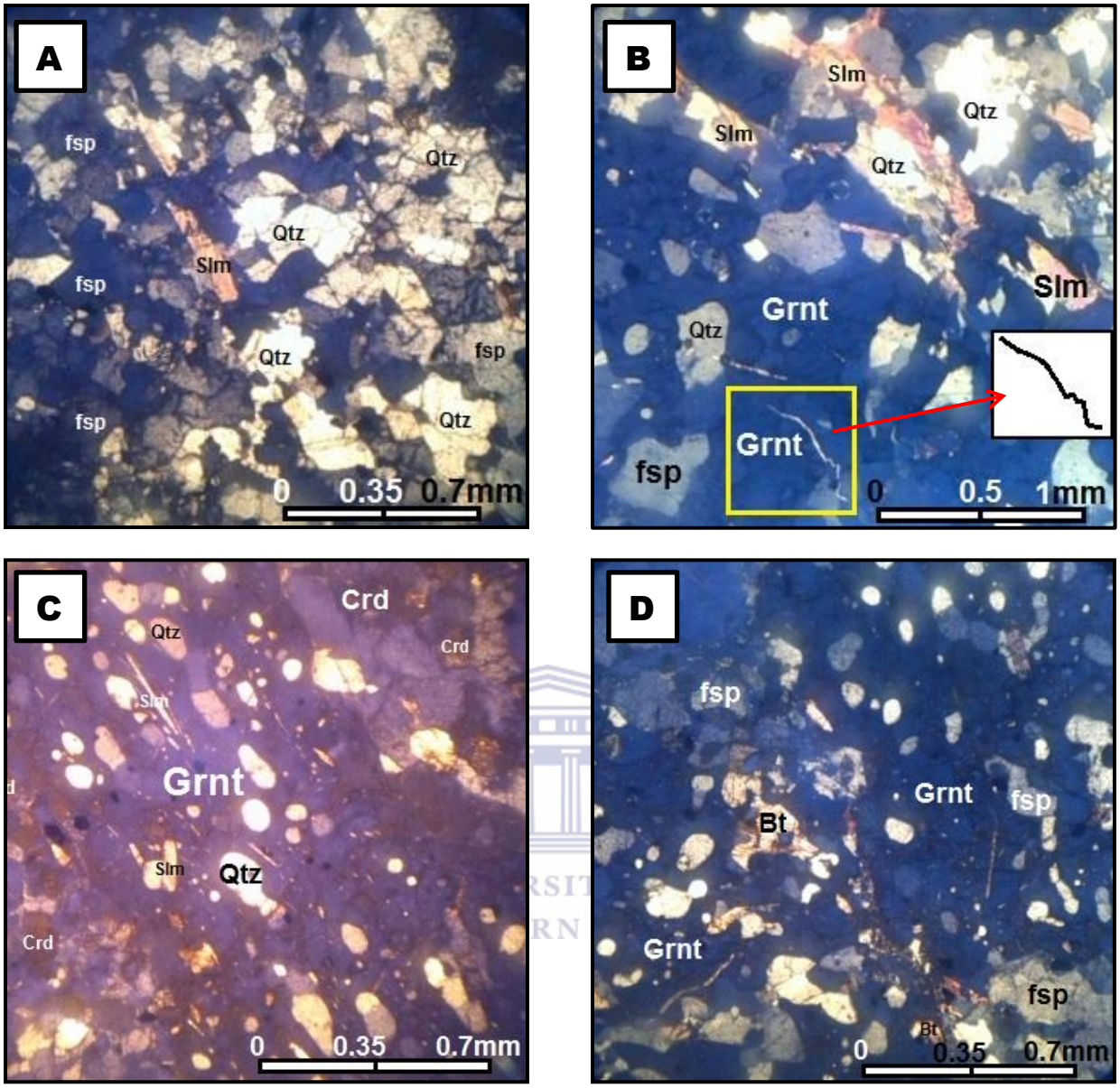

Figure 3-12. A) Image of sample M205 displaying relatively well aligned sillimanite needles. B) Image of sample M103 which displays the appearance of well aligned euhedral sillimanite needles that are found as inclusions within the garnet crystals. C) Image taken of sample M205 displaying an elongate sillimanite needle as well as well-rounded slightly elongate quartz grain inclusions within an anhedral elongate garnet. D) Image of sample M205 showing well rounded quartz inclusions as well as biotite inclusions within an anhedral garnet crystal.

3.5 Gabbro-norite

3.5.1 Macroscopic description and field relations

These mafic rocks are commonly foliated (S_2 gneissic fabric) and exposed in the southern and eastern closure of the Kliprand domal structure (Figure 3-1). In the Kliprand area these medium to coarse grained gabbro-norites are locally found adjacent to large bodies of charnockite (Maier et al., 2012). The mafic gneisses are dark red to black in colour, they do not have a distinct shape but are commonly observed as narrow, low lying rounded boulders (Figure 3-13A). Field exposures display 5-10m rounded boulders separated by narrow bands of alluvium; together these minor rounded boulders forms 100m dyke like bodies. The gabbro-norites are locally observed as dykes intruding into the pink gneiss (Figure 3-13B, C) and commonly found occupying fold hinges. Due to their rather dark colour (Figure 3-14) some field exposures closely resemble the metasomatic charnockites.

In hand specimen (Figure 3-14), however, it can be seen that the mafic rocks are medium to coarse grained and have a distinctly black colour in comparison to the grey looking charnockites. These gabbro-norites are characterised by pervasive S_2 foliation and do not intrude the late tectonic Spektakel Suite granitoids, as was also observed by Albat (1984); Macey (2001) and Macey et al., (2011). In hand specimen (Figure 3-14) it is rather difficult to confirm whether or not the mafic rock contains two pyroxenes. The medium to coarse grained mafic rock resembles a gabbro with its major mineral composition being plagioclase, pyroxene and abundant well aligned biotite, with minor amounts of quartz and other accessory minerals making up the rest of the rock. Mclver et al. (1983); Maier et al., (2012) states that the meta-gabbro-norite represents a possible significant source of nickel and chromium.

3.5.2 Microscopic descriptions

Albat (1984) termed the gabbro-norite a granulite due to the presence of hypersthene; in cases where this rock contains both clinopyroxene and plagioclase in addition to orthopyroxene the rock is referred to as a hypersthene granulite. The two-pyroxene granulite or gabbro-norite as it is more commonly known (Hamman, 1996; Macey, 2001; Macey et al., 2011) consists of plagioclase (26%), K-feldspar (18%), moderately aligned biotite (15%), orthopyroxene (12%), quartz (10%), clinopyroxene (7%), hornblende (6%), olivine (4%) and opaque (2%) (Appendix D, Table AD-7). It is a medium grained (0.5-2mm) rock and has an equidimensional, interlobate, and granoblastic texture as was confirmed by Hamman (1996).

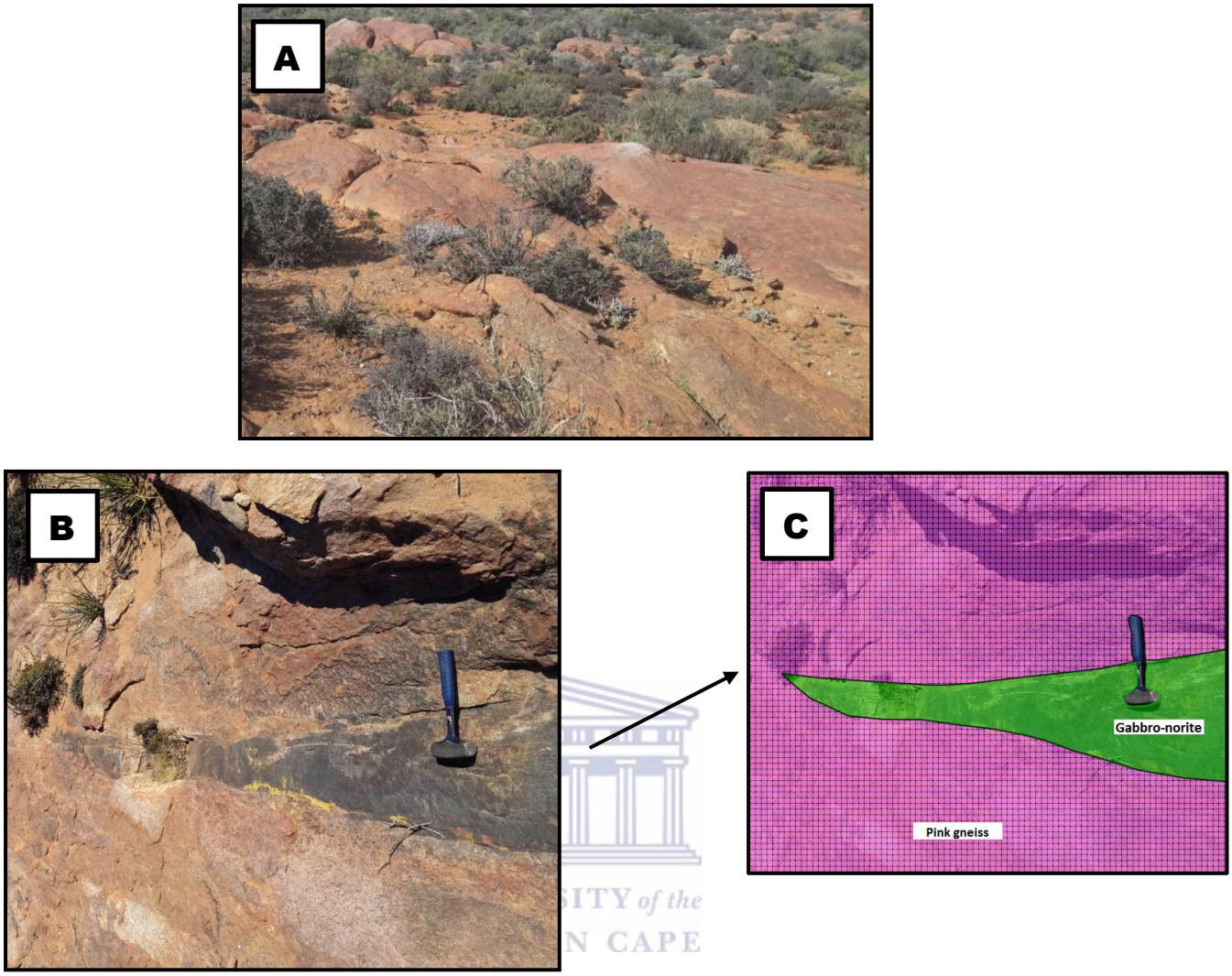

Figure 3-13*. A) Rounded boulders of gabbro-norite outcropping east of the interior domal structure. B) Lense of gabbro-norite within the pink gneiss. The gabbro-norite is clearly younger than the pink gneiss.C) A graphic view of the above image, outlining the contact between the two lithologies.*

Figure 3-14*. Sample of meta-gabbro-norite from the large mafic body that outcrops as lenses within the Kliprand domal structure. Pawn piece is 6 cm in size.*

Subhedral plagioclase is the most abundant mineral accounting for about 26% of the modal abundance of the average granulite specimen, with more than 70% of these grains ranging in size from 0.5-1.2mm and the remaining 30% being less than 0.5mm in size. Most of the plagioclase in the gabbro-norite has thin (0.2mm), well-defined twin bands, while broad, well developed albite twins were also observed (Figure 3-15A). Polysynthetic twinning is common, although Carlsbad twins and cross hatching (Figure 3-15A) are also observed. These twins display deformation textures, notably the termination of lamellae inside grain boundaries with tapered terminations and bent albite twins (Figure 3-15B). Recrystallization of grains is indicated by serrated grain boundaries as was also viewed by Hamman (1996).

Petrographic observations confirm field observations where the gabbro-norite is rich in biotite, forming a well-defined foliation. Similarly to field observations, the microscopic analyses also show abundant biotite (average of 15%) in comparison to the majority of the rock types in the Kliprand dome. The majority of the biotite grains have a distinctly dark red to brown pleochroism and occur as laths that are smeared out between plagioclase and alkali feldspar grain boundaries (Figure 3-15D-E). They are moderately to well aligned forming a moderate foliation (Figure 3-15D). Larger biotite grains were also observed but occur as idioblastic crystals with a moderate dimensional preferred orientation (Figure 3-15D) (Albat, 1984).

For the two pyroxenes present in the gabbro-norite, orthopyroxene has a higher modal abundance (12%). The mineral occurs as small xenoblastic grains and is commonly interstitial (Figure 3-15B); they are always pleochroic, but the intensity of the pleochroism is very weak (Albat, 1984). Under plane polarised light the clinopyroxene is pale green to brown. The grains range in size between 0.3-0.7mm although larger grains of 1.3mm have locally been observed.

Clinopyroxene makes up 7% of the average modal abundance for the gabbro-norite. They have a pale-green colour and usually lack pleochroism, but in some specimens it is weakly pleochroic (Albat, 1984). The clinopyroxene has a subhedral to anhedral granular shape and the grains are commonly quite small ranging between 0.2-0.7mm (Figure 3-15E). The mineral forms equidimensional xenoblastic grains with embayed contacts. Hornblende is locally observed along cleavage traces and grain boundaries overgrowing and replacing clinopyroxene (Albat, 1984). Where clinopyroxene is in contact with hornblende, the grain boundaries are commonly serrated as was also found by Albat (1984).

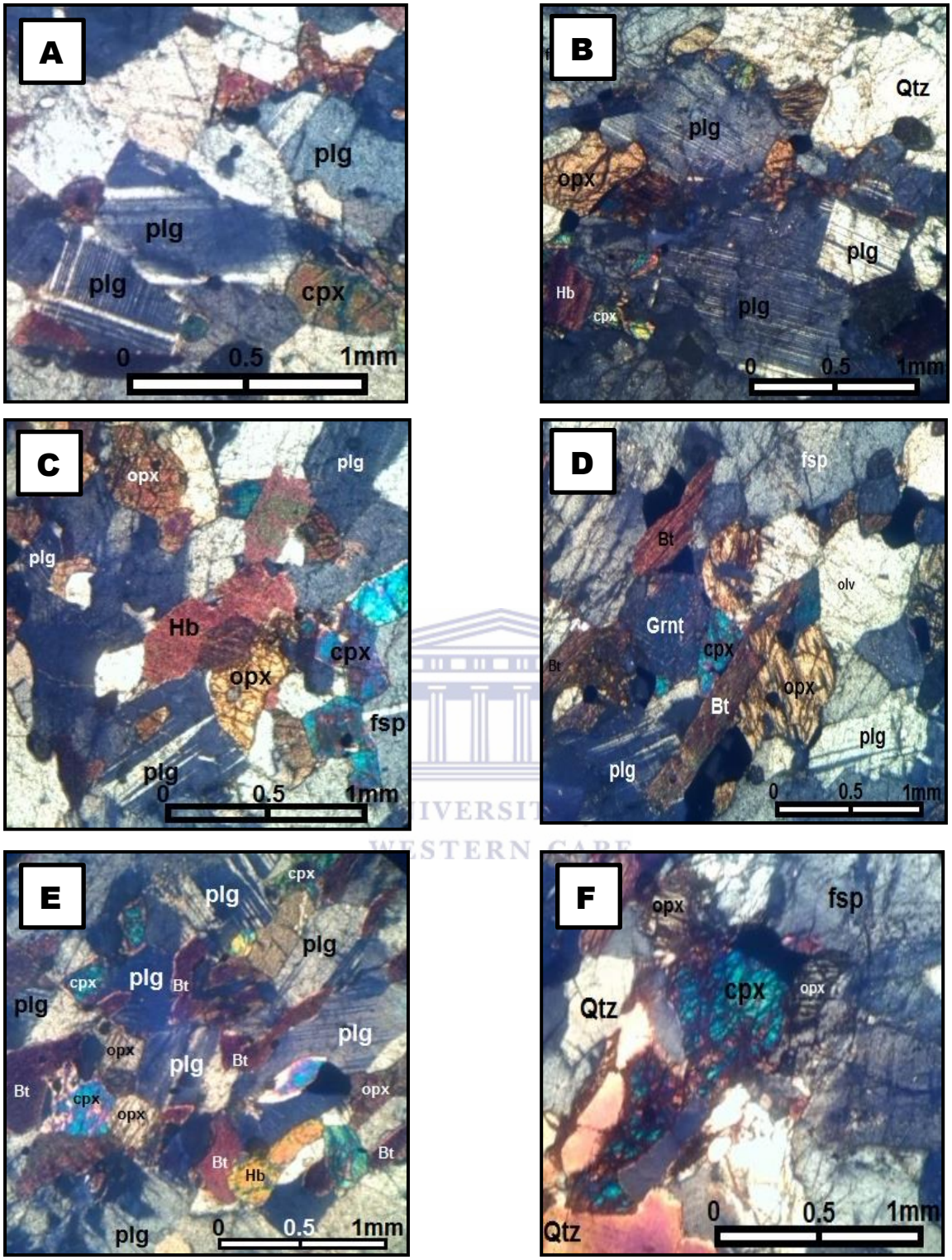

Figure 3-15. *Petrographic photomicrographs of the gabbro-norite. A) Sample from specimen G184 displaying subhedral plagioclase crystals with thick albite twins as well as thin polysynthetic twins, displaying varying anorthite content. B) Sample 167 displays plagioclase with. All images taken under crossed polars. C) Sample G184 displays highly fractured anhedral orthopyroxenes adjacent to subhedral plagioclase. One of the plagioclase crystals has tapered albite twins. D) Sample 167 displays clinopyroxene adjacent to biotite while orthopyroxene has overgrown part of the biotite. E) Sample 184 - Clinopyroxene ranges in size from 0.2-0.5mm and has abundant fractures. They have prismatic grain boundaries and are adjacent mainly to biotite and orthoclase feldspar. F) Image of Sample 33 under crossed polars displaying an anhedral clinopyroxene with 90° cleavage planes.*

3.6 Charnockite

3.6.1 Macroscopic description and field relations

The contacts between the lithologies of the highly deformed Kliprand domal structure are commonly obscured and difficult to determine. The conventional approach for determining whether this rock type is magmatic via the appearance of a cross cutting relationship between the charnockite and the older rocks in the study area does not necessarily apply in this case, as high grade metamorphic terrains and in particular upper granulite facies areas (metamorphic grade of this area), represents lower crustal sections. Similarly to the majority of the rock types in the study area, the charnockite also has a gradational contact (Figure 3-16A, B), however, the gradational contact for many rocks in the study area can be unclear given the P-T conditions to which the rocks have been subjected. Field evidence suggests that the charnockite within the Kliprand dome does not appear to be related to the post-tectonic magmatism, so a metasomatic origin is possible. More evidence needs to be provided before metasomatic could definitely be confirmed as the origin for these charnockites. These rounded boulders and large dome-like slabs of charnockite are found within the southern and eastern closures of the Kliprand domal structure (Figure 3-1). On the southern limb of the large Kliprand domal structure the charnockites lie adjacent to the mafic gabbro-norite.

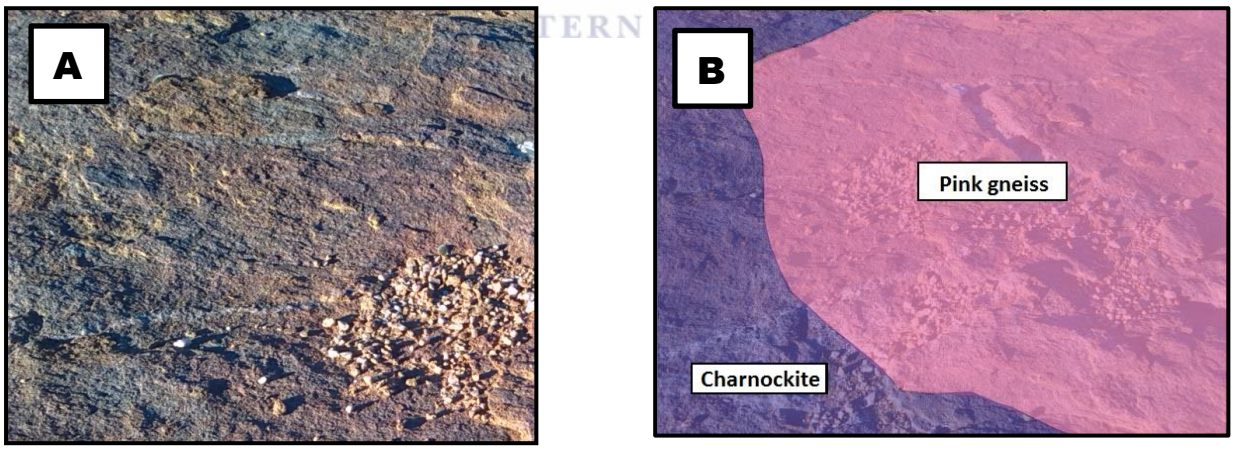

Figure 3-16. A) Gradational contact between the pink gneiss and a fresh exposure (dark green to olive-brown colour) of metasomatic Charnockite/Granulitic ("charnockitised") pink gneiss, characteristic of the metamorphogenic charnockites in outcrop. B) Graphical representation of the gradational contact between the two rock types. Pawn piece is 6 cm in size.

The charnockite may be a metasomatised pink gneiss, as they are commonly observed (field observations) as lenticular bodies adjacent and texturally and mineralogically (except for the presence of pyroxene) similar to the pink gneiss. In hand specimen and fresh exposures (Figure 3-

16A), the charnockite is characterized by a dark green to olive-brown colour, whilst weathered outcrops are dark red/brown in colour; these are characteristic of Macey (2001) and Macey et al. (2011) metamorphic charnockites within the Loeriesfontein area. The charnockite in the Kliprand dome could also be termed enderbite (igneous rock of the charnockite series) as it is mainly constituted of quartz, olive-brown alkali feldspar (responsible for the green hue in the rock) and pyroxene.

3.6.2 Microscopic descriptions

This metamorphic charnockite is a granulite facies rock characterized by the co-existence of both orthopyroxene and K-feldspar (Yardley et al. 1990). Regarding to the mineralogy, this rock consists of orthoclase feldspar, quartz, plagioclase, together with interstitial orthopyroxene (hypersthene) and tabular biotite grains (Appendix D, Table AD- 9) as also found by Macey, (2001). The texture of these rocks can be described as "granoblastic interlobate."

Felsic minerals

Orthoclase feldspar is the most abundant mineral, with a bulk modal composition of 33%. 50% of the orthoclase contains albite lamellae and can thus be termed perthite (Figure 3-17A, B). These large anhedral-subhedral crystals have well rounded embayed lobate crystal boundaries. Perthite occurs as xenoblastic grains with large embayments, indicating that they were not in thermal equilibrium at the peak of metamorphism. Locally some of the cloudy orthoclase feldspars display crossed hatched twinning, this crossed-hatch twinning is typically thinner and not as well developed or as clear as in microcline.

Quartz has the second highest modal abundance of 26%, and is observed as both granoblastic and interstitial grains. Under crossed polars quartz (Figure 3-18C, D) displayed undulose extinction observed. Figure 3-17B below displays a quartz grain with a biotite inclusion, possibly indicating a metamorphic reaction involving both.

Plagioclase accounts for 16% of the charnockite. These anhedral to subhedral plagioclase grains, with local rounded quartz inclusions, form 0.3-0.8mm grains that display albite bands, localised cross-hatched twinning and commonly a myrmekitic intergrowth with quartz (Figure 3-17C). With regards to ductile deformation of plagioclase, the albite twin lamellae are slightly bent in places (Figure 3-17D).

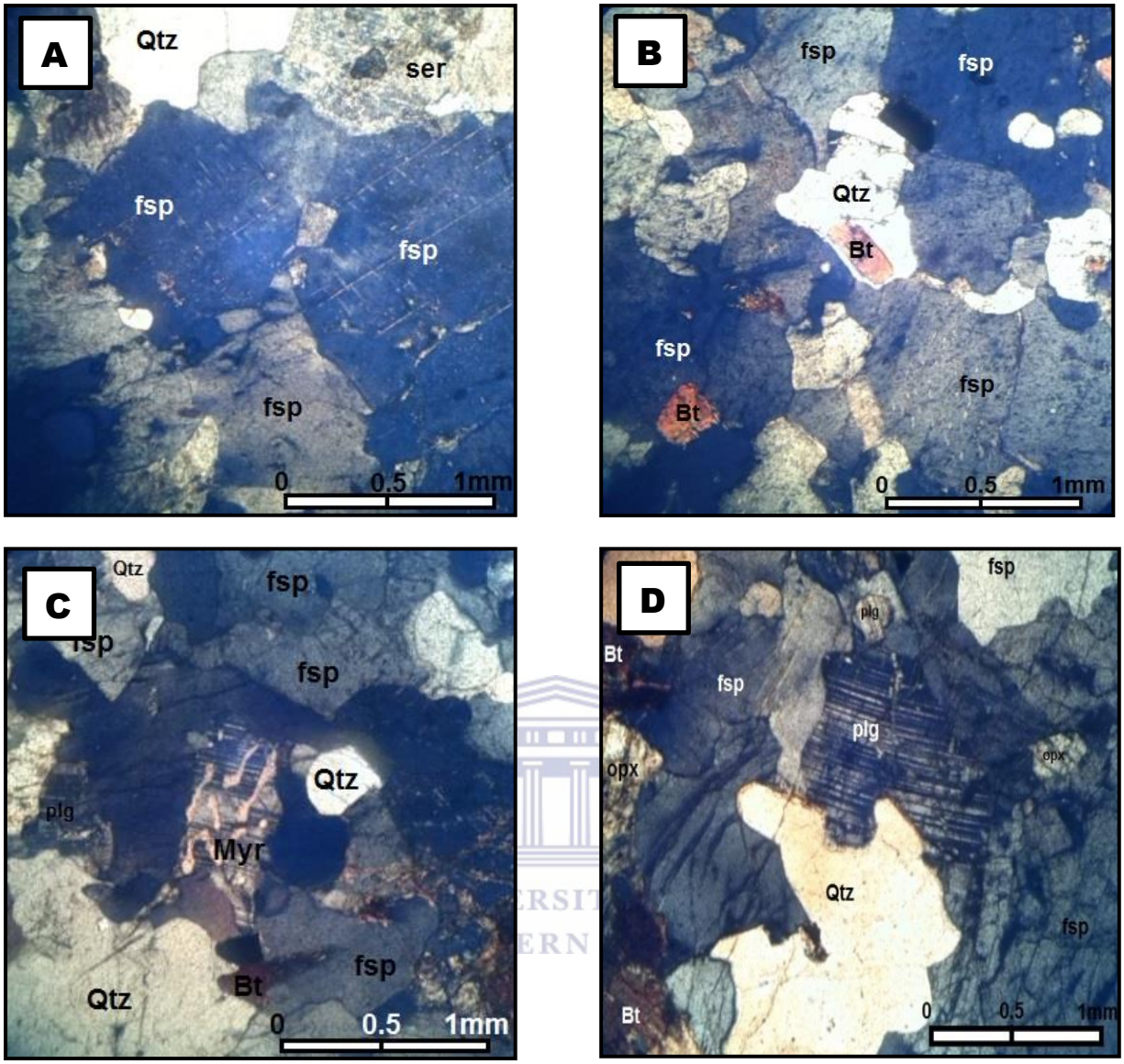

Figure 3-17. Photomicrographs of the charnockite taken under crossed polars. A) Sample C35 displays a 2.5mm subhedral perthite grain with sharp grain boundaries and containing white albite lamallae. 2% of these feldspar grains are perthitic while 15% underwent secondary sericitization alteration. A sericitized feldspar is seen at the top of the photo. B) Sample C63 displaying anhedral quartz grains with well rounded grain boundaries and a biotite inclusion within a quartz crystal. C) An anhedral plagioclase with a myrmekitic texture surrounded by a quartz grain that displays undulose extinction. Alongside the myrmekite there is a plagioclase grain that has both thick and thin polysynthetic twin bands. D) Image of sample 222 displaying a plagioclase with slightly bent and tapered albite twins; this feature was not seen in any other specimen.

Mafic minerals

Biotite is present in the majority of the thin sections examined, generally in small amounts (12%). Sample C63 has a higher abudance of biotite with a modal composition of 16% (Figure 3-18B). The mineral has a very dark red-brown pleochroism, and is commonly observed as thick biotite laths of 0.2-0.9mm in length (Figure 3-18A, B). Orthopyroxene has a low modal abundance of 4% and is 0.2-

0.7mm in size. The orthopyroxene grains have a low birefringence from colourless to pale green, and forms subhedral to anhedral grains with well-rounded grain boundaries (Figure 3-18D) in comparison to the feldspars and quartz that display sharp grain boundaries. The mineral is partially altered to chlorite along the grain (Figure 3-18D), with some portions of the minerals being entirely replaced.

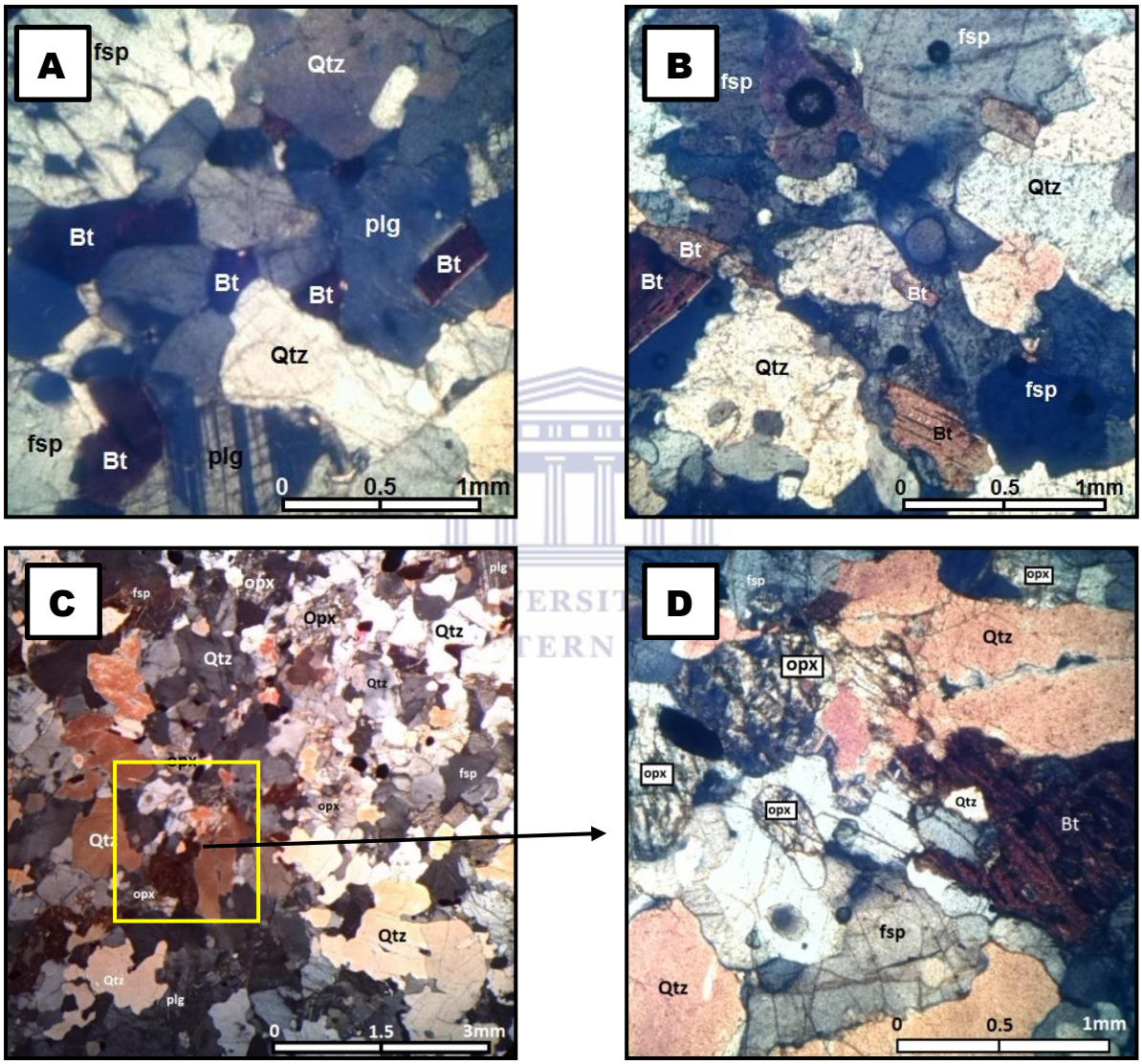

Figure 3-18. A) Image of sample C133 under crossed polars. Dark red biotite was found interstitially between the feldspars and as inclusions in both feldspar and quartz grains. B) An image of sample C63 displays a light brown biotite with a prominent cleavage about 0.5mm in length. C) A large scale view of sample 222 under crossed polars. D) Anhedral orthopyroxene as well as anhedral to subhedral feldspar grains.

3.7 Ibequas granite

3.7.1 Macroscopic description and field relations

The Ibequas granite is a leucocratic magmatic rock characterized by a snow white colour and spotted 0.5-2cm red coloured garnet porphyroblasts (Figures 3-19, 3-20). Unlike most lithologies found in the study area the Ibequas granite is dispersed rather than clustered at a particular site, and often appears to be cross cutting older rock types in the area. The Ibequas granite is often found in close proximity to a metapelitic migmatite, such as the large exposure of this rock found at the Hondekloof nickel deposit, where it is sandwiched between the metapelite and the overlying quartzite. The Ibequas granite is also found as thin melt segregates within the pink gneiss and charnockites. There has been controversy regarding the origin of these rocks, with Albat (1984) suggesting that these rocks could be supracrustals due to their gradational contact with the pink gneisses. However, he does not rule out the possibility that they might be large in situ leucosomes produced by partial melting of the pre-existing gneisses. The milky-coloured Ibequas granite highly resembles a fractionated melt or leucosome (Figure 3-19). These leucosomes are commonly devoid of preferred mineral orientation, cleavages or even joints (Figure 3-19). Similarly to the study by Macey et al. (2011), this study also observed leucosomes with garnet porphyroblasts oriented parallel to the regional tectonic fabric indicating a late tectonic development. The most prominent minerals that could be identified with the hand lens are alkali feldspar, plagioclase, quartz and large euhedral garnet (Figure 3-20). The grain size of quartz and feldspar in the thicker leucosomes is proportionally coarser (2–3 mm) than the grain size in thinner leucosomes (1–2 mm), suggesting slower cooling and more time to grow for the thicker leucosomes. Penetrative axial planar fabrics are not observed on outcrop scale, which suggests that much of the deformation was syn- to post-tectonic.

3.7.2 Microscopic descriptions

The garnetiferous leucosomes consist predominantly of felsic minerals and large euhedral garnet crystals. The felsic minerals constitute mainly plagioclase (5%), K-feldspar (37%) and quartz (43%) with garnet (8%) and biotite (6%) being the major mafic minerals (Appendix D, Table AD- 11). The leucosome has a predominantly granoblastic texture and is medium to coarse grained with poikilitic garnet porphyroblasts of 2-3 cm size containing quartz inclusions.

Figure 3-19. A 5m wide exposure of Ibequas granite on the southern limb of the Kliprand domal structure.

Figure 3-20. Sample of coarse grained Ibequas granite displaying a 2cm large euhedral garnet surrounded by large milky feldspars and quartz. Pawn piece is 6 cm in size.

The garnet is deep red to black in colour suggesting that it is probably an almandine rather than a pyrope (pinkish red). Some garnet crystals are euhedral with well-defined prismatic shapes (Figure 3-21A). However, the majority of the garnet crystals are subhedral to anhedral with rounded grain boundaries (Figure 3-21B). Deer et al. (2013) states that almandine megacrysts found in leucosomes have been interpreted as the solid products of incongruent melting reactions. The garnet crystals are commonly partially replaced by biotite, along fractures (Figure 3-21B) and also contain quartz inclusions. Biotite is another common mafic mineral (modal composition 6%) which is normally observed as separate randomly oriented subhedral lath-shaped grains. As mentioned above biotite is also found within fractures of the garnet crystals as an alteration filling and rarely biotite rims garnet porphyroblasts.

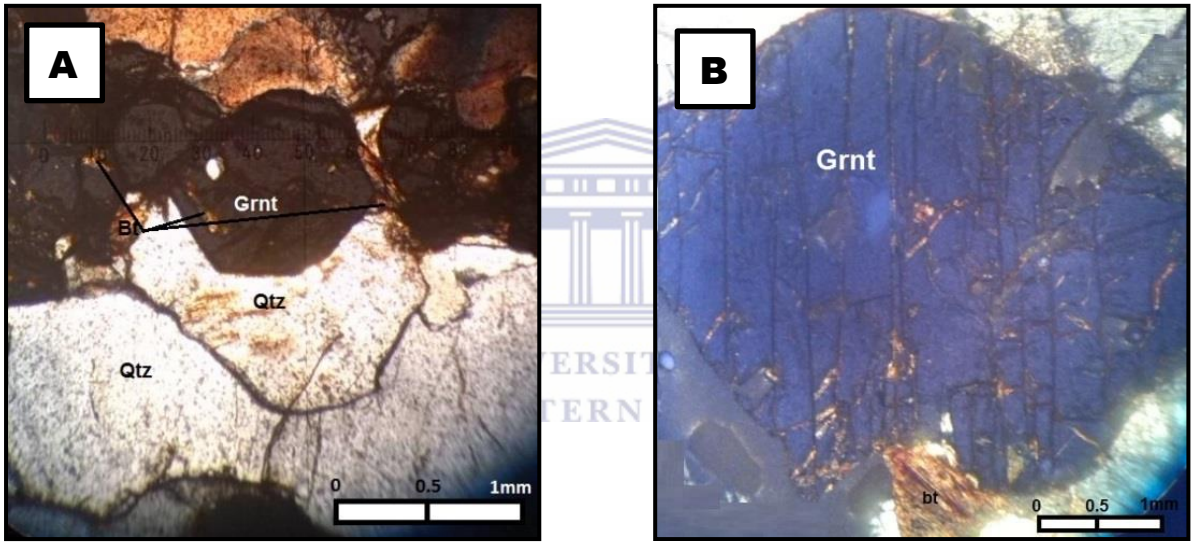

Figure 3-21*. Petrographic photomicrographs of the Ibequas granite taken under crossed polars. A) Sample from specimen IG30 displaying a 1.2mm euhedral garnet crystal surrounded by smaller (0.4-0.8mm) subhedral garnet crystals. B) Sample 142 displays a subhedral garnet with rounded boundaries and a very weak pressure shadow resembling that of an augen.*

Quartz is the most abundant mineral making up 42% of the total rock abundance. Quartz within the Ibequas granite displays undulatory extinction which means that despite being a late anatectic melt it was still subjected to some degree of deformation, and has euhedral grain boundaries with hardly any traces of grain boundary migration. The presence of undulose extinction means that the recovery processes and, thus grain boundary migration have been in progress but did not go to completion due to P/T conditions no longer being favourable. Fluid inclusions, with an average size of 0.1mm, are found within some quartz crystals.

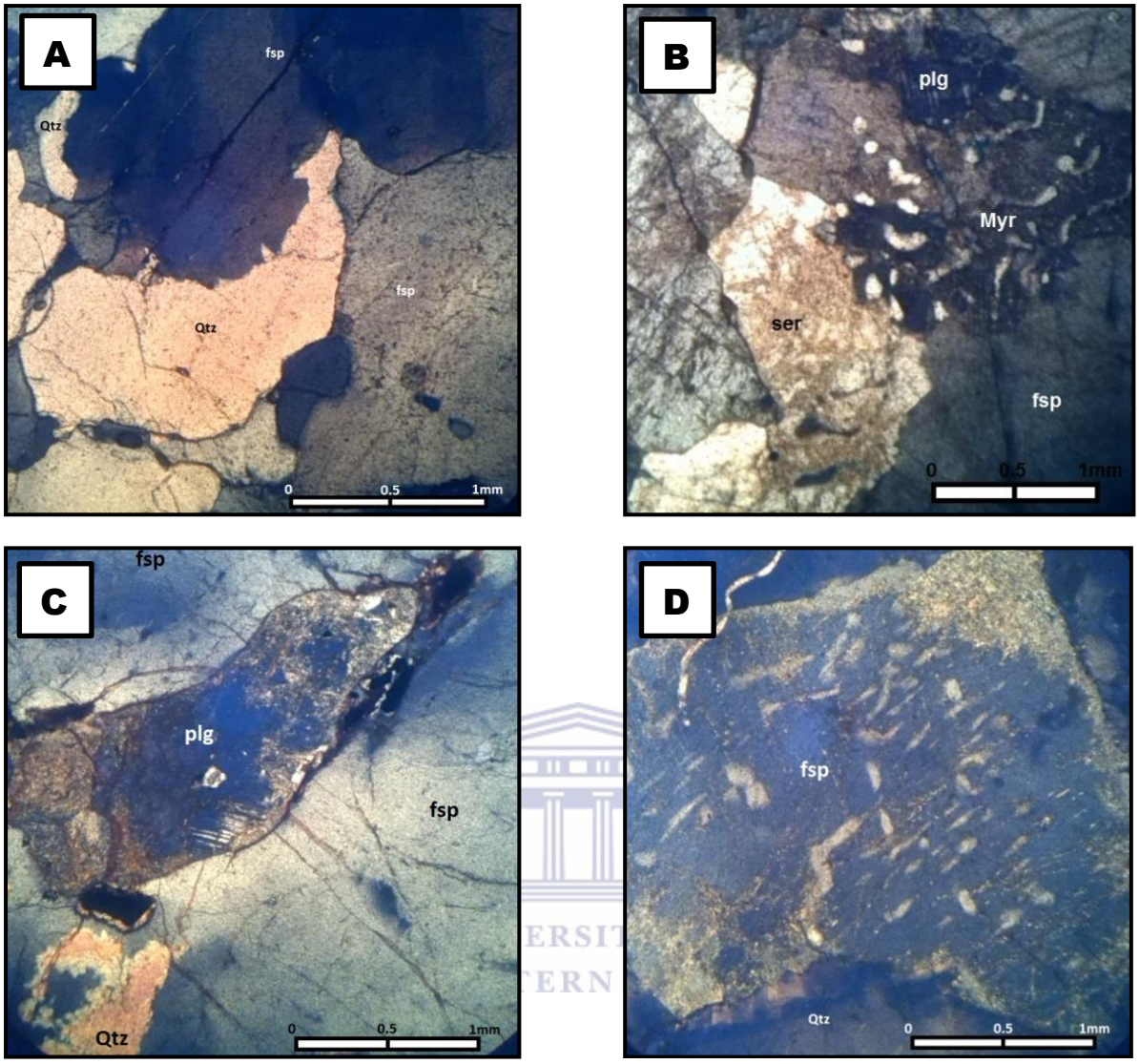

Figure 3-22. Petrographic photomicrographs of the Ibequas granite taken under crossed polars. A) Orange coloured anhedral quartz grains adjacent to subhedral feldspar crystals. B) Image of sample 142 under crossed polars displaying a myrmekitic texture alongside a sericitized orthoclase feldspar. C) View of an anhedral plagioclase grain that has been sericitized. D) Huge perthite grain being subjected to secondary alteration.

These leucogranites contain eqiugranular euhedral to subhedral potassium feldspar (orthoclase) and plagioclase. Orthoclase feldspar is a major constituent of the Ibequas granite, with a whole rock content of 37%. Locally orthoclase feldspar host albite lamellae forming perthite grains (Figure 3-22D) and is locally partially replaced at the borders by myrmekitic intergrowths (Figure 3-22B). Sericite replacing plagioclase (Figure 3-22C) and perthite (Figure 3-22D) was also observed. Plagioclase crystals range in size from 0.5-2.0 mm and make up about 4% of the total abundance.

Chapter 4 : Structural Geology

4.1 Introduction

Based on field observations, four main phases of deformation, D_1 to D4, were identified in the study area. This agrees with the earlier findings of work done by Albat (1984), Macey (2001) and Macey et al. (2011).

Conventions used are as follows:

- S - planar fabrics
- L- linear fabrics
- F - folding of planar and linear fabric
- 1, 2, 3 and 4 refers to the phases of planar fabric, linear fabric, folding and deformation, e.g. F_1 = the first phase of folding. F_2 = second phase of folding etc.

Deformation stages D_1 – D_3 are considered to be the main collisional stages of the Namaqua Orogeny producing high metamorphic grades (Colliston and Schoch, 2013). The 4 major Namaqua deformational events produced intrafolial folds (F_1), large scale tight-isoclinal folds (F_2), open folding (F_3), and localized, mainly antiformal structures (F_4), respectively, within the Garies Terrane (Clifford et al., 2004). The Kliprand domal structure is the most obvious regional structure in the Kliprand District and is dominated by ESE/WNW trending F_3 open folds resembling that of the Springbok Antiform as described by Clifford et al., (2004). Due to the variations in the main structural elements (F_2, F_3 and F_4 folds), the study area was subdivided into four smaller subareas (Subarea 1-4). The purpose of dividing the area into subareas was to create homogenous structures that can be easily described and classified. Subareas 1, 2 (contain a large scale F_3 fold) and 4 (contains a large scale F_4 fold) correspond to the western interior fold closure, the eastern closure and the southern fold closure (Figure 4-1). Subarea 2 was further sub-divided into two subareas, namely subarea 2a, characterized by the eastern fold closure of the interior Kliprand dome, and subarea 2b, characterized by the eastern closure of the large Kliprand domal structure (Figure 4-1). Both domains form part of the approximately east-west trending Kliprand domal structure. The main reason for subdividing subarea 2 into various domains (Figure 4-1) was to correlate them and identify whether or not they they where influenced by the same event. Subarea 3 (contains large F_2 folding) encompasses the entire Kliprand domal structure while excluding the closures (Figure 4-1).

In order to visualise and understand the stress field which created the structures, various stereographic projections were constructed. If large amounts of data were available, a contoured plot of poles to planes (Pi-diagram) was preferred in comparison to plotting a β-diagram. A β-diagram in this case would be cluttered due to all the plotted planes. For this reason, a Pi-diagram is preferred. In order to accurately characterize the various folds in the study area both the β-diagram and the Pi-diagram were utilized. Owing to the fact that the area was subdivided into smaller subareas, certain subareas, such as the western and eastern interior fold closures and southern fold closure, contain a data set of less than 20 points. Due to the relatively low number of points for subareas 1, 2a and 4, β-diagrams were displayed as this was more appealing. However, Pi-diagrams (utilizing both poles to planes and contours) aided in obtaining the two limbs of the fold.

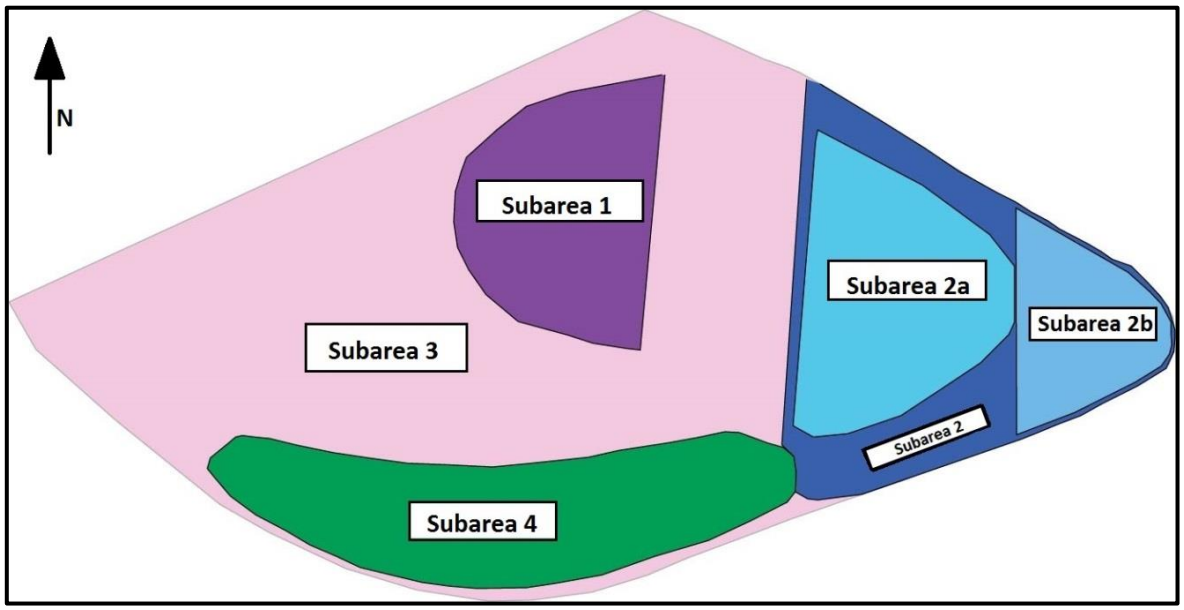

Figure 4-1. Outline of the study area showing the extent and boundaries of Subarea 1, 2 (subdivided into 2a and 2b), 3 and 4.

By contrast, subareas from which abundant data was collected, such as the larger subareas 2b and 3, were plotted on Pi –diagrams. Both the Pi-diagrams and β-diagrams were constructed using the Midland Valley Move^{TM} software. Density contours were constructed in order to identify the cluster at two maxima corresponding to the two limbs of the fold on the pi diagrams. The orientations of these limbs were then plotted as great circles. The intersection of the great circles at the β-pole represents the fold axis. As the Kliprand domal structure has been subjected to multiple-phases of deformation only the current orientation of the folds axis and current interlimb angle are certain conclusions. The interlimb angle was measured directly off the Pi-diagram between the fold limbs, this offers an estimate of the intensity of folding (Van Der Pluijm et al., 2004; Davis et al., 2011). Before characterizing the axial plane, field and other observations were used in order to classify

whether the fold was symmetrical as this was not always the case. If the axial plane was not measured in the field (and preferably along the fold axis), it may be classified by plotting a girdle, approximately half way between the two limbs of the fold on a stereonet. In a multi-phase deformed area, such as the Kliprand domal structure, it is impossible to conclude the orientation or magnitude of the stresses

4.1.1 First deformation event (D_1)

The only sedimentary rocks found in this study area are the quartzite and metapelite. These rocks, similarly to the remainder of the rocks in the study area, have been greatly reworked and metamorphosed. This area is also highly deformed leaving no clear stratigraphic units within the dome, thus no bedding (S_0) was observed within the study area. The earliest fabric observed in the field area is designated as S_1. The S_1 foliation is characterized by an ESE-WNW gneissic banding (Figure 4-2), developed due to recrystallization of igneous and sedimentary rocks during high-grade metamorphism. Gneissic banding is characterized by a preferred planar orientation of platy minerals such as biotite (Figure 4-2). According to Davis et al. (2011), gneissic banding can develop in granitic rocks that have been deformed and metamorphosed at medium to high grades, or in sedimentary and volcanic rocks that have been metamorphosed at relatively high grades. As this gneissic banding is the earliest fabric observed in the area, the intrafolial folds (developed during its formation are considered to be the first generation of folds (F_1), and are therefore accepted to represent D_1. The rarely observed intrafolial folds F_1 in the Kliprand area are typically less than 6cm in length.

Figure 4-2. S_1 gneissic banding within the metapelitic gneiss. S_1 distinguished on the basis of field evidence

4.1.2 Second deformation event (D_2)

The next pervasive deformational event recorded in the Kliprand domal structure is D_2, the main feature of which is a pervasively developed, subparallel axial planar fabric (S_2) (Appendix E). Kisters et al. (1996) and Raith (1995) labelled the first discernible deformation event after the formation of intrafolial folds the "Namaqua Event" due to its widespread occurrence in Namaqualand and even beyond. The D_2 deformational event formed macro-scale, ESE/WNW trending isoclinal folds (F_2) with an S_2 axial planar cleavage plunging NNE. The S_2 foliations have been observed in all of the lithologies (including the charnockite) except for the Ibequas granite, implying that the Ibequas granite was emplaced late- to post-D_2. In the granitic-gneisses of the LNS as well as in the metapelites, the S_2 fabric is commonly observed as a boudinage in a penetrative gneissic compositional banding, as similarly seen by Kisters et al. (1996) in the other portions of the Bushmanland Subprovince. D_2 augen textures, defined by a biotite foliation wrapped around coarse grained feldspar augen, are observed in the centre of the Kliprand domal structure.

4.1.3 Third deformation event (D_3)

Both Albat (1984) and Macey et al. (2011) describe the third deformational event as characterised by kilometre-scale ESE–WNW trending upright to inclined open folds. In the current study area these folds are clearly observed as antiformal fold closures. In addition to these large structures, F_3 parasitic folds and an S_3 foliation are commonly observed (Figure 4-3A). Parasitic folds have different shapes at different positions within a major fold (Lisle et al., 2011). Z-folds indicate that the major antiformal closure is to the right of the exposure in the direction of viewing, as was observed along the southern limbs of the ESE/WNW trending D_3 open folds as well as the larger scale D_4 folds (Figure 4-5). The S_3 foliation may be described as a non-penetrative, sub vertical planar cleavage (Figure 4-3A), locally filled with thin white to cream-coloured quartz-feldspar-garnet leucosomes, as was also observed by Macey et al. (2011). D_3 definitely postdates the intrusion of the Ibequas granite and charnockites as both of these rock types are folded by D_3 and D_4. Locally an S_2 foliation, defined by the melanosome/ leucosome banding in the migmatites, has been refolded by the D_3 deformation to form refolded folds, as shown in Figure 4-3; a similar relationship was seen in the study area of Larrovere et al. (2011). Two generations of folds (F_2 and F_3) affect the S_1 foliation (Figure 4-3B). F_2 folds are isoclinal and parallel to the S_1 and S_2 main Namaqua fabric, while F_3 folds appear to re-fold the F_2 folds in the migmatites (Figures 4-3A, B).

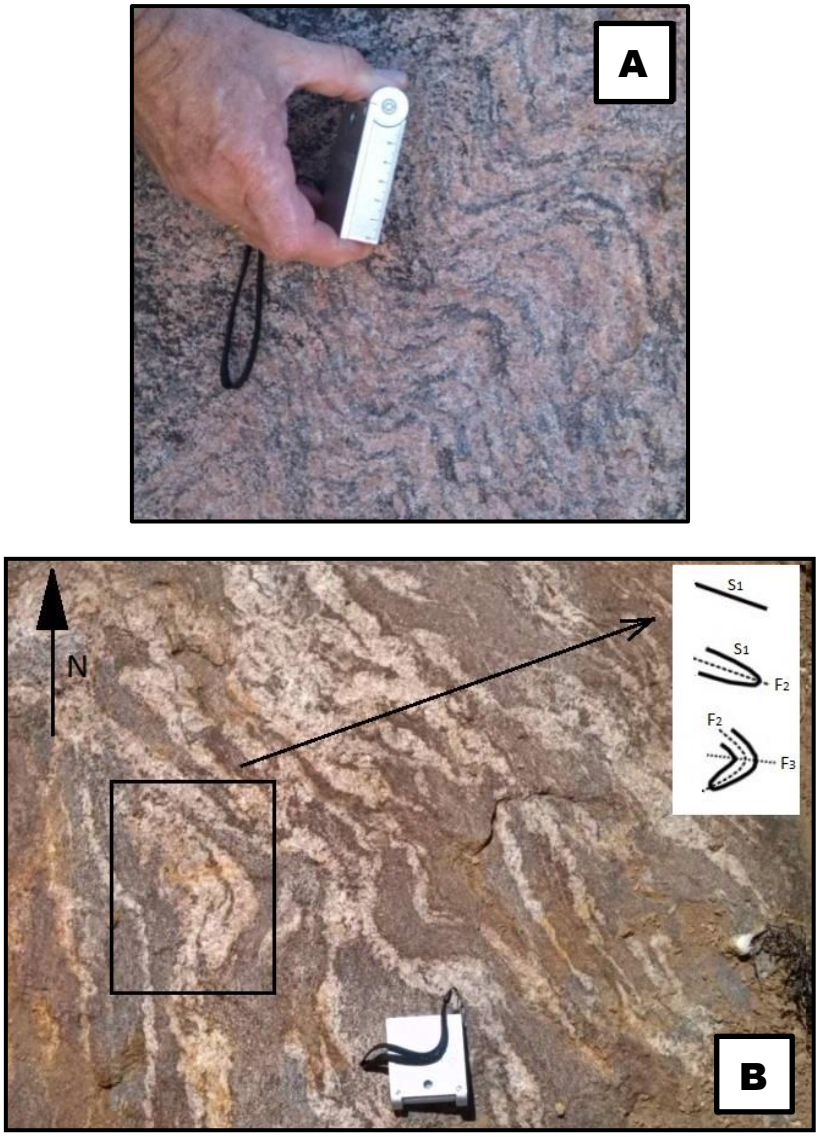

Figure 4-3. A) Crenulation/folding of the dominant S_2 foliation during the development of F_3 folds. The S_3 foliation hasn't quite developed here yet. This is typically found toward fold hinges where S_2 and S_3 change from subparallel on the limbs of the major folds and become more discordant to each other. B) Fold generations affecting the S_1 foliation in a migmatite. F_4 folds are not shown in this figure (too large scale).

4.1.4 Fourth deformation event (D_4)

The D_4 phase is associated with large-scale, NNE-trending gentle folds. According to Macey et al. (2011), the D_4 deformational event folded all previously existing structures, but did not produce any new foliations. They further state that evidence for the existence of F_4 folding includes the reorientation of the S_2 and S_3 fabrics, and can only really be seen when plotting S_2 and S_3 fabrics on stereonets, particularly for the latter (S_3). Within the vicinity of the southern closure of the Kliprand domal structure (Figure 3-1, 4-1, 4-6) a distinct ESE/WNW boudinage and S_2 fabric has been observed to have been folded during a later D_4 deformational event and further cross-cut by jointing

in a yet later brittle tectonic environment (Figure 4-4). Albat (1984) and Macey (2001) and Macey et al. (2011) concluded that the Kliprand domal structure was produced by the interference patterns of D_3 and D_4 fold generations. Interference folding features have not been observed in the field, and would thus be further discussed below.

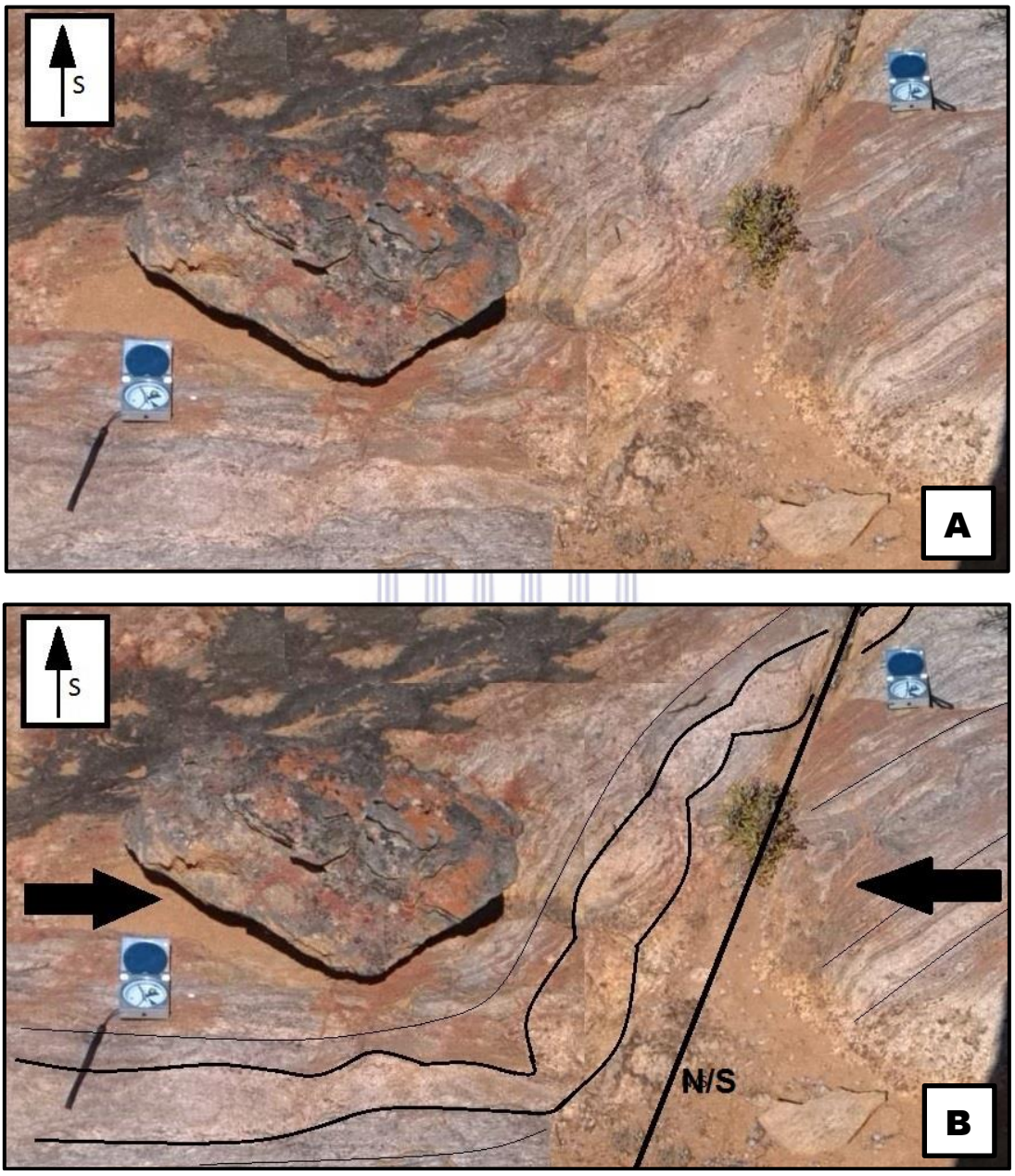

Figure 4-4. A, B – S_2 gneissic banding and boudinage being folded during D4 and later cross cut by jointing in a brittle environment.

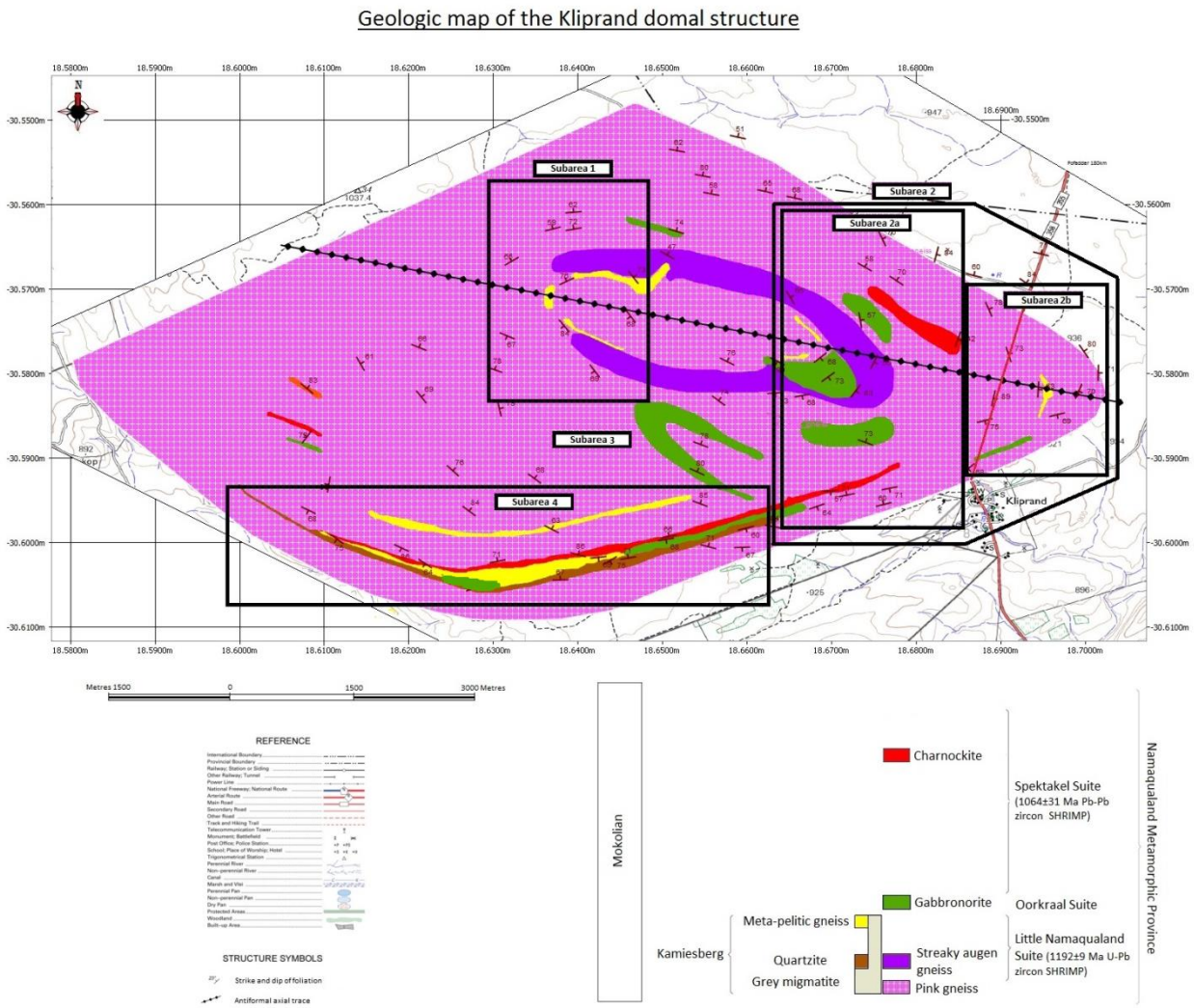

Figure 4-5. Geologic map of the Kliprand domal structure displaying the various structural subareas. Subarea 3 is not outlined as it constitutes the remaining area surrounding the fold closures. Outcrop of the Ibequas Granite was too small to be displayed on the geological map.

4.2 Description of the various subareas

4.2.1 Subarea 1 (macroscale F_3 fold)

Subarea 1 is the smallest of the four subareas with a length (N-S) of 1.7 km and a width (E-W) of 1.3km. In subarea 1, rocks of the LNS containing a distinct foliation of the first and second/ deformation phase, along with rocks of the Kamiesberg Subgroup are folded around the fold closure (Figure 4-7A). The S_3 foliation occurs mainly along the limbs of this structure, with bands of metapelite and leucosomes found in the hinge of the fold. There reason for this is that metapelites contain micas and thus sliding surfaces. The leucosomes are the same as quartz mobilisation, here they move to where there is space which in this case is most likely to be in the hinge area. Dips of the S_3 foliation are at moderate to steep angles (60-80°) to the northwest (285-355°) and southwest (212-262°) as measured on the two limbs of the structure (Figure 4-5). It could thus be speculated that the western interior closure of the Kliprand domal structure is actually developed as a moderately to steeply plunging antiform, cored by rocks of the Little Namaqualand Suite and pink gneiss. A more detailed explanation of domain 1 is given in the stereographic description below. Based on Google Earth image analysis and field data the fold axis trends in a westerly orientation, with the interlimb angle defining an open fold. Cross section A-A' (Figure 4-7B), drawn through the western closure of the Kliprand dome, illustrates the antiformal nature of the western closure of the Kliprand dome, with the core formed by the streaky augen gneiss (LNS) and the pink gneiss (Lekkerdrink suite). Based on this cross section the western closure of the interior Kliprand dome could be categorized as an upright open fold. The augen gneiss in subarea 1 contains an ESE-WNW trending boudinage (Figure 4-6A and B).

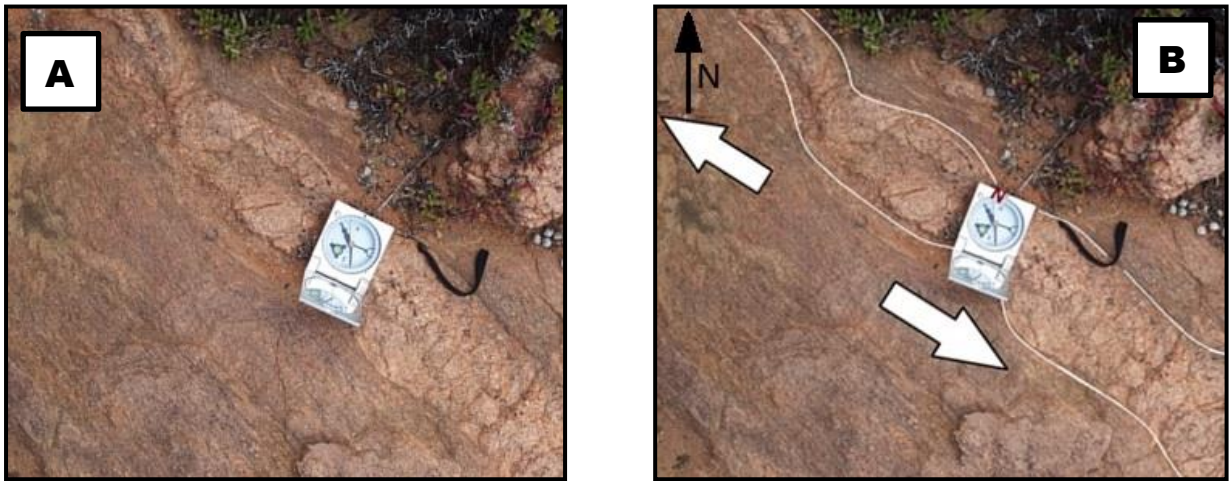

Figure 4-6. A, B - The ESE/WNW trending boudinage and S2 gneissic fabric formed during the high strain D_2 deformational event.

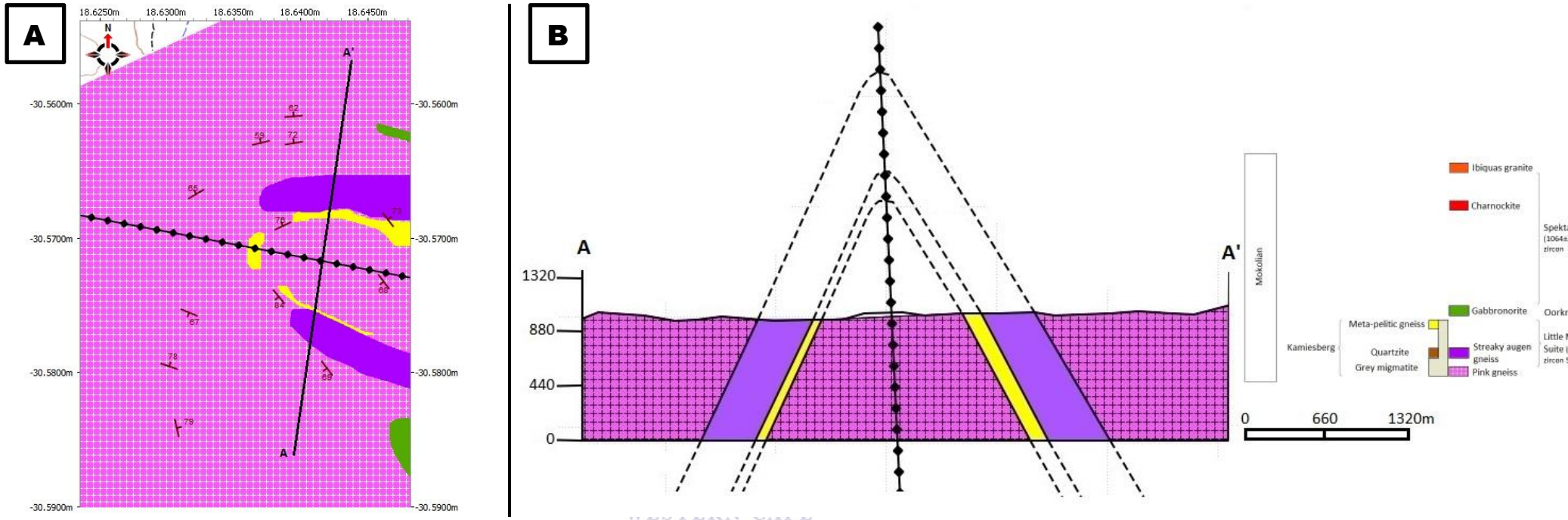

Figure 4-7. (a) Geologic map of subarea 1 with the location of cross section A-A'. The colours shown represent the same lithologies as shown in the geological map (Figure 31). (b) Cross section A-A'.

Due to the small amount of data obtained for subarea 1 a β-diagram was constructed in order to classify the structure (Figure 4-8a, b). As the interlimb angle is approximately 65°, the D_3 structure is best described as an open fold with a fold axis (F_2) plunging 43° towards 284° (Figure 4-8b). As the axial plane dips 85° towards 010° this structure is classified as a moderately plunging upright open fold. The western closure supports the interpretation that this fold closure is a D_3 structure, as mesoscopic folds of this generation of deformation are generally open folds (Albat, 1984; Macey, 2001; Macey et al., 2011). Mineral lineations (L_2), mainly defined by the alignment of amphiboles and micas, are not oriented parallel to the fold axes (Figure 4-8b), but plunge in a NW and SW direction (lineations lie on a great circle) indicating that the later D_3 deformation event have caused the rotation of the earlier L_2 mineral lineation.

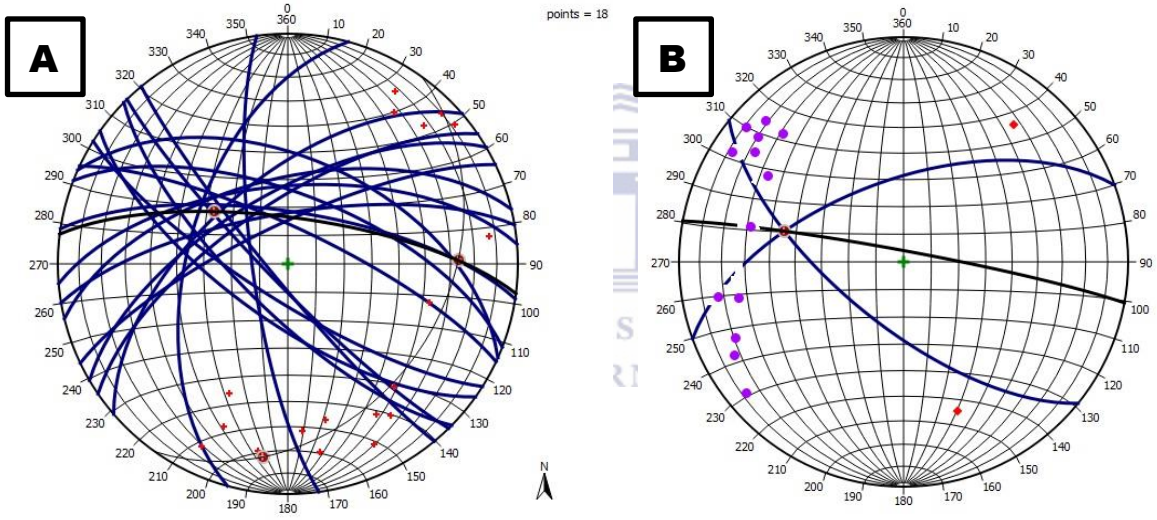

Figure 4-8. (a) β diagram for subarea 1. (b) Lower hemisphere stereographic projection of the two limbs of the fold as well as the lineations found in the subarea. The purple points in b) are L_2 lineations, the red points in a) are poles, the blue lines are planes and the black lines the axial plane. 18 data points plotted.

4.2.2 Subarea 2 (macroscale F_3 fold)

In comparison to Subarea 1, which only constitutes one closure, Subarea 2 was further sub-divided into two subareas (Figure 4-5), namely subarea 2a, characterized by the eastern fold closure of the interior Kliprand dome, and subarea 2b, characterized by the eastern closure of the large Kliprand domal structure. Both domains form part of the approximately east-west trending Kliprand domal structure. The main reason for subdividing subarea 2 into various domains was to correlate them stereographically. The eastern hinge zone of the E-W trending minor dome found within the larger scale Kliprand domal structure is approximately 2km long (N-S) and approximately 1.5km wide (E-W). Exposures of the pink gneiss, streaky augen gneiss, and the charnockites dominate subarea 2 with abundant 100-200m wide lenses of gabbro-norite found east and south of the eastern interior Kliprand dome fold closure (Figure 4-9A). Similarly to the western interior domal closure, the S_3 foliation is also moderate to steeply dipping with angles varying between 60-80°, with the only difference being the foliation orientation of northeast (25-72°) and southeast (102-178°) respectively. Both subarea 2a and 2b contain a steeply NNE dipping axial plane. Cross section B-B' (Figure 4-9B) was drawn through subarea 2a (the eastern interior Kliprand domal structure). Similarly to the western fold closure, subarea 2 is also antiformal in nature with the remaining lithologies wrapping around the core of the central pink gneiss. Based on the cross section given in Figure 4-9b the eastern closure (Figure 4-9A) of the interior Kliprand dome could be categorized as an upright open fold in a similar fashion to the western fold closure. Based on the analysis of aerial photographs and the overall geological map (Figure 4-5) an ESE trending fold axis is evident. The entire subarea contains open folds, easily recognized by field observaion and aerial photographic analysis.

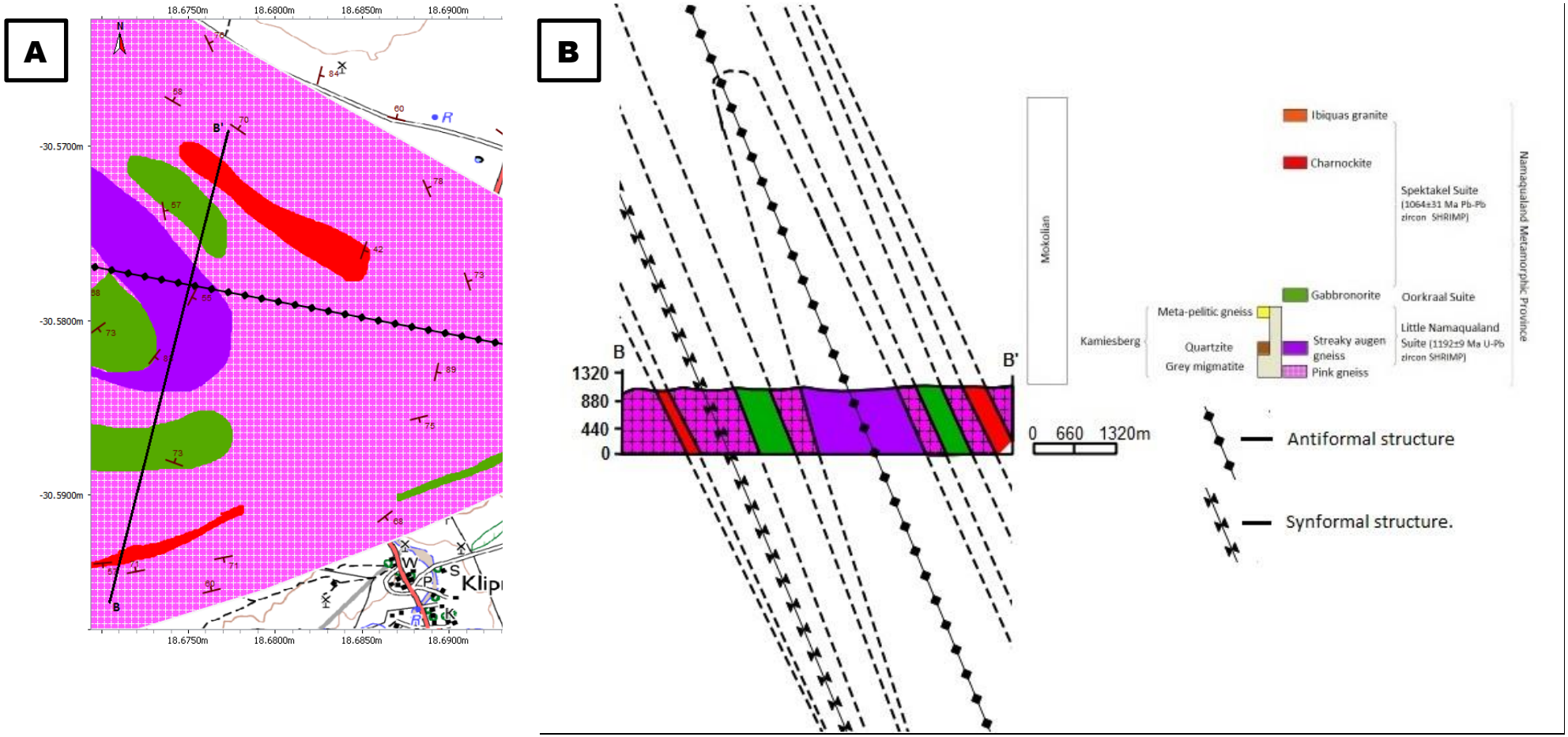

Figure 4-9. (a) Geologic map of subarea 2a with the location of cross section B-B'. The colours shown represent the same lithologies as shown in the geological map (Figure 31). (b) Cross section B-B'.

In a similar fashion to the western interior structure not many data were obtained from its eastern counterpart (subarea 2a), hence a β-diagram was constructed in order to classify the structure. An interlimb angle of 82° was measured for Figure 4-10A, B. As the axial plane dips 85° towards 018°and the fold axis plunges 60° towards 098° the structure is classified as an upright, moderately plunging open fold (Figure 4-10A, B). The axial plane of the eastern closure of the large Kliprand domal structure (subarea 2b) is also moderately inclined to steeply dipping and is thus characterised by upright folds similar to those of subarea 2a. The fold axis of subarea 2b plunges 57° towards 110°, with the orientation of the axial plane dipping 89° towards 198°. This structure is also classified as an upright, moderately plunging open fold as it has an interlimb angle of 73° and a steeply dipping axial plane (Figure 4-10C, D). Both the fold closures in subareas 2a and 2b seem to confirm that they belong to the same fold generation. Subareas 2 and 2b contain 54 data points and 39 data points, respectively, resulting in the construction of π rather than β-diagrams as was done for subarea 2a. The π diagram of subarea 2 displays a strong clustering with an interlimb angle of 85°; the axial plane dips 88° towards 187° with the fold axis plunging 60° towards 097° (Figure 4-10E, F). By correlating all the values of the dip direction and dip of the axial plane and fold axes, as well as for the interlimb angles, it could be confirmed that subareas 2a, 2b and 2 (overall) are part of the same D_3 deformational event.

The mineral lineations, unlike those of domain 1, are not located close to the closure, as shown in Figure 4-10F. However, the lineations from both hinges (subarea 1 and 2) lie on great circles, and were, therefore, deformed by F_3, confirming that the eastern closure was formed due to the D_3 deformation event. The Kliprand domal structure consists of 2 antiforms, the one forming the western interior closure (subarea 1) of the Kliprand domal structure and the other forming the eastern closure (subarea 2 and various subdivisions) of the dome, with the trace of the axial plane of the fold together forming one continuous plane (Figure 4-5). This leads to the conclusion that the Kliprand domal structure is, in fact, a well-rounded dome.

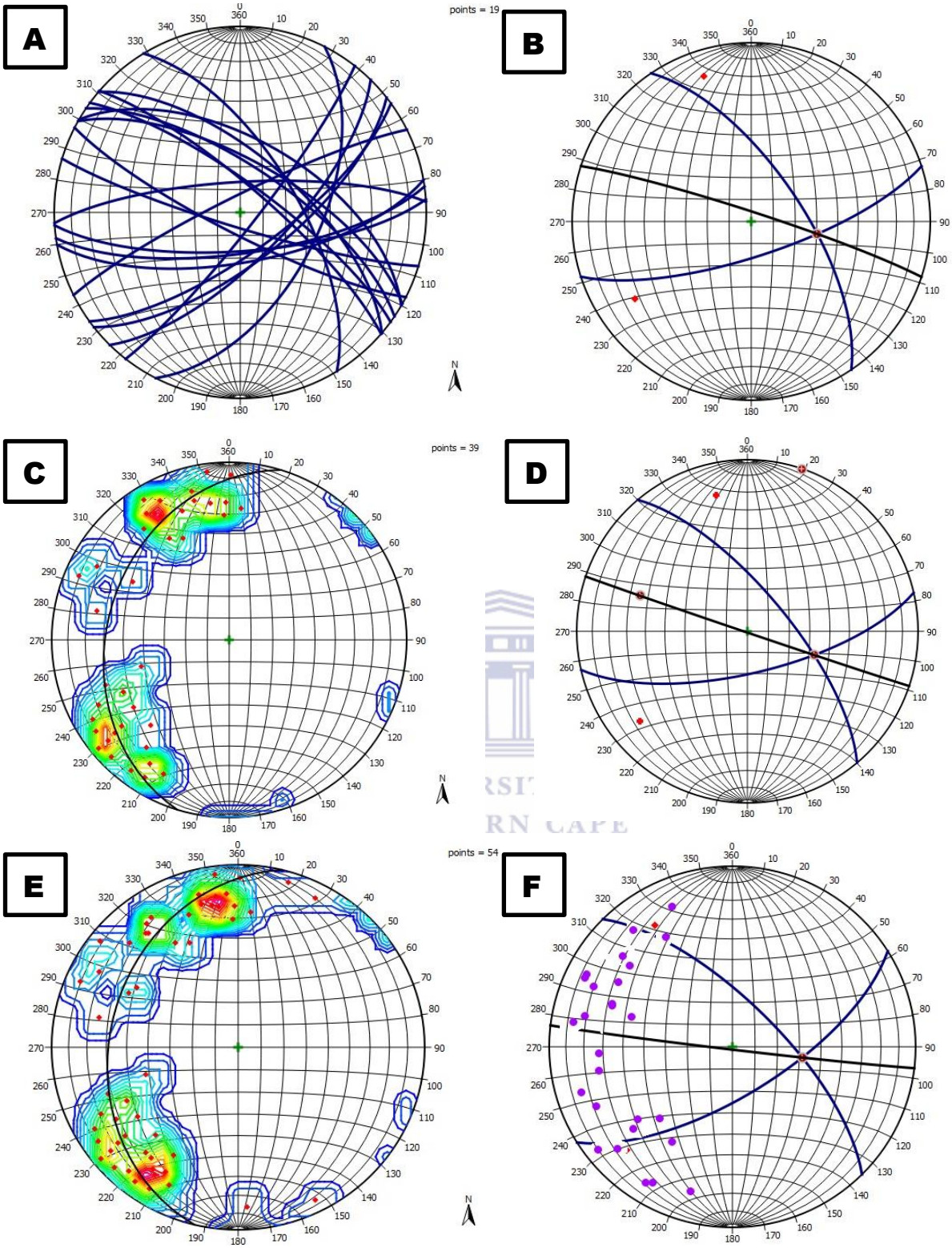

Figure 4-10.. A) β-diagram for subarea 2a. B) Lower hemisphere stereographic projection of the two limbs of the fold. C) Pi diagram of pole to S2 foliation plot for subarea 2b. D) Lower hemisphere stereographic projection of the two limbs of the fold. E) Pi diagram of poles to S2 foliation plot for subarea 2. F) Lower hemisphere stereographic projection of the two limbs of the fold as well as the lineations found in the subarea. Lineations represented by purple dots are spread away from the fold limbs suggesting a further deformation event to cause them to have a spread like that. The purple points in f) are L_2 lineations, the red points in c,e) are poles, the blue lines are planes and the black lines the axial plane.

4.2.3 Subarea 3 (macroscale F_2 fold)

Subarea 3 encompasses the entire Kliprand domal structure while excluding the closures (Figure 4-5), which are the main focus of subareas 1, 2 and 4. On a regional scale, the S_1 and S_2 foliations in subarea 3 are mostly subparallel to one another, dipping steeply NNE. The parallelism between the S_1 and S_2 foliations is due to the tight- to isoclinal F_2 folding that has resulted in intense fabric transposition as a result of intense deformation under high grade of metamorphism in large parts of subarea 3 as was also reported by previous researchers in the area (Albat, 1984; Macey, 2001). Bedding is non-existent for the same reasons. The degree of fabric intensity of the D_2 folds decreases from the central minor Kliprand domal structure towards the metapelites in the southern portion of the Kliprand dome (Figure 4-5). The structure occupying Subarea 3 is interpreted as an anticline-syncline-anticline pair because of the lithological sequence and not based on structural features. This succession of anticline-syncline-anticline pairs stretches from the southern limb of the Kliprand dome towards the northern limb of the structure (Figure 4-5). In the core of the dome the major lithologies found are the pink gneiss, the streaky augen gneiss and gabbro-norite outcropping as thin lenses on either side of the interior domal structure (Figure 4-5). Here, the streaky augen gneiss has an intense structural fabric displayed by the presence of distinct gneissic banding, well defined feldspar augen and ESE-WNW trending boudinage. This corresponds to the regional NNE-SSW shortening strain, responsible for the formation of macro-scale ESE-WNW -trending folds.

A π-diagram of poles to S_2 foliation was constructed for subarea 3 from a data set of 69 measurements. A strong clustering, showing the two limbs of the fold is displayed in Figure 4-13a. In comparison to domains 1 and 2, which contain a rotated S_2 cleavage and macroscopic parasitic folding, subarea 3 contains mainly a steep NE dipping S_2 axial planar foliation. Based on the presence of the axial planar foliation it would be difficult to identify the type of structure present as the limbs of the fold would most probably cluster at one point, as was previously displayed by both Macey (2001) and Albat (1984). In this study a similar situation is found where the majority of the 69 data points plot as a cluster. However, by removing error prone data points two clusters were observed with the one being better defined than the other (Figure 4-13a). Once the great circles were plotted on a separate β-diagram an interlimb angle of 33° was obtained indicating that a major part of the Kliprand domal structure is composed of macro-scale tight-isoclinally folded structures (Figure 4-13b). The fold axis plunges 72° towards the NNE (022°), with the orientation of the axial plane dipping 73° towards 005°. This structure could thus be classified as a steeply inclined steeply plunging tight fold. In a similar way to subareas 1 and 2, the mineral lineation is not oriented parallel to the fold axes, but girdled between 245° further confirming that the later (D_3) deformational event has caused the rotation of the earlier L_2 mineral lineation formed during D_2 (Figure 4-13b). On the fabric diagram (Figure 4-18) the point reflecting the fabric shape plots close to the K=1 line and thus falls in the field of plain strain or the L=S tectonite region.

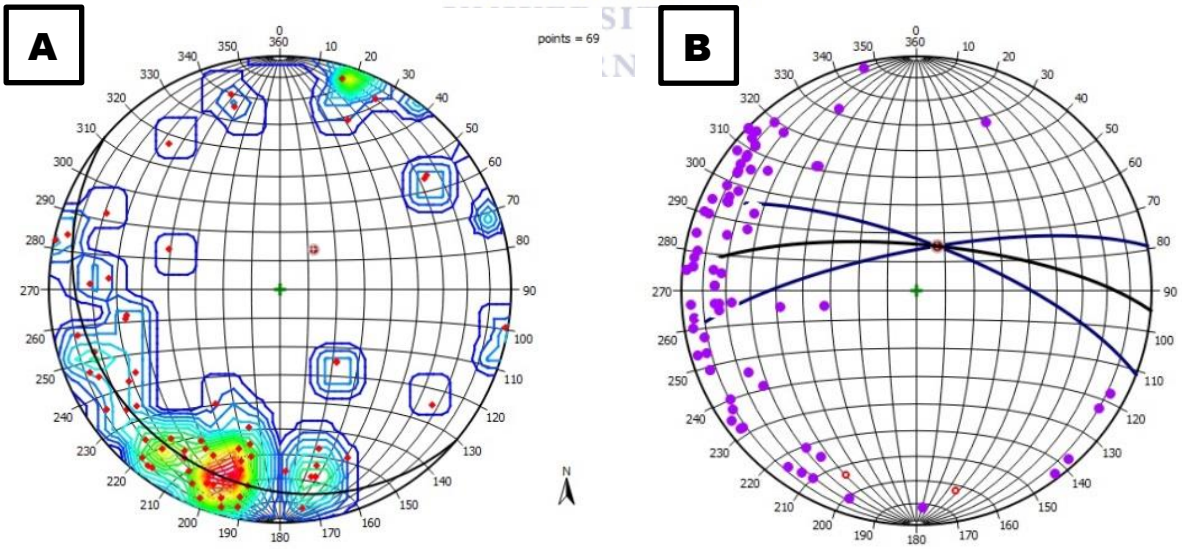

Figure 4-11. (a) Pi diagram of poles to S_2 foliation for subarea 3. (b) Lower hemisphere stereographic projection of the two limbs of the fold, as well as for lineations found in subarea 3.

4.2.4 Subarea 4 (macroscale F_4 fold)

Subarea 4 is situated in the southern part of the Kliprand domal structure (Figure 4-5) and forms the largest closure within the study area (Figure 4-5) with a length of 8km (E-W) and a width of 1km (N-S). Based on the shape of the structure identified, the southern fold closure, similarly to the other three fold closures, could be classified as an anticline. The anticline in subarea 4 is a relatively flat-lying gentle fold; it is unique in that it represents a later, weaker, D_4 deformational event oriented perpendicular to the previously active NNE/SSW directed major compressional stress. An approximate 300m wide valley is situated along the southern limb of the structure exposing 5 of the 7 major lithologies within the Kliprand domal structure. A succession of streaky augen gneiss, quartzites with thin (2 X 4m), interlayered lenses of the Ibequas granite and metapelites is present in the southern portion of the area (Appendix 4-15a). The two-pyroxene granulite (gabbro-norite) forms the base of a large portion of the valley, with a meta-sedimentary succession forming the southern slope of the valley overlying the gabbro-norite. The major joint set dominating this area is N/S with abundant horizontal stress release joints resulting in a sub-horizontal to gently dipping pseudo-layering in the metasedimentary succession resembling bedding, even though bedding in the area has not been observed either during this project or during the mapping done by Albat (1984) and Macey (2001).

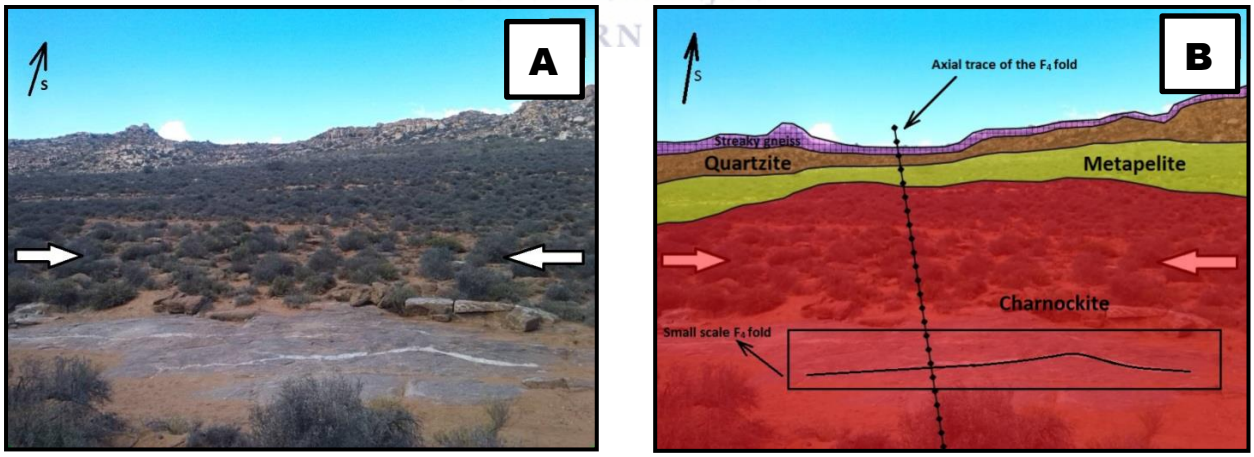

Figure 4-12. (a) The hinge of the southern closure of the Kliprand domal structure plunging in a SSW direction which is clearly displayed by folding of the leucosome seen in the foreground. (b) The major lithologies forming the southern limb of the valley as well as the structures are outlined here.

Due to the small amount of data obtained for subarea 4 a β-diagram was constructed in order to classify the structure (Figure 4-16a, b). The fold closure of the D_4 structure is situated along the southern closure of the Kliprand domal structure. The interpretation of this fold closure as a D_4 structure is based on the fact that it is defined by deformation of all the previous foliations with the formation of no new foliations. As the interlimb angle is approximately 135°, the D_4 structure is best described as a gentle fold, with a fold axis plunging 67° towards 187° (Figure 4-16b). As the axial plane dips 89° towards 277° this structure is classified as a steeply plunging upright gentle fold. The southern closure supports the interpretation that this fold closure is a D_4 structure, as agreed by Albat (1984), Macey (2001) and Macey et al. (2011) whereby they have identified the D_4 mesoscopic folds of this generation as being gentle folds caused by a weaker E-W compressional event. Mineral lineations in this domain were minimal to non-existent and were thus not added to the β diagram as was conducted in the other fold closures.

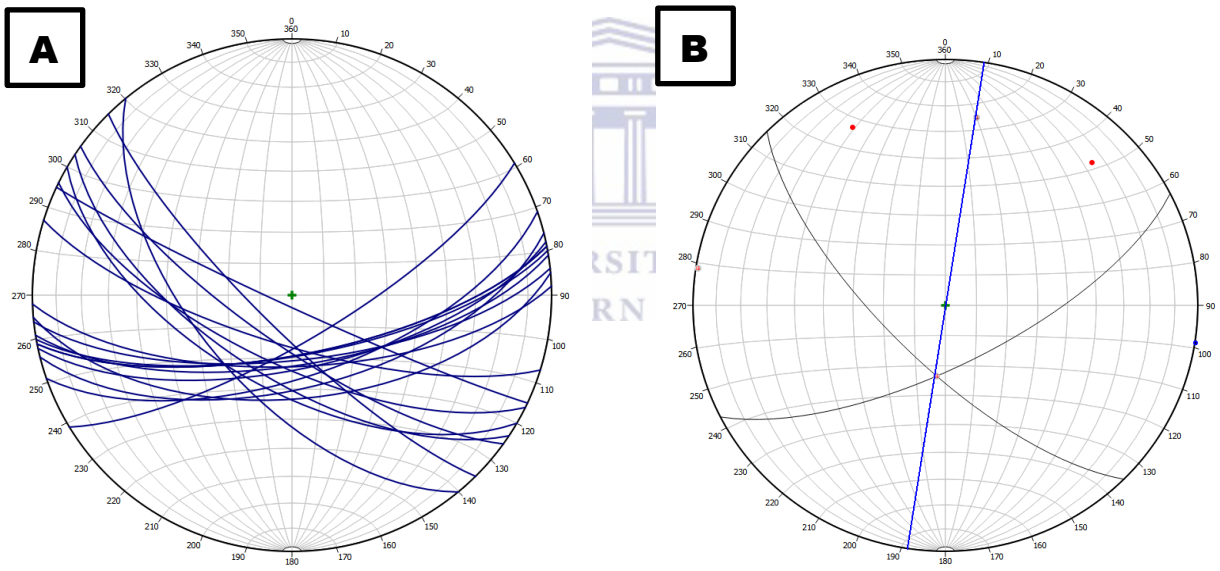

Figure 4-13. (a) β diagram for subarea 4. (b) Lower hemisphere stereographic projections of the two limbs of the fold, as well as for lineations found in subarea.

4.3 Lineation analysis of the entire Kliprand domal structure

The development of lineations in the Kliprand domal structure is defined by the preferential grouping of minerals such as elongate quartz, alkali feldspar, and the alignment of amphibole and biotite. Lineations are typically measured with plunge down-dip on the local foliation. The majority of the lineation orientations in the Kliprand domal structure plunge shallowly between 130 and 250° with a number of linear trends trending southeasterly, and, because the gneissic fabrics have been correlated with D_1 and dominantly D_2, these lineations are considered to be dominantly L_2 lineations. This is further confirmed whereby the intersection of the F_2 limbs coincides with the pole to the great circle defined by the lineations (Figure 4-13B). Although the lineations in the field have been observed to be L_2, a lineation map (Figure 4-17) was further used in order to indicate whether the L_2 lineations may have been rotated by a later deformational event. On the stereographic plots, the D_3 fold axis is not parallel to the lineations in subareas 1 and 2, but rather has the lineations forming a girdle. It is important to note that the lineations in the folds of domain 4 are similar in orientation to the lineations in domains 1 and 2 and follow the general shape of the larger Kliprand domal structure and the interior western and eastern closures (Figure 4-17). This relationship suggests that the lineations found in all three subareas are rotated L_2 lineations, because the fold axis is not parallel to the lineations for all three domains. This confirms that the later D_3 deformational event was the cause of the rotation of the L_2 lineations in both subareas 1 and 2 respectively. The D_4 event was responsible for the rotation of L_2 in subarea 4.

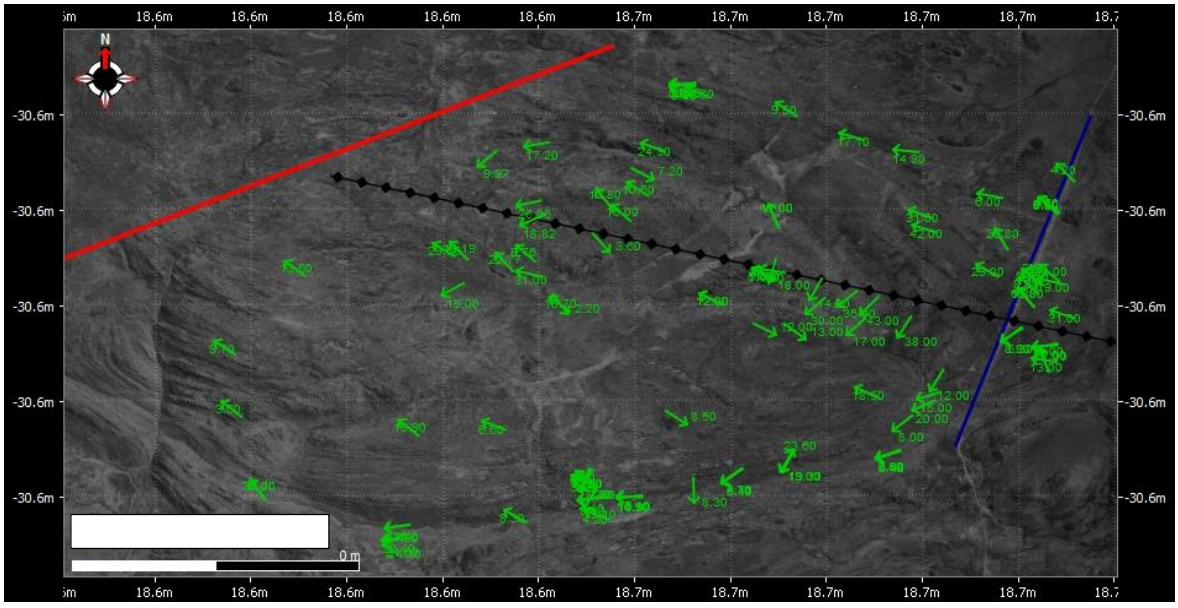

Figure 4-14. Map displaying the orientation of lineations within the Kliprand domal structure. The red line represents the end of the study area. As it was impossible to get rid of the academic license (writing bottom left), a text box was placed there to block it off.

4.4 Joint analysis

Joints were measured throughout the Kliprand domal structure whereby the mode of deformation (opening or shearing), termination relationships, and evidence of displacement, fracture length and joint spacing were carefully analysed. Several sets of joints were measured in each structural domain (subareas 1, 2, 3 and 4). Five joint sets were defined based on orientation data. Members of a fracture set share both a common range of strike and dip orientation. The Midland Valley Move^{Tm} software was used to construct Pi-diagrams and rose diagrams of the joint orientation data. Jointing within the Kliprand domal structure was not influenced by folding as folding occurred in a high grade metamorphic ductile environment. Hence the F_2, F_3 and F_4 macroscale folds in subareas 1, 2, 3 and 4 contain the same joint sets and thus were not analysed as subareas but rather as a coherent set throughout the study area. joints trending NNW and NW represent the main lineaments traversing the gneisses of the Kliprand domal structure as similarly seen by Macey, (2001) and Macey et al. (2011). Subordinate lineament sets trend roughly ESE-WNW and WSW–ENE (joint set 1). They are commonly observed displaying a coarse mineral fill that is indicative of an opening mode, as was observed in the current study, as well as by Macey (2001) and Macey et al. (2011). However, the NW-trending joints tend to terminate at the ESE/WNW joints indicating that the NW/SE joints formed after the ESE/WNW and thus have been termed joint set 2.

4.4.1 Joint set 1

Joint set 1 contains a total of 20 data points (Figure 4-19), the strike trends ESE/WNW (dip direction of 301-329° and 129-159°) with a steep plunge of >75° (Figure 4-19b). The ESE/WNW joints are the longest of all the joints ranging in length of 1-10 m. These long fractures are linear and their spacing varies from 1 to 3 m. Macey (2001) and Macey et al., (2011) state that the ESE-WNW is a second generation joint set which is probably of Karoo-age whereas the N/S striking joints were formed in response to the Pan-African orogeny. Field studies display a cross cutting relationships between the N/S striking joints and the ESE/WNW joints. With regard to the cross cutting relationship, the typical age constraint theory cannot be applied and therefore one cannot conclude whether the one joint is younger than the other (Figure 4-19C, D).

4.5.2 Joint set 2

Joint set 2 fractures are oriented NW/SE (Figure 4-20a, b) containing a total of 18 data points; they terminate against set I fractures (Figure 4-21a, b) and, as a result, are less than a meter in length. Shearing along these joints is rarely found; one example of left lateral shearing was observed between the NW/SE joint and what seemed to be a younger ESE/WNW joint. Even though the

majority of the NW/SE joints terminate at the ESE/WNW joint sets it is difficult to confirm that they are younger seeing that there is the occasional cross cutting relationship. Macey (2001) states that the near vertical orientation of the majority of these fractures should indicate that these joints belongs to a strike-slip regime (with $\sigma_{1.3}$ horizontal and σ_2 vertical). Macey (2001) locally observed Riedel shearing along a few of these joints, suggesting that locally, strike slip or oblique movement occurs. However, in order to prove that a conjugate set exists (Twiss and Moore, 2009), many cross-cutting joints where analysed, with 99% of them displaying a relationship with no displacement of the one by the other. Only a conjugate set can be used to find the stress directions for strike-slip deformation. As only one incident of shearing was observed (Figure 4-21c, d), the stress orientation cannot be confirmed.

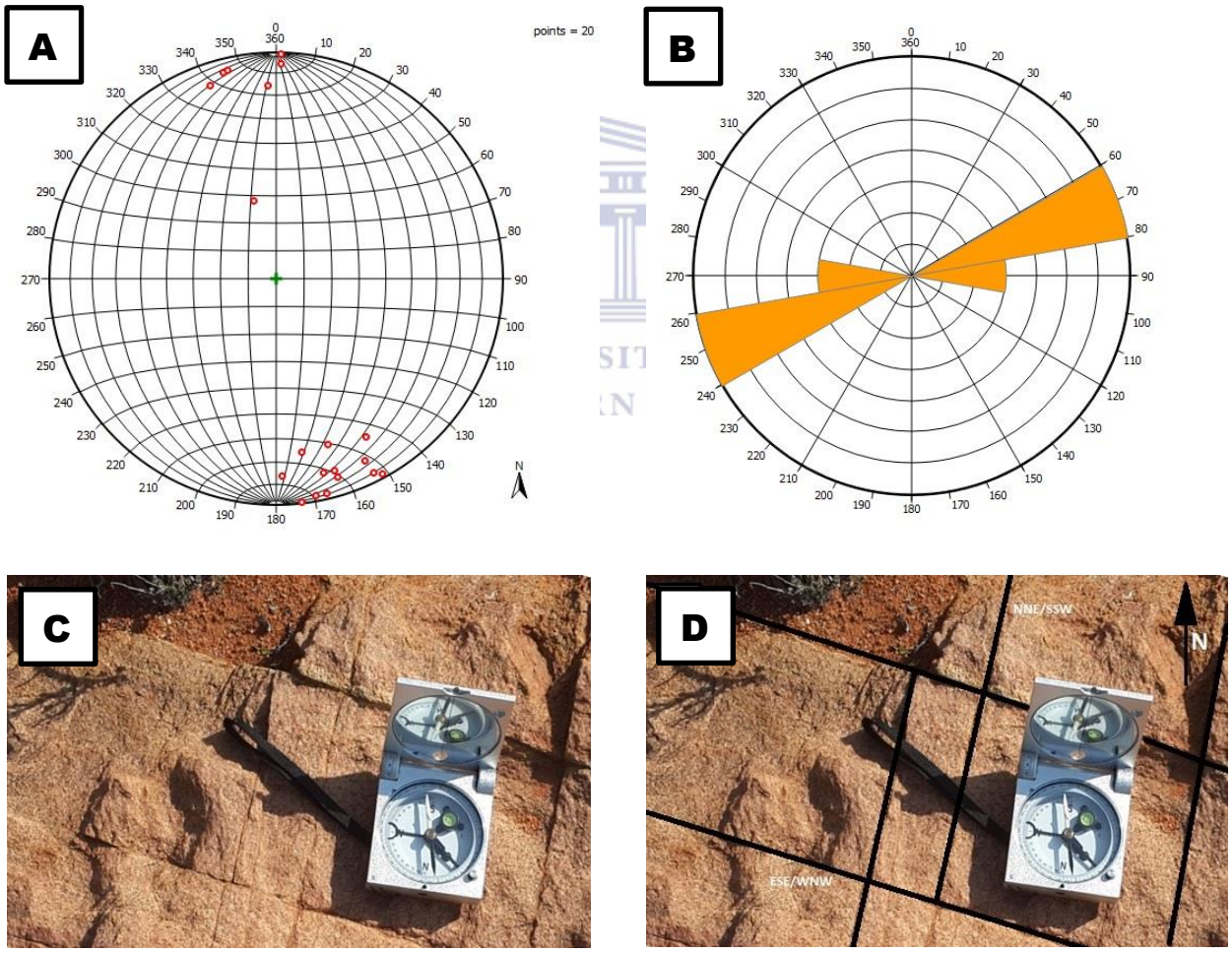

Figure 4-15. A) pi-diagram of 20 joint measurements plotted as poles to planes. (B) Rose diagram of the 20 joint measurements displaying the major strike orientation. C) Non digitized image of the NNE/SSW joints cross cutting the ESE/WNW joints. (D) Digitized image of the NNE/SSW joints cross cutting the ESE/WNW joints.

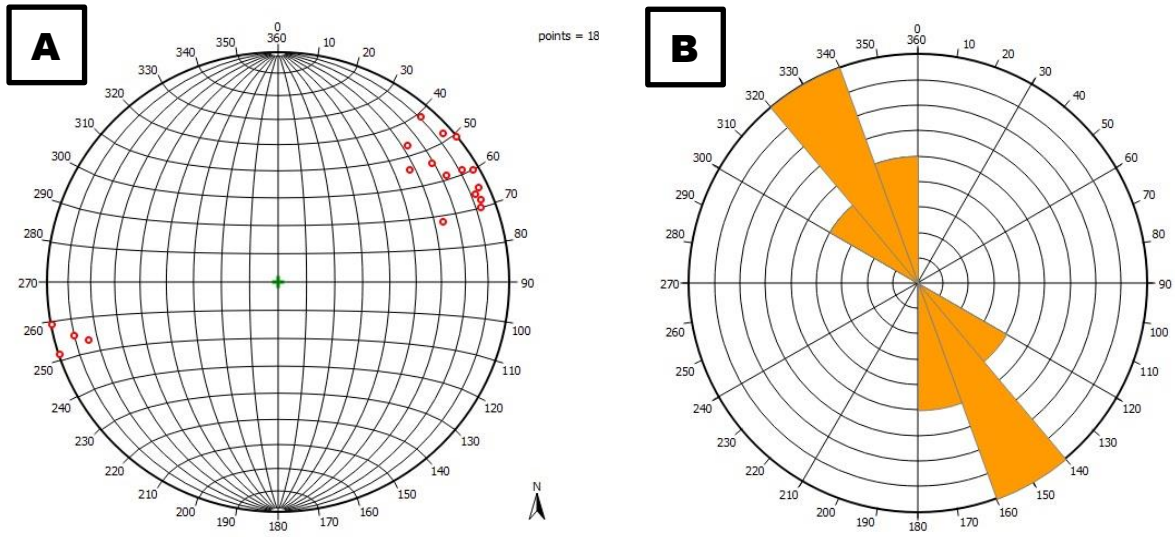

Figure 4-16. *a) pi-diagram of 18 joint measurements plotted as points. (b) Rose diagram of the 18 joint measurements displaying the major strike orientation.*

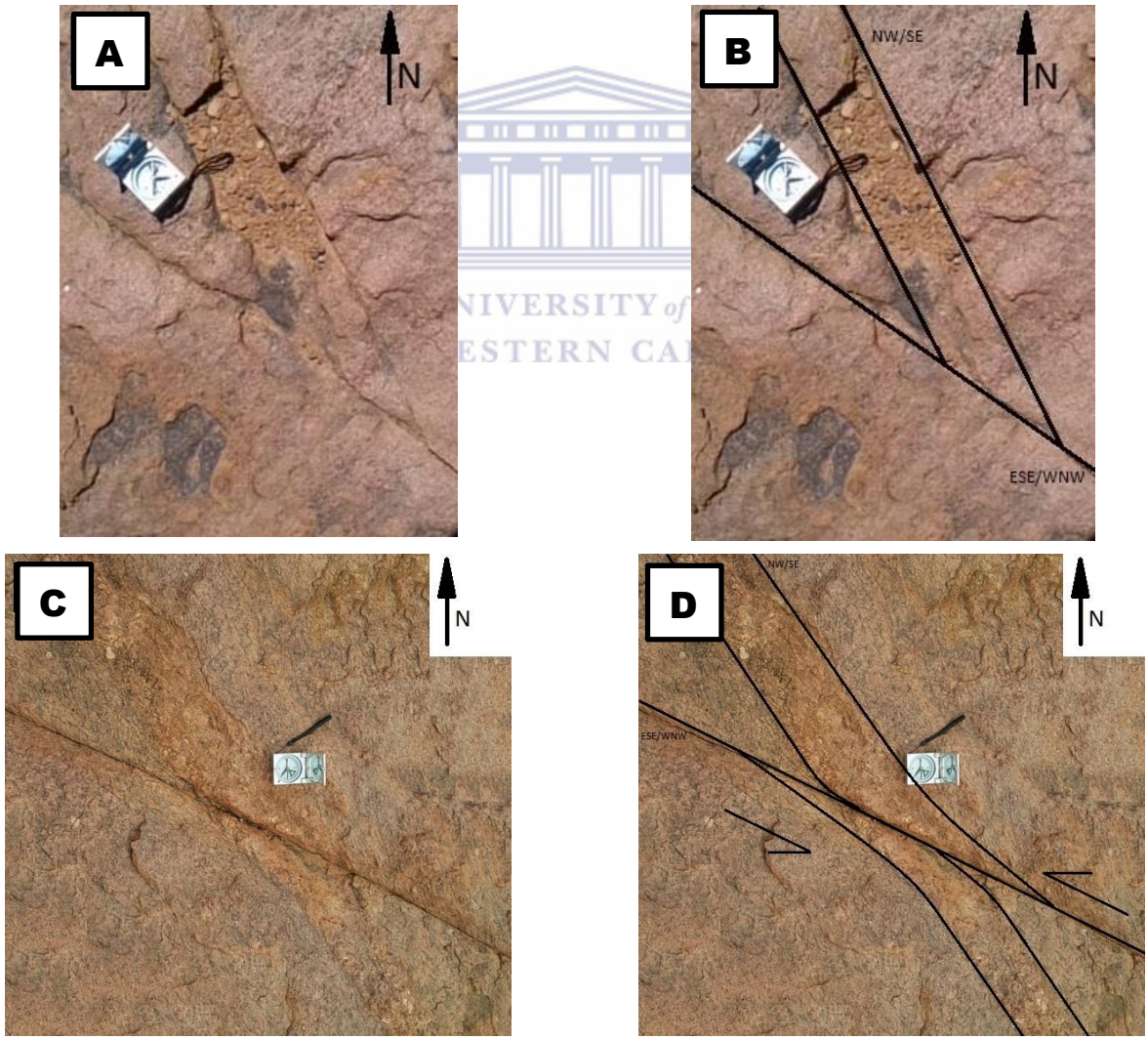

Figure 4-17. *a) Non digitized image of the NW/SE joints terminating at the ESE/WNW joints. (b) Digitized image of the NW/SE joints terminating at the ESE/WNW joints. c) Non digitized image of sinistral shearing along the ESE/WNW joints (d) digitized image of sinistral shearing along the ESE/WNW joints.*

4.4.3 Joint set 3

Joint set 3 trending N/S – NNE/SSW (figure 4-22b) is the most prominent joint set in the study area containing a total of 54 data points (figure 4-22a), with a steep plunge of >75°. This Joint set terminated at the NW/SE. These joints were found striking parallel to the NNE-SSW direction of maximum compression σ_1 and thus developed as a tensile fracture formed during the continuous deformation once the environment changed from a ductile to a brittle one.

4.4.4 Joint set 4

A fourth joint set trending NE/SW (Figure 4-23b) is also quite abundant containing a total of 48 data points (Figure 4-23a), similarly to the rest of the joint sets in the area they too plunge at >75°. Deformation history of these joints is an exception to the first three, in that field exposures of joints set 4 are mainly observed cross cutting the N/S joint set (Figure 4-23c, d). The steep dip of these joints and their cross cutting relationship with joint set 3 resulted in further speculation that Riedel shearing was present. Even though joint sets 3 and 4 intersects each other at an angle of 60°, necessary for a conjugate set to form, the shear offset is generally not visible at the outcrop scale. The exact nature of these fractures remains uncertain because we do not know if they initiated in a shearing mode (e.g. as deformation bands) or in an opening mode (as joints) and subsequently were sheared. If the joint set 4 fractures formed as shear fractures, they would have formed obliquely to the direction of greatest compression. If they formed as joints, they would be associated with the NNE/SSW directed compression. Further study is needed to constrain the nature and origin of these joint sets, in order to accurately identify their deformational history.

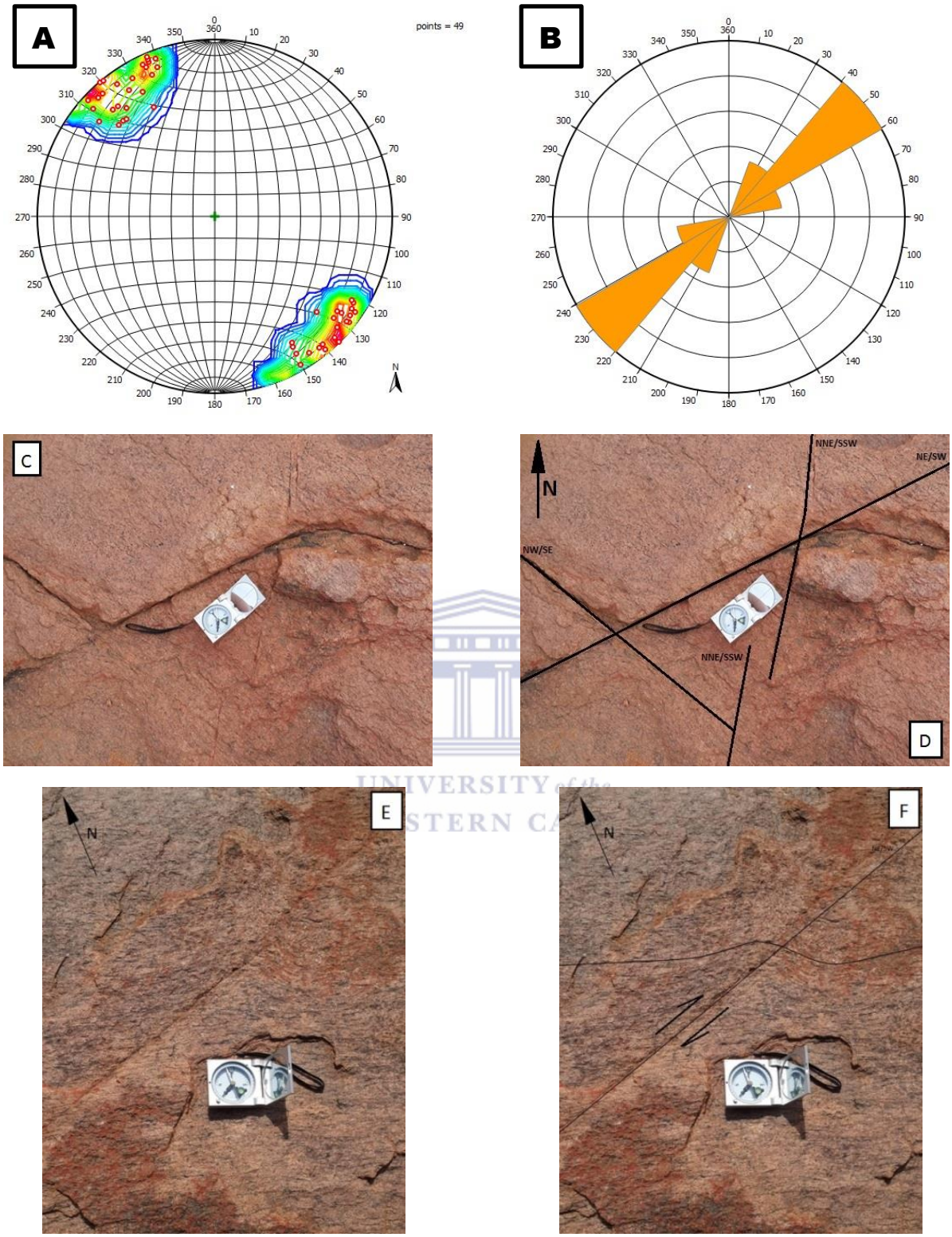

Figure 4-18. a) pi-diagram of 48 joint measurements plotted as points. (b) Rose diagram of the 48 joint measurements displaying a NE/SW strike orientation. c) Non digitized image of the N/S joints cross cutting the NE/SW joints. (b) Digitized image of the N/S joints cross cutting the NE/SW joints. e) Non digitized image of dextral shearing along the NE/SW joints (f) digitized image of dextral shearing along the NE/SW joints.

Chapter 5 : Structural geology discussion

This chapter is an investigation into, what the cause was for the development of the Kliprand domal structure. This chapter will consider the various possibilities and/or alternatives as to how such a domal structure may have formed, and weigh the pros and cons of each against the data obtained in the field to come to some conclusion as to how the Kliprand domal structure formed. The study of Yin (2004) will be of major importance, when considering the various possibilities of dome formation, as this study has an array of various mechanisms. Other non-conventional methods of dome formation (such as large scale boudinage and sheath folding) shall also be considered.

5.1 Dome system analysis

Gneiss domes are commonly found occurring as groups of ovoid structures with a variety of sizes and geometric arrangements (Yin 2004). Yin (2004) suggests that the geometric arrangements of gneiss domes are linked to their formation, and thus subdivided gneiss-dome systems into: (1) linear array and (2) non-linear array systems (Figure 5-1) in order to identify their origin of formation. Yin (2004) further subdivided the linear array into an evenly spaced and unevenly spaced system (Figure 5-1). The evenly spaced linear array (Figure 5-1) gneiss dome systems are related to detachment faulting, whereas the unevenly spaced gneiss dome systems (Figure 5-1) are commonly found as huge anticlines associated with the presence of large thrust ramps (Yin 2004). Similarly, the non-linear array system (Figure 5-1) was also divided into evenly spaced and unevenly spaced systems (Yin 2004). The unevenly spaced, nonlinear-array gneiss-dome systems (Figure 5-1) have been attributed to superposition of magmatic injection Cordilleran-style extension, or polyphase superposition of contraction (Yin 2004). Yin (2004) separated the evenly spaced subclass into an orthogonal (produced by elastic buckling) and non-orthogonal alignment (Figure 5-1) of gneiss domes (produced by Rayleigh - Taylor instability or by the superposition of multiple shortening events from various directions, with the heterogeneous mechanical properties of the rocks that compose the dome system possibly also contributing). The Kliprand domal structure is the largest dome within the Kliprand area (Figure 5-2) and thus is more of a single dome than a domal system. However, there are small domes and basin structures surrounding the large Kliprand domal structure (Figure 5-2).

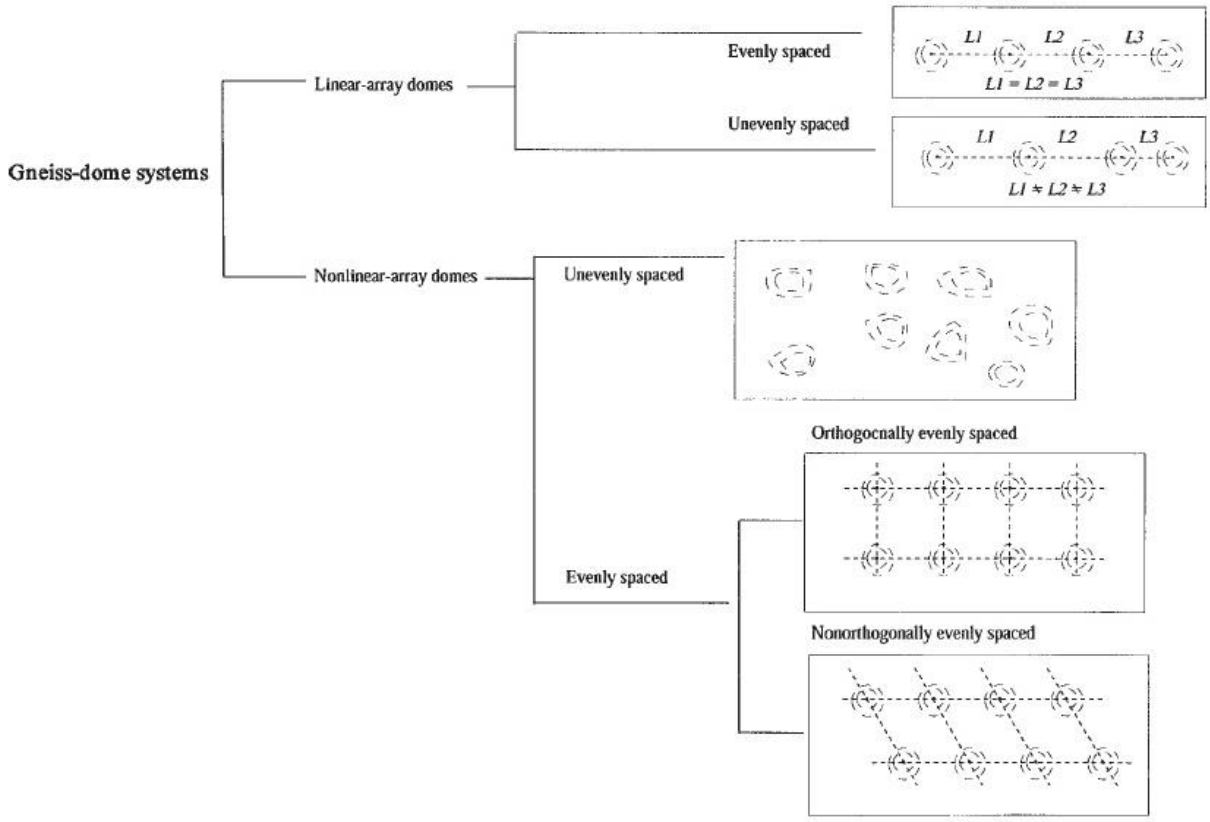

Figure 5-1. Gneiss dome system classification scheme. Taken from Yin (2004).

Although the smaller dome and basins are not part of this study they do have a nonlinear non-orthogonal and approximately evenly spaced relationship with one another (Figures 5-1, 5-2). By comparing the smaller domes (not part of the study) to the larger Kliprand domal structures , one may speculate that the larger Kliprand domal structure formed as a result of the superposition of multiple shortening events from various directions or due to the heterogeneous mechanical properties of the rocks that compose the dome system (Yin 2004). Once the spatial distribution of the larger Kliprand domal structure is compared to the smaller domal structures (Figure 5-2), they would form a non-linear array of unevenly spaced domes (Figure 5-1). The unevenly spaced, nonlinear-array gneiss-dome systems (Figure 5-1) have been attributed to superposition of magmatic injection Cordilleran-style extension, or polyphase superposition of contraction (Yin 2004). Although the spatial distributions of domal structures are important, the individual interpretation of the Kliprand domal structure and the interior dome gives a more accurate conclusion because it links observations and formational processes (large scale geologic features).

Yin (2004) grouped the individual dome formation mechanisms into two categories, namely domes formed due to faulting, and domes formed without the presence of faults (Figure 5-3). Diapirism, superposition of multiple folding events, and contrasts in mechanical rock properties are the major causes for the formation of fault unrelated domes (Figure 5-3). Fault related domes were subdivided into various subcategories, such as strike slip shear zones, ductile shear zones detachment faulting, or thrusting (Figure 5-3). This discussion will focus mainly on the fault unrelated domes as there are no major faults found within close proximity of the Kliprand domal structures (Figure 4-5). A major point in this discussion is the presence of the smaller dome within the larger scale domal structure.

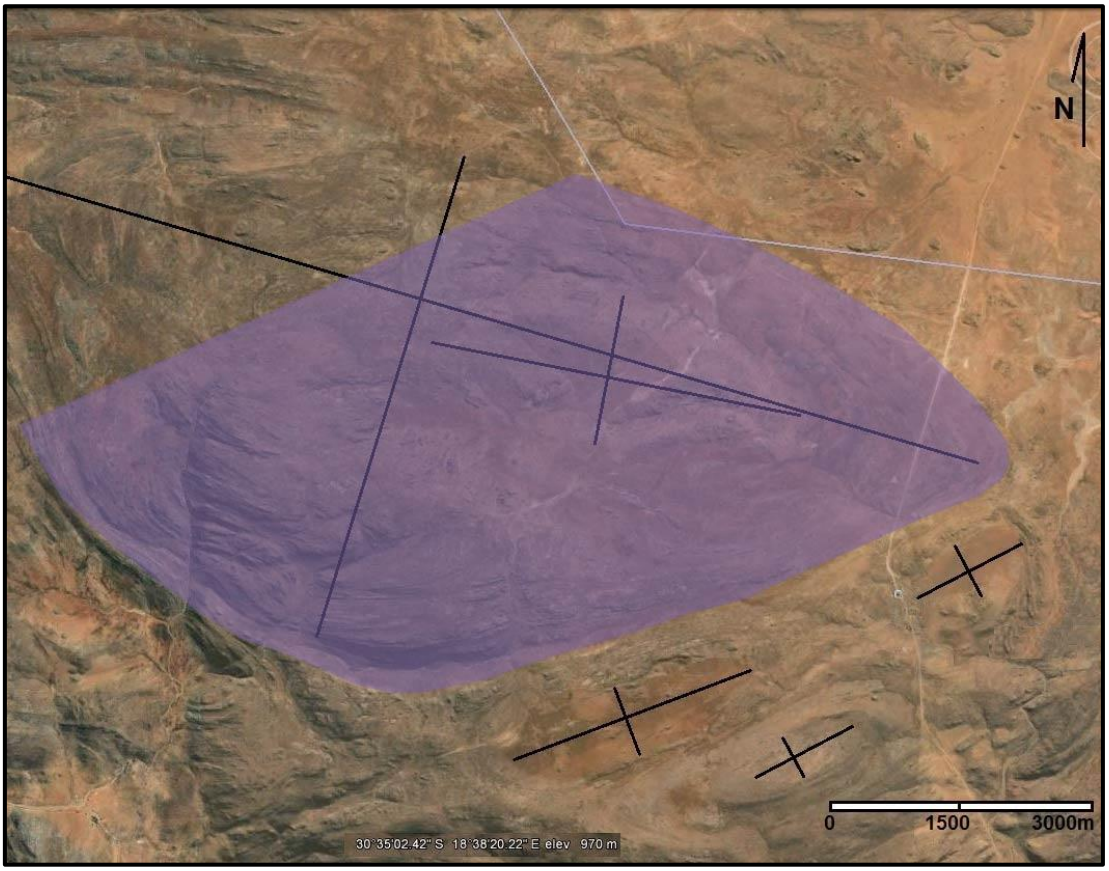

Figure 5-2. Location of the large Kliprand domal structure (location of study area is given by the Purple highlighted area) as well as smaller domes and basins below it (not part of this study). This study is mainly focused on the main dome (Kliprand domal structure) and the smaller internal dome, whilst excluding the dome and basin structures to the south and southeast of it.

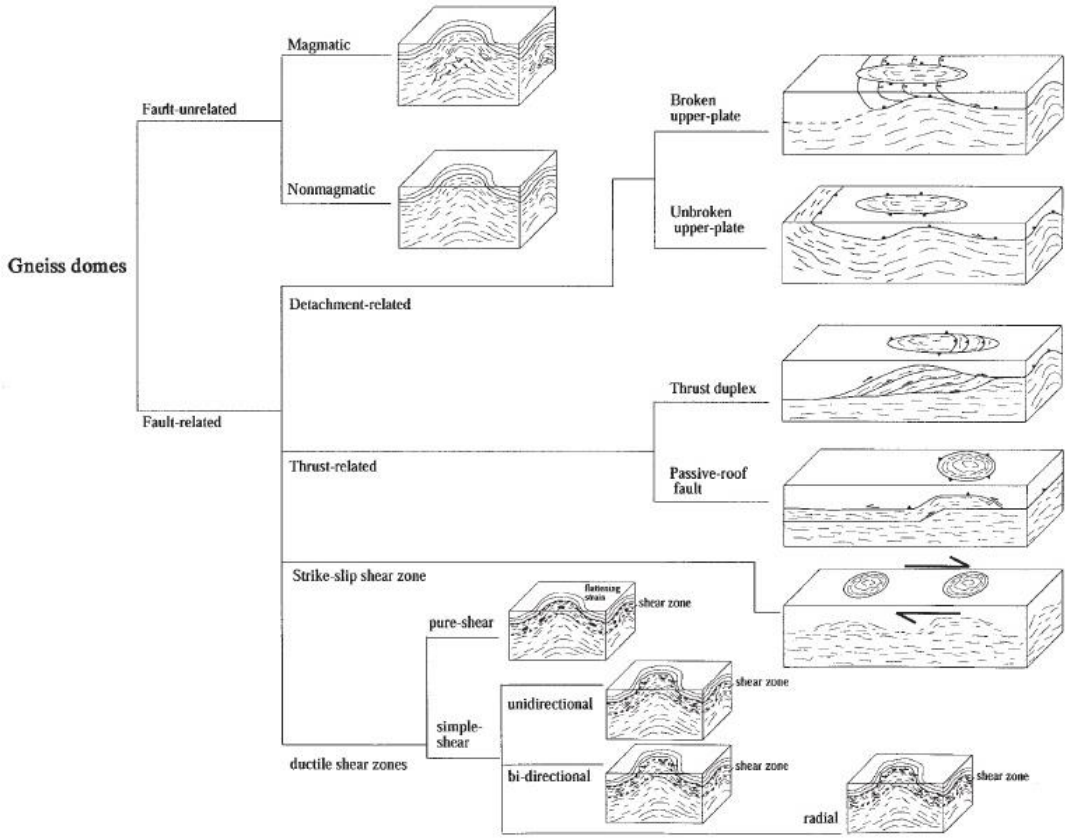

Figure 5-3. Schematic diagram of gneiss dome classification system displaying both fault related and fault unrelated dome systems. From Yin (2004).

5.2 Fault-unrelated domes

5.2.1a Non-magmatic - domal structures produced by multiple folding events

One of the major mechanism for producing gneiss domes is polyphase folding. On a regional scale, large folds surrounding the study area could assist in identifying the direction of major compression and thus indicate whether or not the stress and strain pattern favours the dome creation. The geometry of interference patterns, resulting from superposed folding has resulted in the formation of three principle types of interference patterns (Pandey 1973). The dome and basin pattern described here corresponds to the type 1 pattern in which an anticline crosses an anticline (Figure 5-4, 5-5) (Pandey 1973). The effect would produce a culmination in both folds and a dome structure results (Pandey 1973). For domes to be produced by multiple folding events, the two anticlines have to be at an angle to one another (Figures 5-4, 5-5), which indicates that the axial planes must have different strike orientations.

The closer the axial planes are to striking at 90° to one another (type 1 interference folding; Figure 5-4) the more likely they would be to produce a domal structure, whereas if the axial planes strike at

small angles (Figure 5-5) to one another an elongate ellipse, not clearly resembling a domal shape shall be produced (Sendek 2012). Adding variations in dip of the axial plane and hinge plunge further complicates the possible folding patterns. Once the axial planes are close to parallelism doming will not occur (Sendek 2012).

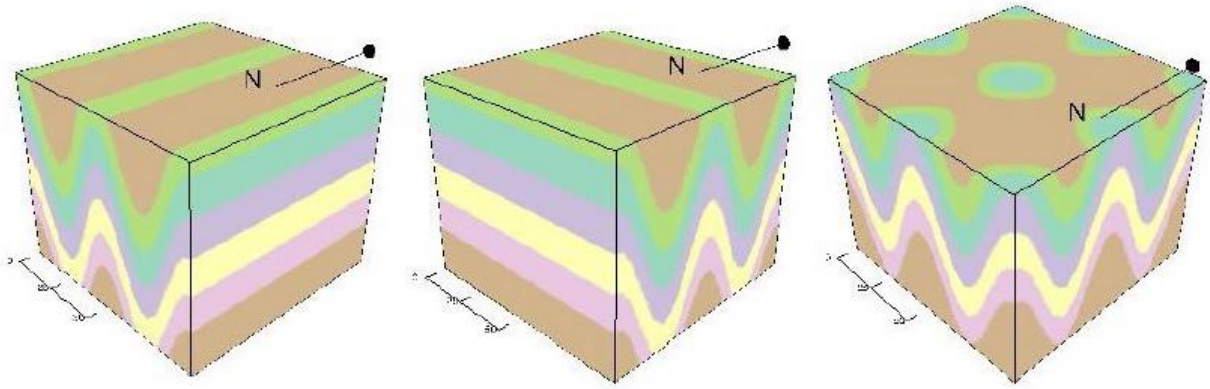

Figure 5-4. Superposition of orthogonal folding events. The first folding event (left) has axial planes striking north-south. The axial planes of the second event (middle) strike east-west. The polyphase result (right) produces a doubly plunging anticline, with a dome structure evident in map view. After Sendek (2012).

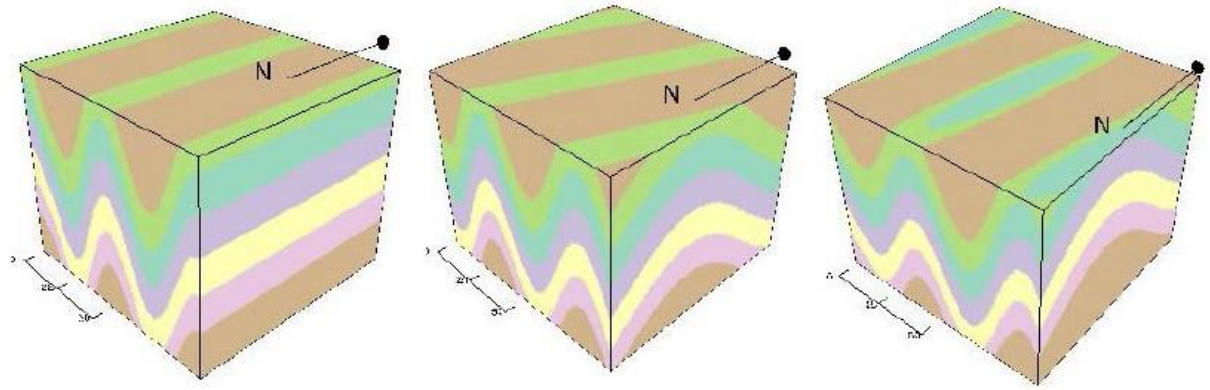

Figure 5-5. Superposition of non-orthogonal folding events. The first folding event (left) has axial planes striking north-south. The axial planes of the second event (middle) strike 20° NE. The polyphase result (right) produces a visible anticline in map view that has an elongate oval geometry. After Sendek (2012).

5.2.1b Application to the Kliprand domal structure

The ESE-WNW axial planar orientation of the F_3 fold closures in subareas 1 and 2 (Figures 5-6) are relatively sub-parallel, slightly plunging NNE and classified as open folds. The only difference is that the fold axis of subarea 2 (plunge towards 097°/ESE) does not plunge in the same direction as that of subarea 1 (plunge towards 284°/WNW). The axial planes of the F_2 (steeply inclined steeply plunging tight fold), and the F_3 (moderately plunging upright open fold) fold strike in a similar orientation

(Figures 5-6), but are not exactly in the same orientation, as shown by the F_2 fold dipping at a steeper angle to the NNE in comparison to the F_3 fold (Figures 5-6). The difference in S_2 and S_3 is also prevalent in the field where S_2 and S_3 are subparallel along the limbs and but cross-cutting and at a high angle to each other at the closure. Subarea 4 is an exception to the rest of the subareas, as here the fold closure is more a gentle fold with an axial plane perpendicular to the previous fold closures (subareas 1, 2 and 3). Based on these observations the major Kliprand domal structure could possibly have formed by 3 macroscale deformational events, namely D_2, D_3 and a weaker D_4. The slight difference in alignment between the axial planes of the F_2 and F_3 folds (Figures 5-6) may have caused the formation of an elongated oval geometry (as shown in Figure 5-5) of the anticline resulting in the dome being more elongated in the ESE-WNW orientation. Type 1 interference patterns possibly caused the interference folding of the F_3 and F_4 folds resulting in the formation of a domal structure (Figure 5-4). Although there are various possibilities that suggest that the Kliprand domal structure might have formed as a result of multiple folding events, the only major problem is the fact that the larger Kliprand domal structure has a smaller dome within its core (a dome within a dome; Figure 4-5) and it is highly improbable that interference folding would result in the formation of a dome within a dome. For this reason, another solution must be found to explain the dome within a dome feature. The axial plane of the large dome has a gradual dip in comparison to the interior dome, they are not exactly parallel and thus could be a feature of lithologies.

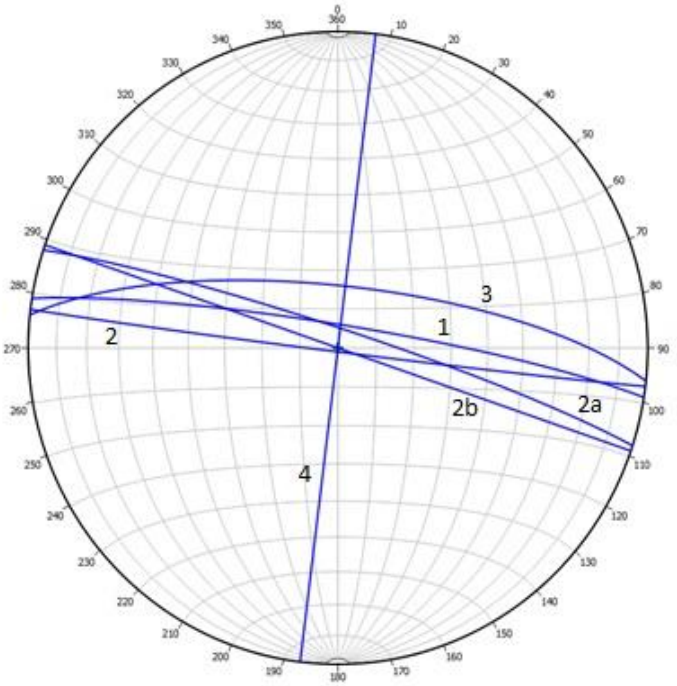

Figure 5-6. The relationship between the axial planes of the four subareas.

5.2.2a Diapirism

Diapirs are rounded to elongate dome-shaped structures where the rocks in the core have risen ductily and pierced through the overlying rock (Twiss and Moores 2009). This upward movement may have been driven by buoyant forces caused by density inversion, with the deeper lower-density rock or magma of the intruding diaper rising up through the overlying higher density rock (Twiss and Moores 2009). This upward movement is aided by decompression melting and rheologic weakening of the host rock due to heat flux from the diapir (Sendek 2012). Density inversions can also be created during regional metamorphism that exposes layered rocks to high pressure and temperature conditions resulting in metamorphic gneiss domes. A series of experiments using layers of putty to examine the structural patterns of diapiric domes, were performed by Dixon (1975). The dome core was represented by a low specific gravity layer (1.40), and was overlain by a layer with a slightly higher specific gravity of 1.5. At the core of the dome (Figure 5-7, line A) foliations are usually horizontal, followed by the foliation dipping moderately away from the dome core as one moves further away from the centre; lineations usually show the same characteristics as foliations (Sendek 2012). At a deeper level in the dome (Figure 5-7, line B), foliations are vertical to steeply dipping in the centre of the dome and become more shallowly dipping moving away from the dome centre. In the dome centre the lineations were vertical, and transition from plunging towards the dome centre, to plunging away (Sendek 2012).

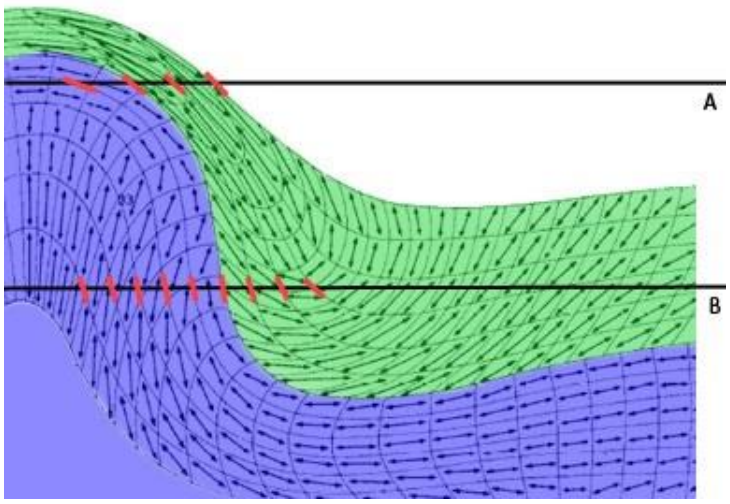

Figure 5-7. Structural patterns of a diapir, displaying how 200 originally horizontal segments have been deformed during diapirism. The maximum elongation direction is represented by the double arrows, which act as a proxy for stretching lineation direction within the dome. The dip of the foliation is represented by the red lines along the cross section. After Sendek (2012). The green is the denser layer and the blue the less dense underlying layer.

5.2.2b Application to the Kliprand domal structure

In relation to the Kliprand domal structure the S_1 foliation within the study area is steeply dipping throughout the Kliprand domal structure; whilst the mineral lineations plunge gently along azimuths varying from 200°-340°. This observation is not consistent with domes formed as a result of diapirism where horizontal foliations occur in the core, but are steeper as one moves to the edges of the dome. The Kliprand domal structure is part of the upper granulite facies terrain, so that, as it was deep crustal, all contacts were largely gradational and concordant so that the contact relationship between lithologies, which is a key element to use in determining magmatic diapiric relationships, is not useful in this study area. Based on foliation and lineation relationship alone one cannot conclude whether diapirism affected the area or not.

5.2.3a Boudinage

Unlike diapirism and multiple folding events, boudinage does not form part of the Yin (2004) classification scheme. Field studies, however, have displayed abundant boudin structures (Figures 4-5, 4-7), and thus have resulted in the hypothesis that the Kliprand domal structure might, in fact, be a large scale boudin-like structure. Boudins form when the ductile extension of the competent layer, which flows very slowly under a given stress relative to the other surrounding rock types, or requires a very high stress to force it to flow at a given rate, cannot keep pace with that of the incompetent matrix, which, relative to the other surrounding rock types, flows very rapidly at a given stress, or requires a very small stress to force it to flow at a given rate (Twiss and Moores 2009). The deformational behaviour of various minerals is strongly dependant on the metamorphic grade. The Kliprand domal structure has been subjected to high grade metamorphic conditions, resulting in crystal plasticity being the dominant deformational feature (Twiss and Moores 2009).

There are various factors that could influence the competency of certain rock types, these are:

1) The mineralogy - the deformational behaviour of various minerals is strongly dependent on the metamorphic grade, where, under high grade metamorphism, minerals such as feldspars (both plagioclase and K-feldspar), biotite, quartz, hornblende and garnet all deform by crystal plastic deformation and have a small contrast in strength (Passchier and Trouw 2005). In most cases olivine is coarse grained and has a weak flow rate and, in addition to mica, would probably not deform as a result of crystal plasticity (Passchier and Trouw 2005). Under low metamorphic conditions garnet is highly resistant to deformation when in a quartzo-feldspathic matrix, and even though feldspar, quartz and garnet show similar deformation intensity and seem to have formed under relatively high metamorphic grade,

they have slightly different characteristics under certain metamorphic conditions (Passchier and Trouw 2005; Figure 5-8). It has been found that feldspar-rich rocks are more competent than micaceous rocks (seeing that muscovite in particular is not as resistant to deformation, as feldspar), whereas mafic rocks consisting of plagioclase and pyroxene are more competent than quartzo-feldspathic gneiss, unless the mafic rocks have undergone intense metamorphism so that they consist mainly of biotite and hornblende (Ramsay and Huber 1988). The difference in competence is mainly because of pyroxene and feldspar being more deformation resistant, whilst the alterations that led to the formation of biotite and fine grained amphibole would have changed the ductility of the rock in general.

2) The variation in grain size (where fine grained rocks are thought to be more competent than coarse grained rocks) (Ramsay and Huber 1988).

3) The mineral hardness, e.g. where hard minerals are highly abundant and are in contact with one another, the strength of the rock type increases dramatically (Passchier and Trouw 2005). The presence of the "soft" minerals thus serve as the strength-determining factor causing the rock to act in a "soft" fashion depending on how much "soft" minerals are present, as the hard minerals are likely to behave similarly to that of the soft grains (the hard grains may rotate in the flow of the soft material).

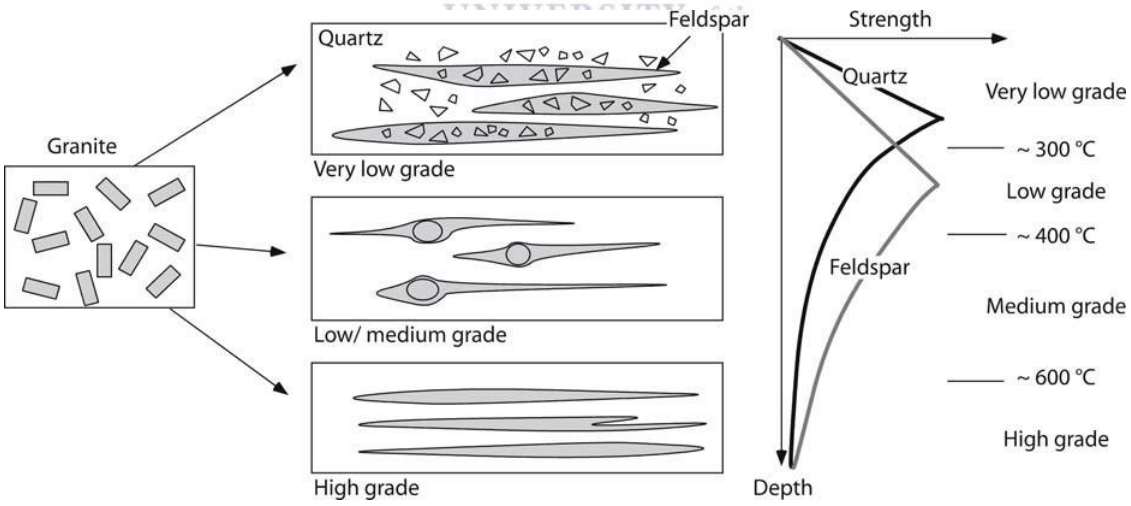

Figure 5-8. Changes in the deformation behaviour of quartz-feldspar aggregates under various metamorphic conditions. At right, a depth-strength graph with brittle (straight line) and ductile (curved line) segments of quartz and feldspar is shown. At very low grade, both quartz and feldspar are brittle, but feldspar is the weaker mineral. At low to medium-grade conditions, quartz deforms by dislocation creep and feldspar is the stronger mineral, developing core-and-mantle structures. At high grades, feldspar and quartz deform by dislocation creep and have similar strength. After Passchier and Trouw (2005).

5.2.3b Application to the Kliprand domal structure

On a small scale most boudins found within the study area form within the metapelite with its surrounding rock type being the pink gneiss. The pink gneiss is dominated by feldspar and quartz, whilst the metapelite is composed of more deformation resistant minerals such as garnet, sillimanite and cordierite in the paleosome with mainly hard quartz and deformation resistant garnet found in the leucosomes. These large quartz and garnet crystals are in contact with each other. Both the paleosome and leucosome of the metapelite are coarse-grained, in general, whilst the streaky gneiss is finer grained. All this suggests that the metapelite is more competent than the streaky gneiss resulting in the formation of boudins within the field. As the difference in competence increases from small to large, the form of the boudins changes from a pinch and swell structure to separate boudins with pronounced necks (Figure 5-9, Twiss and Moores 2009). The competency difference between the streaky gneiss and the metapelite was small seeing that separate boudins did not form but, instead, formed many pinch and swell structures throughout the area

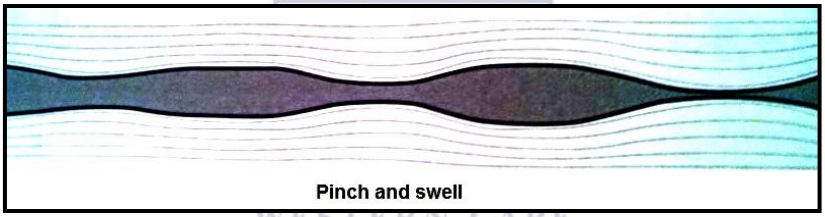

Figure 5-9. Schematic displaying the change from pinch and swell structures (where the competency difference is shown by increasing shades of blue) is small, to separate boudins where the competency difference is large. After Twiss and Moores (2009).

As stated above, the large scale Kliprand domal structure with the smaller interior dome within its core may have formed as a result of large scale boudinage. For both the interior dome and the larger Kliprand domal structure to form as a result of boudinage a strong competency difference is required. However, as mentioned above the core of the dome is composed of streaky augen gneiss surrounded by the streaky gneiss and both rock types are dominantly composed of quartz and feldspar, with the only difference being that the feldspars in the streaky augen gneiss are large augen crystals. The feldspar augen are hard, resilient minerals. However, the surrounding minerals are fine-medium grained and thus would flow (hence the formation of boudins on the outcrop scale), which would not cause an increase in the strength of the rock. But if there was a slight competency increase, it would not result in the formation of the interior pinch structure and would most definitely not be able to form the large scale Kliprand dome as it shows the same relation to

that of the interior dome where the streaky gneiss dominated. Also you don't see a string of them next to each other. A sausage (boudin) inside another sausage (boudin) would be unusual.

5.2.4a Sheath fold

Both Albat (1984) and Macey (2001) have suggested that the Kliprand domal structure formed because of fold interference patterns of F_3 and F_4. However, type 1 interference patterns are unlikely to have formed a dome within a dome (Figure 4-5). Fossen (2010) states that some fold interference patterns can result from a single period of non-steady-state flow, where the orientation of the instantaneous stretching axes (ISA) changes during the deformation. For example, type 1 patterns can be the result of a single phase of heterogeneous non-coaxial deformation (Fossen 2010). Non-cylindrical folds, also known as sheath folds or tongue structures, are commonly found to have formed in high strain shear zones, the shearing normally takes place after formation of the fold (Figure 5-10), resulting in the sheath fold having a reduced interlimb angle, thus resulting in them being observed as tight to isoclinal folds (Ramsay and Huber 1988). The main requirements for the formation of sheath folds are that they form in high strain areas (e.g. a ductile shear zone is commonly associated with high strain); the presence of shear zones is thus not a requirement for the formation of sheath folds (Ramsay and Huber 1988). Even though shear zones are not a requirement for the formation of sheath folds, shear strain plays a major role in Namaqualand tectonics so the possibility that sheath folds are formed due to shear strain is likely.

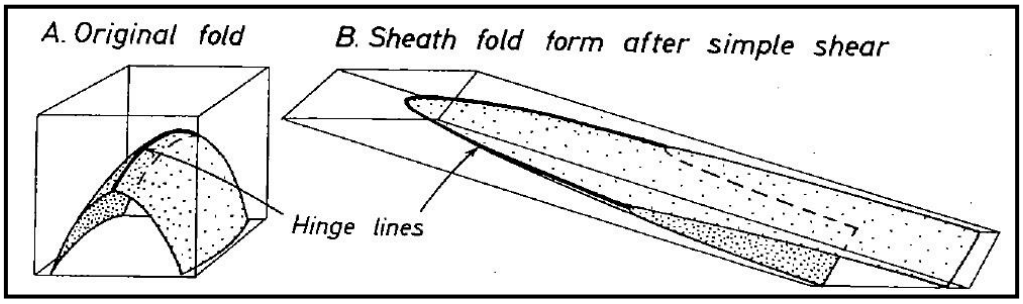

Figure 5-10. The development of sheath folds by strong shearing of an initial fold form that had a slightly curving hinge. After Ramsay and Huber (1988).

Sheath folds are composed of a long x axis along the length of the tube, whilst cross sections normal to the x axis display elliptical rings (eye-folds) where one has intermediate (y) and short (z) axes (Figure 5-11). The x, y and z geometries are thought to be subparallel to that of the strain ellipsoid (Alsop and Holdsworth 2006). There are various ways of categorising whether the Kliprand domal structure is, in fact, a sheath fold. These are, as follows:

1) Identifying the type of eye fold :- By measuring the inner and outer ellipses of sheath folds, and classifying them as either a Type A or analogous-eye-fold, a Type B or bull's eye fold or a Type C or cat's-eye-fold (Alsop and Holdsworth 2006).
2) Depending on the type of eye fold that the Kliprand domal structure is, it could thus have formed as a result of: 1) Simple shear deformation, which includes intense planar foliations and lineations associated with S-L tectonites (Alsop and Holdsworth 2006), 2) those formed as a result of general shear, which commonly have intense foliations associated with S and S > L tectonic fabrics (Alsop and Holdsworth 2006), and 3) those developed in constrictional regimes whose criteria typically include the presence of L and L > S tectonites (Alsop and Holdsworth 2006) along with shortening along the Y axis of the finite strain ellipsoid, coupled with greater shortening along Z.

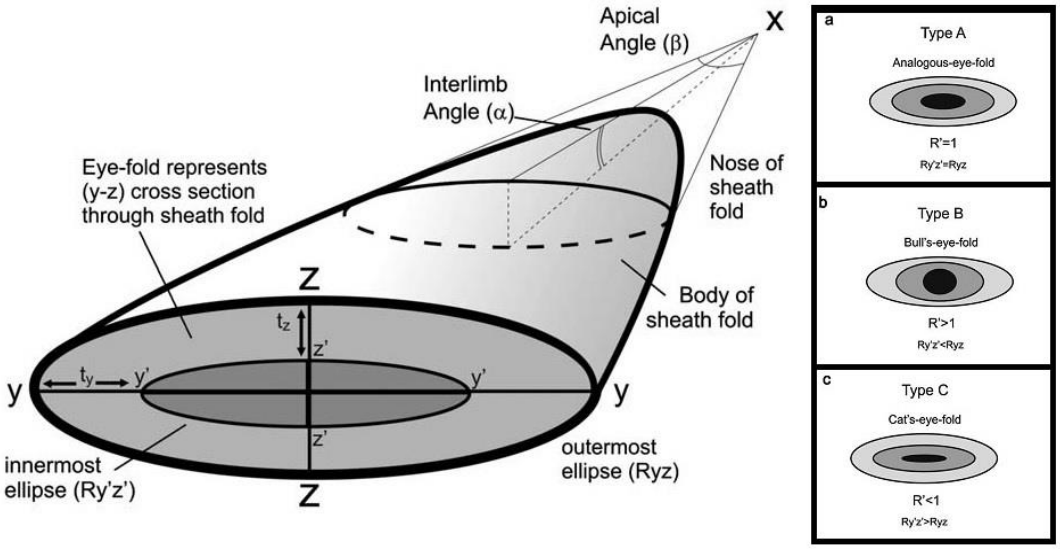

Figure 5-11. Schematic sketch illustrating the x, y and z axes of a sheath fold together with the inter-limb angle (α) and apical angle (β) of the curvilinear fold hinge-line. Y-Z orientated cross sections across the sheath fold result in eye-fold geometries. The schematic inset diagrams to the right illustrate the variation in elliptical ratios within: (a) Type A, analogous-eye-fold, (ellipticity of the inner-most ring is equivalent to that of the outermost ring) (b) Type B, bull's-eye-fold (cross sectional ellipticity of the inner-most ring is less than that of the outermost ring, whilst the overall ellipticity decreases towards the centre), and (c) Type C, cat's eye-fold(ellipticity of the inner most ring (Ry'z') is greater than that of the outermost ring such that the overall ellipticity increases towards the centre). Image taken from Alsop and Holdsworth (2006).

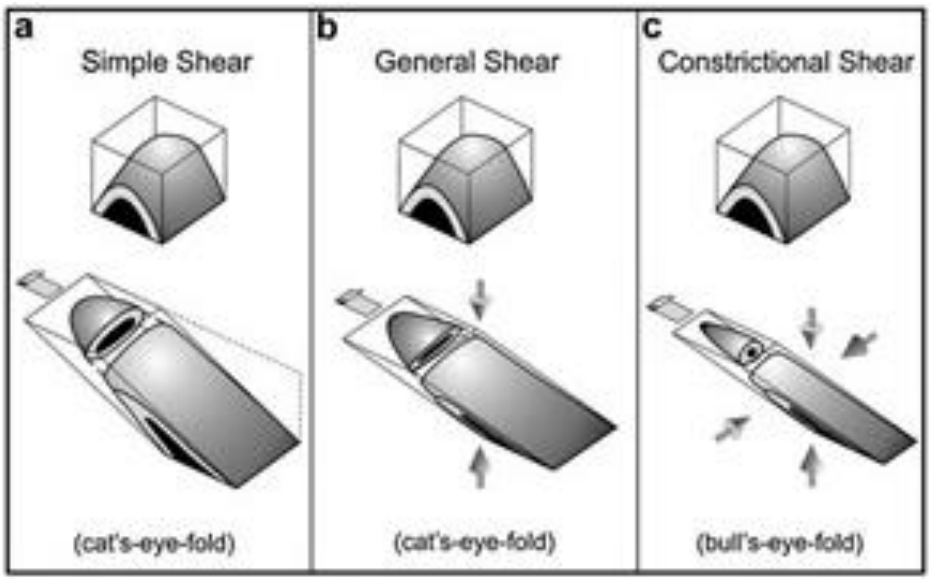

Figure 5-12. Summary diagram illustrating the geometry of cat's-eye and bull's-eye folds associated with sheaths generated during (a) simple shear, (b) general shear and (c) constrictional shear. Image taken from Alsop and Holdsworth (2006).

5.2.4b Application to the Kliprand domal structure

Based on the stereographic projections presented in Chapter 4, subareas 1 and 2 were identified as open folds, whilst subarea 3 was interpreted as a tight fold. As stated above, during the formation of sheath folds, the pre-existing fold is commonly stretched causing a reduction in the interlimb angle. Therefore, subareas 1 and 2 might have consisted of foliations of the pre-existing fold whilst the axial planar fabric that is found throughout the Kliprand domal structure has been formed during the formation of the sheath fold. This interpretation is strengthened by the fact that a strong cleavage and a subparallel lineation are present. The major factor that results in the formation of sheath folds is that a high strain needs to be available for these types of folds to develop with or without the presence of shear zones (Alsop & Holdsworth, 2006). The abundant boudins within the study area and the fact that this study area was subjected to upper granulite facies metamorphism suggest that the ductility and the strain value were both high enough for this type of fold structure to develop. This structure also best describes the dome within a dome concept, seeing that sheath folds commonly display eye structures. The tongue or the long axes (x-axes) of the sheath fold might have been eroded over time, thus displaying the "eye" or x-axis of the fold when looking down from above. The Kliprand domal structure resembles a cat's eye fold (Figure 5-11, 5-12) as the ellipticity of the inner dome is higher than that of the outer dome. On the Flinn diagram, Subarea 3 is an S-L tectonite (Figure 4-18) further pointing to the fact that this structure is, in fact, a cat's eye fold.

Chapter 6 : Whole rock geochemistry

6.1 Introduction

The main objective of this chapter is to describe the geochemical characteristics of the different rock types within the Kliprand domal structure. Sixty-five samples from the Kliprand domal structure were taken for detailed geochemical analysis to establish their whole rock composition. With the variation in lithologies within the study area a variety of geochemical plots have been constructed for classifying and characterising, along with source or provenance determination and tectonic setting establishment. An important point to note when viewing the geochemical data below is that the Cr concentrations are unreliable and inaccurate due to the possible contamination effect from the steel mill used to mill the samples for analysis. The strong Cr anomaly is thus likely due to contamination.

6.2 Element mobility

Element mobility can result due to an array of various causes. The chemical change that takes place in a rock often occurs during weathering, diagenesis and metamorphism or even through its interaction with hydrothermal fluid. Middelburg et al. (1988) investigated the chemical processes that affected the mobility of elements during weathering of granitic rocks. They found that Zr, Hf, Fe, Al, Th, Nb, Sc and the Rare Earth Elements (REE) are typically immobile during weathering, whereas the major elements Ca, Na, P, K, Mg and Si, as well as Sr, Ba and Rb are highly mobile during weathering (Middelburg et al. 1988). Even though the major elements may be mobile during upper granulite facies metamorphism, certain diagrams in this study does make use of major elements, it should thus be kept in mind that observations based on major elements are not definite. The mobile elements are mainly derived from minerals such as the feldspars and micas, whilst the immobile elements are concentrated in the remaining material after weathering has occurred or adsorbed by secondary minerals. Even though the REEs are immobile during moderate stages of weathering, they become mobile and fractionate out during the later stages of weathering (Middelburg et al. 1988). Unlike the rest of the elements mentioned above the geochemical behaviour of Fe and Ce, and the transitional elements Mn, Cr and V, are highly dependent on the redox conditions to which the rock is subjected (Middelburg et al. 1988).

The high-grade granulite facies Garies terrane is composed of gneisses, migmatites, granites, charnockites and supracrustal rocks. From the previous studies of Macey (2001) and Macey et al. (2011) it was stated that the younger charnockite of the Spektakel Suite intruded the streaky augen

gneiss of the Little Namaqualand Suite, whilst locally charnockite of metamorphic origin was also described as having formed by the metasomatism of the pink gneiss or streaky augen gneiss. Charnockites may only develop from the metamorphism of granitic gneisses if a fluid phase with a relatively high CO_2/H_2O ratio is present (Allen et al. 1985). Allen et al. (1985) states that evidence for prograde metamorphism of the gneiss to charnockite, are provided by the enriched in Pb, and the transition metals relative to Mg, and are depleted in the REE and Y compared to the adjacent gneiss protoliths. Mafic igneous rocks that have been affected by weathering and / or a wide range of metamorphic conditions, are expected to display HFSE (Y, Zr, Hf, Ti, Nb and Ta), HREE (Lu, Yb) and the transition metals (V, Cr, Ni and Sc) to be generally unaltered (Escuder-Viruete et al. 2010). The major (e.g., Si, Na, K, Ca) and large ion lithophile (LIL) trace elements (Cs, Rb, Ba, Sr) are easily mobilised by metamorphism and magmatic fluids (Escuder-Viruete et al. 2010). Due to the immobility of the HFSE and REE, these elements were mainly used in the characterization and the petrogenetic discussion. Even though the major elements are mobile in both magmatic rocks and metasedimentary rocks they have been used in the characterization of these rocks in the study area.

6.3 Geochemistry of the magmatic rocks

The streaky augen gneiss of the Little Namaqualand Suite and the post-tectonic Ibequas Granite of the Spektakel Suite has SiO_2 values ranging between ~71-76 wt%. These granites generally display major element compositions similar to that of the Upper Continental Crust (UCC) of Taylor and McLennan (1985). These rocks, however, have lower MnO, CaO and Na_2O contents relative to the UCC. The total alkalis vs. silica (TAS) diagram of Cox et al. (1979) was used to classify the plutonic rocks of the Little Namaqualand and Spektakel Suites according to major element geochemistry. The TAS diagram is also useful in that it divides the rocks into ultramafic, mafic, intermediate, and felsic on the basis of their silica content (Rollinson 1993). Even though the $Nb/Y–Zr/TiO_2$ plot of Pearce (1996) (Figure 6-2) is a far better and more reliable classification diagram given the high grade metamorphic nature of the area, It is however mainly used for volcanic rocks, therefore the intrusive total alkalis vs. silica diagram was also used. By plotting the streaky augen gneisses and Ibequas granites on the total alkalis vs. silica diagram it was thus confirmed that these rocks are felsic and plot mainly within the granitic field (Figure 6-1).

According to Zhai et al. (2011) the alkali elements (K_2O and Na_2O) are not suitable for classifying plutonic rocks by using the TAS diagram as these elements are mobile during metamorphism. It is rather preferable to use the incompatible elements, such as Zr, Nb and Ti in discussing the nature of these rocks (Zhai et al. 2011). In the $Nb/Y–Zr/TiO_2$ plot of Pearce (1996) (Figure 6-2), the streaky augen gneiss and Ibequas granites fall in the field of rhyodacite confirming their rhyolitic (if volcanic)

or granitic (if intrusive) nature. However, unlike the streaky augen gneiss and the Ibequas granite that are rhyolitic in nature, the charnockites vary between rhyolites and rhyodacites and andesites (felsic to intermediate) within the Nb/Y–Zr/TiO_2 plot of Pearce (1996) (Figure 6-2). These charnockites are therefore pyroxene-bearing monzogranites to granodiorites (charnockites to enderbites, respectively).

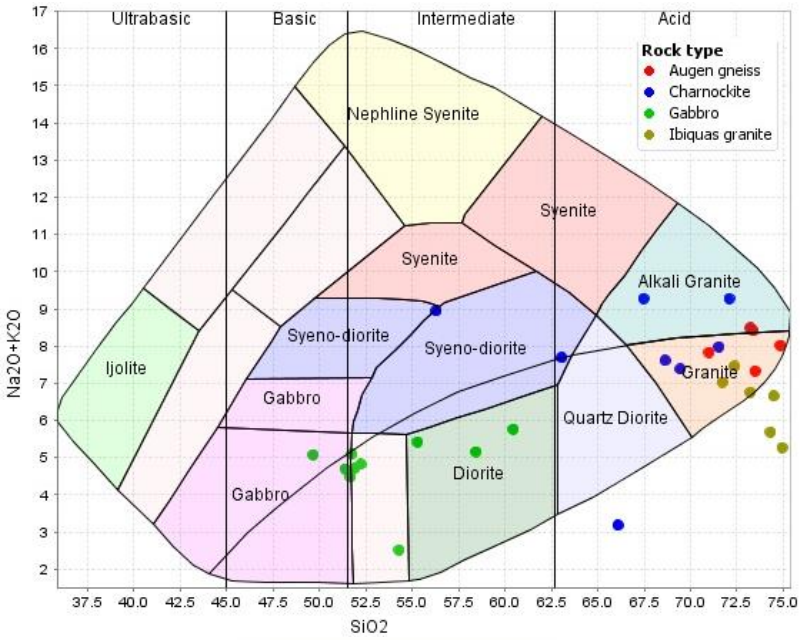

Figure 6-1. *TAS classification diagram of Cox et al. (1979) classifying magmatic rocks of the Kliprand dome. The charnockites are of metasomatic origin.*

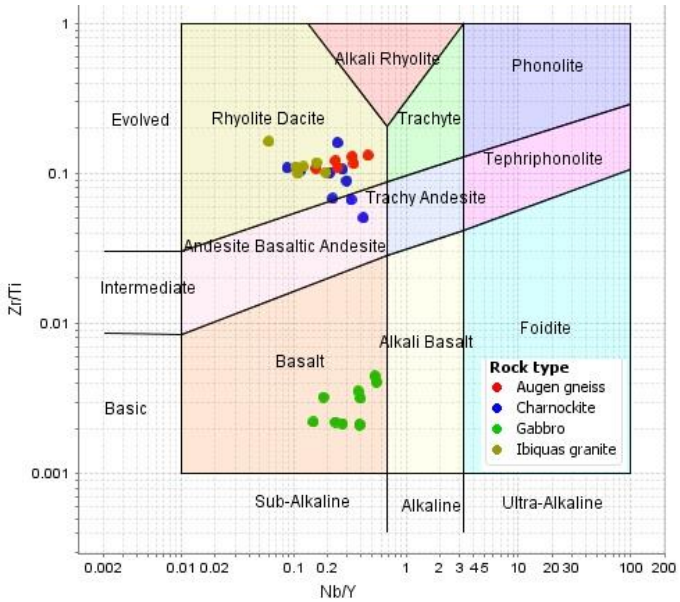

Figure 6-2. *The Zr/TiO_2–Nb/Y diagram for volcanic rocks (after Pearce, 1996).*

With regard to the major element compositions of these magmatic rocks, Al_2O_3 has the second highest content in these rocks and could thus be used for further characterization (Figure 6-3a).

Shand (1927) grouped igneous rocks based on the total molar alkali versus aluminium content (known as the alumina saturation index) as either peralkaline [$Al_2O_3 < (Na_2O + K_2O)$], peraluminous [$Al_2O_3 > (CaO + Na_2O + K_2O)$], or metaluminous [$Al_2O_3 < (CaO + Na_2O + K_2O)$] but [$Al_2O_3 > (Na_2O + K_2O)$] (Winter, 2010). On the (A/CNK ($Al_2O_3/(CaO + Na_2O + K_2O)$) vs. (A/NK ($Al_2O_3/(Na_2O + K_2O)$) plot of Barton and Young (2002) the majority of the streaky augen gneiss samples plot as weakly peraluminous, whilst the Ibequas granites plot in the strongly peraluminous field (Figure 6-3a).

In terms of FeO composition there is a significant difference between rocks that have undergone iron enrichment during differentiation while silica remains low, and those that have undergone minimal enrichment of FeO relative to MgO while silica enrichment remains low (Frost et al. 2001). The rocks following these “ferroan” and “magnesian” trends, respectively, can be distinguished on an $FeO^{tot}/(FeO^{tot} + MgO)$ versus SiO_2 plot (Figure 6-3b) (Frost et al. 2001). On the $FeO^{tot}/(FeO^{tot} + MgO)$ versus SiO_2 plot (Figure 54b) the streaky augen gneiss clearly plots within the ferroan field whilst the Ibequas Granite straddles the boundary between the ferroan and magnesian fields (Figure 6-3b).

Another useful diagram to use in the classification of felsic magmatic rocks is the alkali-lime index Frost et al. (2001) whereby the volcanic suites are separated into the calcic, calc-alkalic, alkali-calcic and alkalic classes. On the modified alkali lime index vs. SiO_2 plot (Figure 6-3c) the streaky augen gneiss straddles the calc-alkalic to alkali-calcic fields and the Ibequas granite ranges from calcic to calc-alkalic.

In the K_2O vs. SiO_2 diagram (Figure 6-3d) the Ibequas granite mainly plots within the high K calc-alkaline series, with samples IG201 and IG31 plotting within the medium K (calc-alkaline series) and sample IG73 plotting within the shoshonite series. All of the streaky augen gneiss samples plot within the shoshonite series. These rocks are highly potassic, likely an indicator of a crustal influence on their origin.

The rare earth elements (REE) contain a large amount of information in proportion to their abundances within rocks. Being immobile, it is beneficial to use them in characterising the protolith of these magmatic rocks. In the REE diagram, the degree of compatibility increases from left to right, so that certain shapes in the REE diagram can be interpreted as being caused by retention of certain minerals in the magma or in the source (Solanki 2011). In the chondrite-normalized rare earth element (REE) plot (the rare earth element normalization is to the normalizing values of Boynton (1984)), the streaky augen gneiss has a fractionated REE pattern (Figure 6-4) with an average $(La/Lu)_N$ of 9.5 (Table 4), where the N subscript represents chondrite normalisation. Enrichment in

the LREE is shown by $(La/Sm)_N$ = 2.78-3.59 (Table 4), whereas the HREE show a more variable pattern from a fractionated, sloping trend (Figure 6-4) to enrichment of Lu [$(Gd/Yb)_N$ = 0.78 – 3.21] (Table 4).

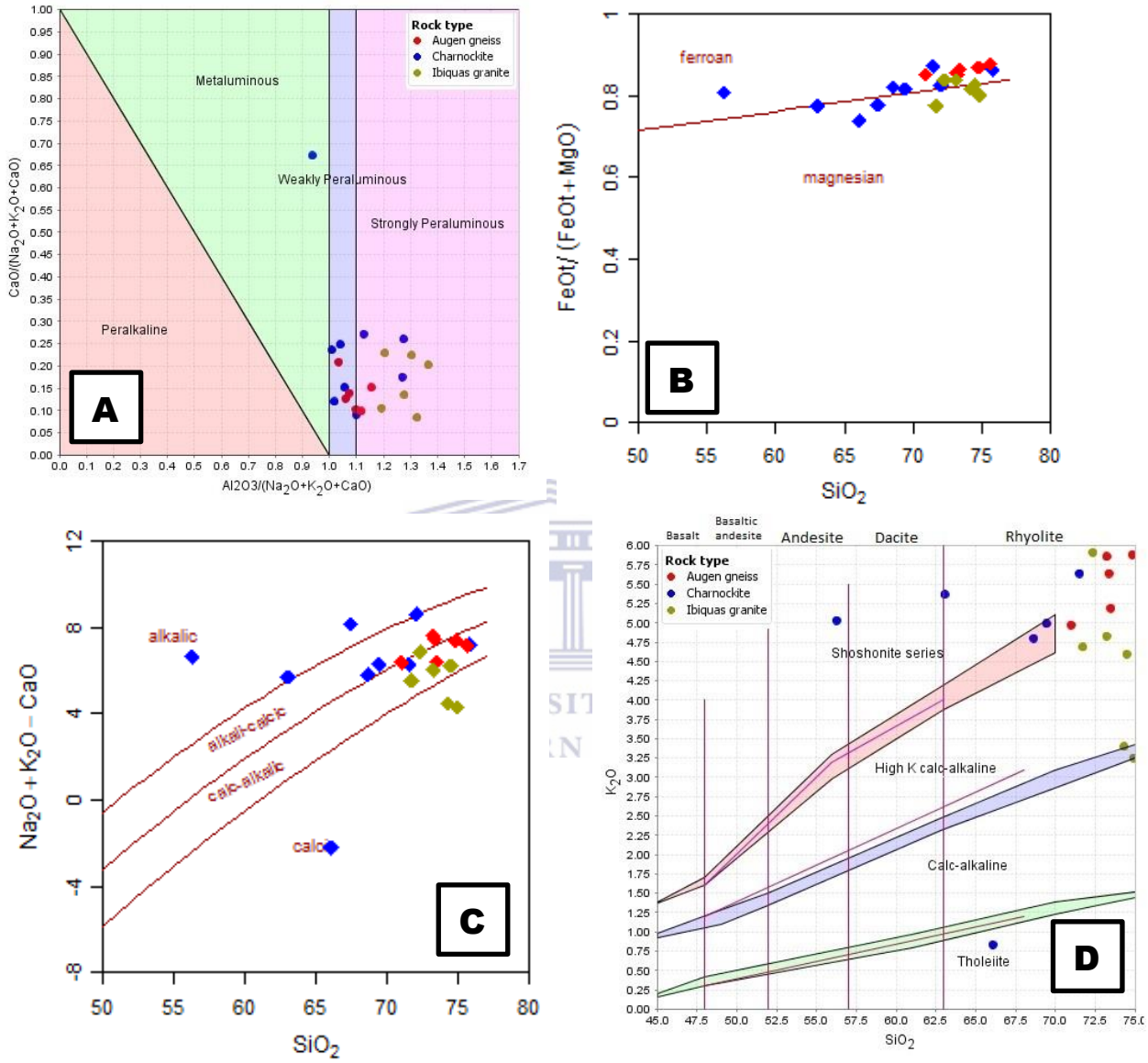

Figure 6-3. (A) A/CNK – A/NK plot of Barton and Young (2002). (B) $FeO_{tot}/(FeO_{tot} + MgO)$ vs. weight percent SiO_2 diagram of Frost et al. (2001). (C) $Na_2O + K_2O – CaO$ vs. weight percent SiO_2 diagram of Frost et al. (2001). (D) K_2O vs. SiO_2 diagram. The red line subdivisions on the K_2O vs. SiO_2 diagram were proposed by Le Maitre et al. (1989), whereas the shaded fields are the boundary lines proposed by Peccerillo and Taylor (1976).

Table 2. Major element geochemistry of the magmatic and metamorphic rocks of the Kliprand domal structure.

	Gabbro-norite							*Streaky augen gneiss*									OIB	UCC	LCC	ACC
Sample	**G33**	**G36**	**G125.2**	**G182**	**G115**	**G196**	**G169.1**	**G162**	**G216**	**G124**	**AG212**	**AG148**	**AG112**	**AG113**	**AG114**	**AG170**	Macdonald 1968	Taylor and McLennan 1985		
SiO_2	58.42	60.44	55.29	51.72	51.38	51.89	51.67	54.29	52.22	49.64	73.48	73.22	73.37	75.65	74.84	71.00	49.4	66	45.4	57.3
TiO_2	1.58	2.08	2.75	2.98	2.92	1.50	1.75	1.29	1.17	2.89	0.39	0.36	0.36	0.29	0.34	0.66	2.5	0.5	1	0.9
Al_2O_3	16.04	15.36	14.97	15.73	15.85	17.79	16.45	16.12	16.83	15.29	12.43	12.94	13.29	11.95	12.09	13.16	13.9	15.2	16.1	15.9
Fe_2O_3	9.01	7.47	10.27	10.86	12.71	9.00	10.11	10.05	8.93	11.82	3.46	2.53	2.25	2.16	2.37	4.10	3.03	4.04	9.53	8.188
MnO	0.10	0.11	0.13	0.14	0.19	0.12	0.15	0.16	0.13	0.16	0.07	0.04	0.02	0.02	0.01	0.03	0.16	0.1		
MgO	3.22	1.95	3.24	4.29	3.95	5.81	6.26	6.58	6.19	5.60	0.49	0.38	0.35	0.27	0.32	0.64	8.44	2.2	6.3	5.3
CaO	4.56	4.47	5.84	7.09	6.34	7.22	7.16	7.21	7.67	7.05	0.90	0.85	0.95	0.58	0.62	1.46	10.3	4.2	8.5	7.4
Na_2O	2.99	2.85	3.14	2.97	3.11	3.22	2.89	0.80	3.12	2.74	2.13	2.63	2.77	2.23	2.14	2.86	2.13	3.9	2.8	3.1
K_2O	2.17	2.91	2.28	2.13	1.59	1.50	1.60	1.71	1.70	2.33	5.19	5.86	5.64	5.52	5.88	4.97	0.38	3.4	0.34	1.1
P_2O_5	0.40	0.62	0.85	0.73	0.94	0.35	0.48	0.18	0.33	1.01	0.12	0.09	0.14	0.07	0.14	0.17	0.26			
Cr_2O_3	0.01	0.01	0.02	0.03	0.02	0.04	0.04	0.07	0.03	0.03	0.02	0.01	0.01	0.02	0.02	0.01				
L.O.I.	**0.93**	**0.97**	0.81	0.62	0.57	1.07	0.84	0.98	1.20	0.62	1.05	0.76	0.87	1.01	0.72	0.67				
Total	99.43	99.24	99.59	99.29	99.57	99.51	99.40	99.44	99.52	99.18	99.73	99.67	100.02	99.77	99.49	99.73				

	Charnockite								*Ibequas granite*						
Sample	**C35**	**C63**	**C106**	**C188**	**C133**	**C141**	**C125.1**	**C171**	**C144**	**IG30**	**IG31**	**IG61**	**IG73**	**IG201**	**IG142**
SiO_2	69.45	75.81	63.05	68.63	71.51	56.28	72.08	67.47	66.09	73.22	74.93	74.49	72.35	74.31	71.72
TiO_2	0.49	0.32	1.28	0.83	0.46	1.05	0.27	0.84	1.16	0.57	0.62	0.38	0.38	0.39	0.30
Al_2O_3	14.36	11.44	14.92	13.61	13.12	20.51	14.15	13.86	13.67	12.40	11.71	12.12	11.92	12.48	13.95
Fe_2O_3	4.14	2.39	6.78	5.58	3.78	8.28	1.78	4.51	6.64	4.07	4.69	3.67	2.55	3.84	3.42
MnO	0.08	0.02	0.06	0.07	0.04	0.18	0.02	0.05	0.14	0.09	0.07	0.07	0.05	0.07	0.09
MgO	0.84	0.34	1.77	1.09	0.50	1.78	0.34	1.16	2.10	0.71	1.05	0.69	0.44	0.78	0.89
CaO	1.09	0.74	1.98	1.79	1.69	2.31	0.64	1.10	5.40	0.73	0.95	0.43	0.58	1.18	1.46
Na_2O	2.39	2.26	2.33	2.82	2.33	3.92	2.98	1.95	2.36	1.93	2.02	2.07	1.55	2.28	2.34
K_2O	4.99	5.71	5.37	4.80	5.64	5.03	6.29	7.32	0.83	4.83	3.25	4.59	5.91	3.40	4.69
P_2O_5	0.08	0.05	0.51	0.27	0.12	0.13	0.08	0.26	0.37	0.06	0.08	0.11	0.14	0.07	0.06
Cr_2O_3	0.02	0.05	0.03	0.01	0.01	0.01	0.01	0.01	0.06	0.02	0.02	0.02	0.02	0.02	0.02
L.O.I.	0.68	0.76	1.74	1.00	0.90	0.21	0.93	0.77	1.09	0.67	0.56	0.83	0.84	2.79	0.68

Note: G, gabbro-norite; AG, augen gneiss; C, charnockite; IG, Ibequas granite; OIB, Ocean island basalt; UCC, LCC and ACC are upper, lower and average continental crust.

The Ibequas Granite has a negative LREE slope (Figure 6-5) with an average $(La/Sm)_N$ = 4.11 (Table 4) indicating fractionation within the LREEs. The chondrite-normalized REE plot of the Ibequas granite is not as fractionated [average $(La/Lu)_N$ of 4.8] as the streaky augen gneiss, but has a LREE fractionation greater than that of the streaky augen gneiss. Sample IG30 is an exception as it has a steep slope [average $(La/Lu)_N$ of 11.82] (Figure 6-5), so that the LREE are thus more fractionated than the HREE (Figure 6-5). The Ibequas granite has a prominent negative Eu anomaly (average Eu/Eu*= 0.36) (Figure 6-5) whilst sample IG73 (Eu/Eu*= 0.73) and IG201 (Eu/Eu*= 0.98) display negligible Eu anomalies (Figure 6-5). Sample IG142 (Eu/Eu*= 1.19) is the only sample with a positive anomaly (Figure 55b). The majority of the Ibequas granite samples have flat HREE trends (Figure 6-5) [average $(Gd/Yb)_N$ = 1.91], with sample IG30 (negative slope [$(Gd/Yb)_N$ = 2.71]), and sample IG201 (positive slope [$(Gd/Yb)_N$ = 0.59]) displaying variable HREE patterns (Figure 6-5).

Europium is found in both a 3+ and 2+ valence states. Eu^{2+} could, therefore, substitute for Ca^{2+} in plagioclase giving rise to depletion in this element in the REE pattern known as the europium anomaly (Rollinson 1993). Both the streaky augen gneiss and the Ibequas granite have prominent negative Eu anomalies (average Eu/Eu*= 0.34 for the former; average Eu/Eu*= 0.66 for the latter) (Figure 6-4, 6-5). The prominent Eu anomalies denote the role of either plagioclase retention in the source, or plagioclase fractionation in the parental magma.

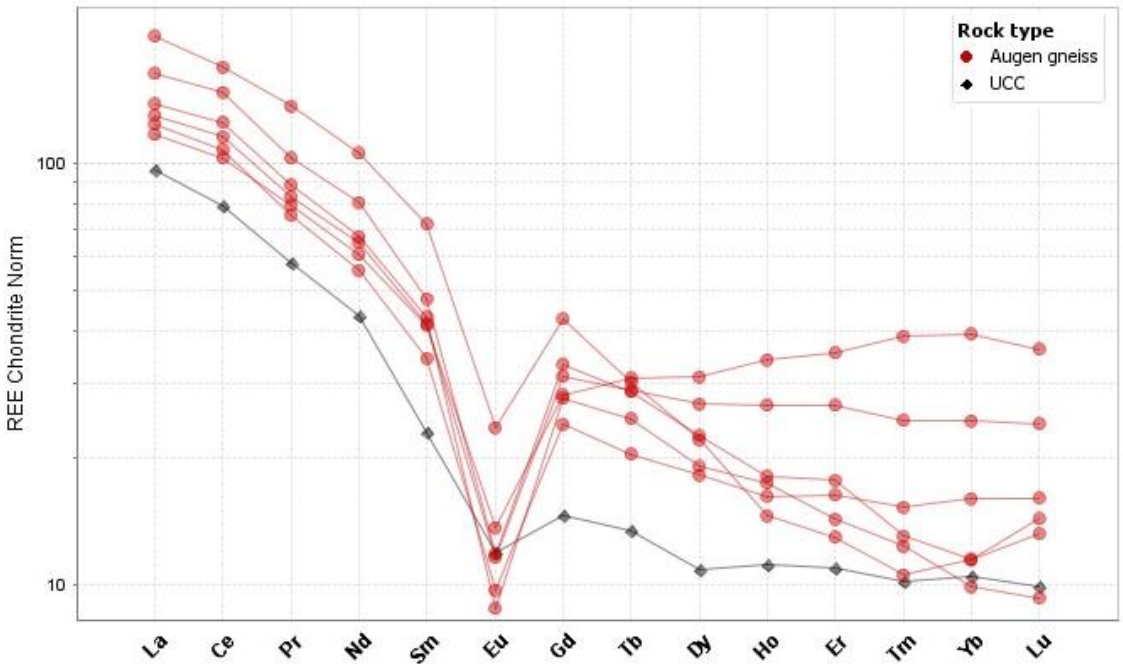

Figure 6-4. Chondrite normalized REE plot (after Boynton, 1984) of the streaky augen gneiss.

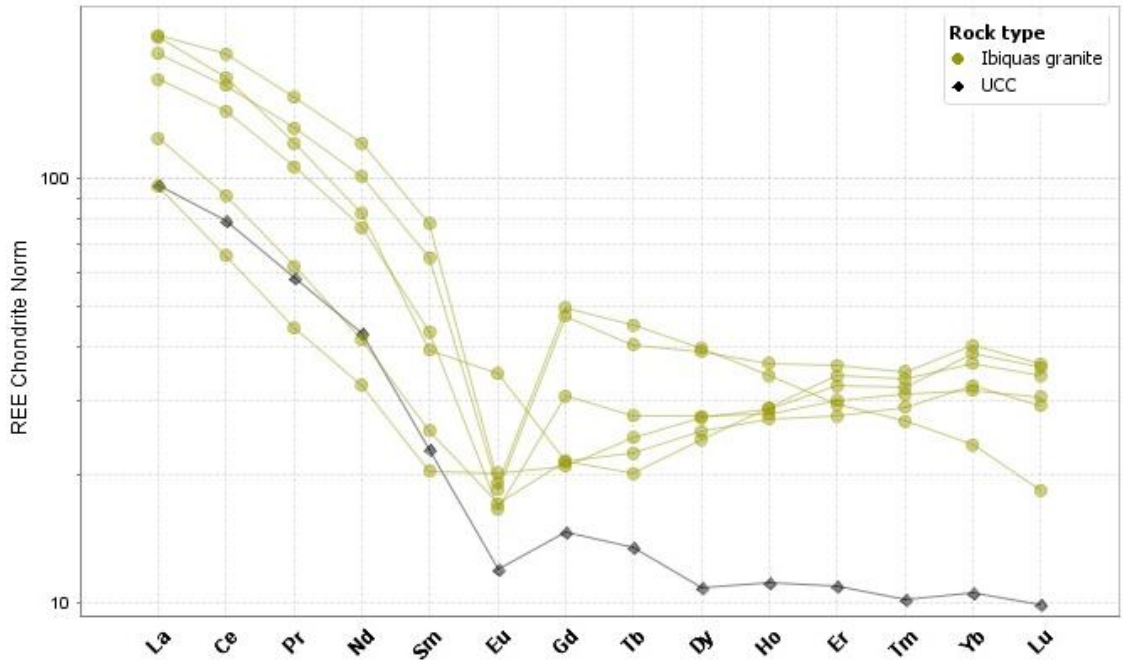

Figure 6-5. Chondrite normalized REE plot (after Boynton, 1984) of the Ibequas granite.

Figure 6-6 is a multi-element trace element plot (spider diagram) plotted according to the plotting order of Sun and McDonough (1995). The upper continental crust (UCC) values of Taylor et al. (1981) have also been plotted on the spider diagram (Figure 6-6) for comparison with the streaky augen gneiss and the Ibequas granites. The elemental concentrations of the streaky augen gneiss and the Ibequas granite gradually decrease from Cs to Pb exhibiting a negatively sloping trend (Figure 6-6). However, the slope is not smooth, as there are several well-developed enrichments and depletions (Figure 56). The streaky augen gneiss and the Ibequas granite slopes on the spider diagram are very similar to the upper continental crust (UCC) in comparison to the lower continental crust (LCC) and average continental crustal (ACC) curves (Figure 6-6).

With regard to the LILE of the Streaky augen gneiss and Ibequas granites, Pb, Rb and K exhibit enrichments (Figure 6-6a, b) in comparison to the UCC whilst the remaining LILEs (Cs, Ba and Sr) are depleted (Figure 6-6a, b). Hf, Zr, Ce, U and Th are the HFS elements that exhibit positive anomalies (Figure 6-6a, b) in comparison to the UCC. Relative to the UCC trend Nb and Ti are the only HFS elements that have prominent negative anomalies (Figure 6-6a, b). The enrichment in Pb, Rb, K, U and Th all denote the influence of continental crust in the origin of these rocks and in their parental magmas. The Cr contents of both rocks are fairly high in terms of magmatic rock compositions. This is likely due to the use of a Cr-steel mill, leading to contamination of these samples.

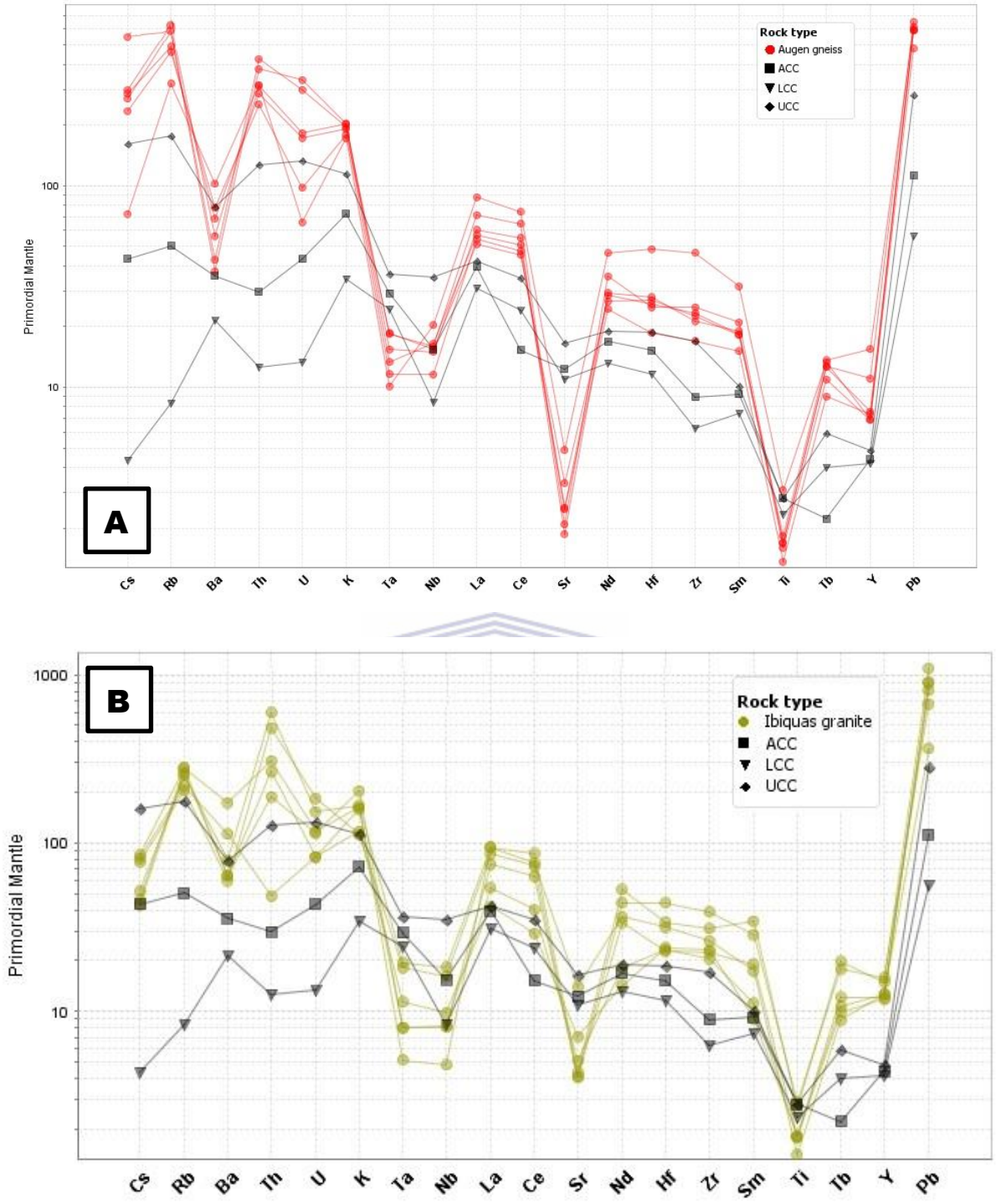

Figure 6-6. Primordial mantle normalised multi-element (spider) diagrams (plotting order and normalizing values of McDonough et al., 1992) of A) The streaky augen gneiss and B) The Ibequas granite. UCC – Upper Continental Crust, Average Continental Crust and Lower Continental Crust.

Table 3. Rare earth element (REE) geochemistry of the gabbro-norite, Streaky augen gneiss, Ibequas granite and Charnockite.

	Gabbro-norite							*Streaky augen gneiss*									N-MORB	E-MORB	OIB
Sample	**G33**	**G36**	**G125.2**	**G182**	**G115**	**G196**	**G169.1**	**G162**	**G216**	**G124**	**AG212**	**AG148**	**AG112**	**AG113**	**AG114**	**AG170**	**Sun and McDonough 1989**		
La	44.59	59.33	75.04	58.21	63.59	47.46	41.94	24.94	44.97	56.68	36.27	40.32	50.62	38.36	42.89	62.02	2.5	6.3	37
Ce	91.12	127.65	157.4	125.91	164.55	95.82	90.56	55.93	94.89	126.2	83.17	93.38	119.04	87.12	101.24	136.29	7.5	15	80
Pr	10.99	15.74	18.96	16.05	23.40	11.61	11.39	7.55	11.86	16.02	9.71	10.18	12.58	9.20	10.85	16.63	1.32	2.05	9.7
Nd	44.81	64.92	78.29	65.38	102.48	46.57	47.66	32.27	48.42	66.64	36.44	38.92	48.44	33.41	40.17	63.42	7.3	9	38.5
Sm	9.32	13.73	15.32	12.82	24.38	8.58	9.62	8.16	8.90	12.40	8.07	8.12	9.31	6.72	8.44	14.04	2.63	2.6	10
Eu	2.34	3.00	3.12	2.91	2.65	2.29	2.46	1.64	2.38	3.00	1.01	0.85	0.87	0.72	0.65	1.74	1.02	0.91	3
Gd	8.73	12.50	12.87	11.77	22.15	6.92	9.07	8.42	7.56	11.14	7.32	8.10	8.66	6.23	7.18	11.09	3.68	2.97	7.62
Tb	1.14	1.79	1.75	1.60	3.28	1.04	1.31	1.47	1.07	1.57	1.47	1.37	1.36	0.97	1.18	1.44	0.67	0.53	1.05
Dy	6.03	10.21	10.08	9.45	19.98	5.72	7.56	8.89	6.38	8.36	10.02	8.65	7.28	5.87	6.16	7.11	4.55	3.55	5.6
Ho	1.09	1.90	1.88	1.83	3.83	1.15	1.52	1.77	1.32	1.66	2.46	1.92	1.30	1.17	1.25	1.05	1.01	0.79	1.06
Er	2.71	4.86	5.33	4.90	10.45	2.96	4.40	5.18	3.47	4.42	7.47	5.62	3.72	3.44	3.01	2.74	2.97	2.31	2.62
Tm	0.39	0.58	0.72	0.65	1.45	0.43	0.62	0.74	0.48	0.56	1.26	0.80	0.42	0.50	0.40	0.34	0.45	0.35	0.35
Yb	2.55	3.57	4.45	4.33	9.39	2.85	3.88	4.91	3.33	3.89	8.24	5.12	2.41	3.35	2.07	2.40	3.05	2.37	2.16
Lu	0.39	0.46	0.62	0.59	1.25	0.40	0.57	0.66	0.48	0.55	1.17	0.78	0.46	0.52	0.30	0.43	0.45	0.35	0.3
∑ LREE / HREE	8.72	7.84	9.15	7.93	5.27	9.78	6.95	4.02	8.68	8.65	4.41	5.90	9.37	7.93	9.45	10.99	1.26	2.64	8.44
Ce/Ce*	0.99	1.01	1.00	0.99	1.03	0.98	1.00	0.98	0.99	1.01	1.07	1.11	1.14	1.12	1.13	1.02	0.99	1.00	1.02
Eu/Eu*	0.79	0.70	0.68	0.72	0.35	0.91	0.81	0.61	0.89	0.78	0.40	0.32	0.30	0.34	0.26	0.43	1.00	1.00	1.05
$(Gd/Yb)_N$	2.76	2.83	2.33	2.19	1.90	1.96	1.89	1.38	1.83	2.31	0.72	1.28	2.90	1.50	2.80	3.73	0.97	1.01	2.85
$(La/Yb)_N$	11.79	11.20	11.37	9.06	4.57	11.23	7.29	3.42	9.10	9.82	2.97	5.31	14.16	7.72	13.97	17.42	0.55	1.79	11.55
$(La/Sm)_N$	3.01	2.72	3.08	2.86	1.64	3.48	2.74	1.92	3.18	2.88	2.83	3.12	3.42	3.59	3.2	2.78	0.59	1.52	2.32
$(Gd/Lu)_N$	2.78	3.38	2.58	2.48	2.21	2.15	1.98	1.58	1.96	2.52	0.78	1.29	2.34	1.49	2.98	3.21	1.01	1.05	3.15
$(La/Lu)_N$	11.88	13.4	12.57	10.25	5.3	12.32	7.64	3.92	9.73	10.7	3.22	5.37	11.43	7.66	14.85	14.98	0.57	1.86	12.81

Note: N-MORB, normal mid-ocean ridge basalts; E-MORB, enriched mid-ocean ridge basalts; OIB, Ocean island basalt. All these are normalized relative to Boynton (1984)

Table 4 (cont.) Rare earth element (REE) geochemistry of the gabbro-norite, Streaky augen gneiss, Ibequas granite and Charnockite.

	Charnockite									*Ibequas granite*						UCC
Sample	**C35**	**C63**	**C106**	**C188**	**C133**	**C141**	**C125.1**	**C171**	**C144**	**IG30**	**IG31**	**IG61**	**IG73**	**IG201**	**IG142**	**Taylor and McLenan 1981**
La	172.55	125.90	594.55	166.19	153.48	373.84	170.52	128.68	179.68	67.12	60.94	52.92	38.44	29.70	66.71	30
Ce	134	114.11	452.69	139.64	118.19	319.98	134.31	96.62	140.51	158.7	133.63	116.39	73.57	53.2	139.56	64
Pr	102.13	83.69	330.57	113.52	85.82	255.66	90.90	75.66	112.87	18.94	16.00	12.99	7.56	5.42	14.72	7.1
Nd	78.93	60.88	240.88	90.13	69.17	197.77	69.42	59.93	88.08	72.55	60.64	45.89	25.03	19.58	49.65	26
Sm	50.62	41.38	111.74	63.23	34.72	124.82	35.23	38.31	51.38	15.27	12.69	8.49	4.98	4.00	7.69	4.5
Eu	26.12	7.35	39.86	18.23	29.93	21.77	16.73	33.06	25.99	1.41	1.36	1.22	1.26	1.49	2.55	0.88
Gd	39.23	29.46	59.34	44.40	17.07	86.06	19.77	24.29	33.09	12.86	12.30	7.96	5.59	5.45	5.58	3.8
Tb	39.66	26.58	36.92	39.87	12.66	82.28	15.40	21.52	24.89	2.14	1.93	1.31	1.07	1.16	0.96	0.64
Dy	43.85	25.65	26.86	39.01	10.78	83.26	11.43	24.13	22.02	12.81	12.61	8.85	8.15	8.80	7.81	3.5
Ho	46.66	22.42	22.14	36.77	7.38	87.19	11.28	22.42	18.94	2.46	2.64	2.01	1.95	2.06	2.07	0.8
Er	50.90	23.67	18.00	35.24	7.14	94.57	11.62	24.00	17.71	6.16	7.61	6.31	5.79	6.81	7.19	2.3
Tm	52.47	19.44	14.51	34.57	5.56	94.44	12.35	23.46	14.81	0.87	1.14	1.00	0.94	1.04	1.09	0.33
Yb	54.59	20.57	13.30	37.75	6.17	103.83	16.22	23.16	15.36	4.93	8.44	6.62	6.79	8.12	7.67	2.2
Lu	50.93	17.08	12.42	37.89	6.21	100.62	15.22	18.63	18.32	0.59	1.17	0.99	0.94	1.15	1.11	0.32
∑ LREE / HREE	4.21	6.37	21.75	5.29	16.56	5.12	12.95	6.11	9.38	7.77	5.93	6.75	4.79	3.24	8.31	9.47
Ce/Ce*	1.01	1.11	1.02	1.02	1.03	1.04	1.08	0.98	0.99	1.07	1.03	1.07	1.04	1.01	1.07	1.06
Eu/Eu*	0.59	0.21	0.49	0.34	1.23	0.21	0.63	1.08	0.63	0.31	0.33	0.45	0.73	0.98	1.19	0.65
$(Gd/Yb)_N$	0.72	1.43	4.46	1.18	2.76	0.83	1.22	1.05	2.15	2.10	1.18	0.97	0.66	0.54	0.59	1.39
$(La/Yb)_N$	3.16	6.12	44.7	4.4	24.87	3.6	10.51	5.56	11.7	9.18	4.87	5.39	3.82	2.47	5.86	9.19
$(La/Sm)_N$	3.41	3.04	5.32	2.63	4.42	3	4.84	3.36	3.5	2.76	3.02	3.92	4.86	4.67	5.46	4.19
$(Gd/Lu)_N$	0.77	1.72	4.78	1.17	2.75	0.86	1.3	1.3	1.81	2.71	1.31	1	0.74	0.59	0.62	1.47
$(La/Lu)_N$	3.39	7.37	47.86	4.39	24.71	3.72	11.21	6.91	9.81	11.82	5.41	5.55	4.25	2.68	6.24	9.73

Table 4. Trace element geochemistry of the gabbro-norite, Streaky augen gneiss, Ibequas granite and Charnockite rocks in the Kliprand study area.

	Gabbro-norite									*Streaky augen gneiss*							N-MORB	E-MORB	OIB
Sample	**G33**	**G36**	**G125.2**	**G182**	**G115**	**G196**	**G169.1**	**G162**	**G216**	**G124**	**AG212**	**AG148**	**AG112**	**AG113**	**AG114**	**AG170**	Sun and McDonough 1989		
Sc	26.56	22.08	27.13	29.31	35.94	23.47	25.78	32.27	25.10	27.99	18.95	15.81	14.38	14.58	15.78	15.34			
Ti	9472.1	12469.6	16486.25	17865.1	17505.4	8992.5	10491.25	7733.55	7014.15	17325.55	2338.05	2158.2	2158.2	1738.55	2038.3	3956.7	7600	6000	17200
V	186.99	158.61	229.39	242.19	259.14	166.52	186.06	222.08	152.49	234.50	66.22	60.99	60.40	59.64	62.53	73.83			
Cr	271.31	181.27	186.72	183.07	170.56	267.67	264.69	465.28	226.48	236.06	349.08	290.15	300.73	341.66	346.98	257.64			
Co	21.00	15.06	25.81	31.91	27.79	31.81	38.27	34.96	31.98	34.32	6.16	6.75	5.05	4.65	4.69	8.96			
Ni	27.53	19.99	22.37	27.06	22.93	53.94	69.60	69.04	45.94	50.50	19.08	16.48	16.45	18.24	23.43	18.93			
Cu	21.01	18.28	18.02	42.60	19.70	21.03	22.26	26.79	27.68	29.20	25.80	19.54	15.59	33.41	32.33	12.61			
Zn	161.80	103.91	127.03	134.14	185.18	96.10	107.40	96.03	97.77	145.07	77.47	60.38	60.62	43.96	45.34	64.66			
Rb	111.28	99.65	96.93	102.79	67.53	44.01	63.07	93.18	68.28	102.94	292.78	397.97	371.55	312.70	373.02	204.77	0.56	5.04	31
Sr	326.78	429.09	650.31	483.07	357.37	1159.41	653.86	207.55	868.71	589.94	70.56	53.33	44.04	52.27	39.42	102.92	90	155	660
Zr	383.74	556.74	522.60	380.46	618.74	192.29	231.27	170.69	226.30	363.49	252.62	262.32	279.32	190.54	237.53	521.33	74	73	280
Nb	15.82	25.67	19.38	18.03	38.61	7.91	9.62	7.16	6.34	16.30	11.02	11.75	11.37	8.23	10.69	14.52	2.33	8.3	48
Y	28.85	48.66	49.53	46.93	102.68	29.01	40.99	47.82	34.41	42.35	70.40	50.16	34.40	33.48	31.23	31.65	28	22	29
Cs	1.95	1.15	0.97	1.24	0.53	0.47	1.29	10.14	1.76	1.21	5.39	6.86	12.62	6.60	6.23	1.67	0.007	0.063	0.387
Ba	722.50	1383.89	1096.17	930.05	475.73	999.58	846.08	380.18	1187.12	1120.97	545.27	393.27	299.74	480.63	263.02	715.00	6.3	57	350
Hf	10.41	14.26	13.70	9.96	15.91	5.17	6.42	4.87	5.92	9.20	8.35	7.97	7.68	5.75	8.66	14.98	2.05	2.03	7.8
Ta	0.80	1.34	1.09	1.04	2.18	0.34	0.56	0.57	0.34	0.98	0.76	0.55	0.75	0.48	0.63	0.41	0.132	0.47	2.7
Pb	20.92	33.76	18.42	13.86	13.54	18.81	13.82	13.26	16.44	16.69	43.67	46.23	41.86	41.89	42.38	34.12	0.3	0.6	3.2
Th	4.79	2.76	1.57	1.36	1.20	1.49	3.01	5.43	2.47	1.08	21.30	26.22	35.67	24.12	31.83	26.61	0.12	0.6	4
U	0.90	0.64	0.71	0.86	0.90	0.36	0.75	2.18	0.60	0.72	2.06	3.83	6.29	3.62	7.02	1.38	0.047	0.18	1.02

Table 5 (cont.) Trace element geochemistry of the gabbro-norite, Streaky augen gneiss, Ibequas granite and Charnockite in the Kliprand study area.

	Charnockite								*Ibequas granite*							UCC	LCC	ACC
Sample	**C35**	**C63**	**C106**	**C188**	**C133**	**C141**	**C125.1**	**C171**	**C144**	**IG30**	**IG31**	**IG61**	**IG73**	**IG201**	**IG142**	Taylor and McLenan 1985		
Sc	27.21	19.51	16.54	21.12	13.64	28.67	15.13	18.41	22.69	16.52	19.24	15.81	23.08	21.07	20.67			
Ti	3297.25	1918.4	7673.6	4975.85	2757.7	6294.75	1618.65	5035.8	6954.2	3417.15	3716.9	2278.1	2278.1	2338.05	1798.5			
V	87.01	62.19	122.68	117.33	68.32	116.81	61.7	100.85	142.12	81.58	101.7	73.04	76.19	87.37	94.49			
Cr	444.59	388.35	238.93	284.51	271.35	254.24	296.86	237.47	315.1	459.44	486.55	425.11	480.7	436.11	371.6			
Co	7.63	10.32	14.3	11.22	6.4	8.83	3.97	13.15	14.34	7.73	7.01	7.16	3.3	9.5	5.75			
Ni	24.9	19.8	20.78	19.78	14.12	17.37	16.1	19.56	24.8	20.5	23.8	26.44	18.04	29.53	25.22			
Cu	23.1	29.43	21.2	15.82	7.92	16.01	19.55	20.43	32.69	26.26	50.08	30.33	17.12	30.23	22.47			
Zn	60.92	63.03	118.02	74.18	68.76	126.36	57.08	73.3	102.13	69.47	64.48	63.49	31.82	44.35	43.5			
Rb	146.61	432.5	234.31	323.98	190.86	227.92	201.06	327.63	31.75	160.18	130.76	166.06	177.05	139.48	177.4	112	5.3	32
Sr	109.59	34.44	318	84.06	168.16	117.99	218.73	325.34	269.84	91.74	86.23	85.6	107.55	148.75	294.83	350	230	260
Zr	358.68	193.51	511.96	338.44	442.37	660.28	172.15	446.84	351.33	348.01	437.63	251.19	228.48	259.44	293.26	190	70	100
Nb	7.76	9.44	12.72	15.82	3.4	20.56	5.68	13.36	14.93	13.04	11.54	5.75	5.88	6.99	3.43	25	6	11
Y	88.77	44.85	39.3	71.56	13.8	177.22	20.91	45.46	35.8	67.95	72.38	54.97	53.79	57.6	57.48	22	19	20
Cs	1	9.85	2.11	11.54	1.1	2.36	0.86	3.15	0.41	1.19	1.78	0.98	1.06	1.87	1.96	3.7	0.1	1
Ba	653.92	169.21	1417.7	459.77	990.76	420.01	542.26	1976.16	476.42	553.61	416.14	446.7	448.11	791.26	1212.17	550	1.5	250
Hf	10.6	5.85	14.1	10.74	12.18	20.63	5	12.13	9.4	10.46	13.67	7.05	7.17	7.4	9.74	5.8	3.6	4.7
Ta	0.47	0.65	0.47	1.07	0.1	1.33	0.33	0.74	0.94	0.8	0.74	0.33	0.33	0.47	0.21	1.5	1	1.2
Pb	44.64	52.55	35.72	31.65	31.85	44.94	75.97	35.1	13.07	77.56	47.64	64.47	63.09	25.95	57.49	20	4	8
Th	17.12	31.19	42.58	26.26	13.89	71.33	31.54	7.49	15.41	50.31	40.71	22.27	15.84	4.06	25.93	10.7	1.06	2.5
U	1.83	4.62	0.88	5.89	0.82	4.23	1.81	0.84	1.7	3.23	3.87	1.74	2.4	1.74	2.47	2.8	0.28	0.91

6.4 Geochemistry of the pink gneiss

The pink gneiss has a low variation in maximum and minimum values, with SiO_2 ranging from 73.54 to 77.65 wt%, Al_2O_3 ranging from 10.96 to 12.62 wt%, and Fe_2O_3 ranging from 1.38 to 3.59 wt% (Table 6). The Na_2O and K_2O composition ranges from 1.84 to 3.49 wt% for the former, and 4.14 to 6.70 wt% for the latter. In comparison to the major elements above, the TiO_2, MgO, CaO, and MnO compositions are low. This low variation in the major element composition is more typical of magmatic rocks as sedimentary rocks mainly display large variations (a large gap between the highest and lowest value) in their major element contents.

The amount of weathering can be calculated by using the chemical index of alteration [CIA= (Al_2O_3/ (Al_2O_3+CaO+Na_2O+K_2O))×100] of Nesbitt and Young (1982) (Rollinson, 1993; Elzien et al., 2010). The CIA values may be used to determine 1) the in situ weathering of existing rocks and 2) the degree of weathering of the provenance to sediments, as used in this study. The CIA values of the pink gneiss range from 51.60 to 53.90 (average 50.15), suggesting that the pink gneiss is unlikely to be of sedimentary origin, as they would have been derived from rocks that weren't weathered extensively, or, at least, weren't clay-rich or having much in terms of mafic minerals. Nesbitt and Young (1982, 1984, 1989, 1996) and Nesbitt *et al*. (1996) used the ternary diagrams Al_2O_3-(CaO + Na_2O)-K_2O (the A-CN-K), diagram, and the Fe_2O_3 + MgO-(CaO + Na_2O + K_2O)-Al_2O_3 (the A-CNK-FM) diagram to deduce weathering trends. On both the A-CN-K diagram (Figure 6-7), and the A-CNK-FM diagram (Figure 6-8), the pink gneiss, plot at the origin of the weathering trend. Here, the pink gneiss clearly displays similarities of Al_2O_3, CaO, Na_2O, and K_2O with those of average granite, which is suggestive of a relatively low intensity of weathering.

The plot of Roser and Korsch (1988) (Figure 6-9) is mainly used to interpret the provenance of sedimentary rocks. However, here this diagram does lend support to the idea that the pink gneiss may be of magmatic origin (a felsic magmatic rock). Chen et al. (2014) state that Th and Zr are largely incompatible during most igneous processes (resulting in them being enriched in felsic igneous rocks), while Sc is compatible and will preferentially enter olivine, pyroxene and other minerals that crystallize early in the magmatic cycle. Based on this the Th/Sc and Zr/Sc ratios are ideal parameters in discriminating the source nature of these rocks. The pink gneiss follows the magmatic trend quite well and plots close to the average compositions of granite (Figure 6-10). This is evident that the pink gneiss may be of magmatic origin. A similar conclusion can be further illustrated by the La/Sc–Co/Th binary plots (Figure 6-11).

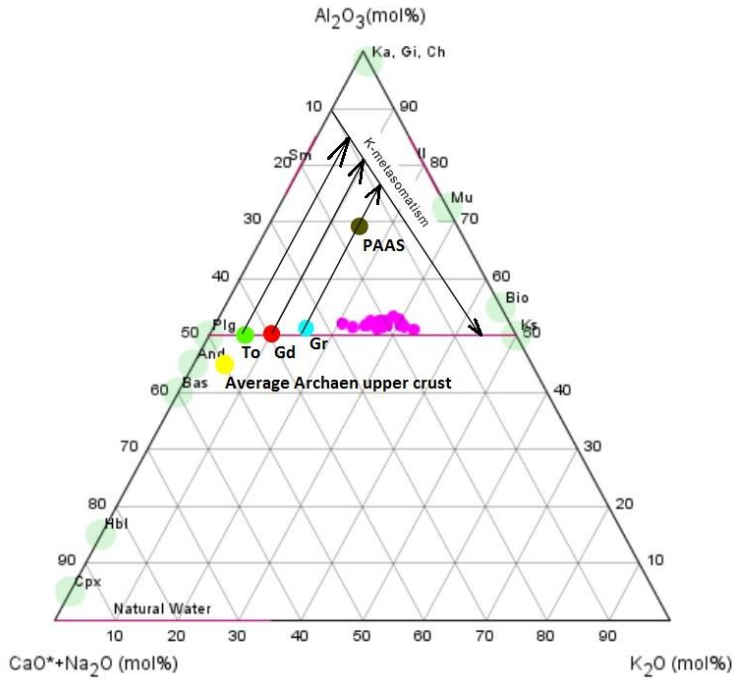

Figure 6-7. *Al_2O_3-(CaO + Na_2O)-K_2O plot used to determine (and show) the CIA (after Nesbitt and Young, 1982, 1984, 1989, 1996; Nesbitt et al., 1996), compared to data for Post-Archean Average Shale (PAAS) and Upper Crust (UC) given by Taylor and McLennan (1985)*. Compositions are plotted as molar proportions and the compositions of various minerals (plagioclase, K-feldspar, muscovite, biotite, ilmenite, kaolinite, hornblende and clinopyroxene, etc.) are shown. Bas = basalt, And = andesite, To = tonalite, Gd = granodiorite and Gr = granite.

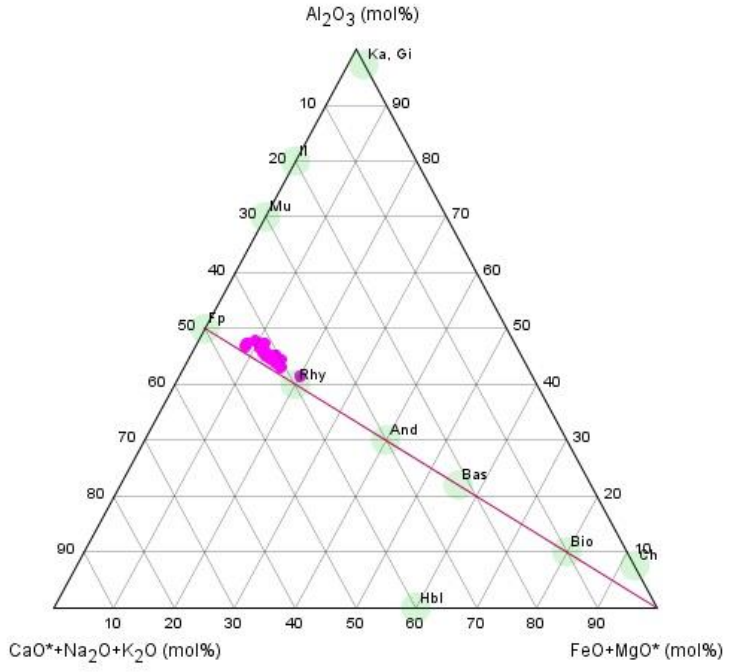

Figure 6-8. Triangular Al_2O_3-(CaO + Na_2O + K_2O)- Fe_2O_3 + MgO plot of sediment samples (after Nesbitt and Young, 1982, 1984, 1989, 1996; Nesbitt et al., 1996). Rhy-Rhyolite, And-And, Bas-Basalt, Bio-Biotite, Fp-Feldspar, Mu-muscovite, Ka-Kaolinite, Hbl-Hornblende.

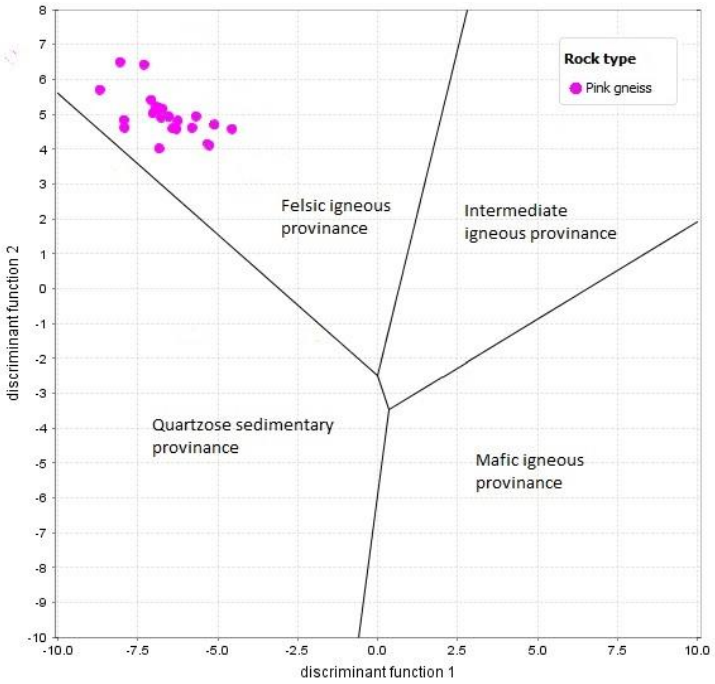

Figure 6-9. Discriminant function diagram for the provenance signatures of sandstone-mudstone suites using major elements (after Roser and Korsch, 1988). Fields for dominantly mafic, intermediate and felsic igneous provenances are shown along with the field for a quartzose sedimentary provenance. The discriminant functions are: Discriminant function 1 = -1.773TiO_2 + 0.607Al_2O_3 + 0.76$Fe_2O_{3(total)}$ – 1.5MgO + 0.616CaO + 0.509Na_2O – 1.224K_2O – 9.09. Discriminant function 2 = 0.445TiO_2 + 0.07Al_2O_3 – 0.25$Fe_2O_{3(total)}$ – 1.142MgO + 0.438CaO + 1.475Na_2O + 1.426K_2O – 6.861.

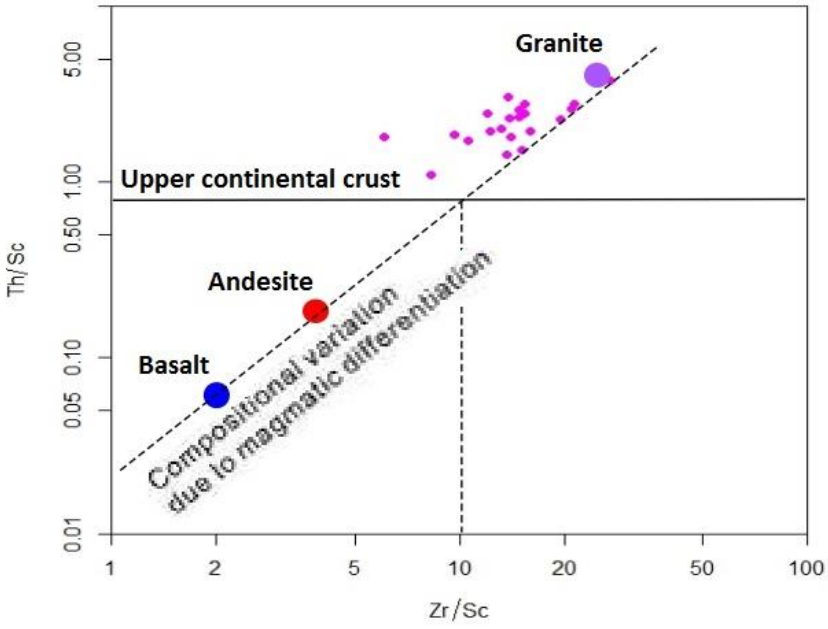

Figure 6-10. Zr/Sc–Th/Sc diagram (after McLennan et al., 1993).

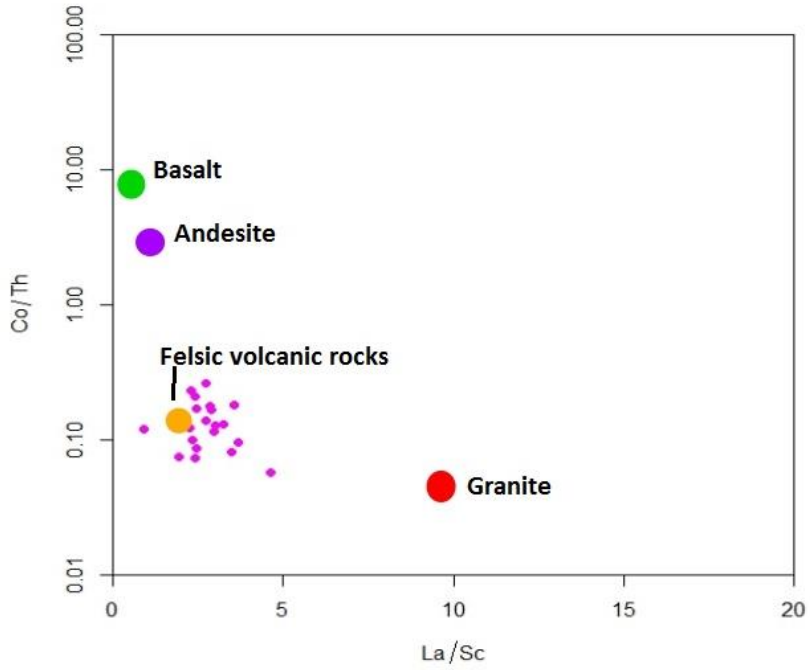

Figure 6-11. La/Sc–Co/Th diagram (after Gu et al., 2002).

The total alkali vs. silica (TAS) diagram of Cox et al. (1979) was used to classify the pink gneiss according to the major element geochemistry. On the total alkalis vs. silica diagram the pink gneiss clearly plots within the felsic and granitic field (Figure 6-12). The Nb/Y–Zr/TiO_2 plot of Pearce (1996) (Figure 6-13), which makes use of less mobile elements, displays the pink gneiss samples as clustering in the field of rhyodacite confirming its rhyolitic (if volcanic) or granitic (if intrusive) nature. The location of the pink gneiss in both classification diagrams (Figures 6-12 and 6-13) is identical to that of the streaky augen gneiss, suggesting an association of some type.

On the A/CNK vs. A/NK plot of Barton and Young (2002) the majority of the pink gneiss samples, like the streaky augen gneiss, plot within the weakly peraluminous field (Figure 6-14a). The close association of the pink gneiss with the streaky augen gneiss can also be seen on the FeO^{tot}/ (FeO^{tot} + MgO) versus SiO_2 plot (Figure 6-14b), the modified alkali lime index vs. SiO_2 plot (Figure 6-14c) and the K_2O vs. SiO_2 diagram (Figure 6-14d). Figure 6-14b has the pink gneiss, similarly to the streaky augen gneiss, plotting within the ferroan field, whilst both of these rock types straddle the calc-alkalic to alkali-calcic fields in Figure 6-14c, and dominantly plot within the potassium- enriched shoshonite series field (Figure 6-14d).

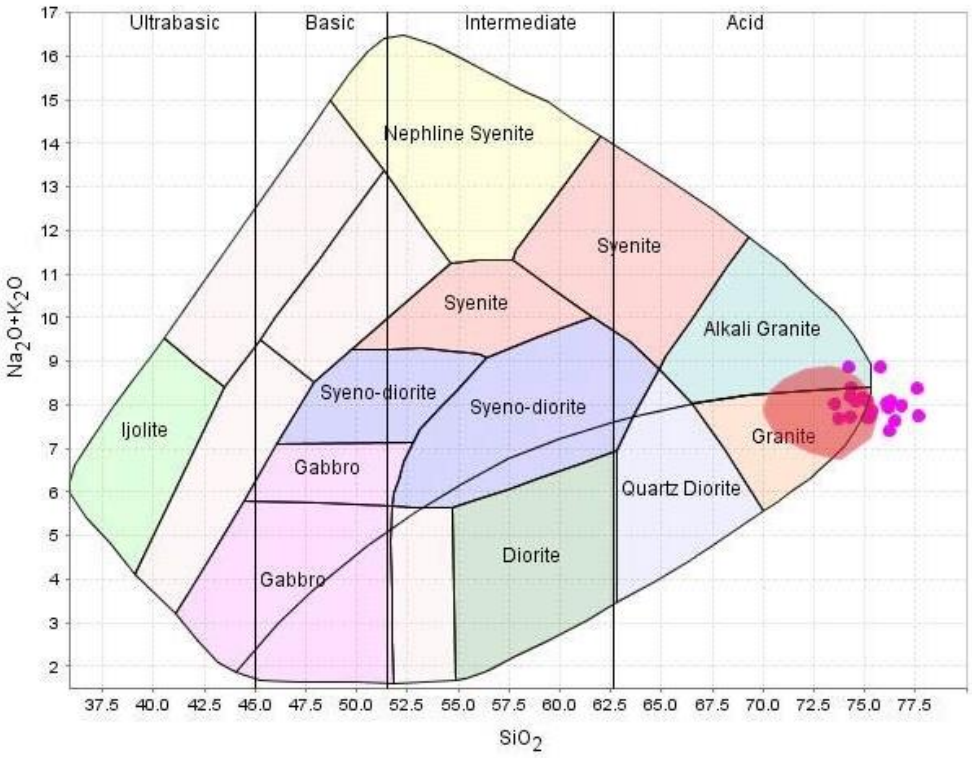

Figure 6-12. TAS classification diagram of Cox et al. (1979) showing the compositions of the pink gneiss relative to the streaky augen gneiss (light red shade).

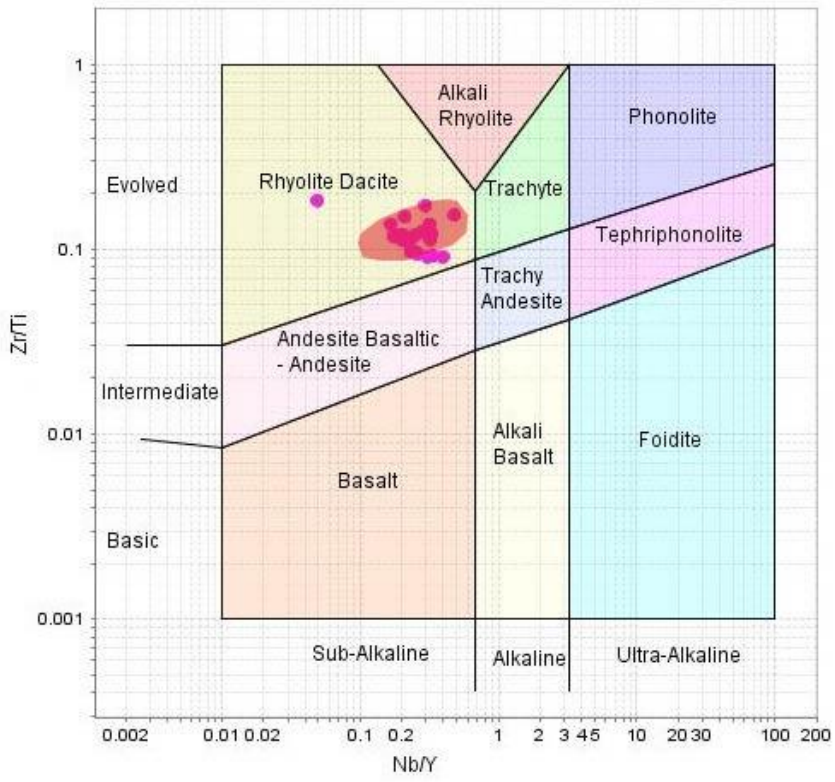

Figure 6-13. *The Zr/TiO_2–Nb/Y diagram for volcanic rocks (after Pearce, 1996) showing the compositions of the pink gneiss relative to the streaky augen gneiss.*

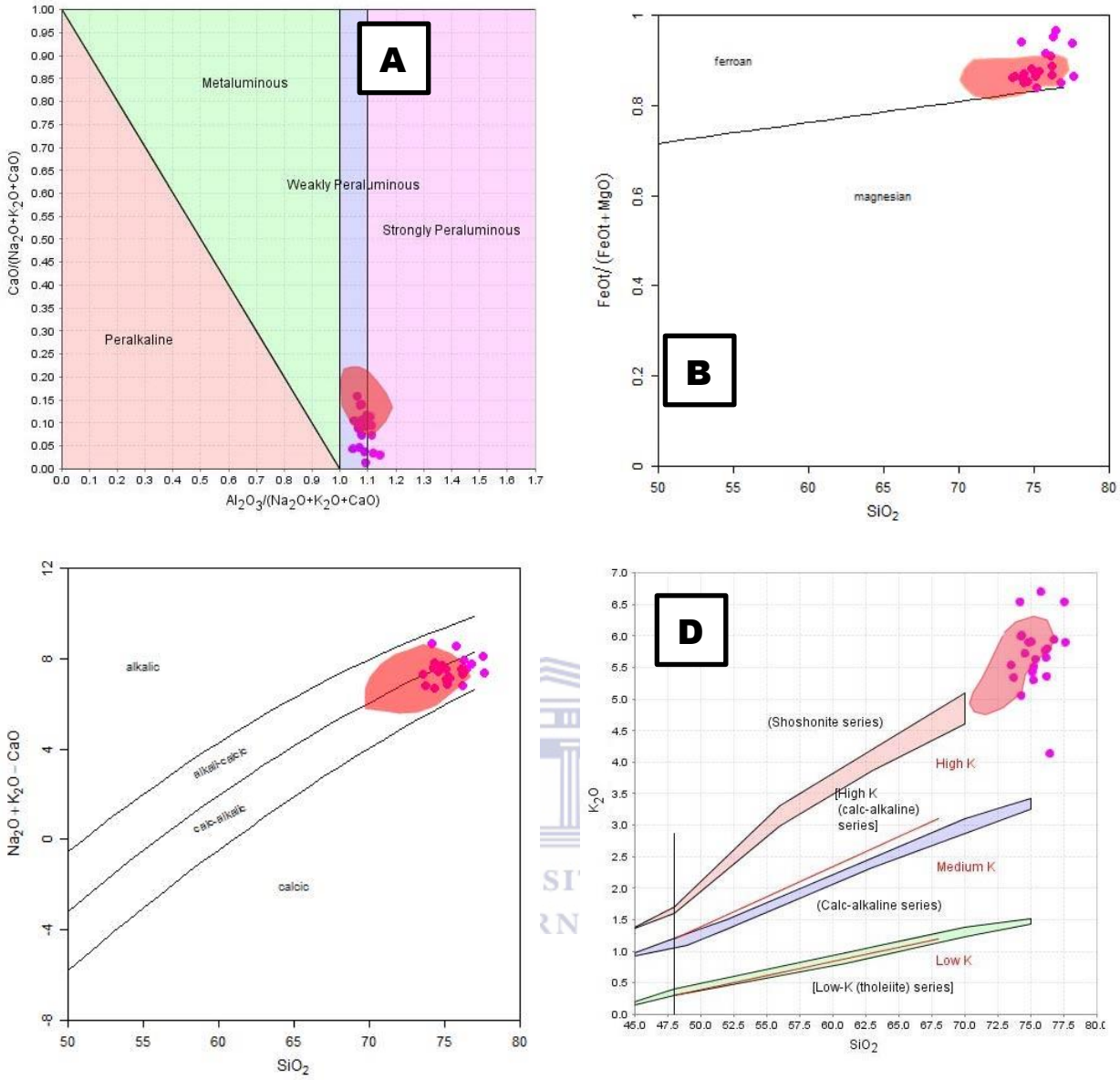

Figure 6-14. (A) A/CNK – A/NK plot of Barton and Young (2002). (B) FeO_{tot}/ (FeO_{tot} + MgO) vs. weight percent SiO_2 diagram of Frost et al. (2001). (C) $Na_2O + K_2O$ – CaO vs. weight percent SiO_2 diagram of Frost et al. (2001). (D) K_2O vs. SiO_2 diagram. The red line subdivisions on the K_2O vs. SiO_2 diagram were proposed by Le Maitre et al. (1989), whereas the shaded fields are the boundary lines proposed by Peccerillo and Taylor (1976).

Table 5. Major element geochemistry of the pink gneiss.

	Pink gneiss												UCC	LCC	ACC
Sample	**PG1**	**PG4**	**PG7**	**PG20**	**PG40**	**PG41**	**PG50**	**PG70**	**PG006**	**PG100**	PG071	PG024	Taylor and McLennan 1985		
SiO_2	74.28	76.80	74.58	76.48	75.12	75.07	76.21	74.88	77.58	76.17	76.11	73.73	66	45.4	57.3
TiO_2	0.32	0.20	0.36	0.29	0.36	0.32	0.34	0.37	0.18	0.32	0.29	0.41	0.5	1	0.9
Al_2O_3	12.07	11.06	11.83	11.32	11.85	11.75	11.05	12.17	11.04	11.70	11.67	12.08	15.2	16.1	15.9
Fe_2O_3	2.32	1.71	2.65	1.98	2.35	2.33	2.35	1.82	1.38	2.21	2.16	3.59	4.04	9.53	8.188
MnO	0.02	0.01	0.03	0.01	0.01	0.02	0.01	0.01	0.01	0.02	0.01	0.05	0.1		
MgO	0.35	0.27	0.41	0.06	0.31	0.33	0.32	0.22	0.08	0.25	0.19	0.51	2.2	6.3	5.3
CaO	0.59	0.21	0.65	0.08	0.64	0.53	0.60	0.44	0.25	0.60	0.53	0.86	4.2	8.5	7.4
Na_2O	2.21	2.04	2.36	3.49	2.28	2.19	2.04	2.27	1.84	2.27	2.28	2.35	3.9	2.8	3.1
K_2O	5.99	5.94	5.72	4.14	5.43	5.91	5.36	5.90	6.54	5.66	5.77	5.34	3.4	0.34	1.1
P_2O_5	0.08	0.12	0.08	0.08	0.06	0.07	0.06	0.06	0.08	0.07	0.08	0.08			
Cr_2O_3	0.02	0.02	0.02	0.01	0.01	0.02	0.01	0.01	0.01	0.02	0.02	0.02			
L.O.I.	**1.09**	**0.89**	0.80	**1.24**	**1.32**	**1.05**	**0.88**	**1.27**	0.56	1.03	0.82	0.70			
Total	99.34	99.27	99.49	99.18	99.74	99.57	99.23	99.42	99.55	100.32	99.93	99.72			

Sample	**PG150**	**PG186**	**PG169.2**	**PG140**	**PG110**	**PG165**	**PG194**	**PG122**	**PG131**	**PG128**
SiO_2	75.77	77.65	74.21	75.37	74.33	73.54	75.23	75.25	74.31	76.28
TiO_2	0.19	0.24	0.24	0.29	0.29	0.34	0.21	0.31	0.38	0.27
Al_2O_3	12.13	10.96	12.62	12.11	12.53	12.59	12.06	11.85	12.45	11.82
Fe_2O_3	1.43	1.76	1.77	2.33	1.99	2.66	2.13	2.30	2.51	2.00
MnO	0.01	0.02	0.00	0.03	0.01	0.03	0.07	0.02	0.03	0.01
MgO	0.12	0.25	0.10	0.30	0.27	0.38	0.37	0.30	0.40	0.09
CaO	0.29	0.41	0.21	0.71	0.59	0.71	0.86	0.55	1.02	0.17
Na_2O	2.17	1.85	2.32	2.23	2.38	2.48	2.41	2.24	2.67	2.28
K_2O	6.70	5.90	6.54	5.63	6.01	5.54	5.30	5.51	5.06	5.80
P_2O_5	0.04	0.06	0.11	0.15	0.21	0.10	0.07	0.11	0.08	0.10
Cr_2O_3	0.02	0.02	0.01	0.02	0.02	0.02	0.01	0.02	0.01	0.01
L.O.I.	0.84	0.77	1.18	0.67		1.71	0.58	1.00	0.66	1.02
Total	99.71	99.89	99.31	99.84	98.63	100.10	99.30	99.46	99.58	99.85

In the chondrite-normalized rare earth element (REE) plot (Figure 6-15), the pink gneiss has a fractionated REE pattern with an average $(La/Lu)_N$ of 10.3 (Table 7), very similar to that of the streaky augen gneiss [average $(La/Lu)_N$ of 9.5] (Table 4). Enrichment in the LREE is shown by $(La/Sm)_N$ = 2.44-4.14 (Table 7), whereas the HREE show a more variable pattern from a fractionated, sloping trend to enrichment of Lu [$(Gd/Yb)_N$ = 0.6 – 5.73] (Table 7). The pink gneiss has a prominent negative Eu anomaly (Eu/Eu*= 0.3) (Figure 6-15) denoting the role of either plagioclase retention in the source, or plagioclase fractionation in the parental magma.

Similarly to the streaky augen gneiss, the elemental concentrations of the pink gneiss gradually decrease from Cs to Pb exhibiting a negatively sloping trend (Figure 6-16). However, the slope is not smooth, as there are several well-developed positive and negative anomalies. The trend of the pink gneiss, in a similar fashion to the rest of the magmatic rocks, resembles a similar trend to the upper continental crust (UCC) in comparison to the lower continental crust (LCC) and average continental crust (ACC).

In comparison to the UCC the pink gneiss has Pb, Rb and K exhibiting the highest positive anomaly, whilst the remaining LILEs (Cs, Ba and Sr) have relatively strong negative anomalies. The HFSE (Hf, Zr, Ce, U and Th) exhibit positive anomalies in comparison to the UCC. Relative to the UCC trend Nb and Ti are the only HFS elements that have prominent negative anomalies (Figure 6-16).

The Pink gneiss is only slightly depleted in Y, has a weak HREE fractionation trend (Figure 6-15, 6-16) and large negative Nb, Sr, P, and Ti anomalies. Most of these features are explainable in terms of relatively high-temperature partial melting of virtually anhydrous granulite facies crustal rocks (Tarney et al. 1987; Sheraton and Black 1988; Sheraton and Sun 1995). These geochemical traits are also similar to that of granitoids (high HFSE, LREE, and Th/U and low Sr), further suggesting that the Pink gneiss is of magmatic origin**.**

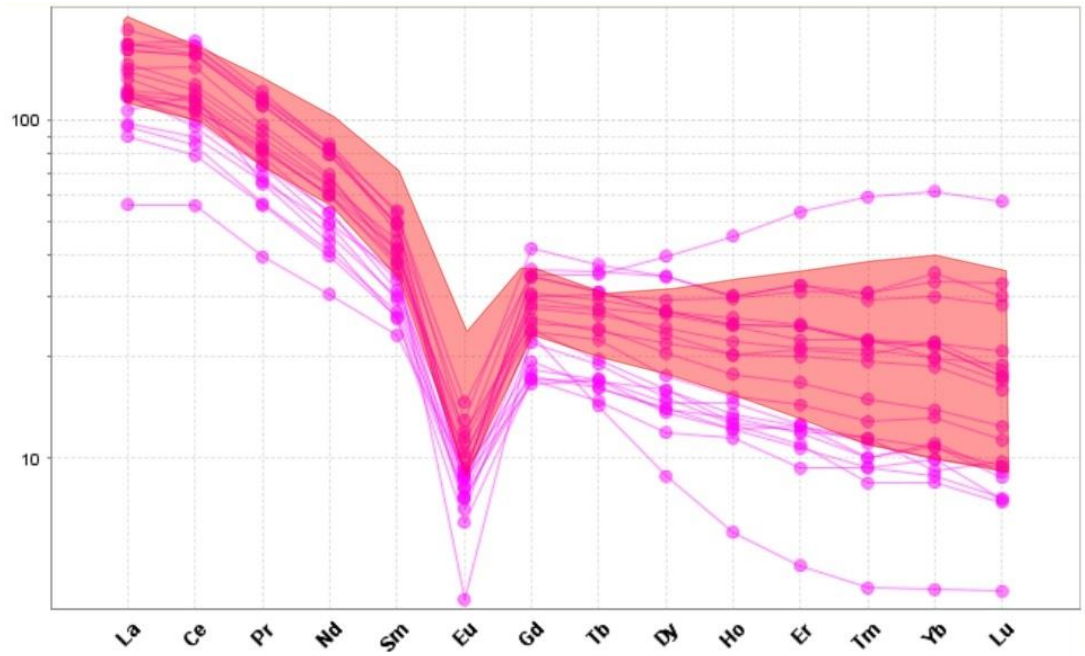

Figure 6-15. Chondrite normalized REE plot (after Boynton, 1984) of the pink Gneiss. The streaky augen gneiss is displayed by the red shaded area, whereas the Pink gneiss is represented by the scatter plot.

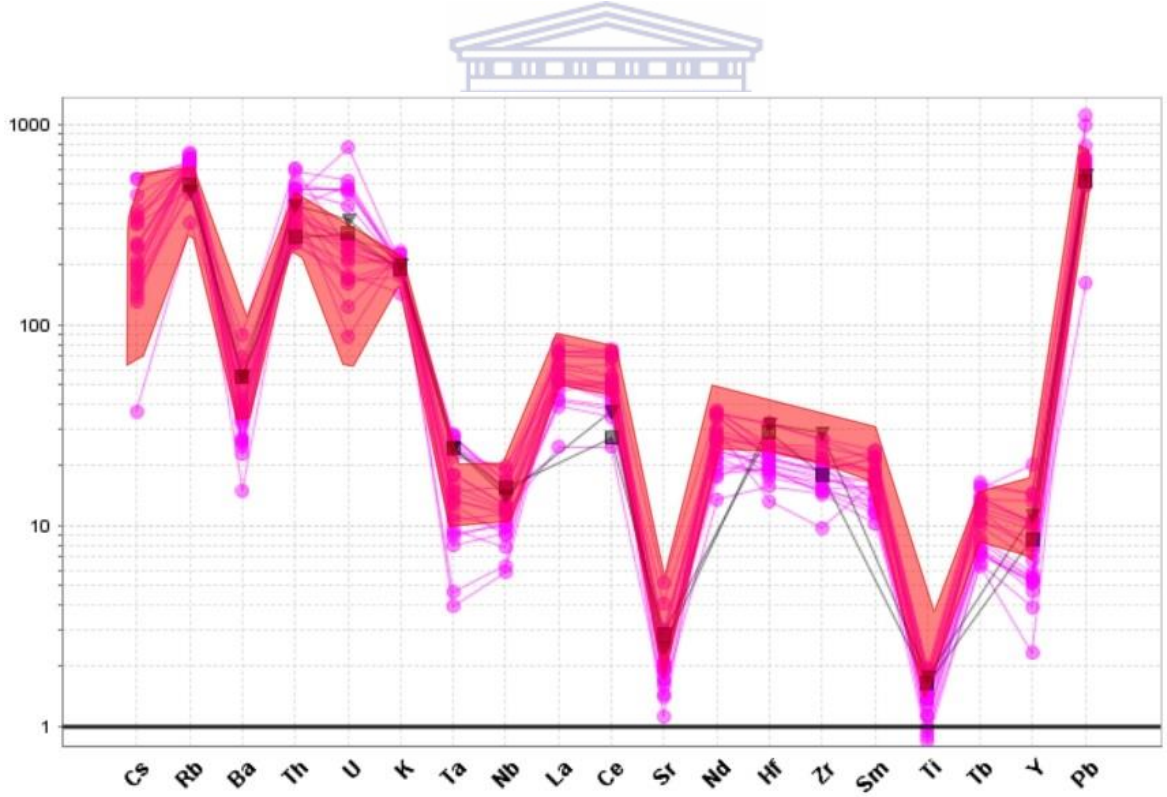

Figure 6-16. Primordial mantle normalised multi-element (spider) diagrams (plotting order and normalizing values of McDonough et al., 1992) of the pink gneiss. The streaky augen gneiss is displayed by the red shaded area, whereas the Pink gneiss is represented by the scatter plot.

Table 6. Rare earth element (REE) geochemistry of the pink gneiss in the Kliprand study area.

	Pink gneiss												UCC
Sample	**PG1**	**PG4**	**PG7**	**PG20**	**PG40**	**PG41**	**PG50**	**PG70**	**PG006**	**PG100**	**PG071**	**PG024**	**Taylor and McLenan 1981**
La	41.06	43.93	38.17	17.49	50.05	36.24	37.47	51.97	33.18	43.05	52.22	52.30	30
Ce	91.47	116.11	94.43	45.22	126.71	80.65	91.89	133.97	96.37	99.68	139.07	127.76	64
Pr	10.03	11.83	10.27	4.82	13.49	8.91	9.53	13.98	7.91	10.83	14.90	14.06	7.1
Nd	35.89	41.47	38.25	18.38	47.50	29.46	32.06	49.79	26.06	38.54	49.38	49.39	26
Sm	7.53	7.42	7.95	4.51	9.73	5.76	6.61	10.55	5.05	8.60	9.16	9.62	4.5
Eu	0.69	0.28	0.81	0.68	0.65	0.56	0.52	0.85	0.56	0.61	0.60	0.95	0.88
Gd	6.71	6.00	7.20	4.53	8.93	4.73	5.69	9.40	4.45	7.73	7.41	10.84	3.8
Tb	1.13	0.68	1.26	0.76	1.48	0.81	0.90	1.69	0.70	1.31	1.30	1.77	0.64
Dy	7.04	2.85	7.85	4.51	8.77	4.72	4.86	11.08	3.83	8.58	7.50	11.15	3.5
Ho	1.45	0.43	1.58	0.94	1.79	1.04	0.90	2.18	0.82	1.77	1.45	2.17	0.8
Er	4.19	1.01	4.48	2.49	5.17	2.65	2.31	6.85	1.97	4.69	4.38	6.82	2.3
Tm	0.63	0.13	0.68	0.32	0.72	0.33	0.27	1.00	0.30	0.73	0.66	0.95	0.33
Yb	3.90	0.85	4.14	2.32	4.50	2.26	1.77	7.42	1.86	4.13	4.64	6.28	2.2
Lu	0.51	0.13	0.55	0.29	0.56	0.28	0.24	0.97	0.25	0.61	0.59	0.92	0.32
∑ LREE / HREE	7.28	18.27	6.82	5.59	7.76	9.57	10.48	6.41	11.89	6.79	9.48	6.19	9.47
Ce/Ce*	1.08	1.23	1.15	1.19	1.17	1.08	1.17	1.20	1.43	1.11	1.20	1.13	1.06
Eu/Eu*	0.30	0.13	0.33	0.46	0.21	0.33	0.26	0.26	0.36	0.23	0.22	0.29	0.65
$(Gd/Yb)_N$	1.39	5.67	1.41	1.58	1.60	1.69	2.59	1.02	1.94	1.51	1.29	1.39	1.39
$(La/Yb)_N$	7.11	34.70	6.22	5.09	7.51	10.81	14.27	4.72	12.06	7.03	7.60	5.61	9.19
$(La/Sm)_N$	3.43	3.72	3.02	2.44	3.24	3.96	3.57	3.10	4.14	3.15	3.59	3.42	4.19
$(Gd/Lu)_N$	1.63	5.73	1.64	1.93	1.97	2.09	2.97	1.20	2.26	1.58	1.57	1.47	1.47
$(La/Lu)_N$	8.33	35.10	7.27	6.21	9.25	13.35	16.32	5.56	14.07	7.34	9.26	5.94	9.73

Table 7 (cont.). Rare earth element (REE) geochemistry of the pink gneiss in the Kliprand study area.

	Pink gneiss									
Sample	**PG1**	**PG4**	**PG7**	**PG20**	**PG40**	**PG41**	**PG50**	**PG70**	**PG006**	**PG006**
La	30.25	36.75	29.86	50.05	37.90	36.91	57.65	45.59	36.44	27.78
Ce	72.03	77.63	68.70	126.71	85.54	86.81	133.48	103.20	87.99	63.64
Pr	8.05	8.32	6.92	13.49	9.01	10.07	14.33	11.34	9.91	6.83
Nd	29.71	27.42	24.64	47.50	32.18	36.21	51.18	40.30	36.18	23.82
Sm	6.89	5.88	5.31	9.73	6.15	8.13	10.36	8.15	7.30	5.12
Eu	0.57	0.66	0.64	0.65	0.77	0.74	1.08	0.66	0.88	0.48
Gd	6.16	5.01	4.30	8.93	6.19	7.81	9.01	7.98	6.51	4.45
Tb	1.06	0.77	0.81	1.48	0.93	1.45	1.66	1.40	1.15	0.80
Dy	5.65	4.54	4.40	8.77	5.12	9.44	12.76	8.73	6.59	5.12
Ho	1.09	0.87	0.87	1.79	0.97	2.13	3.27	1.88	1.27	0.92
Er	3.03	2.62	2.25	5.17	2.62	6.51	11.24	5.25	3.53	2.52
Tm	0.42	0.36	0.30	0.72	0.37	1.00	1.93	0.72	0.48	0.37
Yb	2.77	2.08	2.07	4.50	1.92	6.94	12.88	4.60	2.91	2.25
Lu	0.36	0.30	0.24	0.56	0.31	1.06	1.85	0.67	0.40	0.30
∑ LREE / HREE	7.16	9.43	8.89	7.76	9.26	4.90	4.89	6.68	7.79	7.60
Ce/Ce*	1.11	1.07	1.15	1.17	1.11	1.08	1.12	1.09	1.11	1.11
Eu/Eu*	0.27	0.37	0.41	0.21	0.38	0.28	0.34	0.25	0.39	0.30
$(Gd/Yb)_N$	1.80	1.94	1.68	1.60	2.60	0.91	0.56	1.40	1.81	1.60
$(La/Yb)_N$	7.37	11.91	9.75	7.51	13.31	3.59	3.02	6.69	8.46	8.32
$(La/Sm)_N$	2.76	3.93	3.54	3.24	3.88	2.86	3.50	3.52	3.14	3.42
$(Gd/Lu)_N$	2.10	2.06	2.20	1.97	2.45	0.91	0.60	1.49	2.02	1.82
$(La/Lu)_N$	8.63	12.60	12.76	9.25	12.52	3.62	3.23	7.09	9.46	9.51

Table 7. Trace element geochemistry of the pink gneiss in the Kliprand study area.

	Pink gneiss												UCC	LCC	ACC
Sample	**PG1**	**PG4**	**PG7**	**PG20**	**PG40**	**PG41**	**PG50**	**PG70**	**PG006**	**PG100**	**PG071**	**PG024**	Taylor and McLenan 1985		
Sc	11.61	17.97	13.20	19.33	21.60	11.15	18.09	11.25	13.68	15.19	14.18	17.74			
Ti	1918.40	1199.00	2158.20	1738.55	2158.20	1918.40	2038.30	2218.15	1079.10	1918.40	1738.55	2457.95			
V	60.91	56.35	59.95	57.93	60.30	59.80	61.06	55.93	42.97	64.94	62.18	78.18			
Cr	457.56	503.17	349.26	364.35	353.51	380.96	371.52	355.07	379.50	379.13	419.48	442.44			
Co	4.10	2.77	5.02	2.57	4.01	4.02	3.88	2.46	2.44	6.33	3.53	5.67			
Ni	16.40	18.00	15.48	14.86	16.97	20.38	21.29	15.31	34.91	15.18	16.18	24.54			
Cu	22.03	67.94	17.86	85.99	85.01	12.94	43.37	23.52	15.29	16.09	20.51	14.13			
Zn	41.52	39.72	47.35	24.27	52.14	41.37	37.06	50.48	25.19	61.81	34.80	56.54			
Rb	434.95	400.21	398.70	205.83	413.85	404.62	303.97	451.70	411.88	425.76	455.78	352.60	112	5.3	32
Sr	62.34	23.52	63.69	30.42	35.83	42.71	29.50	39.32	42.98	40.61	33.71	52.31	350	230	260
Zr	184.57	108.88	258.12	160.04	208.81	237.76	191.48	303.54	165.18	226.41	298.79	273.86	190	70	100
Nb	9.16	4.19	8.73	8.25	11.97	6.96	6.46	10.77	8.56	8.03	10.17	13.32	25	6	11
Y	38.99	10.54	43.07	24.48	47.47	25.04	24.87	64.98	17.77	46.05	34.24	65.58	22	19	20
Cs	8.60	4.20	5.89	0.85	12.34	5.70	3.33	4.00	4.81	5.54	4.58	8.03	3.7	0.1	1
Ba	379.96	103.73	310.73	389.55	185.92	181.05	173.28	257.57	436.75	191.26	158.79	274.98	550	1.5	250
Hf	5.55	4.06	7.82	4.84	6.68	6.93	6.16	10.02	5.85	7.31	9.94	7.98	5.8	3.6	4.7
Ta	0.74	0.16	0.65	0.43	1.14	0.46	0.33	1.17	0.60	0.55	1.08	0.98	1.5	1	1.2
Pb	55.27	40.04	48.42	11.50	37.10	48.22	36.69	70.38	36.89	43.10	47.37	35.23	20	4	8
Th	22.77	32.49	29.88	21.29	40.24	31.19	31.09	42.74	33.58	35.61	37.05	49.25	10.7	1.06	2.5
U	4.32	10.32	5.38	3.69	9.94	4.48	5.67	9.55	1.84	4.75	16.15	10.98	2.8	0.28	0.91

Table 8 (cont.). Trace element geochemistry of the pink gneiss in the Kliprand study area.

	Pink gneiss									
Sample	**PG150**	**PG186**	**PG169.2**	**PG140**	**PG110**	**PG165**	**PG194**	**PG122**	**PG131**	**PG128**
Sc	12.29	13.43	13.27	21.60	14.00	16.07	16.67	15.12	15.18	14.39
Ti	1139.05	1438.80	1438.80	1738.55	1738.55	2457.95	1258.95	1858.45	2278.10	1618.65
V	53.38	62.18	55.29	60.30	60.24	66.45	60.97	63.95	62.31	58.35
Cr	382.60	382.79	293.23	353.51	350.23	360.48	334.20	401.27	323.01	343.69
Co	4.81	6.77	3.27	4.01	3.46	5.60	4.14	5.00	4.54	2.65
Ni	15.16	15.02	15.14	16.97	17.35	18.16	19.66	21.30	24.25	16.27
Cu	16.19	23.21	15.34	85.01	12.02	30.56	16.92	14.30	22.31	19.52
Zn	29.34	34.56	28.84	52.14	43.90	50.64	28.41	50.55	61.32	24.48
Rb	408.86	385.61	429.73	413.85	395.98	423.23	283.66	421.19	303.70	361.75
Sr	40.23	44.18	52.90	35.83	41.86	86.24	109.57	40.86	57.04	43.13
Zr	170.30	164.90	175.58	208.81	196.58	242.66	230.60	224.15	206.65	222.05
Nb	6.39	5.57	7.04	11.97	8.43	14.00	4.47	9.09	11.10	7.41
Y	30.39	23.76	21.35	47.47	26.35	60.07	91.49	48.35	36.22	23.44
Cs	4.42	3.16	3.53	12.34	10.19	7.41	3.83	7.83	7.27	2.99
Ba	233.57	256.87	261.74	185.92	290.93	482.34	622.71	241.72	366.98	227.20
Hf	5.31	5.75	5.98	6.68	6.18	7.82	7.39	7.96	6.64	7.30
Ta	0.53	0.39	0.37	1.14	0.54	0.91	0.19	0.73	0.60	0.36
Pb	78.73	44.19	42.62	37.10	44.98	42.47	45.78	42.14	39.97	35.68
Th	28.27	26.06	26.66	40.24	25.25	24.38	50.91	39.27	21.60	35.59
U	5.59	3.57	2.59	9.94	5.02	5.48	4.99	8.20	3.52	3.36

6.5 Geochemistry of the gabbro-norite

Ten samples of the meta-gabbro-norite (or two pyroxene granulite) were sampled for major and trace element analyses. These mafic rocks are characterized by moderate silica (49.64 -54.29 wt.%), moderate to high Al_2O_3 (14.97-17.79 wt.%) and low Mg# (0.34-0.57). The major element total alkali vs. silica diagram of Cox et al. (1979) was also used to classify the gabbro-norite. The gabbro-norite plot mainly within the mafic to intermediate gabbro fields, whilst samples G33, G36 and G125.2 plot within the diorite field (Figure 6-1). The incompatible Nb/Y–Zr/TiO_2 plot of Pearce (1996) (Figure 6-2), does not display any variation, hence all the gabbro-norite samples are clustered within the sub-alkaline basalt field (essentially confirming that they are gabbro-norite).

Seeing that these mafic rocks plot in the subalkaline series (Figure 6-2), an AFM diagram was constructed in order to distinguish between the tholeiitic and calc-alkaline differentiation trends in the sub alkaline magma series based on Kuno (1968) and Irvine and Barager (1971) as quoted in Rollinson (1993). The gabbro-norite samples plot in the calc-alkaline series (Figure 6-17) based on the separation trends of both Kuno (1968) and Irvine and Barager (1971). However, this mafic rock type is closer to the MgO corner indicating that it is derived from an unfractionated parental magma source, whereas the felsic magmatic rocks (streaky augen gneiss and Ibequas granite) plot a lot closer to the alkali (Na_2O + K_2O) corner indicating that these rocks have a more evolved magma source (Figure 6-17).

The sub alkaline basalts can be further subdivided on the basis of their K_2O and SiO_2 concentrations (Figure 6-18). According to the shaded areas of Peccerillo and Taylor (1976) (Figure 6-18), the meta-gabbro-norite plot exclusively within the high K (calc-alkaline) series, except for sample G124 which plots in the shoshonite series.

The rare earth elements (REE) of the meta- gabbro-norite have a strong negative REE slope [$(La/Lu)_N$ = 9.7] (Figure 6-19). These samples contain a very weak average Eu anomaly (Eu/Eu*= 0.76) typical of basaltic rocks. However, sample G115 displays a different pattern to the rest of the samples with a prominent negative Eu anomaly (Eu/Eu*= 0.35) being identified. In addition, sample G115 is also not as enriched in the LREE (La_N/Sm_N = 1.64) as the rest of the samples (average La_N/Sm_N = 2.87). The HREE (Gd_N/Yb_N = 2.4) of the gabbro-norite exhibits a slightly negative slope (Figure 6-19). The overall REE trend of the gabbro-norite closely resembles that of the ocean island basalt (OIB) trend of Sun and McDonough (1989), with the only variation being the weak Eu anomaly not shown by average OIB.

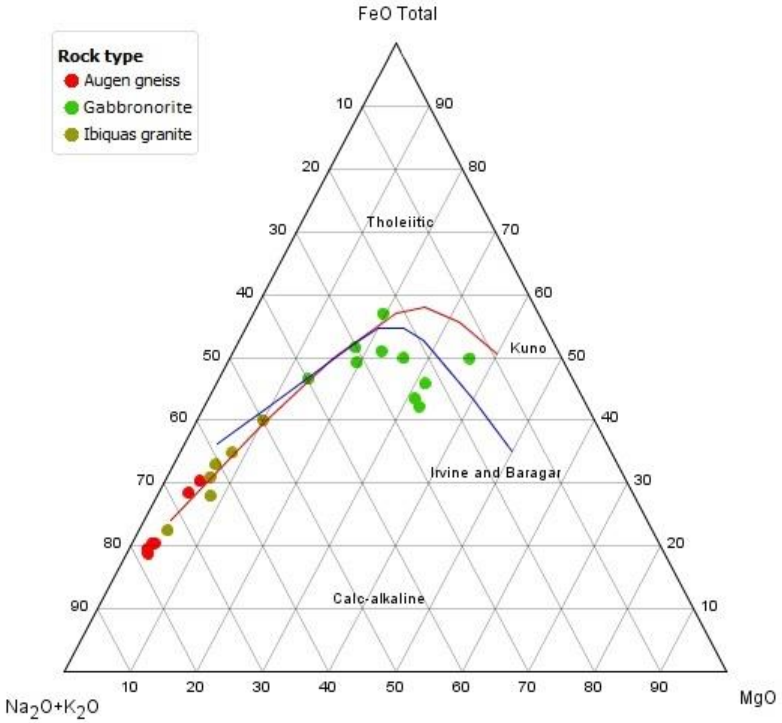

Figure 6-17. AFM diagram in which A (alkalis: $Na_2O + K_2O$), F ($FeO + Fe_2O_3$) and M (MgO) plot as the corners of the triangle (after Kuno (1968) and Irvine and Barager (1971)).

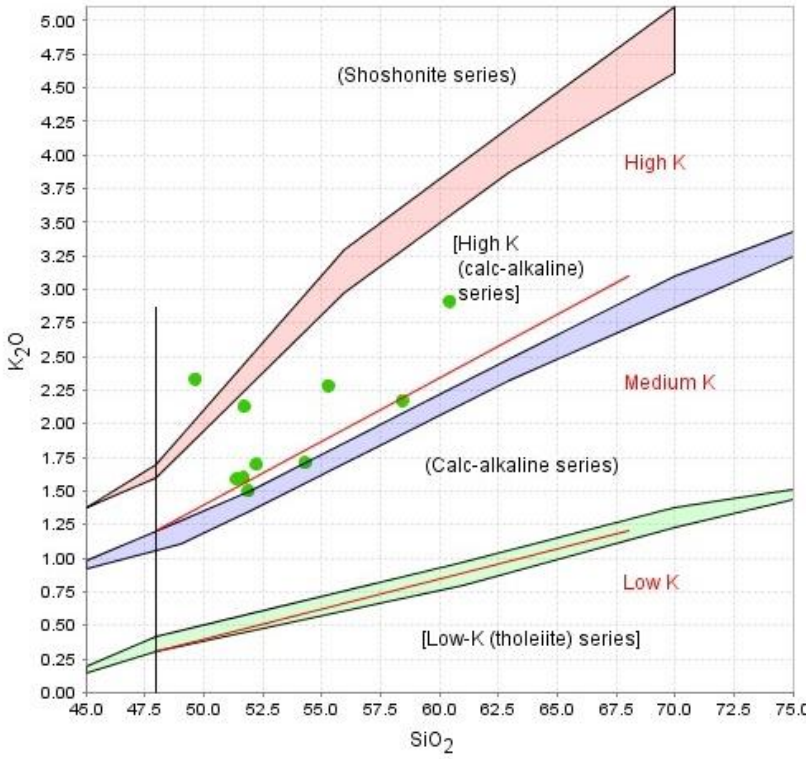

Figure 6-18. Bivariate K_2O vs. SiO_2 diagram for characterising subalkaline rocks. The red lines are subdivisions proposed by Le Maitre et al. (1989) and the shaded fields are the boundaries proposed by Peccerillo and Taylor (1976).

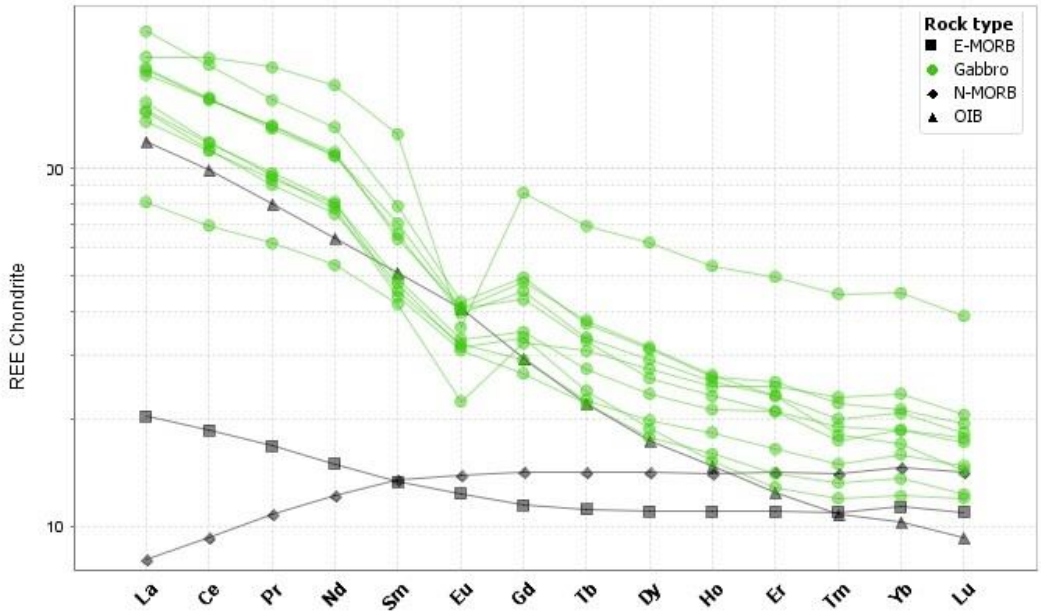

Figure 6-19. Rare earth element concentrations of the meta-gabbro-norite normalized to the chondrite values of Boynton (1984). Also displayed are the trends of N-MORB, E-MORB and OIB (data from Table 4) from Sun and McDonough (1989). The gabbro in the legend refers to the gabbro-norite of the Kliprand area.

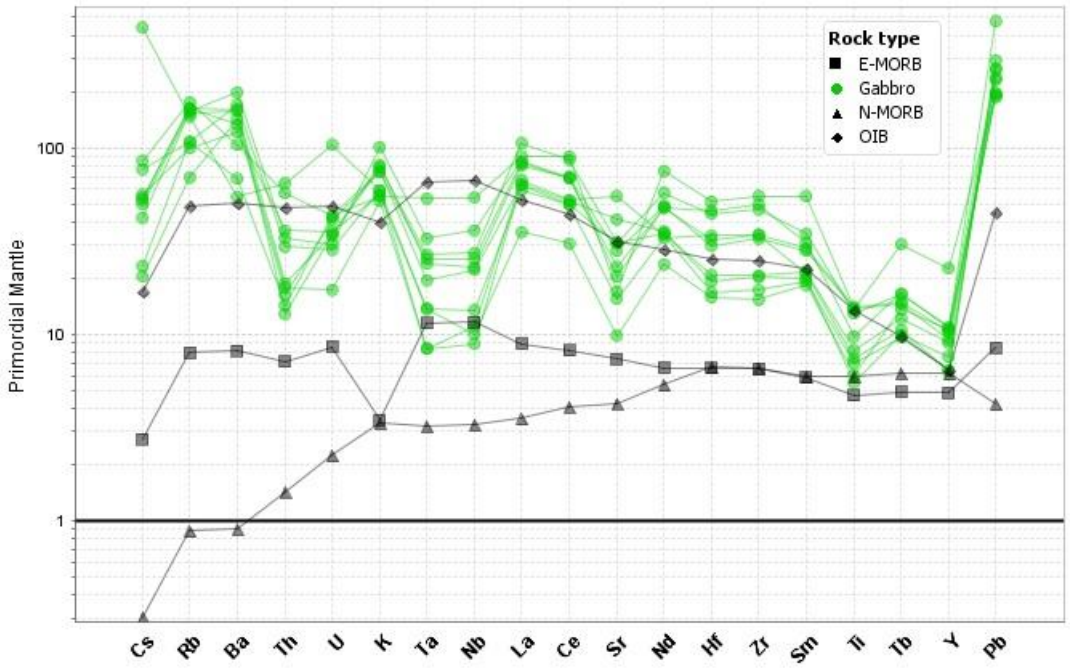

Figure 6-20. Multi-element trace element pattern (spider diagram) of the meta-gabbro-norite normalized to the composition of the primordial mantle and plotted from left to right in order of increasing compatibility in a small fraction of melt of the mantle. The normalizing values are those of McDonough et al. (1992). Also displayed are the trends for N-MORB, E-MORB and OIB (data given in Table 4) from Sun and McDonough (1989).

The trace element concentrations of the meta-gabbro-norite are approximately equivalent to those of ocean island basalt (OIB) (Figure 6-20), but are depleted in the HFS elements (Th, U, Ta, Nb, Zr), as well as Sr and Ti relative to OIB. Ce and, to a lesser extent, Hf, are the only HFS elements that display an enrichment trend relative to OIB (Figure 6-20). With regard to the LILE Pb displays the highest enrichment relative to OIB (values of Sun and McDonough (1989) (Table 4), whilst Cs, Rb and Ba are slightly less enriched and K only slightly enriched.

6.6 Geochemistry of the charnockitised pink and streaky augen gneiss

The pink gneiss and streaky augen gneiss transitions into the charnockite (granulitic charnockitized pink gneiss), and has mineralogical and geochemical affinities similar to that of magmatic rocks (section 6.5). This study shall thus compare the streaky augen gneiss (definitely magmatic) with the charnockites. The mass balance calculations and the Gresens-Grant isocon plot (constructed by using the EASYGRESGRANT excel spreadsheet) was used in order facilitate a comparison between the charnockite and the streaky augen gneiss (as it is definitely magmatic and is mineralogically and geochemically similar to the pink gneiss) and also give an idea as to the origin and element mobility that influenced formation of this metamorphic charnockite.

The major element analysis of the charnockite (SiO_2, TiO_2, MnO and MgO) highly resembles that of granitic rocks. Na_2O and K_2O are the only other major elements that resemble average granitic concentrations. On the immobile Nb/Y–Zr/TiO_2 plot of Pearce (1996) the charnockites vary between rhyolites, rhyodacites and andesites (felsic to intermediate) (Figure 6-2).

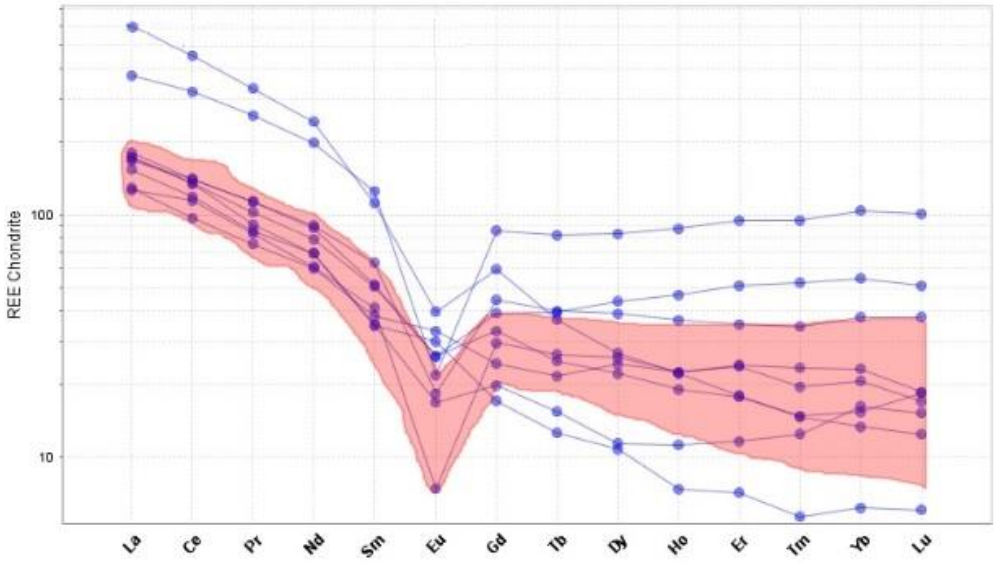

Figure 6-21. Chondrite normalized REE plot (after Boynton, 1984) for the charnockite (actual plotted values) and the streaky augen gneiss (red shaded area).

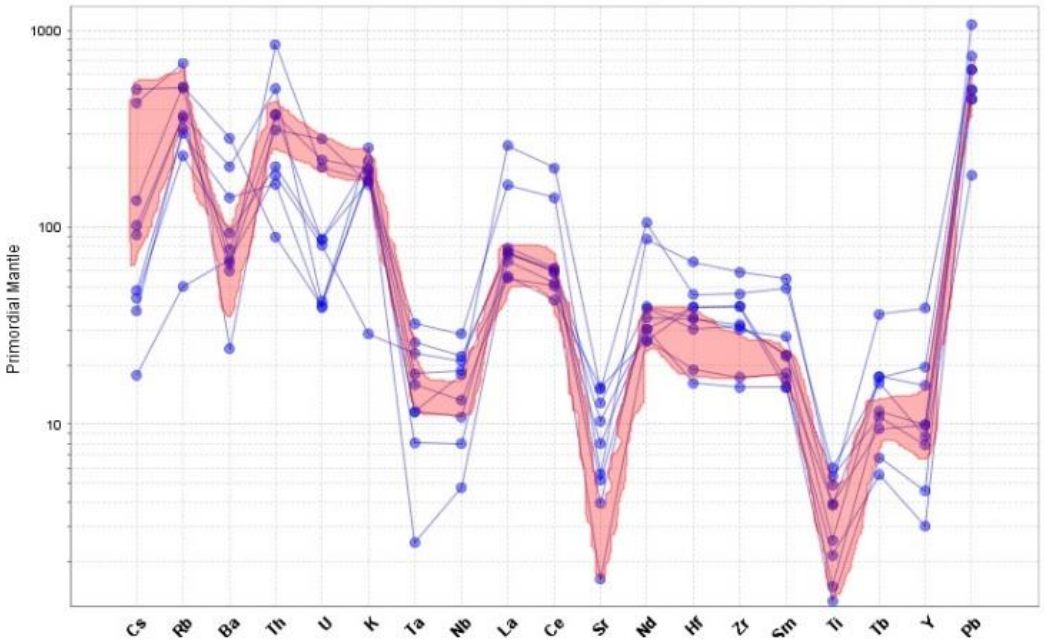

Figure 6-22. Primordial mantle normalised multi-element (spider) diagrams (plotting order and normalizing values after McDonough et al., 1992) for the charnockite (actual plotted values) and the streaky augen gneiss (red shaded area).

The charnockite pattern that was superimposed on that of the augen gneiss was normalized to primordial mantle (normalizing values published by McDonough et al., 1992) for the spider diagram and chondritic values (normalizing values published by Boynton 1984) for the REE plot, respectively, as used for the magmatic rocks (Section 6.4). In terms of the charnockite REE plot, when comparing it to magmatic rocks, the charnockite has a negative LREE slope (Figure 6-21) with an average $(La/Sm)_N$ = 3.72 suggesting a degree of fractionation of the LREE. The HREEs of the charnockite are gently sloping [$(Gd/Yb)_N$ = 1.46] in comparison to the LREE (Figure 6-21), indicating a weak fractionation in the HREE. Samples C133 and C106 have a steeply negative slope for the HREE (Figure 6-21) indicating that they are highly fractionated [$(Gd/Yb)_N$ = 2.75 and $(Gd/Yb)_N$ = 4.78 respectively], whilst samples C141 and C35 have a positive slope ($(Gd/Yb)_N$ = 0.86 and $(Gd/Yb)_N$ = 0.77] (Figure 6-21) and are, thus, rather unfractionated. Fractionation toward Lu is commonly indicative of the influence of garnet. Where garnet is present in the rocks the HREE will fractionate strongly into it. However, the parental magma of the charnockite is garnet poor. Similarly, like the streaky augen gneiss, the charnockites display a negative average Eu anomaly (Eu/Eu*= 0.44) with the only variation being the slightly positive Eu anomaly (Figure 6-21) for sample C171 (Eu/Eu*= 1.08) and C133 (Eu/Eu*= 1.23). These positive Eu anomalies possibly represent the influence of hydrothermal fluids or presence of plagioclase.

The spider plot of the charnockite, when examining a possible magmatic affinity, indicates that the majority of the LILE and HFSE display trends which are almost identical to those of the streaky augen gneiss (Figure 6-22), with the only difference between the charnockite and the streaky augen gneiss being the slightly more positive anomalies of Hf, Zr and Sr for the charnockite (Figure 6-22). Unlike the streaky augen gneiss that has gradual trends for U and Th, the charnockite contains a trough for the latter and a peak for the former.

6.6.1 Metasomatism

Metasomatism is a metamorphic process which alters the chemical composition of a rock which remains in a solid state and involves the introduction and/or removal of chemical components as a result of the interaction of the rock with aqueous fluids / solutions (Zharikov et al. 2007). When metasomatism is associated with magmatism two metasomatic changes could occur, the first is connected with fluids that originated from a magmatic body and which metasomatised the solid host rocks, and the second is of a post-magmatic stage and are connected with hydrothermal fluids originating from both the cooling magma and heated exogenic sources (related to this study) is the third form of metasomatism is when two rocks which were originally in chemical equilibrium with each are no longer so because of increase in temperature and pressure during metamorphism. As a result metasomatism occurs along the contact to bring them back into chemical equilibrium with each other again (Zharikov et al. 2007).

6.6.2 Mass balance

Mass balance is defined as the changes in the chemical composition of the altered rock in comparison to that of the original rock, such as the amount of constituents lost or gained during the alteration process (diffusion in a fluid medium or by infiltration of reactive fluids is commonplace in weathering, diagenesis, metamorphic and igneous processes and generally record mass-transfer processes) (Potdevin 1993). Gresens (1967) proposed the idea of geochemical mass balance, whereby he quantified it as the inter-relationship of change in volume, composition and density of an altered rock to its protolith according to the following formulae (Mukherjee and Gupta 2008):

$$\Delta m_i = fv\ (\rho_a / \rho_o)\ C_a - C_o$$

where the “o” and “a” subscripts represent the original and altered rock, respectively, and ρ_a and ρ_o represent their respective densities; Δm_i is the mass change in component i, C_o and C_a are the initial and final concentrations in the original and altered rock of component i, respectively, and fv is the volume factor or ratio of the final volume to the initial volume (López-Moro 2012).

In addition to Gresens' initial ideas about the mobility/immobility of elements and the gains and losses of material in hydrothermal systems (López-Moro 2012), Grant (1986) proposed a simpler graphical method, whereby the Gresens' equation was rearranged into a linear relationship (the isocon equation) between the concentration of the altered and unaltered composition (López-Moro 2012; Mukherjee and Gupta 2008). Grant (1986) proposed that all immobile elements would plot in a straight line through the origin of the ISOCON plot. The line drawn through these elements are known as the isochemical / ISOCON line (Grant 2005).

In this study the Microsoft excel worksheet program EASYGRESGRANT, based on the Gresens and Grant methods for studying metasomatic systems, is used to perform mass-balance calculations, whilst considering all possible reference frames (immobile elements, constant volume, and constant mass) between the altered and unaltered rock types. EASYGRESGRANT allows the correct selection of immobile elements from clusters of slopes, volume factors, and an improved isocon diagram, providing an error-free mass-balance modeling (López-Moro 2012). The method of clusters of slopes and volume factors consists of estimating the slopes and the volume factors for all the elements considered (López-Moro 2012).

Clusters of elements with close slope or volume factor values were selected as immobile elements, whereby the average of these parameters represented the reference frame for mass-balance calculations. Due to its simplicity and reliability, this method was used for selecting immobile elements (López-Moro 2012). In order to establish the immobile elements, López-Moro (2012) proposed several methods using the EASYGRESGRANT software, such as: the composition-volume diagram, the isocon diagram and the component-ratio diagram.

6.6.3 Mass balance calculations using EASYGRESGRANT

The mass balance equations were applied to investigate the exchange of materials between both the streaky augen gneiss and pink gneiss with that of the charnockite. The data used for the mass balance calculations are presented in Appendix F (Table AF-1). Here the charnockite was taken as the altered rock whilst both the augen and pink gneisses were taken as the unaltered rock (protolith). The EASYGRESGRANT program was used for the mass balance evaluations of the above-mentioned rocks. The immobile elements were selected using the cluster of slopes method showing similar calculated slope values (Grant 2005). The average slope of the immobile elements was automatically calculated and used as the slope of the isocon from which mass gains and losses were calculated. In addition to the data used, Appendix F (Table AF-1) also display the results of the mass lost and gained by the charnockite. The enrichment and depletion diagrams that quantify the gains and

losses of selected elements in the charnockite are graphically shown in Figure 6-23, respectively. Due to the large scale of the isocon plot, the majority of the elements are clustered at lower values. Thus Figures 6-23B is enlarged to produce an expanded view of the tightly clustered region. Due to the abundant data plotted on the isocon plot, bar graphs were also constructed (Appendix F) which shows more distinct patterns.

The trace elements on the streaky augen gneiss (unaltered) vs. charnockite (altered) isocon plot (Figure 6-23a, b) show the highest gains for Ba, Zr, Sr, V and Zn, whilst for the major elements Al_2O_3 and Fe_2O_3 display the highest gains. The rest of the major elements show slight enrichments, with CaO being slightly enriched. The trace elements Sr, V, Sc, Zn, Hf, Y, Nb, and LREE are slightly enriched (Figure 6-23a, b). There is a large loss in terms of SiO_2, Cr, Rb and Th with slight losses in K_2O, Pb, Ni, Ce and U (Figure 6-23a, b), hence the charnockite is potentially less alkali feldspar-rich compared to the streaky augen gneiss. None of these gains and losses is of mineralogical or petrographic importance.

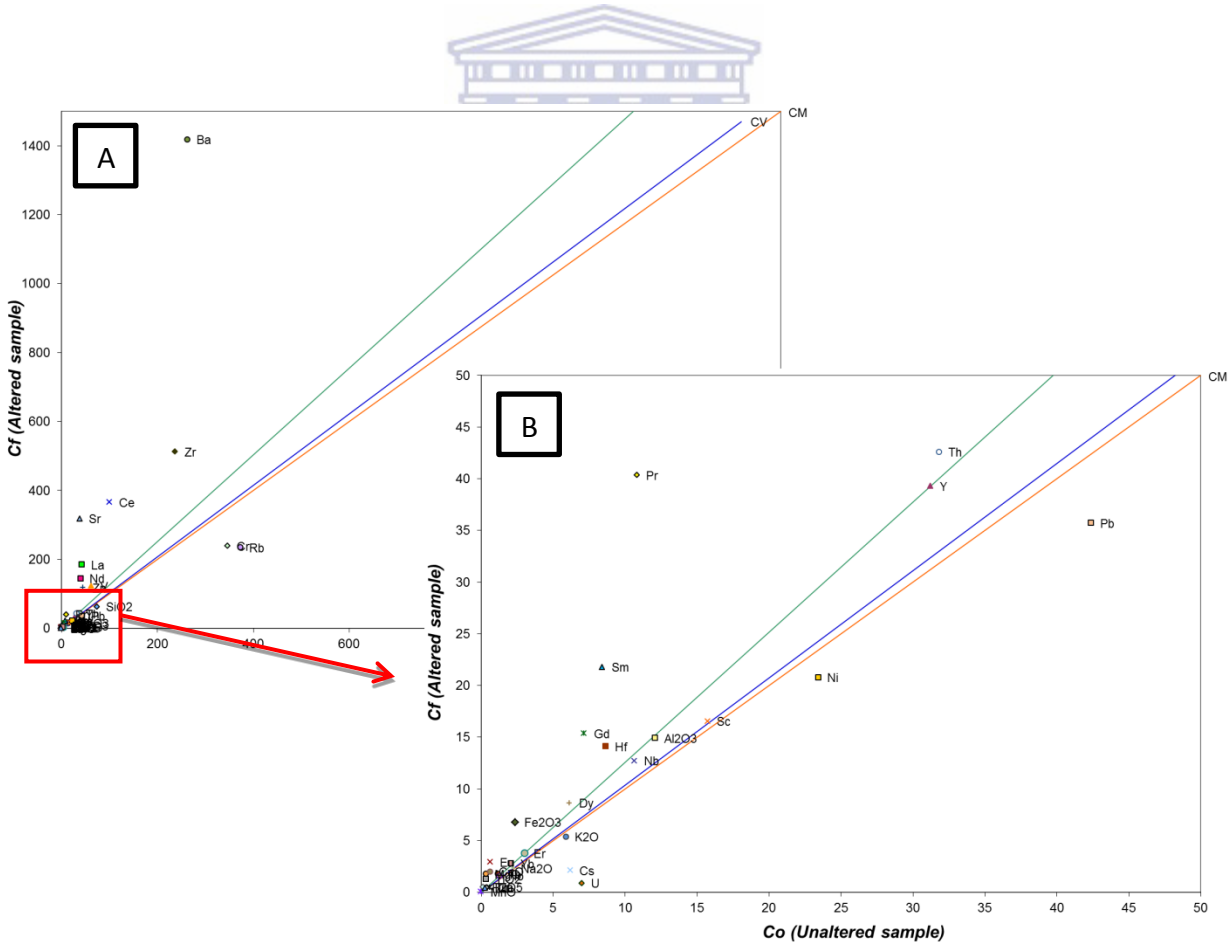

Figure 6-23. a) Isocon plot of streaky augen gneiss vs. charnockite. b) Zoomed in portion of Figure 6-23a.

6.7 Geochemistry of the metasedimentary rocks

6.7.1 Quartzites

Quartzites are formed by the metamorphism of sandstone (Farndon 2010). These rocks have relatively high silica content (SiO_2 wt.% of 74.30 – 83.76) coupled with low concentrations of TiO_2 (0.16-0.46 wt.%), MgO (0.11-0.38 wt.%), and CaO (0.31-1.43 wt.%) of the quartzitic Kliprand samples relative to sandstone values in Table 9. In contrast to the trend of the majority of the samples, sample Q68 is the only sample that displays TiO_2 (0.46 wt.%) and CaO (0.80 wt.%) values similar to those of sandstone. In comparison to sandstone the quartzites contain relatively high values of Al_2O_3 (8.48-12.85 wt.%), Fe_2O_3 (0.90-2.61 wt.%), Na_2O (1.39-3.01 wt.%) and K_2O (2.64-6.05 wt.%) with the exception of sample Q134 that has a relatively low K_2O value of 0.83 wt.% in comparison to the sandstone values of Carmichael (1989) (Table 9). The Na_2O and K_2O contents, as well as the petrography, show that the quartzite is relatively feldspathic.

In order to evaluate whether or not these quartzites formed by the metamorphism of sandstone, the chemical data was plotted on the log (Fe_2O_3/K_2O) vs. log (SiO_2/Al_2O_3) classification diagram (this diagram make use of potentially mobile major elements, particularly K) of Herron (1988). The investigated quartzites plot exclusively within the arkose field, with samples Q68 and Q134 plotting in the litharenite field (Figure 6-24). The concentration of many elements within fine grained sedimentary rocks of continental platforms around the world is similar due to mixing and repeated cycles of erosion (Rollinson 1993). The REE plot of the quartzites was normalized relative to the post-Archean Australian shale (PAAS) values of McLennan (1989) (Figure 6-25). On the PAAS-normalized REE plot the average for all the metaquartzite from Kliprand is characterized by both slight LREE enrichment [$(La/Sm)_N = 1.18$] and slight HREE enrichment [$(Gd/Lu)_N = 1.22$] (Table 10). The entire REE plot (Figure 6-25) has an average $(La/Lu)_N = 1.48$ indicating that it is more fractionated than the average post-Archean Australian shale. With the exception of samples Q66 (strong negative Eu anomaly of Eu/Eu* = 0.40), Q68 (strong positive Eu anomaly of Eu/Eu* = 3.06) and Q134 (slightly weaker positive Eu anomaly Eu/Eu* = 1.32) showing differing Eu values (Table 10) the remaining samples displays a slightly positive Eu anomaly (Figure 6-25) (average Eu/Eu*=1.195).

Table 8. Major Element Geochemistry of the metasedimentary rocks (Quartzite and metapelite).

Metapelite							Pelites	Shales	Greywackes	UCC
Sample	**M10**	**M102**	**M103**	**M105**	**M022**	**M205**	**Carmichael 1989**			**Taylor and McLennan 1985**
SiO_2	72.52	70.57	70.32	71.01	74.03	74.08	54.9	50.7	70	66
TiO_2	0.56	0.55	0.52	0.46	0.33	0.36	0.78	0.78	0.58	0.5
Al_2O_3	12.41	13.8	14.06	13.76	12.6	12.65	16.6	15.1	8.2	15.2
Fe_2O_3	3.71	3.76	4.03	3.3	2.46	2.48	7.7	4.4	0.5	4.04
MnO	0.05	0.04	0.05	0.04	0.02	0.05				0.1
MgO	0.58	0.71	0.72	0.43	0.33	0.35	3.4	3.3	0.9	2.2
CaO	1.09	1.36	1.36	1.21	0.8	1	0.72	7.2	4.3	4.2
Na_2O	2.29	2.74	2.65	2.82	2.45	2.47	1.3	0.8	0.58	3.9
K_2O	5.33	5.22	4.89	5.39	5.92	5.33	2.7	3.5	2.1	3.4
P_2O_5	0.13	0.12	0.12	0.16	0.1	0.05				
Cr_2O_3	0.01	0.01	0.01	0.01	0.02	0.02				
L.O.I.	**1**	0.73	0.9	1.04	0.7	1.07				
Total	99.68	99.61	99.63	99.63	99.76	99.91				

Quartzite							Sandstone	Granites
Sample	**Q68**	**Q066**	**Q134**	**Q190**	**Q145**	**Q164**	**Carmichael 1989**	
SiO_2	80.84	80.29	83.76	78.79	77.04	74.30	70	70.11
TiO_2	0.46	0.16	0.10	0.29	0.20	0.18	0.58	0.42
Al_2O_3	8.48	9.74	9.17	11.05	11.51	12.85	8.2	14.11
Fe_2O_3	2.61	1.53	1.25	0.90	1.50	1.84	0.5	1.14
MnO	0.04	0.02	0.01	0.01	0.01	0.02		
MgO	0.80	0.13	0.17	0.11	0.15	0.38	0.9	0.24
CaO	1.13	0.32	1.43	0.31	0.39	0.78	4.3	1.66
Na_2O	1.39	1.57	2.39	1.82	1.93	3.01	0.58	3.03
K_2O	2.64	5.37	0.83	6.05	6.04	5.40	2.1	6.02
P_2O_5	0.04	0.04	0.07	0.07	0.05	0.05		
Cr_2O_3	0.02	0.02	0.02	0.02	0.01	0.01		
L.O.I.	**0.99**	0.52	0.81	0.78	0.85	0.75		
Total	99.44	99.71	100.01	100.20	99.68	99.57		

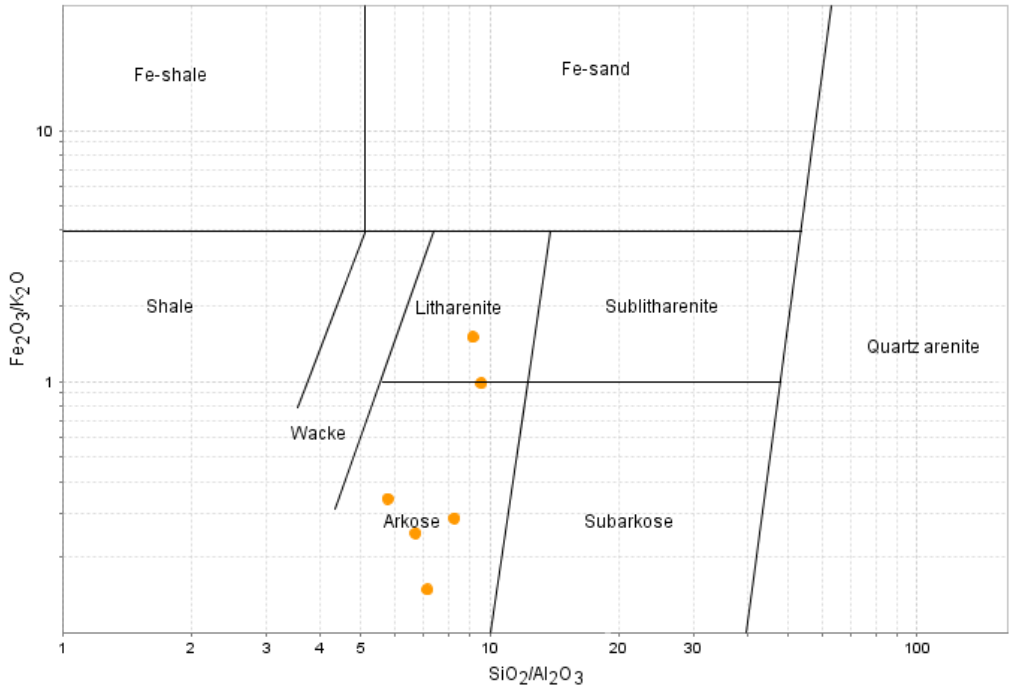

Figure 6-24. The log (Fe_2O_3/K_2O) vs. log (SiO_2/Al_2O_3) classification diagram for the metaquartzites of the Kliprand domal structure after Herron (1988).

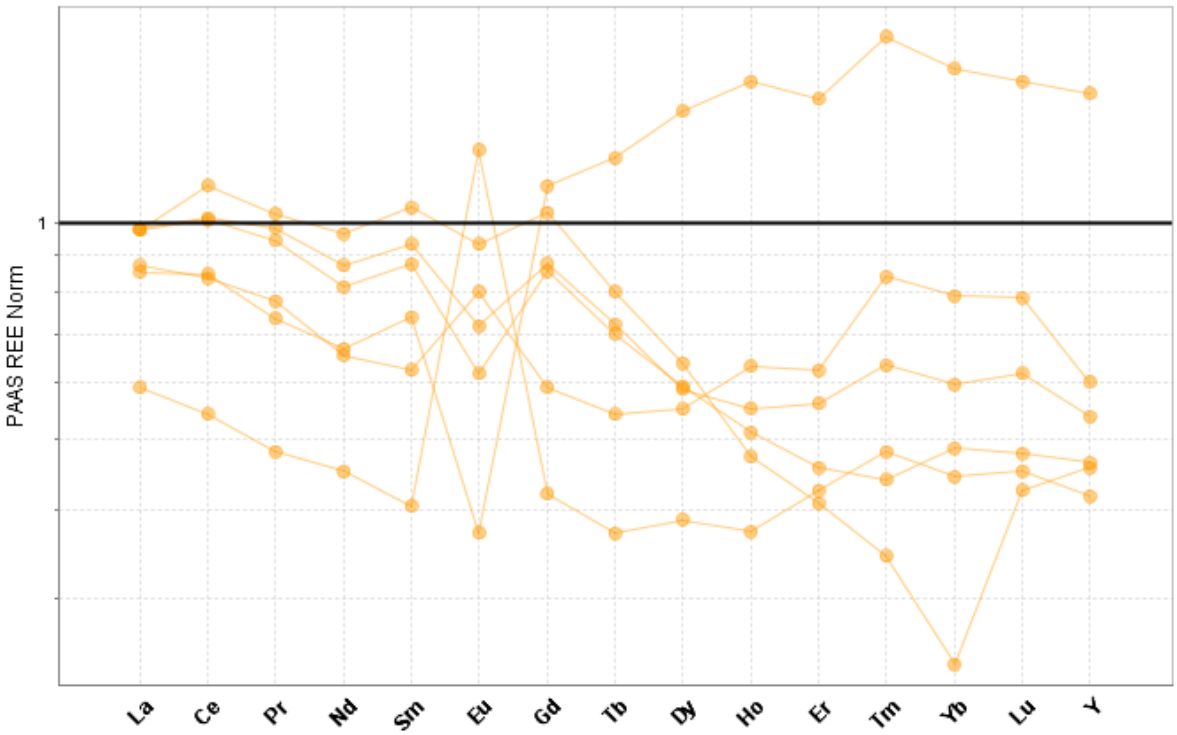

Figure 6-25. Rare earth element concentrations in quartzite normalized to the Post-archaen average Australian sedimentary rock (PAAS) values of McLennan (1989).

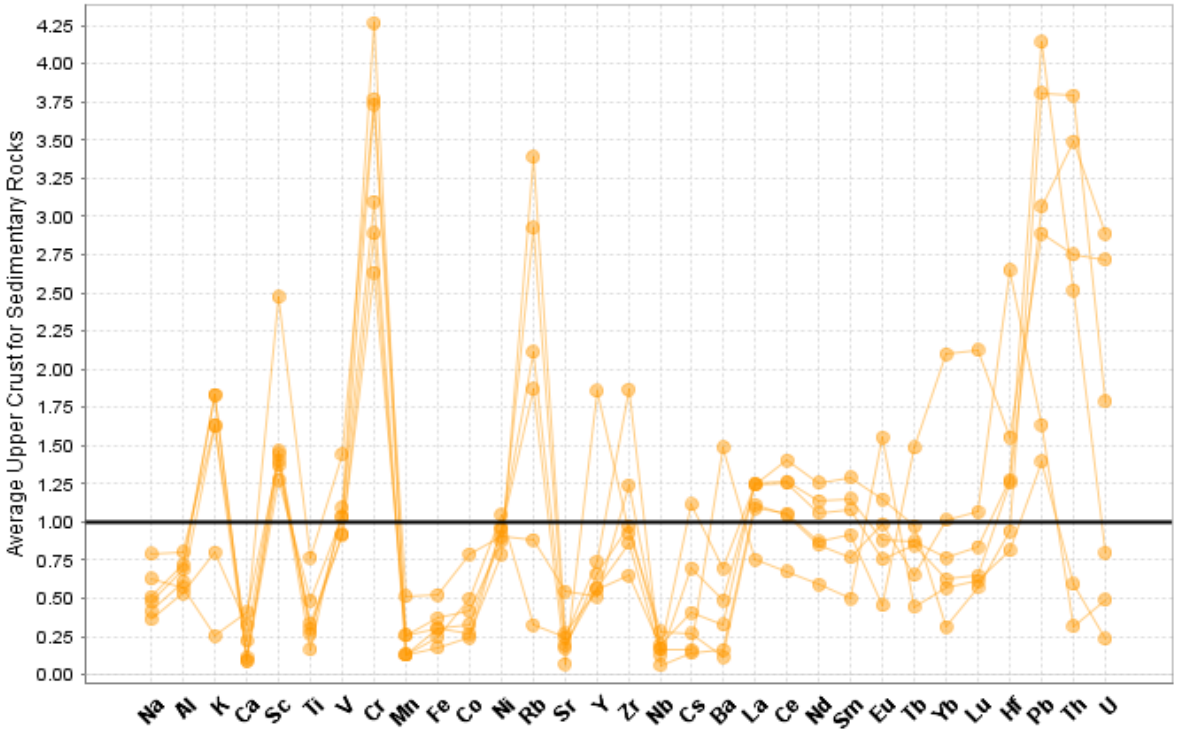

Figure 6-26. Multi-element trace element (spider) diagram for the quartzites normalized to the average upper continental crust. The normalized values were taken from Taylor et al. (1981).

The spider diagram of the quartzites, normalized to average upper continental crustal values (Figure 6-26), shows that the major elements Na and Al are slightly depleted relative to the UCC in addition to Ca and Ti, whilst K displays a positive anomaly. With regards to the LILE, Pb, Rb and K (Table 11) have the highest positive anomalies in comparison to the UCC. The remaining LILE (Cs, Ba and Sr) have relatively strongly negative anomalies. Hf is the only HFS element that contains a positive anomaly; U and Th also display strong positive anomalies (Figure 6-26). Zr and Ce have concentrations almost identical to the UCC for the sedimentary rock values of Taylor et al. (1981). Of the HFS elements Nb and Ti have prominent negative anomalies (Figure 6-26). Of the transition elements (Table 11) Sc strong positive anomalies, whilst V and Ni have values identical to UCC, and Mn and Co have prominent negative anomalies (Figure 6-26).

Table 9. Rare earth element (REE) geochemistry of the metasedimentary rocks (quartzite and metapelite).

	Quartzite						*Metapelite*					
Sample	**Q68**	**Q066**	**Q134**	**Q190**	**Q145**	**Q164**	**M10**	**M102**	**M103**	**M105**	**M022**	**M205**
La	22.57	32.64	33.32	37.48	37.32	37.4	52.28	64.99	63.07	60.2	49.45	33.93
Ce	43.19	67.61	66.65	80.76	89.73	80.34	118.81	141.98	135.1	131.67	111.55	74.81
Pr	4.25	6.51	6.87	8.7	9.1	8.35	13.2	17.26	16.06	15.79	11.72	8.32
Nd	15.29	22.65	22.19	29.57	32.74	27.6	48.25	67.07	63.94	63.09	41.81	29.33
Sm	2.25	4.11	3.47	5.19	5.82	4.86	9.54	13.85	13.45	12.9	8.05	5.98
Eu	1.37	0.4	0.87	0.78	1.01	0.67	0.73	1.99	2.2	2.04	0.78	0.86
Gd	1.96	5.24	2.76	4.09	4.82	3.99	8.79	11.79	12.37	11.48	7.39	6.41
Tb	0.29	0.95	0.42	0.56	0.62	0.54	1.41	1.59	1.92	1.53	1.17	1.41
Dy	1.81	6.7	2.58	2.75	2.99	2.78	8.14	9.02	12.08	7.58	6.01	11.83
Ho	0.37	1.56	0.63	0.55	0.47	0.51	1.58	1.76	2.55	1.27	1.26	3.14
Er	1.21	4.24	1.78	1.6	1.16	1.3	4.18	5.01	7.65	3.15	3.4	10.98
Tm	0.19	0.74	0.34	0.26	0.14	0.18	0.59	0.69	1.06	0.37	0.44	1.72
Yb	1.25	4.62	2.23	1.68	0.69	1.37	3.45	4.88	7.19	2.74	2.38	12.23
Lu	0.2	0.68	0.34	0.27	0.18	0.21	0.5	0.68	1.06	0.42	0.36	1.7
∑ LREE / HREE	12.03	5.4	11.97	13.76	15.79	14.59	8.46	8.62	6.36	9.94	9.93	3.08
Ce/Ce*	1.01	1.07	1.01	1.03	1.12	1.04	1.04	0.98	0.98	0.99	1.06	1.02
Eu/Eu*	3.06	0.4	1.32	0.79	0.89	0.71	0.38	0.73	0.8	0.79	0.47	0.65
$(La/Sm)_N$	1.46	1.15	1.39	1.05	0.93	1.11	0.8	0.68	0.68	0.68	0.89	0.82
$(Gd/Lu)_N$	0.93	0.71	0.75	0.75	2.43	1.78	1.64	1.61	1.09	1.09	1.92	0.35
$(La/Lu)_N$	1.3	0.54	1.1	1.58	2.29	2.04	1.19	1.08	0.68	1.63	1.57	0.22

Note: All these normalisations are relative to PAAS

Table 10. Trace element geochemistry of the metasedimentary rocks (quartzite and metapelite).

	Quartzite						*Metapelite*					
Sample	**Q68**	**Q066**	**Q134**	**Q190**	**Q145**	**Q164**	**M10**	**M102**	**M103**	**M105**	**M022**	**M205**
Sc	24.74	14.43	14.04	12.74	13.71	14.665	13.46	16.13	19.78	15.33	14.73	15.83
Ti	2757.7	959.2	599.5	1738.55	1199	1079.1	3382.979	3297.25	3117.4	2757.7	1978.35	2158.2
V	86.7	62.22	65.74	61.94	55.09	54.97	76.37	81.61	78.3	61.09	64.95	65.81
Cr	469.06	464.73	530.98	385.62	359.75	327.85	316.94	357.33	308.07	289.07	389.62	373.24
Co	7.88	3.29	4.98	2.41	2.66	4.165	5.9	7.68	7.6	6.06	5.14	3.79
Ni	18.07	19.03	20.94	19.31	15.75	17.525	19.55	24.81	22.41	15.88	24.14	14.96
Cu	12.71	15.15	15.06	8.26	11.12	13.08	36.36	29.04	21.2	64.81	15.57	10.45
Zn	53.9	21.19	24.65	25.15	27.3	31.92	59.38	73.53	81.87	73.8	42.39	35.49
Rb	97.03	205.8	35.62	232.5	373.14	322.17	285.65	256.63	239.4	241.39	441.98	333.33
Sr	189.67	24.43	85.16	60.6	93.91	68.525	64.74	106.22	108.14	111.07	42.38	57.88
Zr	297.05	222.03	447.83	233.05	155.39	206.795	357.34	439.51	420.31	401.18	243.25	268.31
Nb	4.14	7.02	1.62	4.92	4.38	3.22	12.28	14.66	13.57	15.03	8.98	9.74
Y	11.25	40.88	16.24	14.51	12.32	12.52	43.42	46.74	68.19	34.24	32.6	87.81
Cs	0.59	1.01	0.53	1.5	4.13	2.575	7.66	5.16	4.18	2.37	7.14	5.4
Ba	1043.08	80.25	112.39	228.93	487.83	339.83	450.69	851.51	829.99	860.74	232	309.03
Hf	4.72	9.02	15.38	7.38	5.43	7.285	10.3	12.74	12.12	11.73	8.1	7.71
Ta	0.18	0.47	0.14	0.31	0.22	0.1835	0.78	0.79	0.68	0.75	0.65	0.72
Pb	20.98	43.33	24.53	62.15	57.14	46.015	56.26	35.67	32.83	35.37	44.38	36.65
Th	6.23	28.89	3.36	26.43	39.83	36.65	30.48	28.53	24.15	24.34	40.19	32.78
U	0.59	6.8	1.23	1.99	4.48	7.215	4.85	2.49	2.08	1.73	5.48	3.6

6.7.2 Metapelites

Relative to the standard compositions of shales and pelites of Carmichael (1989), the majority of the metapelitic samples have major element compositions [Al_2O_3 (12.41 – 14.06 wt.%), Fe_2O_3 (2.46 - 4.03 wt.%), CaO (0.8 – 1.36 wt.%), Na_2O (2.29 – 2.82 wt.%) and K_2O (4.89 – 5.92 wt.%)] almost identical to these average compositions (Table 9). The only major elements that are enriched relative to those of average pelites and shales, and are similar to those of average greywackes, are SiO_2 (70.32-74.08 wt.%) and TiO_2 (0.36-0.56 wt.%). This SiO_2 composition of 70.32-74.08 wt% is high for a pelite and suggests a relatively quartzofeldspathic nature and likely derivation from a quartzose or felsic provenance.

Similarly to the quartzites, the log (Fe_2O_3/K_2O) vs. log (SiO_2/Al_2O_3) classification diagram (this diagram make use of potentially mobile major elements, particularly K) of Herron (1988), discriminating between terrigenous sandstone and shales, was used in order to classify the protoliths of the metapelites. The metapelite samples range from arkose to wacke on the log (Fe_2O_3/K_2O) vs. log (SiO_2/Al_2O_3) classification diagram (Figure 6-27). Showing that they are not typical shales due to their high silica content

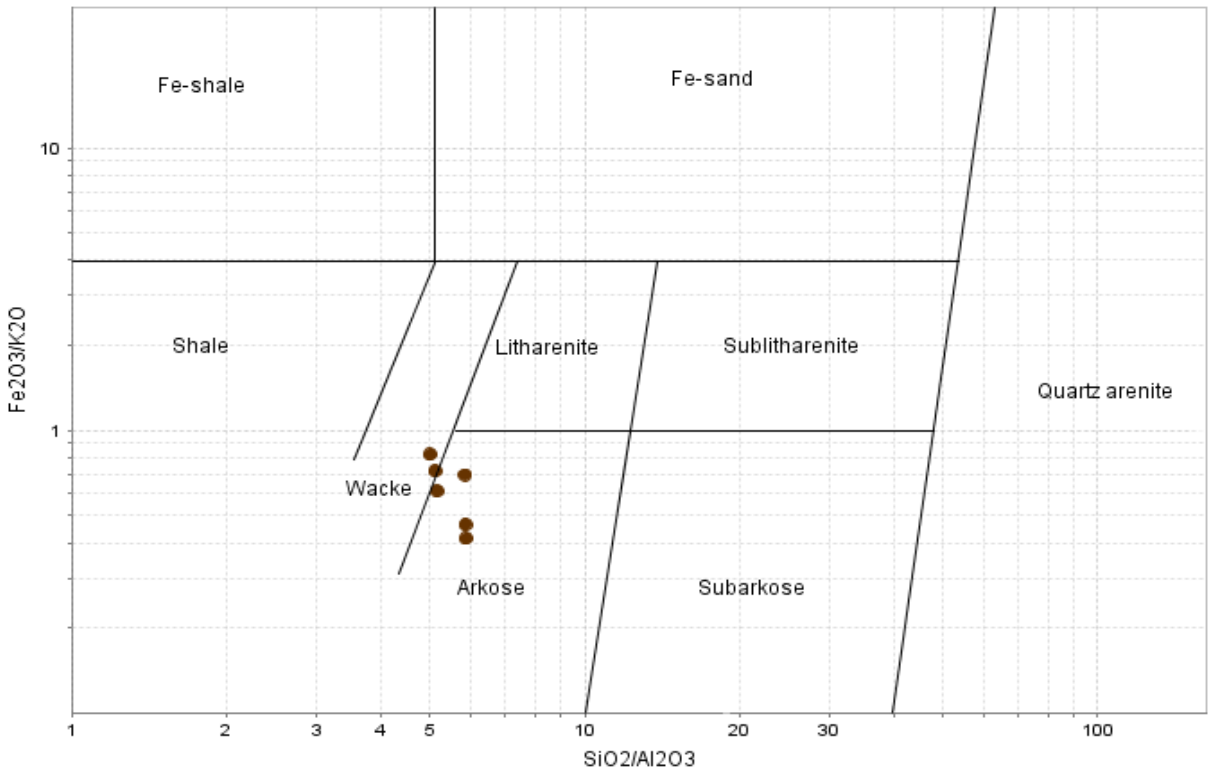

Figure 6-27. The log (Fe_2O_3/K_2O) vs. log (SiO_2/Al_2O_3) classification diagram of the metapelites (after Herron (1988).

The REE concentrations of the metapelites are given in Table 10 and are normalised relative to the Post-Archean average Australian sedimentary rock (PAAS) (Figure 6-28). The North American shale composite values of Gromet et al. (1984) and the upper continental crustal values of Taylor et al. (1981) are plotted on the REE diagram for reference sake. In the normalized PAAS REE plot, the metapelites are characterized by rather flat to slightly negative sloping LREE patterns (Figure 6-28) with an average $(La/Sm)_N$ of 1.18. The LREE trends are enriched relative to both PAAS and the NASC curve (Figure 6-28), with M205 being the only sample with a trend that closely resembles that of the NASC (Figure 6-28). The majority of the HREE display rather weak fractionation trends [$(Gd/Lu)_N$ = 1.35], with sample M22 being slightly more fractionated [$(Gd/Lu)_N$ = 1.92]. Sample M205 (slightly more garnet rich) is the only exception with a steep positive HREE trend ($(Gd/Lu)_N$ =0.35) suggesting that little or no fractionation occurred. Samples M10, M102, M105 and M22 have an average $(La/Lu)_N$ ratio of 1.36 suggesting that there is little fractionation of the LREE relative to the HREE in comparison to PAAS. Due to samples M103 [$(La/Lu)_N$ = 0.68] and M205 [$(La/Lu)_N$ = 0.22] being slightly more garnet-rich than the rest of the metapelites, their HREE are enriched relative to the LREE (Figure 6-28). The HREE tend to fractionate quite strongly into garnet. In terms of Eu anomaly, samples M10 (Eu/Eu* = 0.38), M22 (0.47) and M205 (0.65) have the strongest negative Eu anomalies (Figure 6-28), whilst samples M102 (0.73), M103 (0.80) and M105 (0.79) have much weaker Eu anomalies. The only samples that highly resemble the NASC in terms of REE concentrations are samples M102 and M103. Overall the metapelite are strongly enriched in all the REE relative to the UCC (Figure 6-28).

The trace element concentrations of the metapelites are reported in Table 11 and are shown on the spider diagram normalized to the average upper continental crust for sedimentary rock (Figure 6-29). Similarly to the quartzites, the major elements Na, Al, Ca and Ti have negative anomalies and are thus slightly depleted relative to the UCC. K is the only major element that has a positive anomaly and is thus enriched relative to the UCC (Figure 6-29) suggesting derivation from a potassic (granitic) provenance. The only LILE that have well defined positive anomalies relative to the UCC values are Pb, Rb and Cs (Figure 6-29); these are typical of crustal influence, whilst Ba and Sr are the only large ion lithophile elements that have relatively strong negative anomalies (Figure 6-29).

Relative to the UCC values of Taylor et al. (1981), U and Th are the only HFS elements that display positive anomalies (Figure 6-29). These positive anomalies closely resemble the trend in the quartzites. Hf, Zr and Ce have compositions almost identical to the UCC values of Taylor et al. (1981), whilst Nb and Ti have prominent negative anomalies (Figure 6-29). The transition elements of the

metapelites have Sc displaying strong positive anomalies, and V and Ni having values identical to UCC.

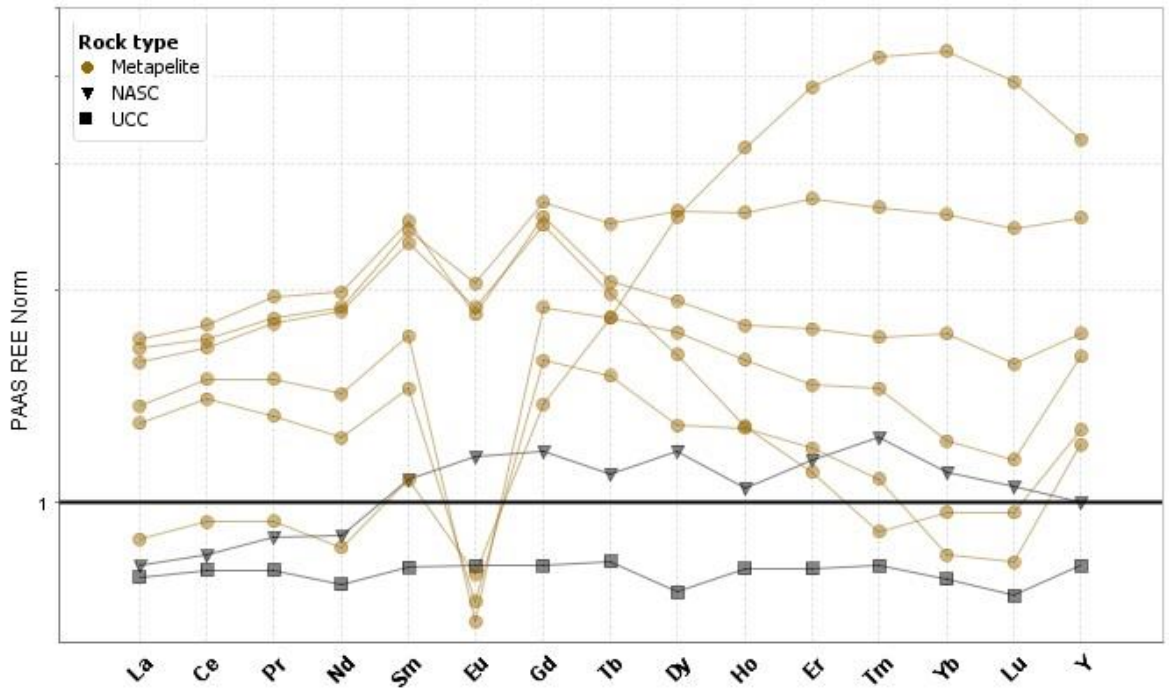

Figure 6-28. Rare earth element concentrations in the metapelite normalized to post-Archean average Australian sedimentary rock (PAAS) (values of McLennan, 1989).

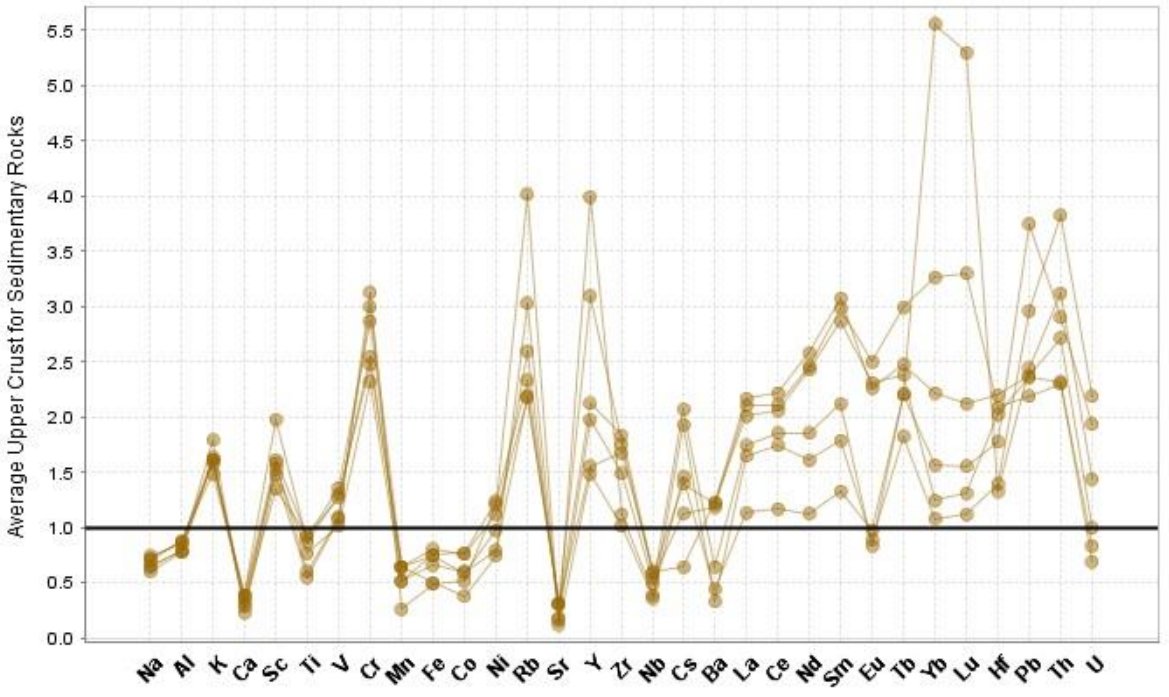

Figure 6-29. Trace element diagram of the metapelite normalized to the average upper continental crust for sedimentary rocks. The normalized values were taken from Taylor et al. (1981).

Chapter 7 : Geochronology

7.1 Pink gneiss (biotite-poor variety)

The pink gneiss (also known as the Lekkerdrink Gneiss) has two varieties which can mainly be distinguished by their biotite content as being either biotite-rich (13%) (the dominant pink gneiss in the study area) or the biotite-poor (locally observed) pink gneiss respectively. The biotite-poor pink gneiss was rather scarce in the study area, as there was only a maximum of about 5 locations where this rock type was found. However, this rock was analysed (geochronologically and isotopically) to check if there are any significant differences between the biotite-rich pink gneiss/biotite-poor pink gneiss and its relationship to the streaky augen gneiss.

The majority of the zircons from the pink gneiss are well rounded, and range in length from 30–110µm (Figure 7-1). The CL images of the least altered grains display distinct bright oval shaped cores which are slightly U poor (e.g. sample 10 with a U concentrationof 149ppm and sample 11 with a U concentration of 330ppm) (Figure 7-1). The rims of the zircons consist of fine scale oscillatory zoning. The cores of sample 10 are interpreted as detrital fragments that were abraded and broken during mechanical transport (Figure 7-1). Samples 10 and 11 (Figure 7-1) are both fractured, whilst the remaining zircons are reworked and metamictized and have high average U contents (>2200 ppm) (Table 12).

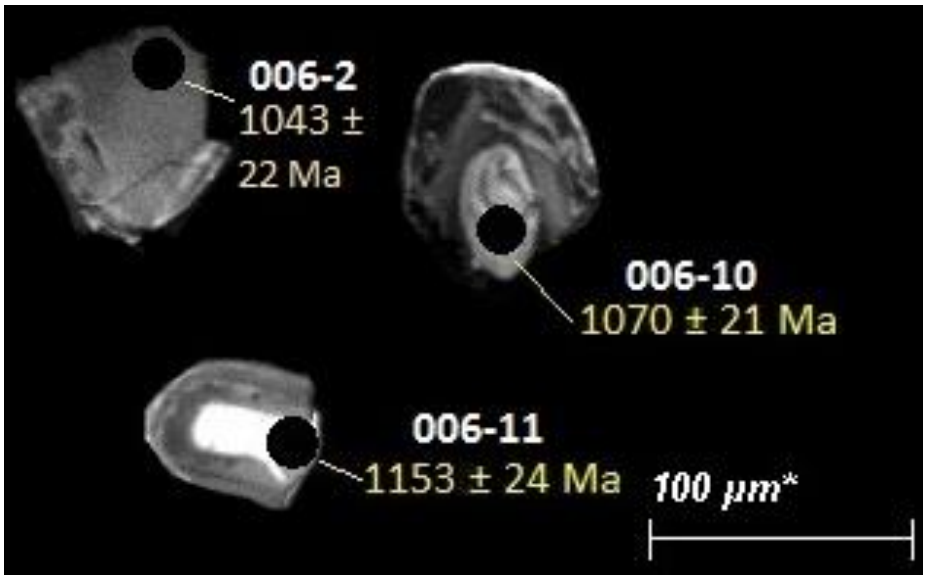

Figure 7-1. CL images of zircons from sample PG006. The position of the laser spot is represented by black circles (they are not representative of the actual 30µm spot). Labels indicate analyses number and the determined $^{206}Pb/^{238}U$ ages. Zircon 006-10 looks rather rounded and detrital, but 006-2 is rather angular.

The Th/U ratios for the analyzed data ranges between 0.32-0.72 ppm (Table 12) which are very close to the Th/U ratio of 0.5 of magmatic zircon, this is characteristic of high grade metamorphism (Hoskin and Black, 2000). The $^{207}Pb/^{206}Pb$ concordia plot (Figure 7-2a) displays only 3 analyses on the concordia curve (samples 2 ($^{206}Pb/^{238}U$ = 1043 ± 22Ma), 10 ($^{206}Pb/^{238}U$ =1153 ± 21Ma) and 11 ($^{206}Pb/^{238}U$ = 1070 ± 21Ma), with the remaining samples scattered below the concordia curve making it impossible for a discordia line to be drawn through the analysed data. These ages likely reflect peak metamorphism. The very high U contents is also the cause of, and symptomatic of isotopic disturbance. A Wetherill concordia plot (Figure 7-2b) was also constructed; however a similar relationship was observed.

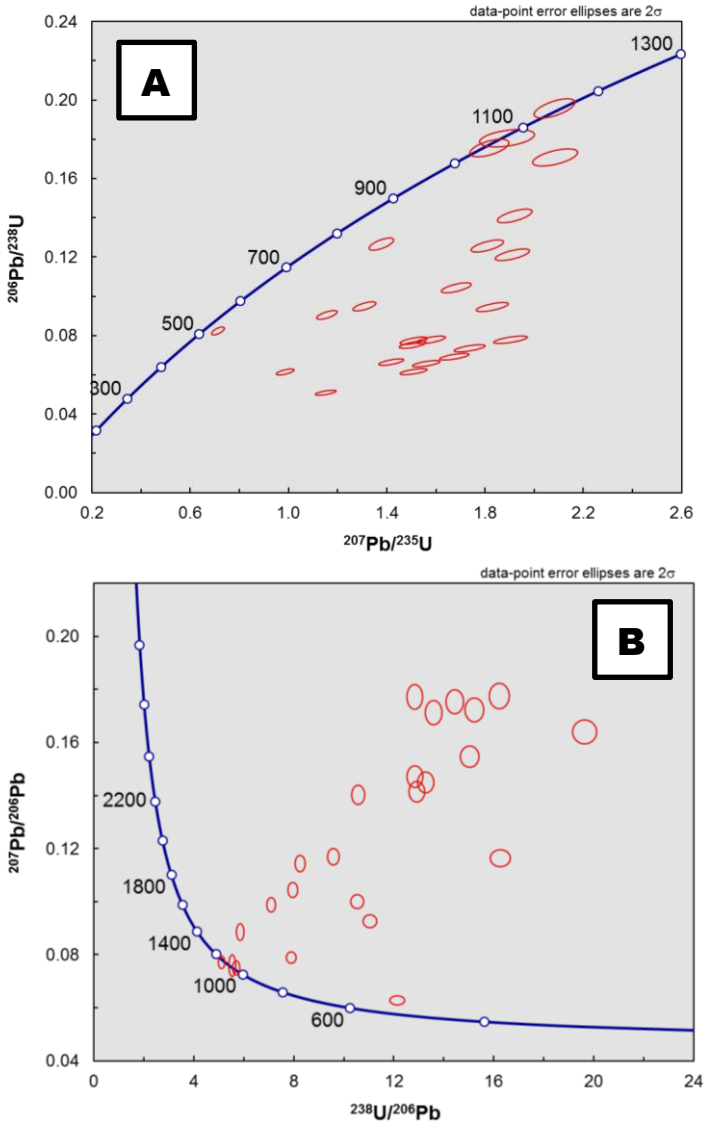

Figure 7-2. (A) U-Pb concordia plot of LA-ICP-MS data for zircon grains from sample PG 006 of the biotite-rich pink gneiss (streaky gneiss) within the Kliprand domal structure. Very little data plots on the concordia curve with most plotting discordantly below it. (B) A Wetherill concordia plot using the same data as the concordia diagram given in a).

Table 11. U-Th-Pb isotopic compositions of zircon grains extracted from sample PG006 of the pink gneiss located within the Kliprand domal structure.

		Concentration			Ratios							Ages [Ma]						Conc.
	Spot no.	U [ppm][a]	Pb [ppm][a]	Th/U[a]	$^{207}Pb/^{235}U$[b]	2 s[d]	$^{206}Pb/^{238}U$[b]	2 s[d]	rho[c]	$^{207}Pb/^{206}Pb$[e]	2 s[d]	$^{207}Pb/^{235}U$	2 s	$^{206}Pb/^{238}U$	2 s	$^{207}Pb/^{206}Pb$	2 s	%
	PG 006																	
Analyses used	006-10	149	29	0.72	2.082	0.068	0.1958	0.0040	0.63	0.0772	0.0020	1143	37	1153	24	1125	51	102
	006-11	330	60	0.32	1.889	0.091	0.1806	0.0036	0.41	0.0759	0.0033	1077	52	1070	21	1092	88	98
	006-2	666	117	0.38	1.817	0.065	0.1756	0.0037	0.58	0.0751	0.0022	1052	38	1043	22	1070	58	97
Analyses not used	006-1	521	89	0.40	2.085	0.075	0.1708	0.0036	0.58	0.0886	0.0026	1144	41	1016	21	1394	56	73
	006-3	2942	204	0.39	1.675	0.049	0.0693	0.0014	0.69	0.1754	0.0037	999	29	432	9	2610	35	17
	006-4	1147	104	0.44	1.156	0.034	0.0905	0.0018	0.68	0.0926	0.0020	780	23	559	11	1481	41	38
	006-5	2358	332	0.08	1.921	0.058	0.1410	0.0028	0.67	0.0988	0.0022	1088	33	850	17	1602	42	53
	006-6	2462	192	0.48	1.580	0.048	0.0779	0.0016	0.67	0.1472	0.0033	962	29	483	10	2313	39	21
	006-7	2359	223	0.22	1.829	0.053	0.0946	0.0019	0.69	0.1403	0.0030	1056	31	583	12	2231	37	26
	006-8	2708	180	0.93	1.419	0.041	0.0665	0.0013	0.69	0.1547	0.0033	897	26	415	8	2398	36	17
	006-12	2163	205	0.24	1.309	0.038	0.0949	0.0019	0.68	0.1000	0.0021	850	25	585	12	1625	40	36
	006-13	2753	181	0.68	1.561	0.046	0.0657	0.0013	0.69	0.1723	0.0037	955	28	410	8	2580	36	16
	006-14	2338	182	0.41	1.903	0.056	0.0779	0.0016	0.68	0.1772	0.0038	1082	32	484	10	2627	36	18
	006-15	1144	119	0.72	1.683	0.050	0.1044	0.0021	0.68	0.1169	0.0025	1002	30	640	13	1910	39	34
	006-16	2598	329	0.15	1.378	0.041	0.1266	0.0025	0.67	0.0789	0.0017	880	26	769	15	1171	44	66
	006-17	2498	184	0.10	1.737	0.051	0.0736	0.0015	0.68	0.1713	0.0037	1022	30	458	9	2570	36	18
	006-18	1795	148	22.67	0.713	0.021	0.0824	0.0016	0.67	0.0628	0.0014	547	16	510	10	701	47	73
	006-19	795	100	0.63	1.809	0.054	0.1257	0.0025	0.67	0.1044	0.0023	1049	31	763	15	1704	41	45
	006-20	989	120	0.42	1.911	0.057	0.1212	0.0024	0.67	0.1144	0.0025	1085	32	737	15	1870	40	39
	006-21	2233	168	0.56	1.506	0.045	0.0753	0.0015	0.67	0.1450	0.0032	933	28	468	9	2287	38	20
	006-22	3252	201	0.84	1.509	0.045	0.0617	0.0012	0.67	0.1775	0.0039	934	28	386	8	2630	37	15
	006-23	2178	134	1.06	0.987	0.030	0.0615	0.0012	0.67	0.1164	0.0026	697	21	385	8	1902	40	20
	006-24	2121	164	0.21	1.510	0.045	0.0774	0.0015	0.67	0.1415	0.0032	934	28	481	10	2245	39	21
	006-25	2711	138	0.59	1.152	0.035	0.0509	0.0010	0.67	0.1640	0.0037	778	23	320	6	2497	38	13

[a]U and Pb concentrations and Th/U ratios are calculated relative to GJ-1 reference zircon.

[b]Corrected for background and within-run Pb/U fractionation and normalized to reference zircon GJ-1 (isotope dilution thermal ionization mass spectrometry values/measured value); $^{207}Pb/^{235}U$ calculated using ($^{207}Pb/^{206}Pb$)/($^{238}U/^{206}Pb$ * 1/137.88).

[c]Rho is the error correlation defined as the quotient of the propagated errors of the $^{206}Pb/^{238}U$ and the $^{207}/^{235}U$ ratio.

[d]Quadratic addition of within-run errors (2 SD) and daily reproducibility of GJ-1 (2 SD).

[e]Corrected for mass bias by normalizing to GJ-1 reference zircon (~0.6 per atomic mass unit) and common Pb using the model Pb composition of Stacey and Kramers [1975].

7.2 Pink gneiss (biotite-rich variety)

The pink biotite gneiss dominates the Kliprand domal structure and hence is more significant than the biotite-poor pink gneiss. The CL images of all the zircons extracted from the pink biotite gneiss look rather rounded. Grain spot 001-12 has a bright, unzoned core (U concentration of 151 ppm and a $^{206}Pb/^{238}U$ age of 1187 ± 24Ma), possibly a remnant of an older zircon. The predominant ages are around 1150-1130 Ma (Figure 7-3). The zircons have an average U content of > 2000 ppm (Table 13) and are extensively recrystallized. Consequently, most of the zircons are metamict (as revealed by the CL images) and show strong Pb-loss (31-185 ppm for the analyses used) (Table 13). Although the cores are highly altered about 80% of the zircon grains display clear oscillatory zoned rims (Figure 7-3). The Th/ U ratios range between 0.22-0.54 (Table 13) for the analyses used. The Th/U ratios and oscillatory zoning point to a magmatic origin, but the metamictization and reworked cores (Figure 7-3) suggest metamorphism. Only four of the analyses have $^{207}Pb/^{206}Pb$ ages that are concordant (Figure 7-4b), whilst the remaining 20 analyses are discordant below the concordia curve (Figure 7-4a). On a concordia diagram all the analyses define upper and lower intercept dates of 1142 ± 35 Ma and 135 ± 55 Ma (Possibly related to Karoo magmatism), respectively (MSWD = 31). The near-concordant analyses give a weighted mean $^{207}Pb/^{206}Pb$ date of 1135±9 Ma, which is the approximate age of emplacement..

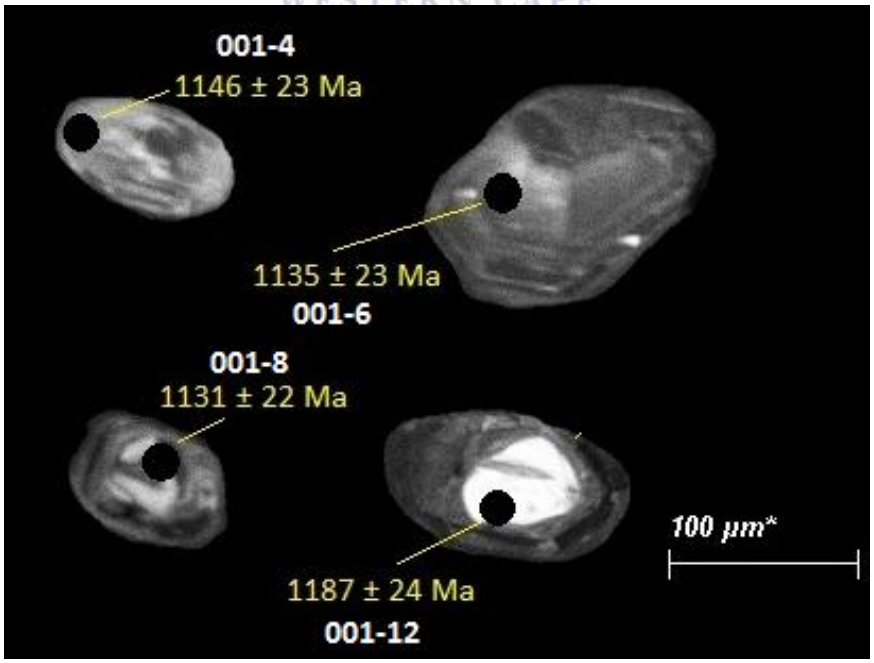

Figure 7-3. CL images of zircons from sample PG001. The position of the laser spot is represented by black circles (they are not representative of the actual 30µm spot). Labels indicate analyses number and the determined $^{206}Pb/^{238}U$ ages.

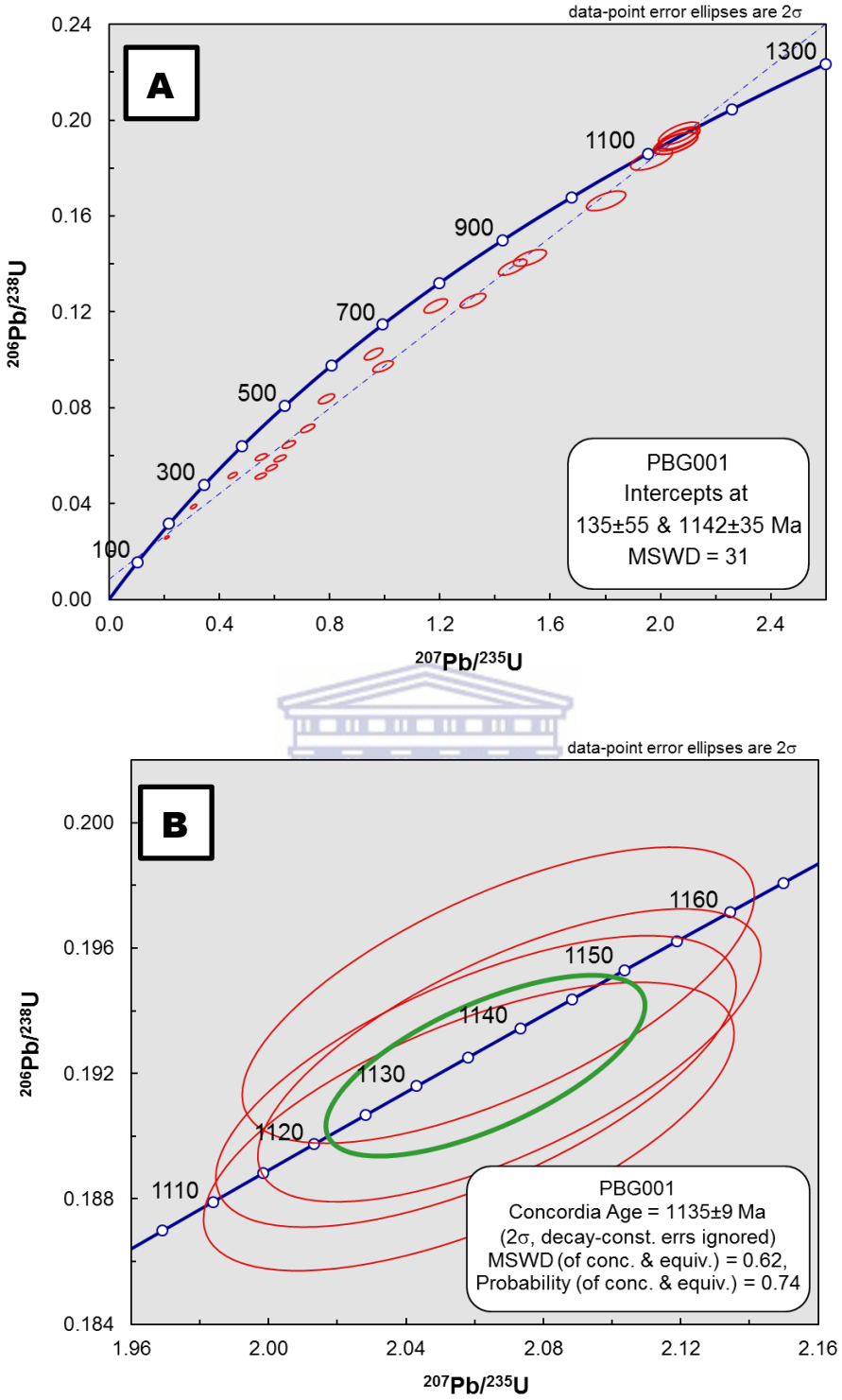

Figure 7-4. (A) U-Pb concordia plot of sample PBG 001. The majority of the data plots below the concordia curve, where a straight line fitted through the discordant zircons back to the concordia curve (known as a discordia line) gave an upper intercept age *of 1142±35 Ma and lower intercept age of 135±55Ma. (B) Enlarged area where data plots on the concordia curve. The concordia plot for near-concordant analyses is used to calculate the weighted mean $^{207}Pb/^{206}Pb$ age of PBG 001. Confidence limit for error ellipses is 2σ. The upper intercept and Concordia ages are within error of each other.*

Table 12. U-Th-Pb isotopic compositions of zircon grains extracted from sample PBG001 of the biotite rich pink gneiss located within the Kliprand domal structure.

		Concentration			Ratios							Ages [Ma]						Conc.
	Spot no.	U [ppm][a]	Pb [ppm][a]	Th/U[a]	$^{207}Pb/^{235}U$[b]	2 s[d]	$^{206}Pb/^{238}U$[b]	2 s[d]	rho[c]	$^{207}Pb/^{206}Pb$[e]	2 s[d]	$^{207}Pb/^{235}U$	2 s	$^{206}Pb/^{238}U$	2 s	$^{207}Pb/^{206}Pb$	2 s	%
Analyses used	001-4	461	90	0.23	2.067	0.061	0.1945	0.0039	0.67	0.0771	0.0017	1138	34	1146	23	1123	43	102
	001-6	961	185	0.54	2.070	0.060	0.1926	0.0038	0.69	0.0780	0.0016	1139	33	1135	23	1146	42	99
	001-8	370	71	0.22	2.060	0.062	0.1918	0.0038	0.66	0.0779	0.0018	1136	34	1131	22	1145	45	99
	001-12	151	31	0.45	2.212	0.068	0.2022	0.0040	0.65	0.0794	0.0019	1185	36	1187	24	1181	46	100
Analyses not used	001-1	2897	159	0.12	0.589	0.017	0.0550	0.0011	0.69	0.0777	0.0016	470	14	345	7	1139	42	30
	001-2	1981	142	0.69	0.720	0.021	0.0714	0.0014	0.69	0.0732	0.0015	551	16	445	9	1018	43	44
	001-3	1112	154	0.20	1.464	0.042	0.1387	0.0027	0.68	0.0766	0.0016	915	27	837	17	1110	42	75
	001-5	2384	244	0.10	0.959	0.028	0.1025	0.0020	0.69	0.0679	0.0014	683	20	629	12	866	43	73
	001-7	556	92	0.52	1.802	0.058	0.1664	0.0034	0.63	0.0786	0.0020	1046	34	992	20	1162	50	85
	001-9	3831	198	0.08	0.448	0.014	0.0518	0.0010	0.65	0.0627	0.0014	376	11	326	6	699	49	47
	001-10	463	88	0.54	2.054	0.066	0.1903	0.0038	0.62	0.0783	0.0020	1134	36	1123	22	1154	50	97
	001-11	1734	216	0.35	1.319	0.038	0.1247	0.0025	0.68	0.0768	0.0016	854	25	757	15	1115	42	68
	001-13	530	76	0.45	1.526	0.049	0.1426	0.0028	0.62	0.0776	0.0020	941	30	859	17	1138	50	76
	001-14	2719	160	0.32	0.620	0.018	0.0589	0.0012	0.68	0.0764	0.0016	490	14	369	7	1106	43	33
	001-15	3200	124	0.09	0.307	0.009	0.0388	0.0008	0.66	0.0573	0.0013	272	8	245	5	503	49	49
	001-16	2590	317	0.11	1.185	0.035	0.1225	0.0024	0.67	0.0701	0.0015	793	23	745	15	932	44	80
	001-17	7855	204	0.15	0.210	0.007	0.0259	0.0005	0.64	0.0586	0.0014	193	6	165	3	552	53	30
	001-18	1094	201	0.62	1.967	0.062	0.1837	0.0037	0.63	0.0777	0.0019	1104	35	1087	22	1139	49	95
	001-19	473	90	0.14	2.058	0.063	0.1903	0.0038	0.64	0.0784	0.0018	1135	35	1123	22	1158	47	97
	001-20	2106	176	0.20	0.789	0.024	0.0837	0.0017	0.65	0.0683	0.0016	590	18	518	10	878	48	59
	001-21	3035	156	0.35	0.550	0.017	0.0515	0.0010	0.65	0.0774	0.0018	445	14	324	6	1133	46	29
	001-22	2683	159	0.29	0.552	0.017	0.0594	0.0012	0.63	0.0674	0.0017	446	14	372	7	850	51	44
	001-23	2668	259	0.25	0.994	0.030	0.0973	0.0019	0.64	0.0741	0.0017	701	21	598	12	1044	47	57
	001-25	3283	212	0.65	0.652	0.020	0.0647	0.0013	0.65	0.0731	0.0017	510	15	404	8	1017	47	40

[a]U and Pb concentrations and Th/U ratios are calculated relative to GJ-1 reference zircon.

[b]Corrected for background and within-run Pb/U fractionation and normalized to reference zircon GJ-1 (isotope dilution thermal ionization mass spectrometry values/measured value); $^{207}Pb/^{235}U$ calculated using ($^{207}Pb/^{206}Pb$)/($^{238}U/^{206}Pb$ * 1/137.88).

[c]Rho is the error correlation defined as the quotient of the propagated errors of the $^{206}Pb/^{238}U$ and the $^{207}/^{235}U$ ratio.

[d]Quadratic addition of within-run errors (2 SD) and daily reproducibility of GJ-1 (2 SD).

[e]Corrected for mass bias by normalizing to GJ-1 reference zircon (~0.6 per atomic mass unit) and common Pb using the model Pb composition of Stacey and Kramers [1975].

7.3 Quartzite

Zircons extracted from sample Q66 are 20–200µm in length, and are oval to round in shape (Figure 7-5). These zircons have a very high average U content of > 2500 ppm (Table 14). CL images reveal that these zircons were subjected to an anatectic event, seeing that the zircons show clear alterations (e.g. growth rims) and are largely metamict. Grain spots 56, 59, 72 and 99 are the exception, as these are well rounded grains showing bright central cores (Figure 7-5) surrounded by increasingly more U-enriched outer rims (analysed spots on samples 59 and 72 were taken on the rim, where U contents of 927ppm was obtained for the former and 877ppm for the latter). The zircon grain (sample 56, 59) has a visible inner core with sector zoning and an oscillatory zoned rim (Figure 7-5). The central core of zircon 72 displays disrupted and vague zoning (Figure 7-5). The U content (Table 14) for the analysed spots of bright cores in zircons 56 (309 ppm) and 99 (396 ppm) are much lower than that of the rims. The Th/U ratios of both the core and the rims range from 0.17 to 0.28 (Table 14) which is close to 0.1, characteristic of recrystallized, metamorphic zircon grains (Hoskin and Black, 2000). One hundred and fifteen spot analyses were performed on 98 zircon grains. Only four of the analyses had data that are between 98% to 102% concordant (Figure 7-6a), giving $^{206}Pb/^{238}U$ ages of between 1121 ± 23 and 1141 ± 24 Ma for the cores, with $^{206}Pb/^{238}U$ ages of 1131 ± 23 and 1134 ± 23 Ma for the rims (Table 14).

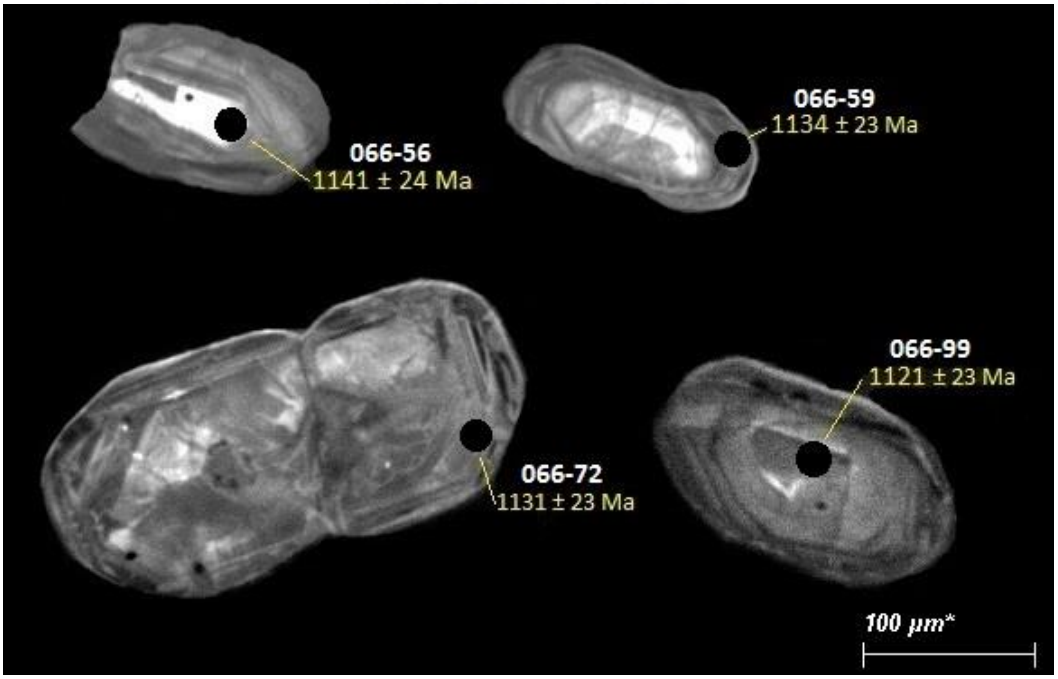

Figure 7-5. CL images of zircons from sample Q66. The position of the laser spot is represented by black dots (they are not representative of the actual 30µm spot). Labels indicate analyses number and the determined $^{206}Pb/^{238}U$ ages.

Because the majority of the analyses are scattered (Figure 7-6a), a discordia line could not be drawn through the data and thus an accurate age could not be determined for this rock type. In addition to the concordia plot, a frequency probability plot (Figure 7-6b) was constructed to more accurately establish the age of deposition. Here eight of the 113 analyses had a 90-110% concordance, with the histogram showing the highest peaks between 1100 and 1125 Ma (Figure 7-6b), and this only from two zircons per peak each).

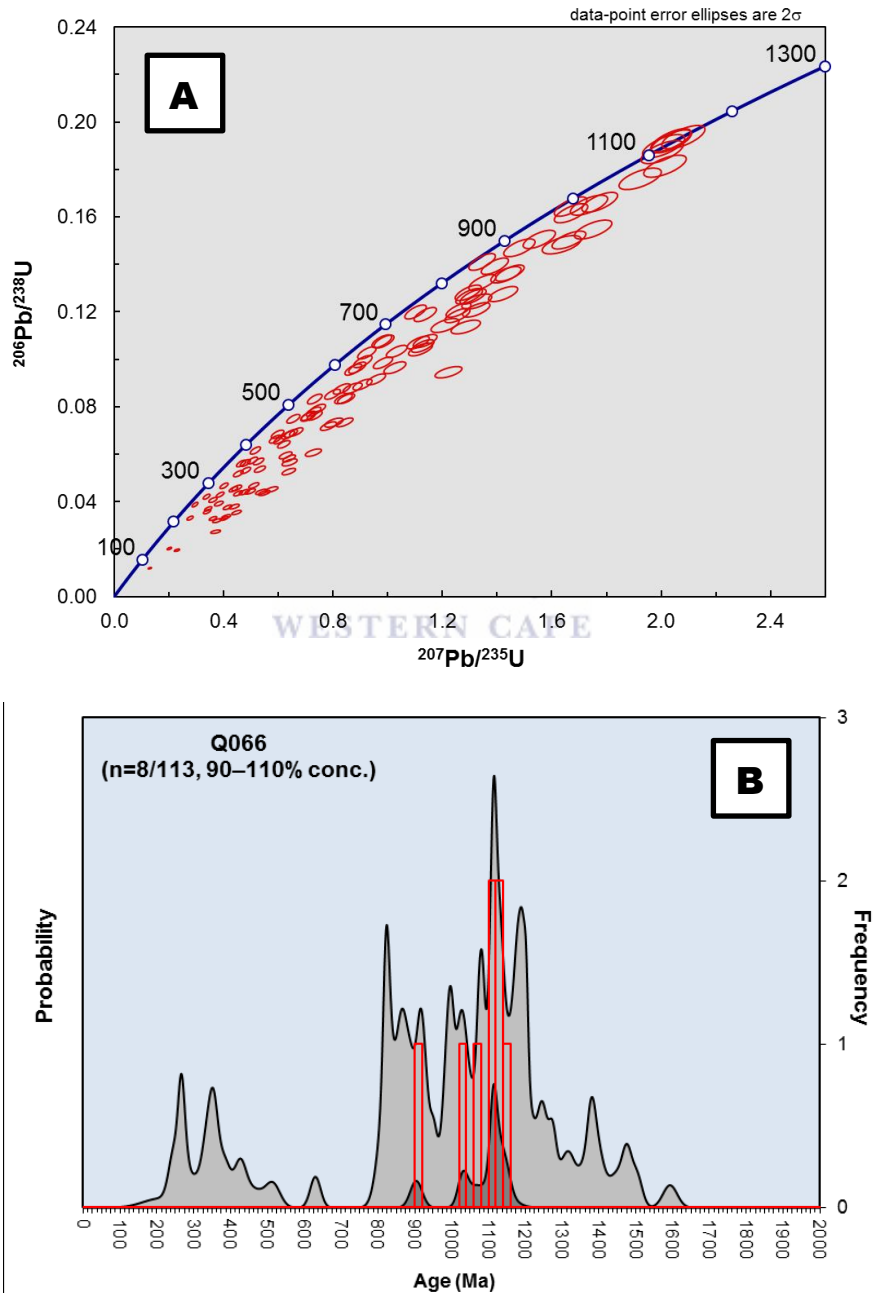

Figure 7-6. (A) U-Pb concordia plot of sample Q066. The data is highly discordant not defining a discordia line. All these have experienced variable lead loss. (B) Frequency probability plot for the $^{207}Pb/^{206}Pb$ zircon ages of sample Q66. Using concordance values of 90-110% indicates that only 8 analyses of the 113 total analyses are concordant, with the highest probability bars at ages of between 1100 and 1125 Ma.

Table 13. U-Th-Pb isotopic compositions of zircon grains extracted from sample Q066 of the quartzites located within the Kliprand domal structure.

	Concentration				Ratios						Ages [Ma]						Conc.
	Spot no.	U [ppm][a]	Pb [ppm][a]	Th/U[a]	$^{207}Pb/^{235}U$[b]	2 s[d]	$^{206}Pb/^{238}U$[b]	2 s[d]	rho[c]	$^{207}Pb/^{206}Pb$[e]	2 s[d]	$^{207}Pb/^{235}U$	2 s	$^{206}Pb/^{238}U$	2 s	$^{207}Pb/^{206}Pb$	2 s	%
	Q066																	
Analyses used	066-56	309	60	0.28	2.081	0.064	0.1937	0.0040	0.67	0.0779	0.0018	1143	35	1141	24	1145	46	100
	066-59	927	178	0.21	2.035	0.060	0.1924	0.0039	0.70	0.0767	0.0016	1127	33	1134	23	1114	42	102
	066-72	877	168	0.20	2.037	0.060	0.1918	0.0040	0.70	0.0770	0.0016	1128	33	1131	23	1121	42	101
	066-99	396	75	0.17	2.009	0.063	0.1899	0.0040	0.67	0.0767	0.0018	1118	35	1121	23	1114	47	101
Analyses not used	066-1	305	35	1.78	1.285	0.044	0.1136	0.0024	0.61	0.0820	0.0022	839	29	694	14	1246	53	56
	066-2	1618	96	2.77	0.627	0.019	0.0595	0.0012	0.66	0.0764	0.0018	494	15	373	8	1104	46	34
	066-3	2241	144	1.24	0.620	0.019	0.0642	0.0013	0.67	0.0701	0.0016	490	15	401	8	931	46	43
	066-4	2258	155	0.38	0.646	0.019	0.0688	0.0014	0.68	0.0682	0.0015	506	15	429	9	873	46	49
	066-5	4421	146	0.22	0.277	0.009	0.0331	0.0007	0.61	0.0608	0.0016	249	8	210	4	633	57	33
	066-6	1740	180	0.60	1.033	0.031	0.1033	0.0021	0.68	0.0725	0.0016	720	22	634	13	1000	45	63
	066-7	2541	243	0.06	0.874	0.025	0.0957	0.0019	0.69	0.0663	0.0014	638	18	589	12	815	44	72
	066-8	1150	109	1.77	1.222	0.040	0.0946	0.0020	0.63	0.0938	0.0024	811	27	582	12	1503	48	39
	066-9	2352	103	7.87	0.548	0.017	0.0437	0.0009	0.65	0.0911	0.0022	444	14	276	6	1448	46	19
	066-10	3785	284	0.34	0.655	0.020	0.0749	0.0015	0.68	0.0634	0.0014	511	15	466	9	721	47	65
	066-11	3594	163	1.00	0.436	0.013	0.0453	0.0009	0.70	0.0699	0.0015	367	11	285	6	924	43	31
	066-12	2220	283	1.34	1.422	0.044	0.1275	0.0026	0.66	0.0809	0.0019	898	28	774	16	1218	45	64
	066-13	3212	173	0.57	0.533	0.017	0.0537	0.0011	0.66	0.0719	0.0017	434	13	337	7	984	48	34
	066-14	3726	359	0.50	0.889	0.026	0.0965	0.0019	0.70	0.0668	0.0014	646	19	594	12	832	43	71
	066-15	3828	142	1.74	0.344	0.011	0.0370	0.0008	0.64	0.0674	0.0016	300	10	234	5	849	51	28
	066-16	2473	109	1.98	0.538	0.018	0.0441	0.0009	0.63	0.0885	0.0023	437	14	278	6	1393	49	20
	066-17	4335	370	0.08	0.798	0.024	0.0853	0.0017	0.68	0.0679	0.0015	596	18	527	11	866	45	61
	066-18	3168	380	0.55	1.102	0.032	0.1199	0.0024	0.69	0.0666	0.0014	754	22	730	15	826	44	88
	066-19	3750	214	1.13	0.528	0.016	0.0570	0.0012	0.68	0.0672	0.0015	430	13	357	7	844	45	42
	066-20	1603	223	0.21	1.392	0.041	0.1393	0.0028	0.69	0.0725	0.0015	885	26	840	17	999	43	84
	066-21	2017	91	2.61	0.576	0.019	0.0452	0.0009	0.64	0.0925	0.0023	462	15	285	6	1477	48	19
	066-22	2944	138	9.64	0.511	0.015	0.0468	0.0010	0.69	0.0791	0.0017	419	13	295	6	1173	43	25
	066-23	3460	230	0.62	0.589	0.018	0.0664	0.0014	0.68	0.0644	0.0014	470	14	414	8	754	47	55
	066-24	1721	144	0.74	0.838	0.026	0.0834	0.0017	0.65	0.0729	0.0017	618	19	516	11	1011	48	51
	066-25	2956	230	0.15	0.729	0.022	0.0779	0.0016	0.67	0.0678	0.0015	556	17	484	10	863	46	56

Table 14 (cont.) U-Th-Pb isotopic compositions of zircon grains extracted from sample Q066 of the quartzites located within the Kliprand domal structure.

	Concentration			Ratios							Ages [Ma]						Conc.
Spot no.	U [ppm][a]	Pb [ppm][a]	Th/U[a]	$^{207}Pb/^{235}U$[b]	2 s[d]	$^{206}Pb/^{238}U$[b]	2 s[d]	rho[c]	$^{207}Pb/^{206}Pb$[e]	2 s[d]	$^{207}Pb/^{235}U$	2 s	$^{206}Pb/^{238}U$	2 s	$^{207}Pb/^{206}Pb$	2 s	%
Q066																	
066-26	1795	177	0.39	0.983	0.029	0.0985	0.0020	0.69	0.0723	0.0015	695	20	606	12	996	43	61
066-27	3342	145	3.59	0.453	0.014	0.0435	0.0009	0.68	0.0755	0.0017	379	11	275	6	1082	44	25
066-28	1626	143	0.74	0.872	0.029	0.0878	0.0018	0.63	0.0720	0.0018	636	21	543	11	985	52	55
066-29	3038	253	0.58	0.848	0.025	0.0834	0.0017	0.68	0.0737	0.0016	624	19	517	11	1034	44	50
066-30	3197	211	0.30	0.605	0.018	0.0660	0.0013	0.69	0.0665	0.0014	480	14	412	8	822	44	50
066-31	791	96	0.69	1.324	0.041	0.1208	0.0025	0.67	0.0795	0.0018	856	26	735	15	1184	45	62
066-32	3358	179	0.29	0.481	0.015	0.0532	0.0011	0.67	0.0656	0.0015	399	12	334	7	793	47	42
066-33	2902	312	0.07	0.978	0.029	0.1076	0.0022	0.68	0.0659	0.0015	693	21	659	13	804	46	82
066-34	3418	192	0.05	0.464	0.014	0.0561	0.0011	0.68	0.0600	0.0013	387	12	352	7	605	48	58
066-35	5654	115	0.64	0.202	0.007	0.0203	0.0004	0.63	0.0722	0.0019	187	6	129	3	990	52	13
066-36	2448	170	1.42	0.666	0.020	0.0694	0.0014	0.68	0.0695	0.0015	518	16	433	9	915	46	47
066-37	2652	181	0.18	0.636	0.019	0.0681	0.0014	0.68	0.0677	0.0015	500	15	425	9	858	46	50
066-38	1670	275	0.11	1.668	0.049	0.1644	0.0033	0.70	0.0736	0.0015	997	29	981	20	1031	42	95
066-39	2843	163	0.06	0.506	0.015	0.0573	0.0012	0.69	0.0640	0.0014	416	12	359	7	741	46	49
066-40	1967	318	0.28	1.670	0.050	0.1616	0.0033	0.68	0.0750	0.0016	997	30	965	20	1068	44	90
066-41	3119	320	0.08	0.924	0.028	0.1027	0.0021	0.68	0.0652	0.0014	664	20	630	13	781	46	81
066-42	3722	144	0.04	0.295	0.009	0.0388	0.0008	0.69	0.0553	0.0012	263	8	245	5	422	48	58
066-43	314	47	0.89	1.663	0.051	0.1503	0.0031	0.67	0.0803	0.0018	994	30	902	18	1203	44	75
066-44	3089	331	0.61	1.112	0.033	0.1070	0.0022	0.69	0.0753	0.0016	759	22	656	13	1077	43	61
066-45	3549	255	0.28	0.783	0.024	0.0719	0.0015	0.67	0.0791	0.0018	587	18	447	9	1173	45	38
066-46	4022	177	0.83	0.476	0.015	0.0441	0.0009	0.66	0.0783	0.0019	395	13	278	6	1155	48	24
066-47	3767	162	0.72	0.387	0.012	0.0430	0.0009	0.69	0.0654	0.0014	332	10	271	6	786	46	35
066-48	3645	117	1.56	0.375	0.013	0.0320	0.0007	0.62	0.0852	0.0023	324	11	203	4	1319	52	15
066-49	3212	267	0.07	0.733	0.022	0.0833	0.0017	0.69	0.0639	0.0014	558	17	515	11	737	46	70
066-50	1951	179	0.51	0.958	0.028	0.0916	0.0019	0.70	0.0759	0.0016	682	20	565	12	1091	42	52
066-51	3476	117	7.87	0.410	0.013	0.0337	0.0007	0.63	0.0881	0.0022	349	11	214	4	1385	49	15
066-52	1853	261	0.04	1.345	0.040	0.1410	0.0029	0.70	0.0692	0.0015	865	25	850	17	904	43	94
066-53	2324	276	0.07	1.137	0.033	0.1189	0.0024	0.70	0.0694	0.0015	771	23	724	15	910	43	80
066-54	114	14	5.58	1.326	0.045	0.1244	0.0026	0.62	0.0773	0.0020	857	29	756	16	1129	53	67
066-55	406	67	2.31	1.775	0.053	0.1662	0.0034	0.68	0.0775	0.0017	1036	31	991	20	1133	44	87
066-57	1565	119	1.18	0.733	0.023	0.0763	0.0016	0.67	0.0697	0.0016	558	17	474	10	919	47	52
066-58	350	40	0.52	1.209	0.042	0.1143	0.0024	0.61	0.0768	0.0021	805	28	697	15	1115	55	63
066-60	1935	113	2.20	0.640	0.019	0.0582	0.0012	0.69	0.0796	0.0017	502	15	365	8	1188	42	31

Analyses not used

Table 14 (cont.) U-Th-Pb isotopic compositions of zircon grains extracted from sample Q066 of the quartzites located within the Kliprand domal structure.

	Concentration			Ratios							Ages [Ma]						Conc.
Spot no.	U [ppm][a]	Pb [ppm][a]	Th/U[a]	$^{207}Pb/^{235}U$[b]	2 s[d]	$^{206}Pb/^{238}U$[b]	2 s[d]	rho[c]	$^{207}Pb/^{206}Pb$[e]	2 s[d]	$^{207}Pb/^{235}U$	2 s	$^{206}Pb/^{238}U$	2 s	$^{207}Pb/^{206}Pb$	2 s	%
Q066																	
066-61	4404	86	3.01	0.229	0.008	0.0196	0.0004	0.62	0.0851	0.0023	210	7	125	3	1317	53	9
066-62	2124	186	0.14	0.832	0.026	0.0875	0.0018	0.67	0.0690	0.0016	615	19	541	11	898	47	60
066-63	2744	208	0.47	0.709	0.022	0.0759	0.0016	0.66	0.0678	0.0016	544	17	471	10	862	49	55
066-64	4274	168	1.47	0.383	0.013	0.0392	0.0008	0.61	0.0708	0.0019	329	11	248	5	951	56	26
066-65	1313	178	0.58	1.432	0.045	0.1356	0.0028	0.66	0.0766	0.0018	902	28	820	17	1110	47	74
066-66	1335	161	0.48	1.259	0.037	0.1207	0.0025	0.70	0.0756	0.0016	827	24	735	15	1085	42	68
066-67	3204	235	0.04	0.843	0.025	0.0734	0.0015	0.70	0.0832	0.0018	621	18	457	9	1274	41	36
066-68	996	136	0.88	1.446	0.043	0.1363	0.0028	0.69	0.0770	0.0016	908	27	824	17	1120	43	74
066-69	3744	231	0.04	0.516	0.015	0.0616	0.0013	0.69	0.0608	0.0013	423	13	385	8	632	47	61
066-70	6632	79	2.32	0.130	0.005	0.0120	0.0003	0.56	0.0789	0.0025	124	5	77	2	1170	63	7
066-71	354	58	0.36	1.736	0.056	0.1650	0.0034	0.65	0.0763	0.0019	1022	33	984	21	1103	49	89
066-73	490	51	3.30	1.120	0.036	0.1041	0.0022	0.66	0.0780	0.0019	763	24	639	13	1147	48	56
066-74	2468	265	0.08	0.986	0.030	0.1075	0.0022	0.68	0.0666	0.0015	697	21	658	14	824	46	80
066-75	309	46	0.52	1.636	0.058	0.1483	0.0032	0.60	0.0800	0.0023	984	35	891	19	1197	56	74
066-76	3285	250	0.17	0.710	0.021	0.0762	0.0016	0.69	0.0676	0.0015	545	16	473	10	857	45	55
066-77	3757	124	0.18	0.361	0.011	0.0329	0.0007	0.66	0.0795	0.0019	313	10	209	4	1185	47	18
066-78	2616	207	0.35	0.744	0.023	0.0791	0.0016	0.66	0.0682	0.0016	565	18	491	10	876	49	56
066-79	2884	149	0.18	0.454	0.015	0.0518	0.0011	0.65	0.0635	0.0015	380	12	326	7	725	51	45
066-80	4399	179	0.44	0.361	0.012	0.0407	0.0009	0.62	0.0643	0.0017	313	11	257	5	750	56	34
066-81	1355	199	1.01	1.481	0.047	0.1470	0.0031	0.66	0.0731	0.0017	923	29	884	18	1016	48	87
066-82	1485	188	0.24	1.312	0.039	0.1265	0.0026	0.70	0.0753	0.0016	851	25	768	16	1075	43	71
066-83	1794	230	0.23	1.294	0.039	0.1280	0.0027	0.69	0.0733	0.0016	843	25	777	16	1023	44	76
066-84	2862	196	0.09	0.597	0.019	0.0684	0.0014	0.66	0.0633	0.0015	475	15	427	9	719	50	59
066-85	1110	117	1.26	1.128	0.034	0.1056	0.0022	0.69	0.0775	0.0017	767	23	647	13	1134	43	57
066-86	443	78	0.84	1.923	0.063	0.1761	0.0037	0.64	0.0792	0.0020	1089	36	1045	22	1178	50	89
066-87	603	109	0.20	2.014	0.064	0.1814	0.0038	0.66	0.0805	0.0019	1120	35	1075	23	1210	46	89
066-88	1901	252	0.07	1.346	0.041	0.1324	0.0027	0.69	0.0738	0.0016	866	26	801	17	1035	44	77
066-89	5023	166	0.32	0.402	0.012	0.0330	0.0007	0.67	0.0885	0.0020	343	11	209	4	1392	44	15
066-90	4966	220	0.08	0.497	0.016	0.0443	0.0009	0.66	0.0813	0.0019	410	13	280	6	1229	46	23
066-91	3606	152	0.17	0.338	0.010	0.0421	0.0009	0.69	0.0582	0.0013	295	9	266	6	537	48	50
066-92	1512	111	2.59	0.803	0.028	0.0733	0.0016	0.62	0.0795	0.0021	599	21	456	10	1183	53	39
066-93	1701	103	2.87	0.728	0.024	0.0607	0.0013	0.64	0.0870	0.0022	555	18	380	8	1361	49	28

Analyses not used

Table 14 (cont.) U-Th-Pb isotopic compositions of zircon grains extracted from sample Q066 of the quartzites located within the Kliprand domal structure.

	Concentration				Ratios						Ages [Ma]						Conc.
Spot no.	U [ppm][a]	Pb [ppm][a]	Th/U[a]	$^{207}Pb/^{235}U$[b]	2 s[d]	$^{206}Pb/^{238}U$[b]	2 s[d]	rho[c]	$^{207}Pb/^{206}Pb$[e]	2 s[d]	$^{207}Pb/^{235}U$	2 s	$^{206}Pb/^{238}U$	2 s	$^{207}Pb/^{206}Pb$	2 s	%
Q066																	
066-94	1006	151	1.01	1.554	0.048	0.1505	0.0031	0.67	0.0749	0.0017	952	30	904	19	1065	46	85
066-95	2543	274	0.55	1.137	0.036	0.1077	0.0023	0.67	0.0765	0.0018	771	24	659	14	1109	46	59
066-96	3235	122	4.27	0.415	0.013	0.0376	0.0008	0.66	0.0799	0.0019	352	11	238	5	1194	47	20
066-97	3246	115	8.13	0.447	0.014	0.0355	0.0007	0.66	0.0915	0.0022	375	12	225	5	1457	45	15
066-100	1429	169	0.28	1.255	0.038	0.1184	0.0025	0.69	0.0768	0.0017	825	25	722	15	1117	43	65
066-101	3412	192	1.27	0.479	0.015	0.0563	0.0012	0.67	0.0617	0.0014	398	12	353	7	664	50	53
066-102	635	98	1.82	1.751	0.056	0.1547	0.0033	0.66	0.0821	0.0020	1028	33	927	20	1248	47	74
066-103	990	96	1.27	1.026	0.033	0.0965	0.0020	0.66	0.0772	0.0019	717	23	594	13	1125	48	53
066-104	2148	121	1.73	0.641	0.023	0.0566	0.0012	0.61	0.0823	0.0023	503	18	355	8	1251	54	28
066-105	3260	149	3.57	0.448	0.015	0.0458	0.0010	0.64	0.0709	0.0018	376	12	289	6	956	51	30
066-106	2829	280	0.17	0.909	0.028	0.0991	0.0021	0.69	0.0666	0.0015	656	20	609	13	824	46	74
066-107	4009	144	1.19	0.339	0.011	0.0358	0.0008	0.65	0.0687	0.0017	297	10	227	5	890	51	25
066-108	4329	202	0.26	0.402	0.012	0.0467	0.0010	0.69	0.0624	0.0014	343	10	294	6	687	47	43
066-109	3325	91	3.31	0.371	0.015	0.0273	0.0006	0.55	0.0984	0.0032	320	13	174	4	1593	62	11
066-110	3215	169	0.50	0.638	0.020	0.0527	0.0011	0.67	0.0879	0.0021	501	16	331	7	1380	45	24
066-111	893	167	0.54	2.003	0.064	0.1873	0.0040	0.67	0.0776	0.0018	1117	35	1107	23	1136	47	97
066-112	1369	173	0.36	1.298	0.040	0.1266	0.0027	0.69	0.0743	0.0017	845	26	768	16	1051	45	73
066-113	3305	125	1.95	0.439	0.015	0.0379	0.0008	0.63	0.0839	0.0023	369	13	240	5	1289	52	19
066-115	2250	201	0.52	0.908	0.029	0.0893	0.0019	0.67	0.0737	0.0017	656	21	552	12	1033	47	53

Analyses not used

[a]U and Pb concentrations and Th/U ratios are calculated relative to GJ-1 reference zircon.

[b]Corrected for background and within-run Pb/U fractionation and normalized to reference zircon GJ-1 (isotope dilution thermal ionization mass spectrometry values/measured value); $^{207}Pb/^{235}U$ calculated using ($^{207}Pb/^{206}Pb$)/($^{238}U/^{206}Pb$ * 1/137.88).

[c]Rho is the error correlation defined as the quotient of the propagated errors of the $^{206}Pb/^{238}U$ and the $^{207}/^{235}U$ ratio.

[d]Quadratic addition of within-run errors (2 SD) and daily reproducibility of GJ-1 (2 SD).

[e]Corrected for mass bias by normalizing to GJ-1 reference zircon (~0.6 per atomic mass unit) and common Pb using the model Pb composition of Stacey and Kramers [1975].

7.4 Ibequas granite

All of the zircon grains extracted from the Ibequas granite varies from 10 to 120 µm in length, and comrpise both well rounded grains, as seen in cathodoluminescence (CL) images (Figure 7-7). The cores of the majority of the zircon grains generally comprise bright CL areas surrounded by dark oscillatory zoned rims (Figure 7-7). These bright cores are well displayed in zircon grains 1, 2, 6, 8, 10, 13, 14 and 21 where they are commonly lobate and elongate in shape (Figure 7-7). Grain spot 8 has sector zoning at the top portion of the rim (Figure 7-7). In contrast to the features mentioned above, zircons 17-19 are characterised by dark cores, with thin bright metamorphic rims surrounding these cores (Figure 7-7).

Twenty-four analyses of 21 zircon grains were obtained from sample IG30 (Table 15); the bulk of the analysed spots are from the cores with the oscillatory rims also measured in places. The bright zircon cores have low U contents of 217-865 ppm (Table 15) with the dark cores characterised by relatively high U contents (1067-1484 ppm; Table 15). The Th/U ratio of the bright cores ranges from 0.02 (This ratio is definitely considered to be metamorphic) to 0.55, whilst the Th/U ratios of the dark cores ranges from 0.01 (This ratio is definitely considered to be metamorphic, so these zircons have seen some previous action) to 0.23 (Table 15); the ratios in addition to the oscillatory and sector zoning (Figure 7-7) suggest that the zircon grains are a mixture of metamorphic and magmatic zircons. Eighty percent of the U-Pb isotopic analyses yield concordant ages with 20% being discordant (Figure 7-8a); suggesting that the isotopic system has not been excessively disturbed. These data are unique in that there are two highly concordant age populations (Figure 7-8b, c), with an older population (Figure 7-8b) and a younger (Figure 7-8c) highly concordant population of zircons, of which the latter may represent a metamorphic overprint or the crystallisation age of the granite. The analyses (Table 15) for the older concordant population gave a weighted mean $^{207}Pb/^{206}Pb$ date of 1153 ± 4.8 Ma (MSWD = 1.09; Figure 7-8b), whilst the younger concordant population gave a weighted mean $^{207}Pb/^{206}Pb$ date of 1067 ± 8 Ma (MSWD = 0.27; Figure 7-8c). The $^{207}Pb/^{206}Pb$ date of 1067 ± 8 Ma largely overlaps with the age found in the biotite-rich pink gneiss and is the age of high-T metamorphism there. Grain spot 5, 9, 18, 19 and 21 where analysed on dark zoned areas (Figure 7-7). The older ages are from bright, generally poorly to unzoned cores suggesting some inheritance. The younger ages are from generally unzoned, dark rims or generally unzoned zircons

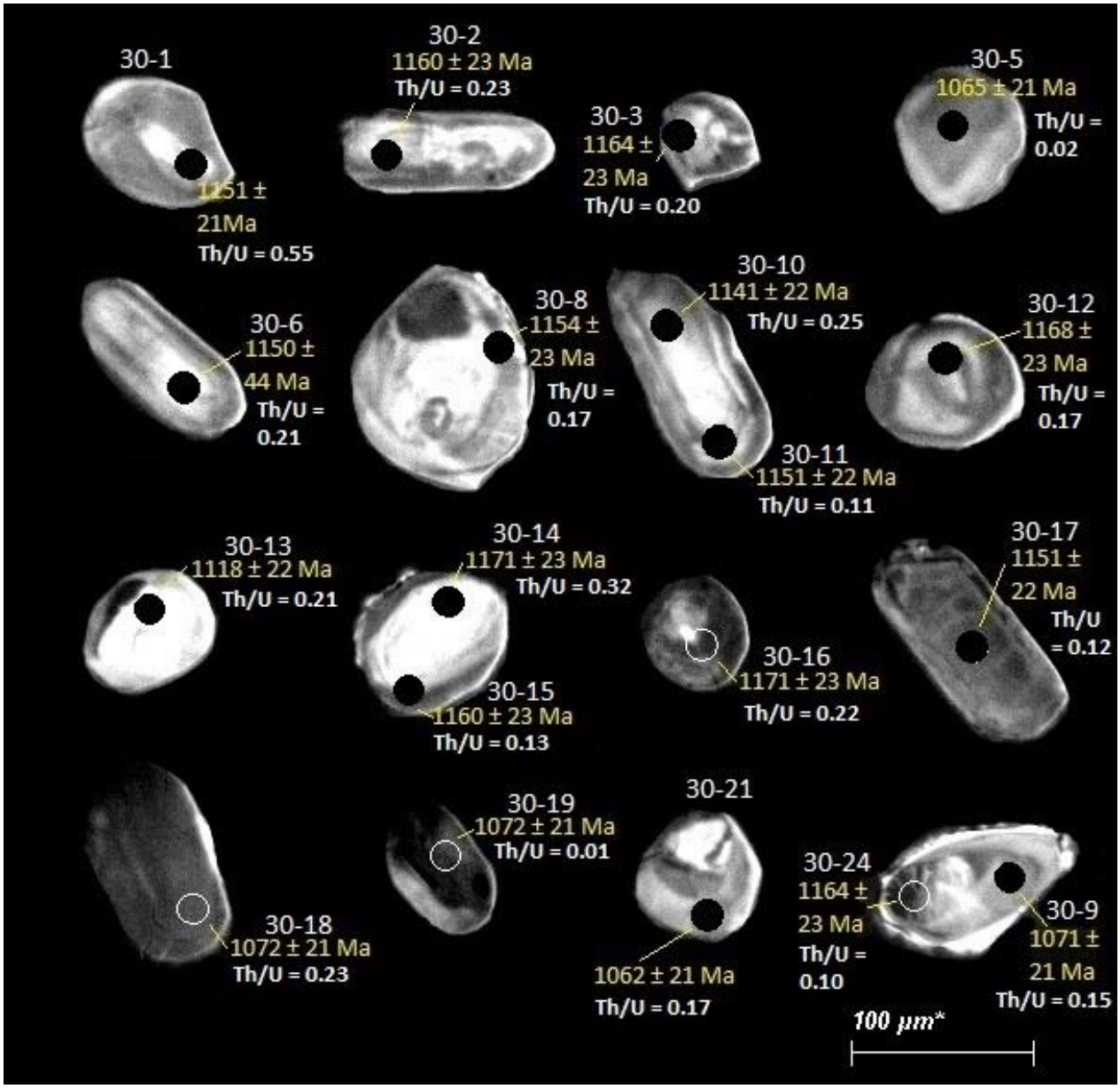

Figure 7-7. CL images of zircons from sample IG30. The position of the laser spot is represented by black circles (they are not representative of the actual 30µm spot). Labels indicate analyses number and the determined $^{206}Pb/^{238}U$ ages.

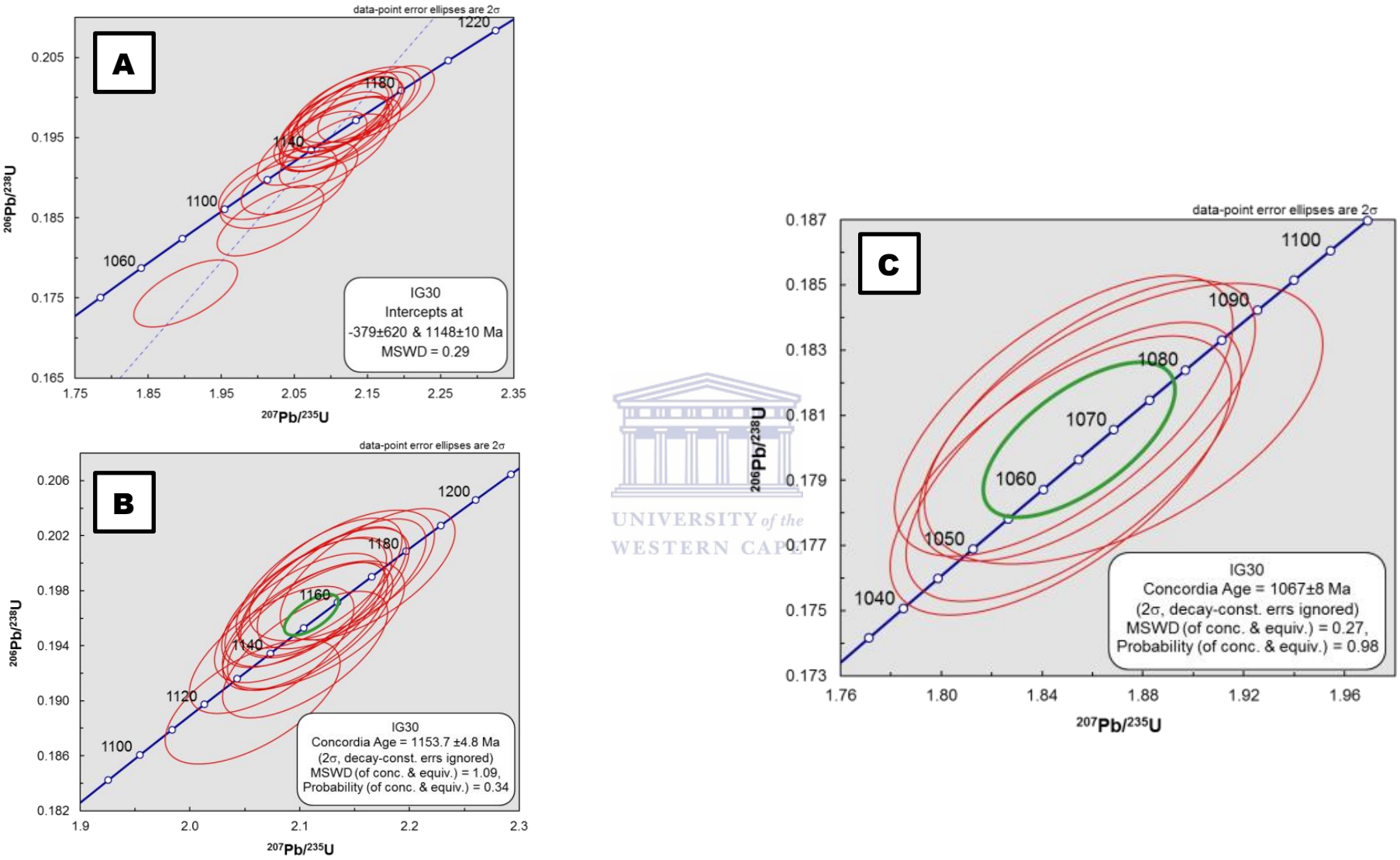

Figure 7-8. (A) U-Pb concordia plot of sample IG30. The majority of the data plots below the Concordia curve . (B) Enlarged area where data plots on the concordia curve for the older set of ages. Concordia plot for near-concordant analyses were used to calculate the weighted mean $^{207}Pb/^{206}Pb$ ages of sample IG30. Unfilled error ellipses are excluded in the weighted mean age. Confidence limits for the error ellipses are 2σ. (C) Enlarged concordia plot of the younger concordant analyses.

Table 14. U-Th-Pb isotopic compositions of zircon grains extracted from sample IG30 of the Ibequas granite located in the Kliprand domal structure.

		Concentration			Ratios							Ages [Ma]						Conc.
	Spot no.	U [ppm][a]	Pb [ppm][a]	Th/U[a]	$^{207}Pb/^{235}U$[b]	2 s[d]	$^{206}Pb/^{238}U$[b]	2 s[d]	rho[c]	$^{207}Pb/^{206}Pb$[e]	2 s[d]	$^{207}Pb/^{235}U$	2 s	$^{206}Pb/^{238}U$	2 s	$^{207}Pb/^{206}Pb$	2 s	%
	IG30																	
Analyses used	30-1	463	91	0.55	2.105	0.061	0.1954	0.0038	0.67	0.0781	0.0017	1150	34	1151	22	1150	43	100
	30-2	444	87	0.23	2.104	0.061	0.1971	0.0038	0.67	0.0774	0.0017	1150	34	1160	23	1132	43	102
	30-3	523	103	0.20	2.122	0.062	0.1980	0.0038	0.67	0.0777	0.0017	1156	34	1164	23	1140	43	102
	30-5	865	155	0.02	1.852	0.054	0.1796	0.0035	0.66	0.0748	0.0016	1064	31	1065	21	1064	44	100
	30-6	413	82	0.21	2.138	0.063	0.1985	0.0039	0.66	0.0781	0.0017	1161	34	1167	23	1150	44	102
	30-8	386	76	0.17	2.100	0.063	0.1960	0.0038	0.65	0.0777	0.0018	1149	35	1154	23	1139	46	101
	30-9	553	100	0.15	1.872	0.065	0.1807	0.0035	0.56	0.0751	0.0021	1071	37	1071	21	1072	57	100
	30-10	371	72	0.25	2.074	0.061	0.1937	0.0038	0.66	0.0777	0.0017	1140	34	1141	22	1138	44	100
	30-11	721	141	0.11	2.109	0.061	0.1954	0.0038	0.67	0.0783	0.0017	1152	34	1151	22	1154	43	100
	30-12	666	132	0.17	2.118	0.062	0.1986	0.0039	0.67	0.0774	0.0017	1155	34	1168	23	1130	43	103
	30-13	250	47	0.21	2.027	0.066	0.1893	0.0037	0.60	0.0777	0.0020	1125	37	1118	22	1138	52	98
	30-14	217	43	0.32	2.162	0.065	0.1992	0.0039	0.65	0.0787	0.0018	1169	35	1171	23	1165	45	101
	30-15	465	92	0.13	2.108	0.062	0.1972	0.0038	0.66	0.0775	0.0017	1151	34	1160	23	1135	44	102
	30-16	528	105	0.22	2.138	0.069	0.1991	0.0039	0.60	0.0779	0.0020	1161	37	1171	23	1144	51	102
	30-17	1484	290	0.12	2.112	0.068	0.1955	0.0038	0.61	0.0784	0.0020	1153	37	1151	22	1156	51	100
	30-18	1150	208	0.23	1.858	0.055	0.1808	0.0035	0.66	0.0745	0.0016	1066	31	1072	21	1055	44	102
	30-19	1067	193	0.01	1.849	0.055	0.1810	0.0035	0.66	0.0741	0.0017	1063	32	1072	21	1044	45	103
	30-21	506	91	0.17	1.847	0.055	0.1792	0.0035	0.65	0.0748	0.0017	1063	32	1062	21	1063	46	100
	30-24	705	139	0.10	2.122	0.063	0.1978	0.0039	0.65	0.0778	0.0018	1156	35	1164	23	1142	45	102
Analyses not used	30-4	516	100	0.14	2.105	0.061	0.1934	0.0038	0.67	0.0790	0.0017	1150	34	1140	22	1171	43	97
	30-7	652	120	0.13	2.017	0.059	0.1846	0.0036	0.66	0.0792	0.0018	1121	33	1092	21	1178	44	93
	30-22	910	160	0.15	1.901	0.058	0.1756	0.0034	0.64	0.0786	0.0018	1082	33	1043	20	1161	46	90
	30-23	377	71	0.15	2.035	0.071	0.1882	0.0037	0.56	0.0784	0.0023	1127	39	1111	22	1158	57	96
	30-25	684	130	0.18	2.057	0.065	0.1899	0.0037	0.62	0.0786	0.0020	1135	36	1121	22	1161	49	97

[a]U and Pb concentrations and Th/U ratios are calculated relative to GJ-1 reference zircon.

[b]Corrected for background and within-run Pb/U fractionation and normalized to reference zircon GJ-1 (isotope dilution thermal ionization mass spectrometry values/measured value); $^{207}Pb/^{235}U$ calculated using ($^{207}Pb/^{206}Pb$)/($^{238}U/^{206}Pb$ * 1/137.88).

[c]Rho is the error correlation defined as the quotient of the propagated errors of the $^{206}Pb/^{238}U$ and the $^{207}/^{235}U$ ratio.

[d]Quadratic addition of within-run errors (2 SD) and daily reproducibility of GJ-1 (2 SD).

[e]Corrected for mass bias by normalizing to GJ-1 reference zircon (~0.6 per atomic mass unit) and common Pb using the model Pb composition of Stacey and Kramers [1975].

7.5 Charnockite

Many zircons separated from sample C144 are subhedral to anhedral (Figure 7-9); are very long and elongate (with variable length of ±20-250µm for both comcordant and discordant grain spots) and poorly zoned with a dull luminosity which is fairly typical of metamorphic zircon. Zircons 9, 17, 18 and 22 have prismatic cores (Figure 7-9). These cores are bright with irregularly shaped sector zoning. Bright unzoned cores were too thin to be analysed. There are, however, grains that are rounded and irregular with no significant rim and core but are characterised by a dull luminosity and lack of zonation (e.g. grains 10 and 11, Figure 7-9). 20 analyses were obtained from 20 zircon grains whereby clear Pb-loss is evident (highly variable Pb contents of 62-220 ppm). It is difficult to confirm whether there is any pattern with regard to the ages and the type of zircon, as the bright faintly zoned areas (zircons 3, 6, 9 and 17; Figure 7-9) have ages ranging from 1066 – 1070Ma, whilst the dark grey shaded areas shows both the youngest (1058 Ma (spot 11), 1050 Ma (spot 15) and 1053 Ma (spot 24)) and oldest (1073 Ma (spot18) and 1079 Ma (spot 20)) ages.

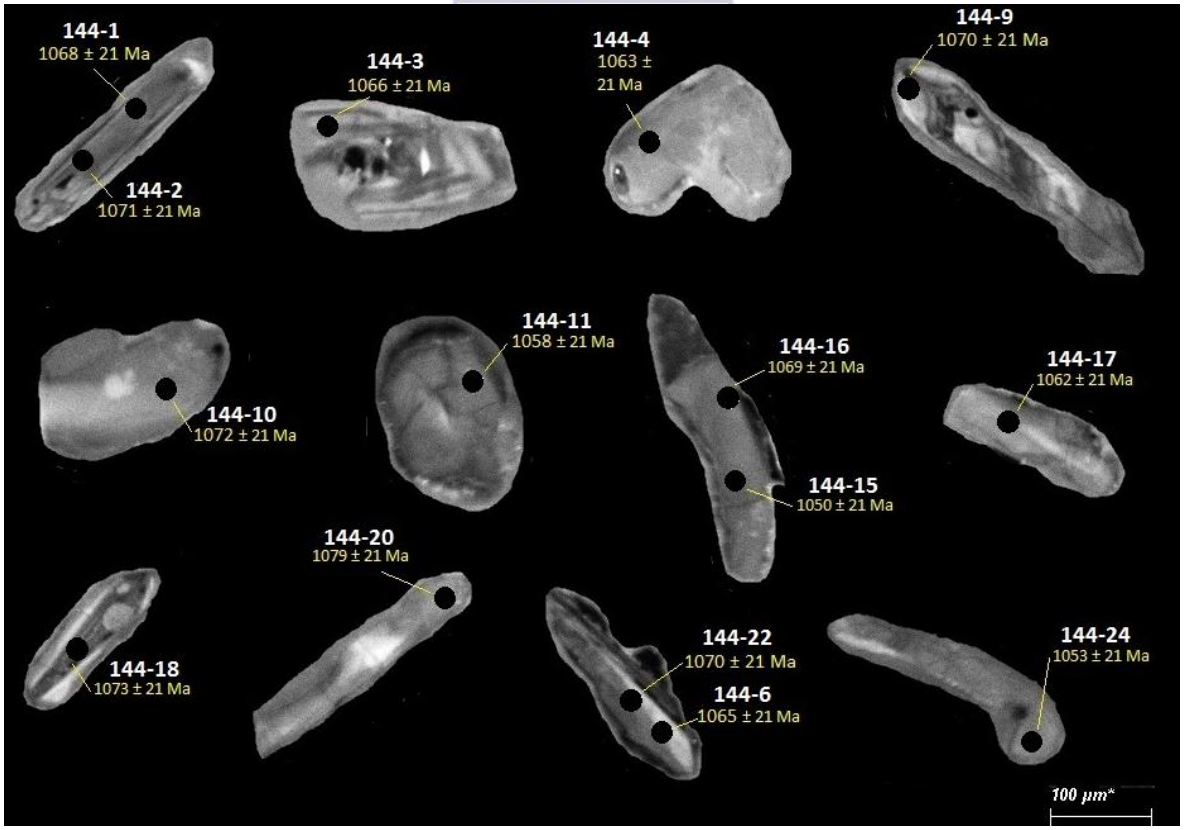

Figure 7-9. CL images of zircons from sample C144. The position of the laser spot is represented by black circles (they are not representative of the actual 30µm spot). Labels indicate analyses number and the determined $^{206}Pb/^{238}U$ ages.

Except for spots 1 (1223ppm), 2 (1122ppm) and 20 (917ppm), all the analysed data have relatively low U contents ranging between 173-675 ppm (Table 16). The Th/U ratios range between 0.17-0.52 (Table 16) which is almost identical to magmatic rocks with hardly any metamorphic effect. Most of the U-Pb analyses yielded ages that are highly concordant (99% concordance) with an upper intercept age 1065 ± 13 Ma (Figure 7-10a) and a concordia age (Figure 7-10b) of 1066 ± 5 Ma. The most concordant ages give ages around 1050 -1079 Ma

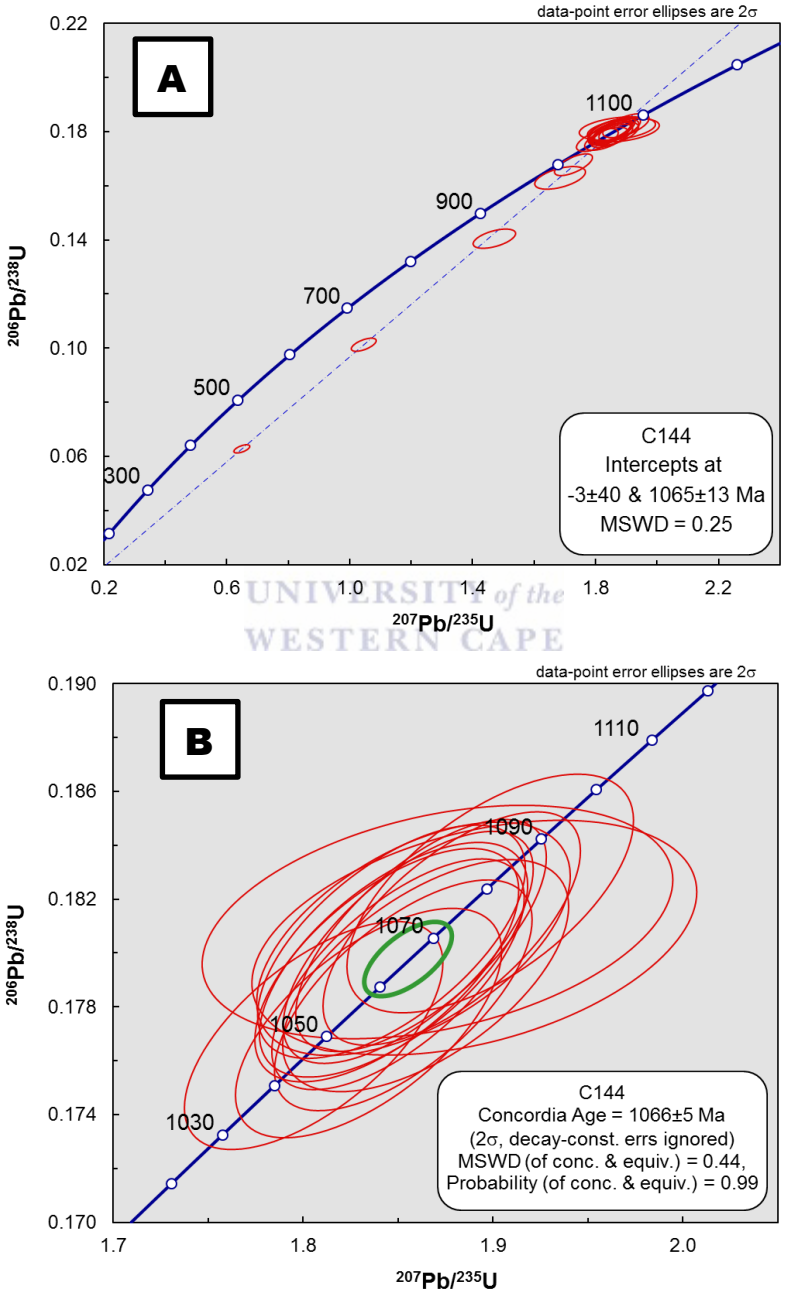

Figure 7-10. (A) U-Pb concordia plot of sample C144. Has almost no discordance with an upper intercept age of 1065 ± 13 Ma. The granite has experienced recent lead loss. (B) Enlarged area where data plots on the concordia curve. Concordia plot for near-concordant analyses are used to calculated the weighted mean $^{207}Pb/^{206}Pb$ age of sample C144. Unfilled error ellipses are excluded in the weighted mean age. Confidence limits for the error ellipses are 2σ.

Table 15. U-Th-Pb isotopic compositions of zircon grains extracted from sample C144 of the charnockite located in the Kliprand domal structure.

		Concentration			Ratios							Ages [Ma]						Conc.
	Spot no.	U [ppm][a]	Pb [ppm][a]	Th/U[a]	$^{207}Pb/^{235}U$[b]	2 s[d]	$^{206}Pb/^{238}U$[b]	2 s[d]	rho[c]	$^{207}Pb/^{206}Pb$[e]	2 s[d]	$^{207}Pb/^{235}U$	2 s	$^{206}Pb/^{238}U$	2 s	$^{207}Pb/^{206}Pb$	2 s	%
	C144																	
Analyses used	144-4	481	86	0.26	1.850	0.054	0.1792	0.0035	0.67	0.0749	0.0016	1063	31	1063	21	1065	44	100
	144-1	1223	220	0.42	1.855	0.054	0.1802	0.0035	0.67	0.0747	0.0016	1065	31	1068	21	1060	43	101
	144-2	1122	203	0.43	1.862	0.054	0.1807	0.0035	0.67	0.0748	0.0016	1068	31	1071	21	1062	43	101
	144-3	589	106	0.31	1.848	0.058	0.1798	0.0036	0.63	0.0746	0.0018	1063	33	1066	21	1056	49	101
	144-6	345	62	0.27	1.844	0.057	0.1796	0.0035	0.64	0.0745	0.0018	1061	33	1065	21	1055	48	101
	144-9	443	80	0.17	1.858	0.067	0.1805	0.0035	0.54	0.0747	0.0023	1066	39	1070	21	1059	61	101
	144-10	505	91	0.20	1.878	0.055	0.1809	0.0035	0.66	0.0753	0.0017	1073	32	1072	21	1077	44	100
	144-11	478	85	0.27	1.853	0.055	0.1784	0.0035	0.66	0.0753	0.0017	1064	32	1058	21	1077	45	98
	144-15	675	119	0.19	1.806	0.056	0.1769	0.0035	0.64	0.0740	0.0018	1047	32	1050	21	1042	48	101
	144-16	495	89	0.20	1.847	0.058	0.1804	0.0035	0.63	0.0742	0.0018	1062	33	1069	21	1048	49	102
	144-17	663	119	0.37	1.865	0.062	0.1792	0.0035	0.60	0.0755	0.0020	1069	35	1062	21	1081	53	98
	144-18	173	31	0.52	1.871	0.101	0.1812	0.0035	0.36	0.0749	0.0038	1071	58	1073	21	1066	101	101
	144-20	917	167	0.29	1.899	0.062	0.1822	0.0036	0.61	0.0756	0.0019	1081	35	1079	21	1084	51	100
	144-22	347	63	0.30	1.890	0.096	0.1806	0.0036	0.39	0.0759	0.0035	1078	55	1070	21	1093	93	98
	144-24	568	101	0.24	1.834	0.057	0.1774	0.0035	0.63	0.0750	0.0018	1058	33	1053	21	1069	49	99
Analyses not used	144-12	1107	186	0.47	1.728	0.050	0.1678	0.0033	0.67	0.0747	0.0016	1019	30	1000	20	1060	44	94
	144-13	317	52	0.35	1.685	0.068	0.1629	0.0034	0.52	0.0750	0.0026	1003	40	973	20	1068	69	91
	144-14	554	78	0.27	1.471	0.056	0.1405	0.0029	0.54	0.0759	0.0025	918	35	847	17	1093	65	78
	144-19	1485	150	0.48	1.046	0.033	0.1013	0.0020	0.62	0.0749	0.0019	727	23	622	12	1065	50	58
	144-23	3287	206	0.24	0.649	0.021	0.0628	0.0012	0.61	0.0749	0.0019	508	17	393	8	1067	52	37

[a]U and Pb concentrations and Th/U ratios are calculated relative to GJ-1 reference zircon.

[b]Corrected for background and within-run Pb/U fractionation and normalized to reference zircon GJ-1 (isotope dilution thermal ionization mass spectrometry values/measured value); $^{207}Pb/^{235}U$ calculated using ($^{207}Pb/^{206}Pb$)/($^{238}U/^{206}Pb$ * 1/137.88).

[c]Rho is the error correlation defined as the quotient of the propagated errors of the $^{206}Pb/^{238}U$ and the $^{207}/^{235}U$ ratio.

[d]Quadratic addition of within-run errors (2 SD) and daily reproducibility of GJ-1 (2 SD).

[e]Corrected for mass bias by normalizing to GJ-1 reference zircon (~0.6 per atomic mass unit) and common Pb using the model Pb composition of Stacey and Kramers [1975].

7.6 Gabbro-norite

The CL images of zircons from the gabbro-norite have no distinct zonation (Figure 7-11). Most of the zircons of sample G162 are subhedral to anhedral, ranging in length from 40-230µm, and are well-rounded with locally slightly elongated grains (Figure 7-11). The cathodoluminescence imaging revealed that the dark cores of the zircon grains are metamict (cores with patchy textures). The majority of these cores have dark overgrowths which are clearly displayed in spots 8 and 12 (Figure 7-11). The bulk of the analysed spots are from the overgrowths (Figure 7-11) seeing that these are the least altered compared to the core. 21 analyses were obtained from 22 zircon grains whereby high U contents (average U content of > 1300 ppm) and Pb concentrations of 113-397ppm clearly signify Pb loss (Table 17). Pb loss in zircon grains is commonly related to major thermal events (Hoskin and Black, 2000). Spots 8 (Th/U=0.12), 12 (Th/U=0.13), 13 (Th/U=0.15) and 18 (Th/U=0.13) have low Th/U ratios, quite near what may be considered metamorphic. Only spot 18 gives a truly concordant age of 1064 Ma, virtually synchronous with ages for the peak high-T metamorphism from the other lithologies. Spot 4 (age of 1002 Ma) has a low, metamorphic Th/U ratio (0.07) consistent with metamorphism. Spot 5 has a very high Th/U ratio (1.22) and a low age 599Ma, possibly Pan-African metamorphism.

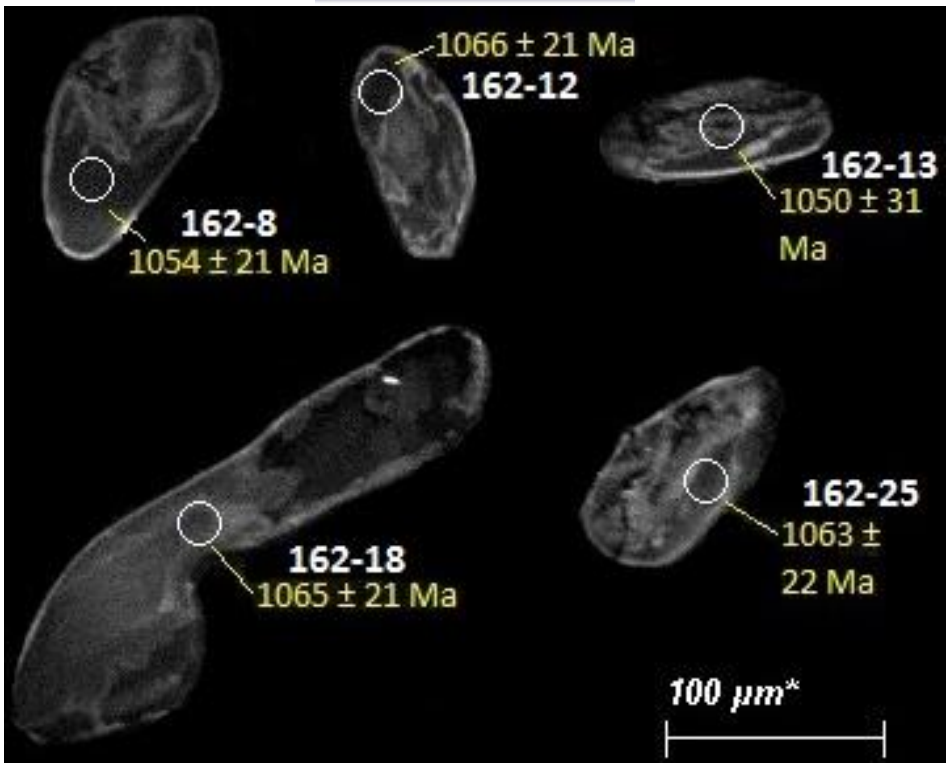

Figure 7-11. CL images of zircons from sample G162. The position of the laser spot is represented by white circles (due to these zircons being dark) they are not representative of the actual 30µm spot). Labels indicate analyses number and the determined $^{206}Pb/^{238}U$ ages.

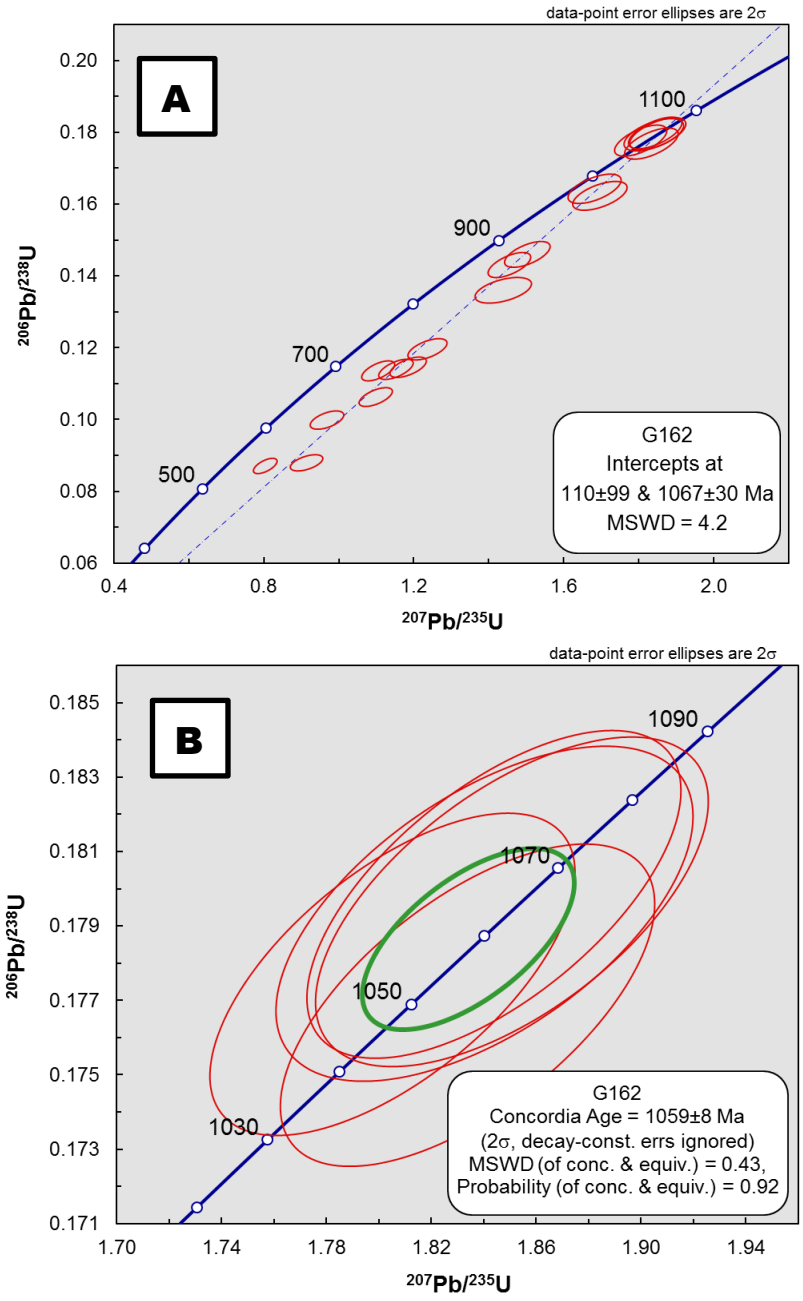

Figure 7-12. (A) U-Pb concordia plot of sample G162. The majority of the data plots below the concordia curve where a straight line fitted through the discordant zircons back to the concordia curve (known as a discordia line) gave upper (1067 ± 30Ma) and lower (110 ± 99Ma) intercept ages. (B) Enlarged area where data plots on the concordia curve. A concordia plot for near-concordant analyses was used to calculate the weighted mean $^{207}Pb/^{206}Pb$ age of G162. Unfilled error ellipses are excluded in the determination of the weighted mean age. Confidence limits for the error ellipses are 2σ.

Due to the Pb loss and high U values many analyses are discordant defining a discordant line (Figure 7-12a) suggesting Pb-loss in recent times with only 5 of the 21 analyses concordant (Figure 7-12b). A regression line of all the data points gave an upper intercept age of 1067±30Ma and a lower intercept date of 110±99Ma (Figure 7-12a).

For the calculation of a date the most concordant values (98-102% conc.) were used. These analyses give a weighted mean $^{207}Pb/^{206}Pb$ date of 1059 ± 8 Ma (MSWD = 0.43; Figure 7-12b).

Table 16. U-Th-Pb isotopic compositions of zircon grains extracted from sample G162 of the gabbro-norite located in the Kliprand domal structure.

	Concentration				Ratios							Ages [Ma]						Conc.
	Spot no.	U [ppm][a]	Pb [ppm][a]	Th/U[a]	$^{207}Pb/^{235}U$[b]	2 s[d]	$^{206}Pb/^{238}U$[b]	2 s[d]	rho[c]	$^{207}Pb/^{206}Pb$[e]	2 s[d]	$^{207}Pb/^{235}U$	2 s	$^{206}Pb/^{238}U$	2 s	$^{207}Pb/^{206}Pb$	2 s	%
	G162																	
Analyses used	162-8	1567	279	0.12	1.805	0.057	0.1777	0.0035	0.63	0.0737	0.0018	1047	33	1054	21	1033	49	102
	162-12	1599	288	0.13	1.844	0.058	0.1799	0.0036	0.63	0.0744	0.0018	1061	34	1066	21	1051	49	101
	162-13	1073	190	0.15	1.834	0.058	0.1769	0.0035	0.63	0.0752	0.0019	1058	34	1050	21	1074	50	98
	162-18	1108	199	0.13	1.851	0.061	0.1797	0.0036	0.61	0.0747	0.0020	1064	35	1065	21	1061	53	100
	162-25	585	105	0.44	1.840	0.065	0.1793	0.0037	0.58	0.0744	0.0021	1060	37	1063	22	1053	58	101
Analyses not used	162-1	1401	197	0.29	1.445	0.047	0.1409	0.0028	0.62	0.0744	0.0019	908	29	850	17	1052	51	81
	162-2	1178	208	0.12	1.844	0.059	0.1769	0.0035	0.63	0.0756	0.0019	1061	34	1050	21	1085	50	97
	162-3	1353	188	0.12	1.391	0.044	0.1386	0.0028	0.63	0.0728	0.0018	885	28	837	17	1008	50	83
	162-4	946	155	0.07	1.682	0.058	0.1643	0.0033	0.59	0.0743	0.0021	1002	34	981	20	1049	56	93
	162-5	4566	397	1.22	0.804	0.026	0.0871	0.0017	0.62	0.0670	0.0017	599	19	538	11	837	52	64
	162-6	1521	218	0.16	1.455	0.047	0.1430	0.0029	0.63	0.0738	0.0018	912	29	862	17	1035	50	83
	162-7	830	113	0.20	1.439	0.062	0.1360	0.0029	0.50	0.0767	0.0028	905	39	822	18	1114	74	74
	162-9	1630	173	0.36	1.099	0.036	0.1063	0.0021	0.61	0.0750	0.0020	753	25	651	13	1068	53	61
	162-10	2362	268	0.74	1.105	0.036	0.1136	0.0023	0.62	0.0706	0.0018	756	25	693	14	945	52	73
	162-14	1606	183	0.55	1.152	0.038	0.1140	0.0023	0.62	0.0733	0.0019	778	25	696	14	1023	52	68
	162-16	1305	149	0.28	1.185	0.040	0.1146	0.0023	0.60	0.0750	0.0020	794	27	699	14	1069	54	65
	162-19	1376	165	0.15	1.237	0.043	0.1196	0.0024	0.59	0.0750	0.0021	817	28	728	15	1069	56	68
	162-20	1305	212	0.37	1.696	0.059	0.1623	0.0033	0.58	0.0758	0.0022	1007	35	970	20	1090	57	89
	162-21	1033	151	0.25	1.503	0.050	0.1460	0.0029	0.61	0.0747	0.0020	932	31	879	18	1059	53	83
	162-22	1914	168	0.33	0.914	0.035	0.0879	0.0018	0.54	0.0754	0.0025	659	26	543	11	1079	65	50
	162-23	2021	202	0.24	0.968	0.037	0.0998	0.0021	0.55	0.0704	0.0022	688	26	613	13	939	65	65

Chapter 8 : Radioactive isotope geochemistry

8.1 Introduction

All the age dates used in the calculations below were taken from the geochronological age data obtained in this study except for the metapelite (1111 Ma) and streaky augen gneiss (1192 Ma) as these rocks have previously been dated by Moore (1989) (metapelite) and Macey et al. (2011) (streaky augen gneiss) respectively. Samples of metapelite were sent for dating, however, the metapelite (sample M103) only yielded zircons that were in the silt fraction (i.e., < 63 microns with most of them < 20 microns) and were, consequently, not amenable to analysis. Eight samples of both the magmatic (streaky augen gneiss, Ibequas granite, gabbro-norite and charnockite) and sedimentary (pink gneiss (biotite rich and poor varieties), quartzite, metapelite) rocks from the Kliprand domal structure were analysed for their Sr and Nd isotope compositions. Initial Sr and Nd isotope ratios for each sample have been calculated from measured $^{87}Sr/^{86}Sr$ and $^{143}Nd/^{144}Nd$ ratios. In addition, $^{87}Rb/^{86}Sr$ and $^{147}Sm/^{144}Nd$ ratios as well as the εNd(t) function was calculated. The εNd(t) function is a useful isotopic ratio which indicates the deviation of the $^{143}Nd/^{144}Nd$ value of the sample from that of CHUR (Chondritic Uniform Reservoir—DePaolo and Wasserburg, 1976) at the time "t" of emplacement or formation, of the rock (Bailie et al., 2010). A positive εNd(t) value suggests derivation from a depleted source (Bailie et al., 2010). On the other hand, a negative εNd(t) value would suggest that the magma originated from an enriched, or crustal-type provenance (Bailie et al., 2010). Another useful isotopic ratio is the $f^{Sm/Nd}$ factor, which is a fractionation factor and is the $^{147}Sm/^{144}Nd$ analogue of the εNd(t) ratio as it is a measure of Sm/Nd enrichment in a given reservoir relative to CHUR (Bailie et al., 2010). Positive $f^{Sm/Nd}$ values reflect derivation from an unfractionated primitive source, whereas negative $f^{Sm/Nd}$ values reflect derivation from a fractionated source (Bailie et al., 2010). The Nd model ages (T_{DM}), calculated using the model of Goldstein et al. (1984), refers to the time elapsed since the melt separated from a depleted mantle reservoir and is often interpreted as the time of a crust-forming event (Will et al. 2010). However, most rocks, especially metamorphosed rocks, have model ages which correspond to an 'average crustal residence age' as these rocks commonly contain components from different sources and different mantle extraction ages (Will et al. 2010).

8.2 Data interpretation

The gabbro-norite has an initial $^{143}Nd/^{144}Nd$ ratio of 0.511322, with a εNd value of +0.9918 (Table 18). The Initial $^{87}Sr/^{86}Sr$ ratio for the gabbro-norite is 0.7067 (Table 18). Both the initial $^{143}Nd/^{144}Nd$ values of the gabbro-norite sample clearly indicates that they are derived from an ocean island basaltic-like source (e.g. 0.512312-0.513095 from Rollinson, 1993) and $^{87}Sr/^{86}Sr$ values (e.g. 0.7027-0.7056 from Rollinson, 1993) . The gabbro-norite has a positive εNd(t) value of 0.99 (Table 18), this value is relatively close to 0 and so there is a small measure of an enriched (possibly crustal) component in the source, or it may reflect crustal contamination or a small degree of mixing with a more enriched source. In terms of the $f^{Sm/Nd}$ ratio of -0.397 (Table 18) the gabbronorite was derived from a relatively fractionated source.

The Ibequas granite has an initial $^{143}Nd/^{144}Nd$ ratio of 0.511273 and an initial $^{87}Sr/^{86}Sr$ ratio of 0.7064 (Table 18). The Ibequas granite clearly plots within the Bulk Silicate Earth field (Figure 8-1) at the base of the mantle array with the gabbro-norite slightly above this field at the base of the mantle array. The Ibequas granite has a slightly positive εNd(t) value of 0.24 (Table 18) indicating that the source was mildly depleted but not srongly so. An enriched component is also present; however, the strongly negative $f^{Sm/Nd}$ ratio of -0.524 (Table 18) indicates that this source was fractionated.

The streaky augen gneiss and pink gneiss are the only magmatic rock that plots above the upper crustal curve (Figure 8-1). This is mainly due to the high initial $^{87}Sr/^{86}Sr$ ratio of 0.7424 (Table 18) for the streaky augen gneiss, biotite rich pink gneiss (0.73661) and biotite-poor pink gneiss (0.73523). This high initial $^{87}Sr/^{86}Sr$ ratio is characteristic of a strong crustal influence. The streaky augen gneiss (-0.14) has a negative εNd(t) value (Table 18), which is only slightly negative and so a significant depleted component is present. The pink gneiss (biotite rich variety= 1.22 and biotite poor variety = 0.79) has slightly positive εNd(t) values (Table 18) indicating that the source was mildly depleted but not strongly so. Its likely source, when taken with the negative $f^{Sm/Nd}$ value (streaky augen gneiss = -0 .319, biotite rich pink gneiss = -0.380 and biotite poor pink gneiss = -0.337) is of a crustal source carrying some depleted signature.

The metapelite and quartzite have virtually the same initial $^{143}Nd/^{144}Nd$ ratio of 0.51120 (Table 18). The initial $^{87}Sr/^{86}Sr$ ratios, for the metapelite and quartzite are not that similar and ranges from 0.73142-0.76344 (Table 18). With such a high initial Sr value the quartzite has suffered anatectic events and had its isotopic ratios severely disturbed. These values are similar to that of the upper continental crustal (initial $^{87}Sr/^{86}Sr$ ratios = 0.71463-0.78662 and initial $^{143}Nd/^{144}Nd$ = 0.511843-0.512261) values of Davies et al (1985). In addition the εNd(t) vs. $(^{87}Sr/^{86}Sr)_i$ plot (Figure 8-1) display

these metasedimentary rocks slightly above that of the UCC curve which further points to a UCC origin. This is further corroborated by the low εNd(t) values (Table 18) recorded by the quartzite (-0.27) and metapelite (-0.03), these values aren't particularly strongly negative at all, so they were derived from a provenance that was itself having a fairly depleted source signature. The metapelite and quartzite has negative $f^{Sm/Nd}$ ratios of -0.3650 (metapelite) and -0.5191 (quartzite) (Table 18). These are strongly negative which means that they are derived from highly fractionated (and upper crustal) sources.

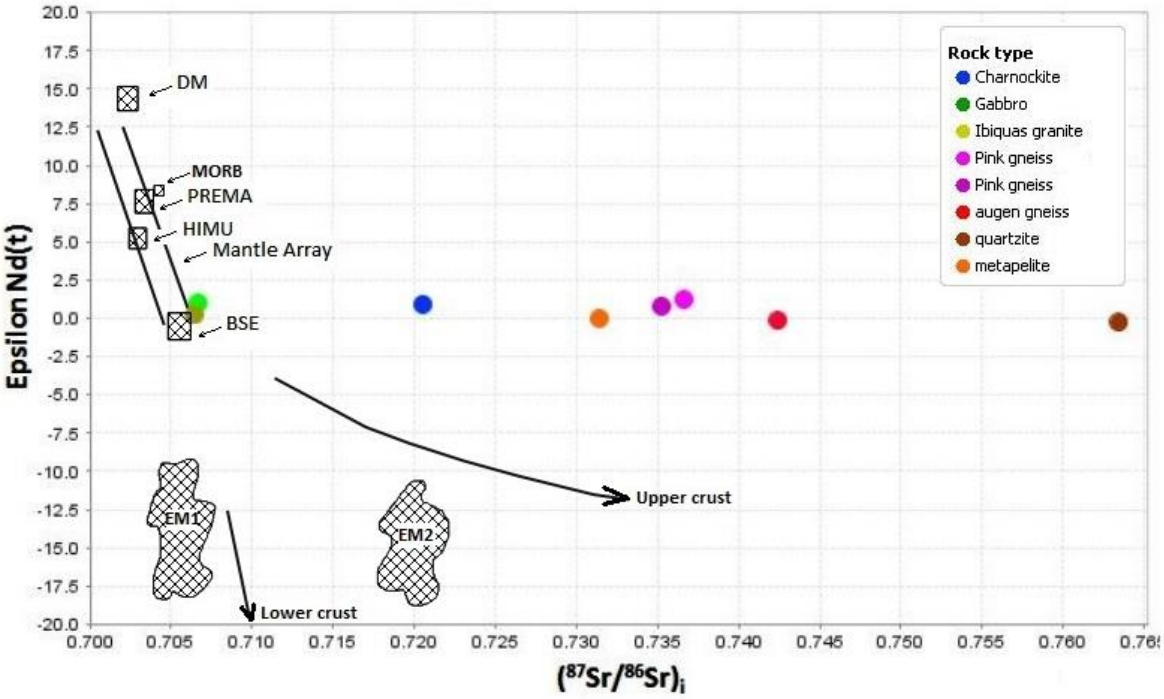

Figure 8-1. ($^{87}Sr/^{86}Sr)_i$ vs. εNd(t) isotope correlation diagram displaying the 8 samples from the Kliprand domal structure. The upper crustal curve (after Harris et al., 1986) and a theoretical lower crustal curve (from Ben Othman et al., 1984) are indicated for reference. The positions of the main oceanic mantle reservoirs identified by Zindler and Hart (1986) are shown: DM = depleted mantle, BSE = bulk silicate earth, EMI and EMII = enriched mantle I and II, HIMU = high mantle U/Pb ratio, PREMA = frequently observed prevalent mantle composition. The mantle sources of MORB and OIB and the mantle end-members DM, PREMA, HIMU, BSE, EMI and EMII are from Zindler & Hart (1986).

As a result of an $(^{87}Sr/^{86}Sr)_i$ value of 0.7205 (fairly high, so there is a substantial crustal influence), the charnockite plots (Figure 8-1) half way between the magmatic rocks (gabbro-norite and Ibequas granite) and sedimentary rocks (metapelite and quartzite). The $(^{143}Nd/^{144}Nd)_i$ value of 0.511309 (This value is fairly high, approaching that of the gabbro-norite suggesting some depleted source component. It may give indications as to the origin of the metasomatic fluids. If CO_2-rich then these

are lower crustal in origin), together with the low $(^{87}Sr/^{86}Sr)_i$ ratio as well as the position of the charnockite sample in Figure 8-1 suggests that the charnockite, like the augen gneiss and metasedimentary rocks, is of an upper continental crustal origin. The charnockite has a positive εNd(t) value of 0.91 (this is similar to that of the gabbro-norite, so a depleted, even mantle-derived component is present. It may well be that the gabbro-norite brought with it fluids that fluxed through the lower crust and metasomatised these upper crustal rocks such as the pink gneiss giving rise to this metasomatic charnockite). A negative $f^{Sm/Nd}$ value of -0.4983 (Table 18) was recorded which, similarly to the rest of the rocks, indicates a fractionated source. Thus the charnockite is from a fractionated, marginally depleted source.

The initial εNd(t) values for the magmatic and metasedimentary rocks from the Kliprand domal structure are plotted against their crystallization ages (Figure 8-2). The majority of the data plots between the CHUR line and the depleted mantle (DM) curve (Figure 8-2) of Goldstein et al. (1984). The, quartzite, metapelite and streaky augen gneiss plot slightly below the CHUR curve (Figure 8-2). The biotite-poor pink gneiss has a Sm-Nd model age of 1.779 Ga (T_{DM}) (Figure 8-2). The biotite-rich pink gneiss has a younger model age (T_{DM}) of 1.671 Ga (Table 18) in comparison to the pink gneiss. With regard to the metasedimentary rocks the quartzite has the youngest T_{DM} age of 1.617 Ga (Table 18), whilst the metapelite has a T_{DM} age of 1.778 Ga (Table 18).

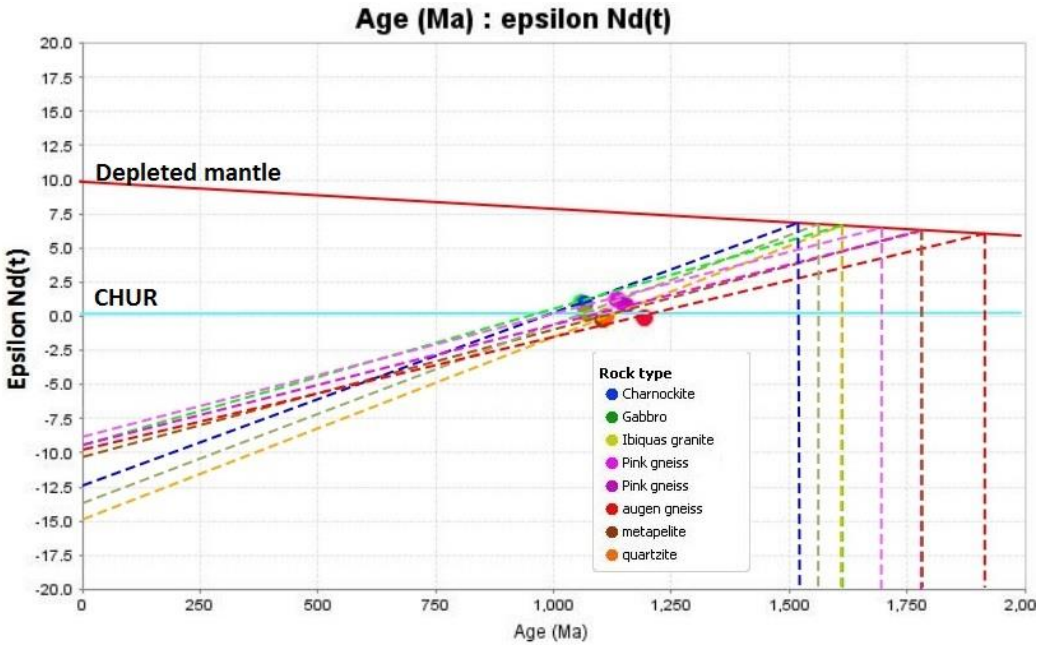

Figure 8-2. Initial ε_{Nd} vs. age plot for all of the lithologies of the Kliprand domal structure. the symbols get a bit obscured and hidden by the lines running through and over them. The calculated T_{DM} age of the gabbro-norite (1.608 Ga) is very close to that of the quartzite (1.617 Ga), thus causing the growth lines to overlap each other.

With regards to the magmatic rocks, the streaky augen gneiss has an emplacement age of ca. 1.192 Ga, with a T_{DM} age of 1.927Ga (Table 18). The gabbro-norite was emplaced at a younger age of ca. 1.059 Ga, with a calculated T_{DM} age of 1.608 Ga (Table 18). The model age (1.549 Ga) of the Ibequas granite is younger than that of the gabbro-norite, whilst the emplacement age is slightly older (1.067 Ga). The charnockite of the Kliprand area has been interpreted as a metasomatic rock with T_{DM} ages of 1.524 Ga (Table 18). The model ages of around 1550 Ma for both the Ibequas granite and the charnockite does not correlate with any event within the Namaqua province, and may therefore represent ages derived from some mixing between older (2.0-1.75 Ga) and younger, juvenile (1.2-1.1 Ga) material.

Table 17: Sr–Nd isotopic data of magmatic and metasedimentary rocks from the Kliprand domal structure.

Sample name	Rock type	Age (Ma)	Rb (ppm)	Sr (ppm)	$^{87}Rb/^{86}Sr$	$(^{87}Sr/^{86}Sr)_0$	±2σ	I_{Sr}
PBG131	Pink gneiss	1135	303.70	57.04	14.1428	0.9664	14	0.7366
PG169.2	Pink gneiss	1153	429.73	52.9	21.5779	1.0914	15	0.7352
AG212	Streaky augen gneiss	1192	292.78	70.56	11.0218	0.9306	14	0.7424
G182	Gabbro	1059	102.79	483.07	0.5652	0.7152	10	0.7067
C133	Charnockite	1066	190.86	168.16	3.0148	0.7665	14	0.7205
IG142	Ibiquas granite	1067	177.4	294.83	1.5983	0.7308	14	0.7064
Q134	Quartzite	1103	35.62	85.16	1.1110	0.7810	11	0.7634
M102	Metapelite	1111	256.63	106.22	6.4176	0.8335	13	0.7314

Sample name	Rock type	Sm	Nd	$^{147}Sm/^{144}Nd$	$(^{143}Nd/^{144}Nd)_0$	±2σ	$\varepsilon_{Nd}(0)$	$f^{Sm/Nd}$	$\varepsilon_{Nd}(T)$	TDM(Ma)
PBG131	Pink gneiss	7.3	36.2	0.1221	0.512144	11	-9.63	-0.3795	1.21	1.671
PG169.2	Pink gneiss	5.3	24.6	0.1304	0.512176	8	-9.01	-0.3373	0.78	1.779
AG212	Augen gneiss	8.1	36.4	0.134	0.51214	29	-9.71	-0.319	-0.13	1.927
G182	Gabbro	12.8	65.4	0.1186	0.512146	10	-9.59	-0.397	0.99	1.608
C133	Charnockite	6.8	41.5	0.0987	0.511999	8	-12.46	-0.4983	0.91	1.524
IG142	Ibiquas granite	7.7	49.7	0.0937	0.511929	9	-13.83	-0.5237	0.24	1.549
Q134	Quartzite	3.5	22.2	0.0946	0.511885	12	-14.68	-0.5191	-0.26	1.617
M102	Metapelite	13.9	67.1	0.1249	0.512113	12	-10.24	-0.365	-0.02	1.778

$\varepsilon_{Nd} = [(^{143}Nd/^{144}Nd)_{sample}/(^{143}Nd/^{144}Nd)_{CHUR}^{-1}] \times 10\,000$; $f_{Sm/Nd} = [(^{147}Sm/^{144}Sm)_{sample}/(^{147}Sm/^{144}Nd)_{CHUR}] - 1$.

Chapter 9 : Geochemistry discussion

Introduction

The main purpose of this chapter shall be to characterise the source and tectonic setting of the three major rock categories (felsic, mafic magmatic and metasedimentary rocks) in this study area. This shall be done by utilising the whole rock geochemistry and isotope analyses findings, and comparing this to previous geochemical data and relationships. Single zircon geochronological analyses on the magmatic and metasedimentary rocks within the Kliprand domal structure shall also be discussed with the purpose of acquiring an estimate age of both, the emplacement of the magmatic rocks, as well as the timing of deposition and relative age of source origin

9.1a Provenance

The major aim of sedimentary provenance studies is to reconstruct and to interpret the history of sediments from the initial erosion of the provenance to the final burial stages (Weltje and von Eynatten 2004). However, as this study involves high grade metamorphic rocks, certain rocks such as the metapelite and the metaquartzite, have been partially melted. Thus the entire history of the sediments shall not be discussed here, but rather the focus will be on determining by mainly utilizing immobile trace elements, the characteristics of the source region that was weathered and eroded to give rise to the sediments that would become lithified to form these rocks.

Many studies concluded that the REE are relatively immobile during weathering, transport diagenesis and metamorphism and thus are useful indicators of the provenance of sedimentary rocks (Chaudhuri and Cullers 1979; Chen et al. 2014). However, as the Kliprand domal structure has been subjected to high grade metamorphism, and partial melting, some elements could have acted in a mobile fashion, particularly the more incompatible LREEs. In this study, the PAAS-normalized REE plot of the metaquartzite displays a shallowly dipping REE pattern [$(La/Lu)_N$ = 1.48], characterized by relatively flat HREE [$(Gd/Lu)_N$ = 1.22] and LREE [$(La/Sm)_N$ = 1.18] patterns (Figure 6-25). The metapelite shows similar relationships to that of the metaquartzite, with a shallowly dipping REE pattern [$(La/Lu)_N$ ratio of 1.36] characterized by a relatively flat HREE [$(Gd/Lu)_N$ = 1.35] and LREE [$(La/Sm)_N$ of 1.18] trend (Figure 6-28). A well-defined negative Eu anomaly was observed for both the quartzite and metapelite. The negative well-defined Eu anomaly is likely because these rocks are plagioclase-poor, and is thus possibly suggestive of being products of anatectic melting. The metasediments have REE patterns that are relatively flat relative to PAAS, as expressed by the

various ratios for the HREE and LREE, thus the average composition of the provenance to the metasedimentary rocks was granodioritic.

The transition elements (e.g. Sc, Ni, Co and V) are commonly concentrated within mafic minerals such as pyroxene and olivine; therefore elevated concentrations of these elements suggests that the sedimentary rocks was derived from a provenance of mafic igneous rocks (Chen et al. 2014). With regard to the transitional elements mentioned above the quartzites and metapelites have strong positive Sc anomalies, with V and Ni values identical to that of UCC, and with Co showing a prominent negative anomaly (Figure 6-26, 6-27).

The positive Cr anomaly (Figure 6-26, 6-27) may be due to contamination caused by milling these samples in a Cr steel mill. However, the relatively flat V and Ni trends as well as the negative Co anomaly (Figure 6-26, 6-27) suggests that other factors could have played a role in concentrating Sc in these metasedimentary rocks. Norman and Haskin (1968) provided evidence for the correlation between Sc and Fe in sedimentary rocks. This is proved in these rocks as they are relatively iron-rich and Sc-rich (being shades of orange and pink showing oxidation of Fe when in contact with the atmosphere) and so it might show that the original provenance, despite having been intermediate to felsic in composition, may have had a fair amount of Fe in it.

The high grade metamorphism and the onset of partial melting could have influenced the transitional and HFS elements, which are considered to be less mobile. These elements are important in discriminating the source of the sedimentary rocks (Armstrong-Altrin and Verma 2005; Chen et al. 2014). As stated in the results, the metapelite and quartzite display positive U and Th anomalies.

These enrichment trends are possibly as a result of these HFS elements being easily incorporated into the parental melt (Feng and Kerrich 1990; Plasma 2007; Bakkiaraj et al. 2010; Chen et al. 2014). This melt crystalized to form the provenance rocks, and was later eroded to form these metasedimentary rocks. The metsedimentary rocks at Kliprand are very Pb- and Th-rich indicating a prominent crustal derivation, in other words the provenance to these sediments already had a strong crustal signature. The LREE, Pb, Th and U-enrichment of the metapelite and quartzite relative to UCC, are all indicative of a highly fractionated crustal provenance.

The Th–Th/U Geochemical diagram (figure 8-3) displays the metapelite and quartzite plotting along the weathering trend. This indicates that the sediments were dominated by the erosion of felsic to intermediate igneous rocks in the source areas.

Th/Sc and Zr/Sc ratios are important parameters in discriminating the source of sedimentary rocks (Chen et al. 2014). This is mainly due to Th and Zr being incompatible during most igneous activities and thus being enriched in felsic rocks, whilst Sc is compatible and will most likely enter olivine, pyroxene and other minerals that crystalize early in the magmatic process (Chen et al. 2014). The metasedimentary samples from the Kliprand region mostly plot along the igneous differentiation line and fall in the area between the average compositions of andesite and granite (Figure 8-4a). There is quite a horizontal variation in the Zr/Sc ratio potentially suggesting some degree of reworking and compositional maturing of the sediments prior to final lithification. Hf partners with Zr, particularly in zircon and so variations in Hf content (Figure 8-4b) suggest variations in zircon content which could be used to varying initial zircon concentrations in the provenance, or due to winnowing and reworking prior to lithification.

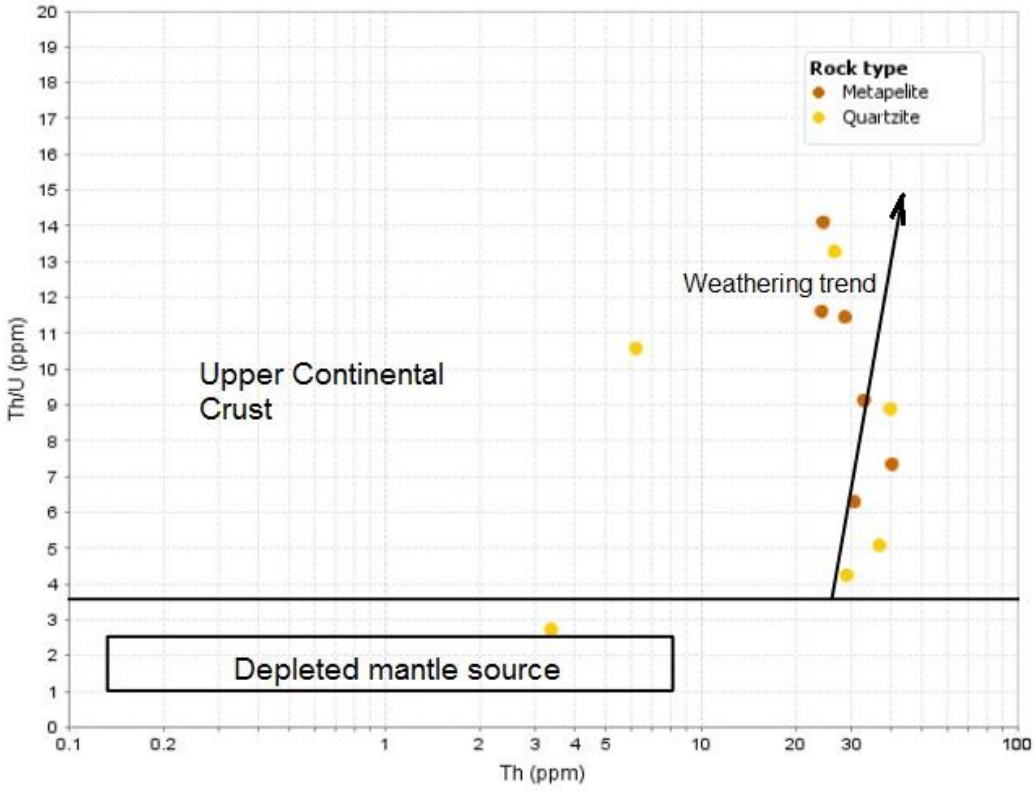

Figure 8-3. Th–Th/U Geochemical diagram showing the source nature of the meta-sedimentary rocks In the Kliprand domal structure (after McLennan et al. (1993).

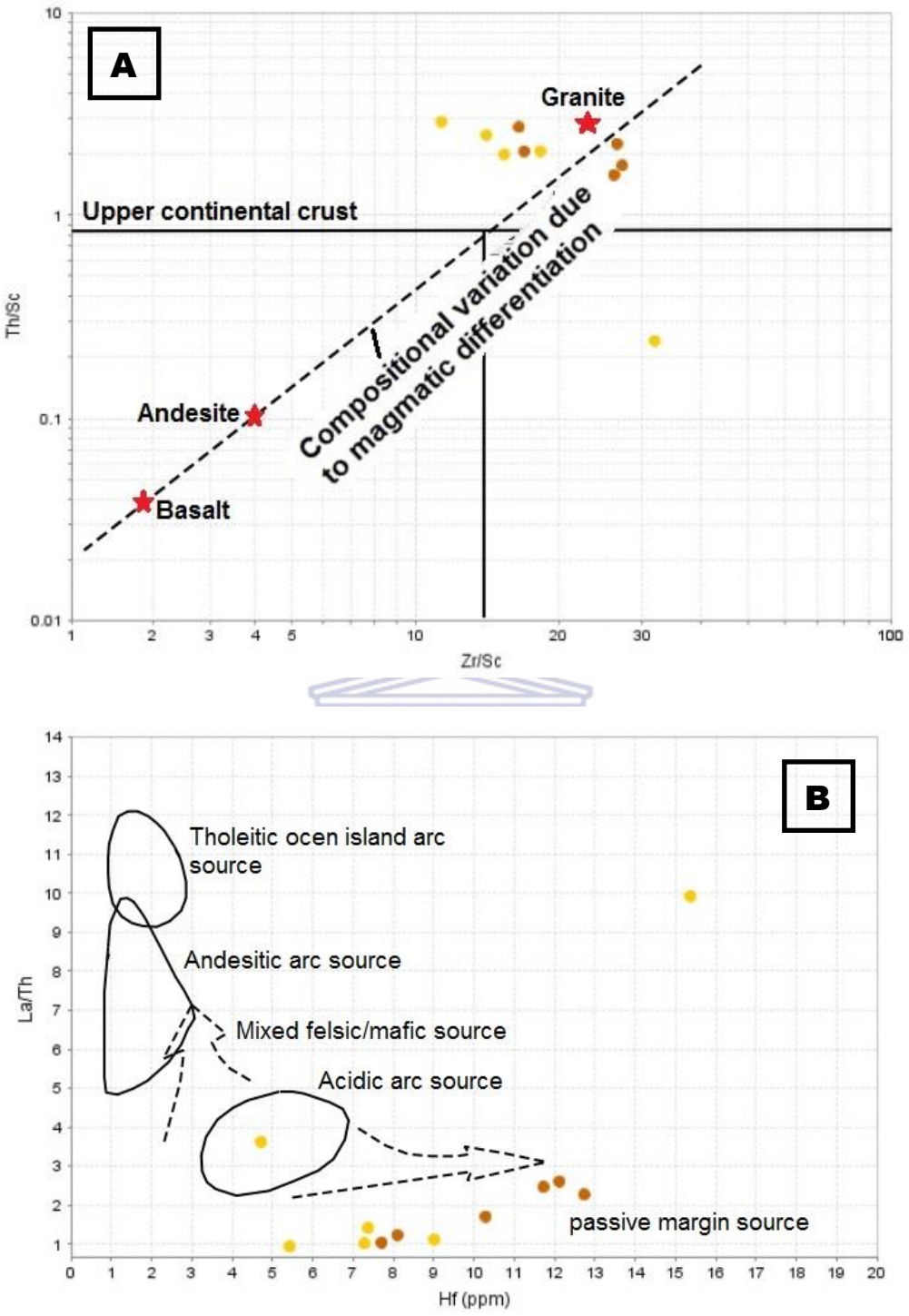

Figure 8-4. Geochemical diagrams showing the source nature of the meta-sedimentary rocks In the Kliprand domal structure (a) Zr/Sc–Th/Sc diagram after McLennan et al. (1993); (b) Hf–La/Th diagram after Floyd and Leveridge (1987).

Table 18: Elemental ratios of meta-sedimentary rocks from the Kliprand domal structure relative to sediments of other sources. Clearly showing that these rocks weren't derived from mafic sources

Elemental ratio [1]	Quartzite [2]	Metapelite [3]	Sediment from felsic sources [4]	Sediment from mafic sources [5]	Upper continental crust [6]
Eu/Eu*	0.4-3.06	0.38-0.8	0.40-0.94	0.71-0.95	0.63
$(La/Lu)_N$	0.54-2.29	0.22-1.63	3.0-27	1.1-7.0	9.73
La/Sc	0.91-2.94	2.14-4.03	2.5-16.3	0.43-0.86	2.21
Th/Sc	0.25-2.90	1.22-2.72	0.84-20.5	0.05-0.22	0.79
Th/Co	0.79-14.97	3.18-8.64	0.67-19.4	0.04-1.4	0.63
Th/Cr	0.01-0.11	0.08-0.10	0.13-2.7	0.018-0.046	0.13
Cr/Th	7.52-16.08	9.69-12.75	4.0-15.0	25-500	7.76
La/Co	2.86-15.55	8.29-9.93	1.80-13.8	0.14-0.38	1.76

Columns 4 and 5 from Cullers (1994, 2000); Cullers and Podkovyrov (2000); Cullers et al. (1988); Armstrong-Altrin (2009); column 6 McLennan (2001); Taylor and McLennan (1985).

Wronkiewicz and Condie (1990) and McLennan and Taylor (1991) state that high Th and La values are indicative of a felsic igneous source, whereas high Sc and Cr values are indicative of a mafic igneous source (Rollinson 1993). Similarly, the source nature can also be addressed by determining ratios between these elements such as La/Sc, Th/Sc, Th/Co, Th/Cr and Eu/Eu* (Cullers 1995; Cullers 2000; Bakkiaraj et al. 2010; Chen et al. 2014; Table 19). The ratios of the metasedimentary rocks fall within the range of felsic sediments (Table 19), and again support a felsic provenance for these rocks.

9.1b Tectonic setting of the metasedimentary rocks

The tectonic discrimination diagram proposed by Roser and Korsch (1986) works better than the diagram by Bhatia (1983) in terms of determining the plate tectonic setting, as was stated by Armstrong-Altrin and Verma (2005). Therefore the more immobile trace element bivariate Ti/Zr versus La/Sc (Figure 8-5) and the La-Sc-Zr ternary plot (Figure 8-6a) of Bhatia (1983) were used.

These diagrams have four major tectonic fields, namely OIA (oceanic island arc), CIA (continental island arc), ACM (active continental margin) and PM (passive margin) (Bhatia and Crook 1986). The

metasedimentary rocks from the Kliprand study area have Ti/Zr and La/Sc ratios similar to those of a continental island arc setting (Figure 8-5). Although no actual arc material is found in either this region or the Garies terrane, seemingly, the metasedimentary rocks carry the signature of an island arc and possibly were deposited on the margin, or within an extensive back-arc environment. This arc may be represented by the Richtersveld Subprovince.

In addition to the bivariate plot of Bhatia (1983), the La-Th-Sc ternary plot was also constructed (Figure 8-6a). This diagram (Figure 8-6a) has the oceanic island arc samples plotting towards the Sc apex, the continental margin samples plotting near the La apex, and the continental island arc samples plot in between the two fields (Bhatia and Crook 1986). Within the La-Th-Sc (Figure 8-6a) and La-Th-Sc/10 (Figure 8-6b) plots, most metapelite and quartzite samples plot on the CIA and ACM boundary and within the ACM field. The samples plotting within the ACM setting could be due to deposition of these sediments within rift basins (a type of active continental margin).

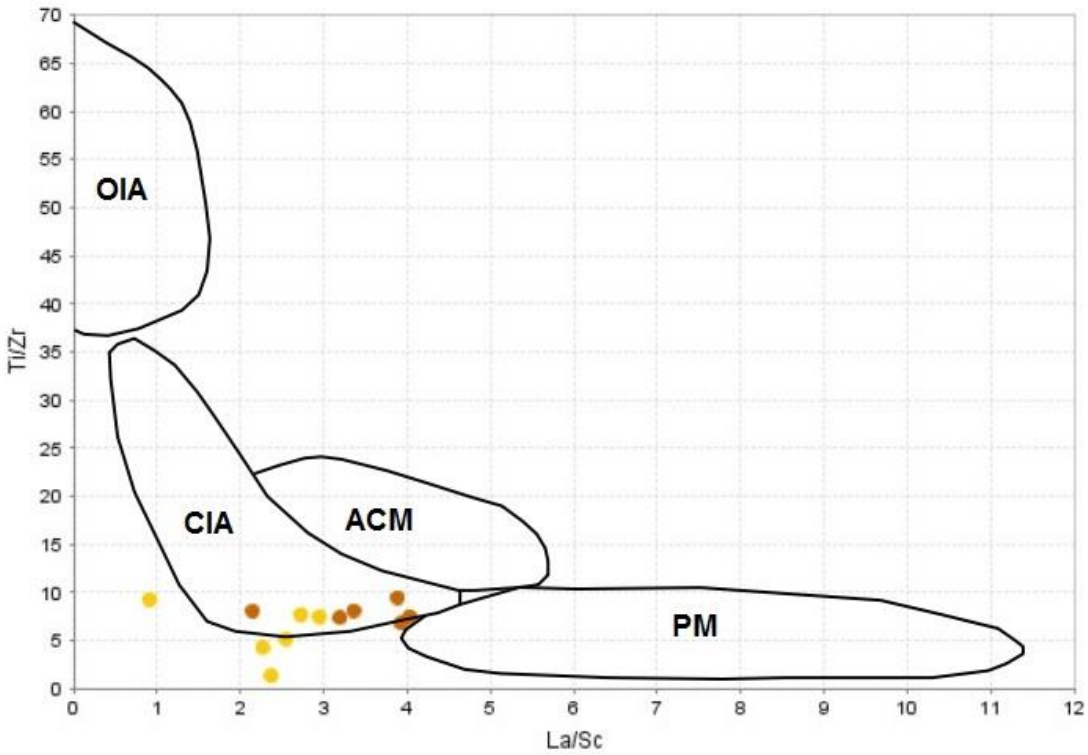

Figure 8-5. Tectonic setting discrimination diagrams for meta-sedimentary rocks within the Kliprand dome. (A) La/Sc–Ti/Zr diagram (after Bhatia and Crook, 1986). OIA: oceanic island arc; ACM: active continental margin; CIA: continental island arc; PM: passive margin.

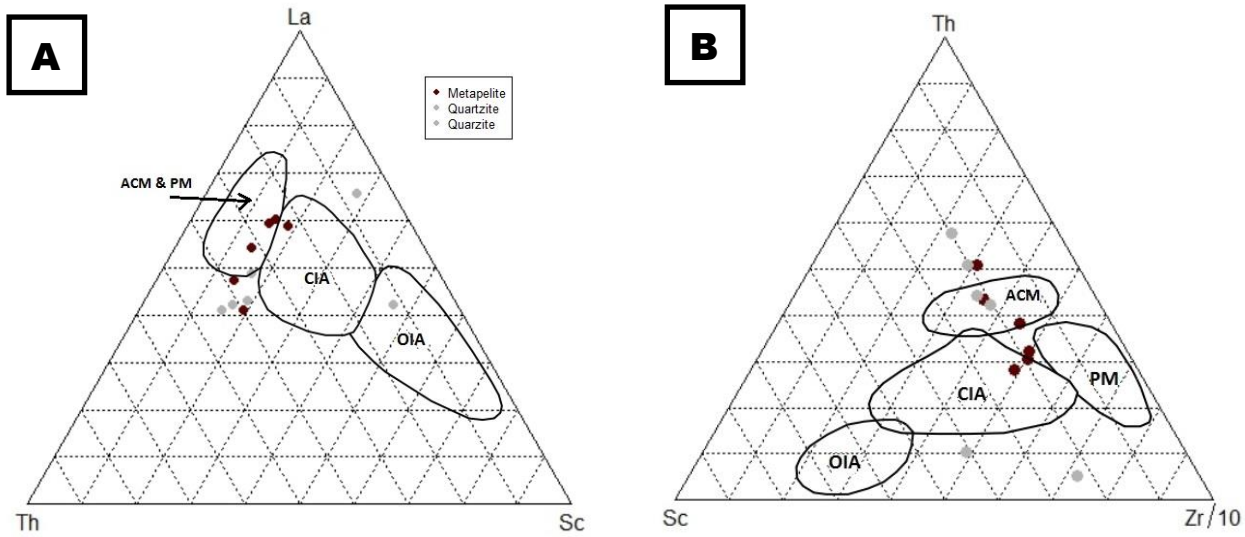

Figure 8-6. Tectonic setting discrimination diagrams for meta-sedimentary rocks within the Kliprand dome (A) La–Th–Sc and (B) Th–Sc–Zr/10 diagrams are after Bhatia and Crook (1986). OIA: oceanic island arc; ACM: active continental margin; CIA: continental island arc; PM: passive margin.

Similarly to the provenance studies above, the immobile REEs are also effective in discriminating the tectonic setting of sedimentary rocks (Chen et al. 2014). Sediments deposited in a continental margin environment are characterized by LREE enrichment (high $(La/Sm)_N$) and high total rare earth elements (ΣREE)), whereas sediments deposited in an oceanic island arc have low $(La/Sm)_N$ ratios, low total rare earth elements (ΣREE) content, and lack of negative Eu anomalies (Bakkiaraj et al. 2010). Sediments deposited in passive margins are typically characterized by uniform REE patterns similar to PAAS, while sediments from active continental margins display intermediate ΣREE abundances with variable negative Eu anomalies in the range of 0.6-1.0 (Bakkiaraj et al. 2010). In this study, the quartzites (Figure 6-25) [average $(La/Sm)_N$ = 1.18] and metapelites (Figure 6-28) [average $(La/Sm)_N$ = 0.77] are characterized by relatively uniform LREE patterns similar to PAAS thus resembling a passive margin depositional setting.

9.2a Petrogenesis of the magmatic rocks

The presence of this Al-beairng silicate mineral (garnet in the Ibequas granite) suggests derivation from an Al-rich source, and, in particular, a sedimentary source. The streaky augen gneiss, pink gneiss and charnockite all contain biotite in their mineral assemblage, which is characteristic of magmas forming from an igneous (I-type) source (Chappell and White 2001).

The charnockite is a metasomatic product and not a direct magmatic fractionate or product of typical magmatic processes, therefore classification and characterisation using typical magmatic

classification and discrimination diagrams don't apply for it. Even though it is inappropriate to plot the charnockite on the same diagrams, it has been added for the purpose of comparison. The pink gneiss are plotted on separate discriminant diagrams below as they would have covered most of the data points of the rest of the magmatic rocks.

With regards to whole rock geochemistry the Ibequas Granite is strongly peraluminous (Figure 6-3a), whilst the streaky augen gneiss, pink gneiss and charnockite are weakly peraluminous and lie close to and within the strongly peraluminous region (Figure 6-3a). Peraluminous compositions for magmatic rocks suggests melting of an Al-rich source rock, therefore the strongly peraluminous nature of the Ibequas granite is typical of partial melting of a sedimentary source rock, so that the Ibequas granites represents the product of partial melting of sedimentary rocks. The streaky augen gneiss and the pink gneiss clearly plots within the ferroan field on the $FeO_T/(FeO_T + MgO)$ vs. SiO_2 diagram (Figure 6-3b for the former and Figure 6-14b for the latter) whilst the Ibequas granite plots along the separation line between ferroan and magnesian (Figure 6-3b), with the majority of the samples lying in the ferroan field and the rest within the magnesian field (Figure 6-3b). The streaky augen gneiss and pink gneiss may thus be classified as peraluminous alkali, ferroan (A-type) granitoids (Collins et al. 1982; Whalen et al. 1987; Eby 1990; Frost et al. 2001), and are probably not I- or S-type granitoids. Their high concentrations of potassium and other large-ion lithophile elements (LILE) and high field strength elements (HFSE), as well as their high Fe/Mg ratios, are furthermore characteristic of Mesoproterozoic A-type granitoids (Anderson and Morrison 2005; Bial et al. 2015).

Whalen et al. (1987) state that highly fractionated I- and S-type granites could be distinguished from A-type granites using Zr+ Nb + Ce + Y as a discriminator (Eby 1990). Whalen et al. (1987) also note that A-type granitoids could possibly represent highly fractionated I-type magmas. Jiang et al. (2009) therefore suggest that, if this is the case, then the chemical discrimination diagrams cannot effectively distinguish strongly fractionated A-type granites from similarly fractionated I-type granites. Nonetheless, the geochemical diagram of Whalen et al. (1987) (Figure 8-7) displays all the samples of the augen gneiss and Ibequas granite mainly plotting within the A-type granite field, with the augen gneiss plotting closer to the separation line. One sample of the augen gneiss plots within the fractionated I- and S-type field. Unlike the Ibequas granite and streaky augen gneiss, the pink gneiss and charnockite both plots within the A-type field as well as the fractionated I- and S-type field. The fact that the majority of the augen gneiss samples plot along the boundary line (between the fractionated I and S field with the A field) (Figure 8-7), with the pink gneiss (Figure 8-8) and charnockite (Figure 8-7) plotting in both the I- and S-type field as well as the A-type field, together

with the fact that all of these magmatic rocks plot both within the I- and S-type granites field and A-type field on the Th vs. (Eu/Eu*) plot (Figure 8-9, 8-10), suggests that they may possibly be highly fractionated I-type granites.

In granitic rocks feldspar is among the most important minerals in fractional crystallization schemes (Eby 1992). The augen gneiss displays a large negative Eu anomaly which suggests extensive feldspar fractionation. For any degree of feldspar fractionation, the A-type granitoids tend to be enriched in Th. It is possible, then, that highly fractionated I-type magmas could have resulted in the composition of the streaky augen gneiss, pink gneiss and charnockite resembling that of A-type granites, as they have high Th contents (an average 27.62ppm for the streaky augen gneiss, an average of 32.97ppm for the pink gneiss and an average of 28.53ppm for the charnockite) (Table 20; Figures 8-9, 8-10).

As both the data of the Ibequas granite and augen gneiss in Table 20 points to an A-type granite nature, they may have been produced by either: (1) extreme differentiation of a mantle-derived tholeiitic or alkaline basaltic magma precursor; (2) partial melting of crustal rocks; and (3) combined crustal and mantle sources, in the form of either crustal assimilation and fractional crystallization (AFC) of mantle derived magmas, or mixing between mantle-derived and crustal magmas (Moghadam et al. 2015).

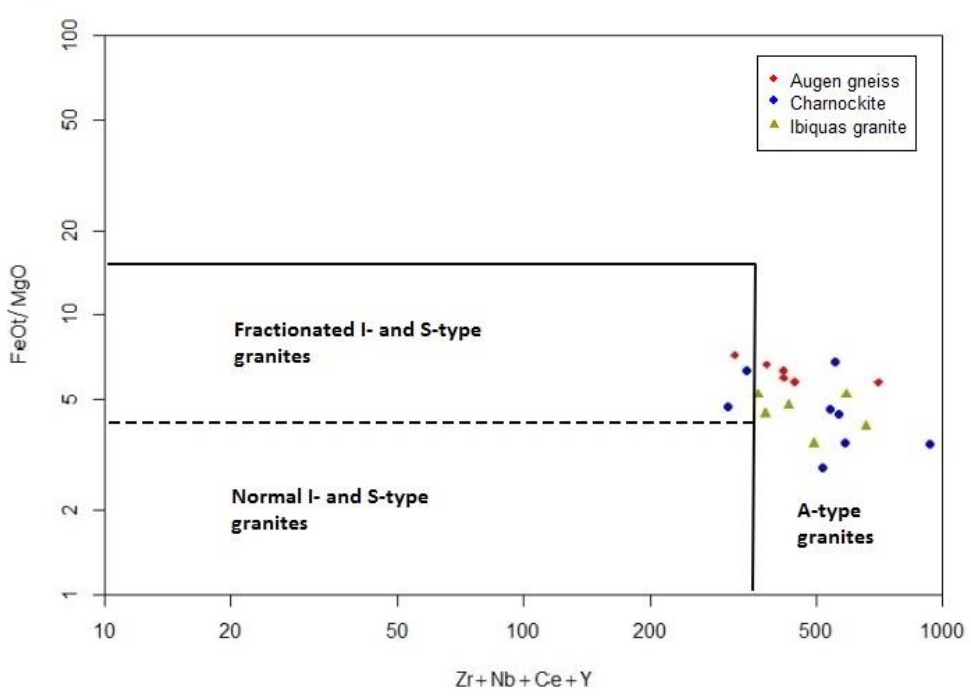

Figure 8-7. FeO_T/MgO vs. (Zr + Nb + Ce + Y) plot to distinguish I- and S-types from A-type granites, after Whalen et al. (1987).

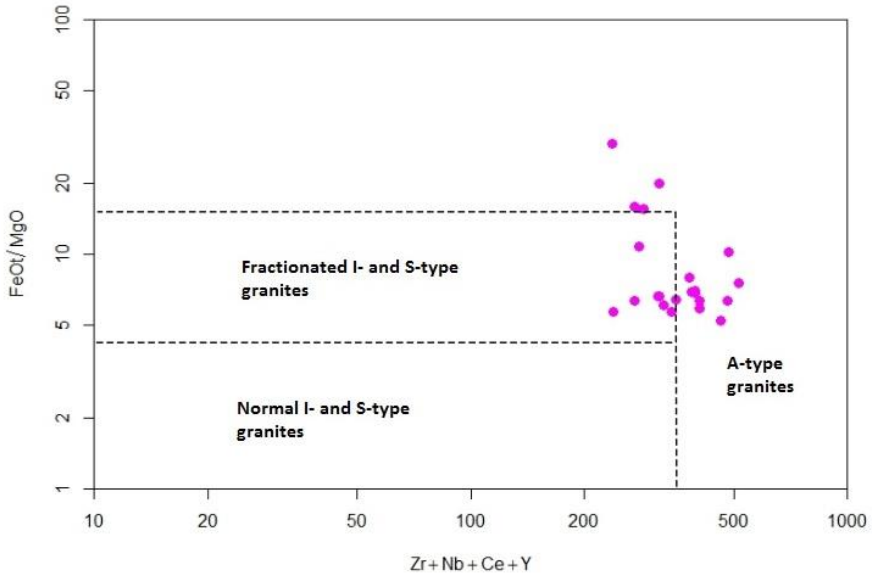

Figure 8-8. FeO_T/MgO vs. (Zr + Nb + Ce + Y) plot of pink gneiss to distinguish I- and S-types from A-type granites (after Whalen et al., 1987).The geochemical plots of the pink gneiss where plotted on seprate diagrams as these data points overly that of the remaining felsic rocks.

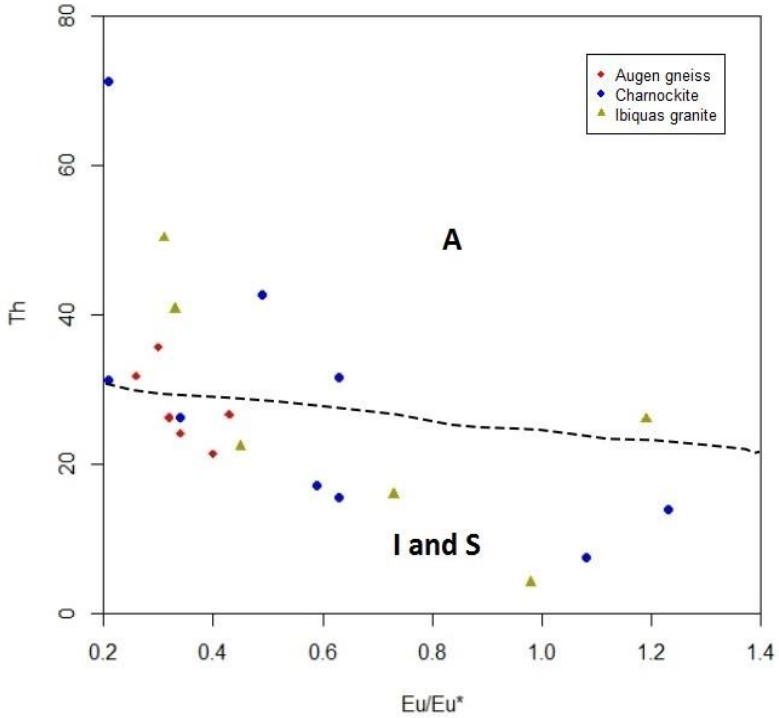

Figure 8-9. Variations in Th as a function of the size of the negative Eu anomaly (Eu/Eu). Data used to construct the boundary of the I-type and S-type (I and S) granite field are from Eby (1992).*

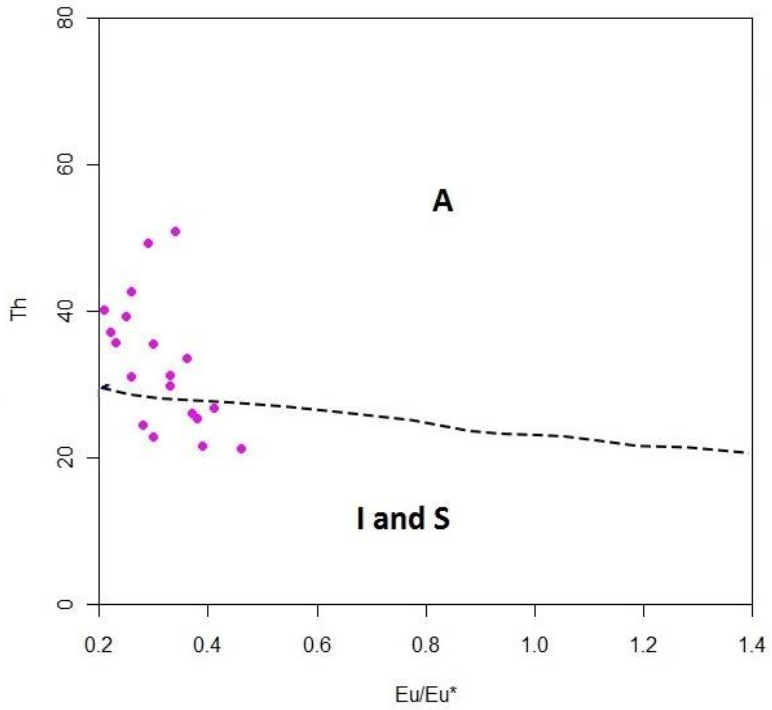

Figure 8-10. Variations in Th as a function of the size of the negative Eu anomaly (Eu/Eu). Data used to construct the boundary of the I-type and S-type (I and S) granite field are from Eby (1992). The geochemical plots of the pink gneiss where plotted on seprate diagrams as these data points overly that of the remaining felsic rocks.*

Compatible vs. incompatible bi-logarithmic diagrams (Bial et al. 2015) (Figures 8-11, 8-12) were constructed in order to distinguish whether partial melting or fractional crystallization was the major process that affected these magmatic rocks. If the trend is sloping, then these A-type granites formed as a result of fractional crystallization, whilst partial melting would result in a horizontal trend (Cocherie 1986; Martin 1987; Martin et al. 1994). The vertical trend displayed by Co vs. Rb and Ni vs. Pb diagrams (Figures 8-11, 8-12) suggests fractional crystallization as the main process of magma differentiation. The charnockite plots close to the origin because it is a metasomatic product, it's not clear what the process is (Figures 8-13, 8-14). These A –type granites define a trend that is consistent with both fractional crystallization and partial melting on the La_N/Yb_N vs. La diagrams.

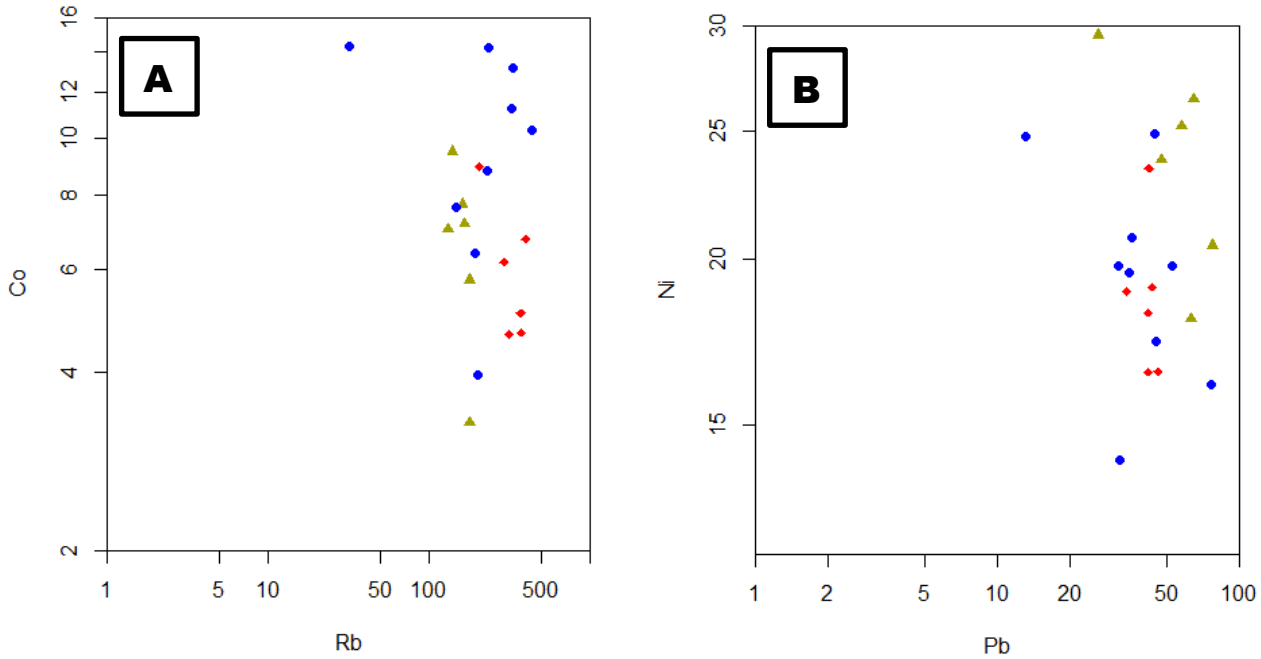

Figure 8-11. Bi-logarithmic compatible element vs. incompatible element diagrams of a) Rb vs. Co and b) Pb vs. Ni after Cocherie (1986). The symbols are the same as that used in the previous figures

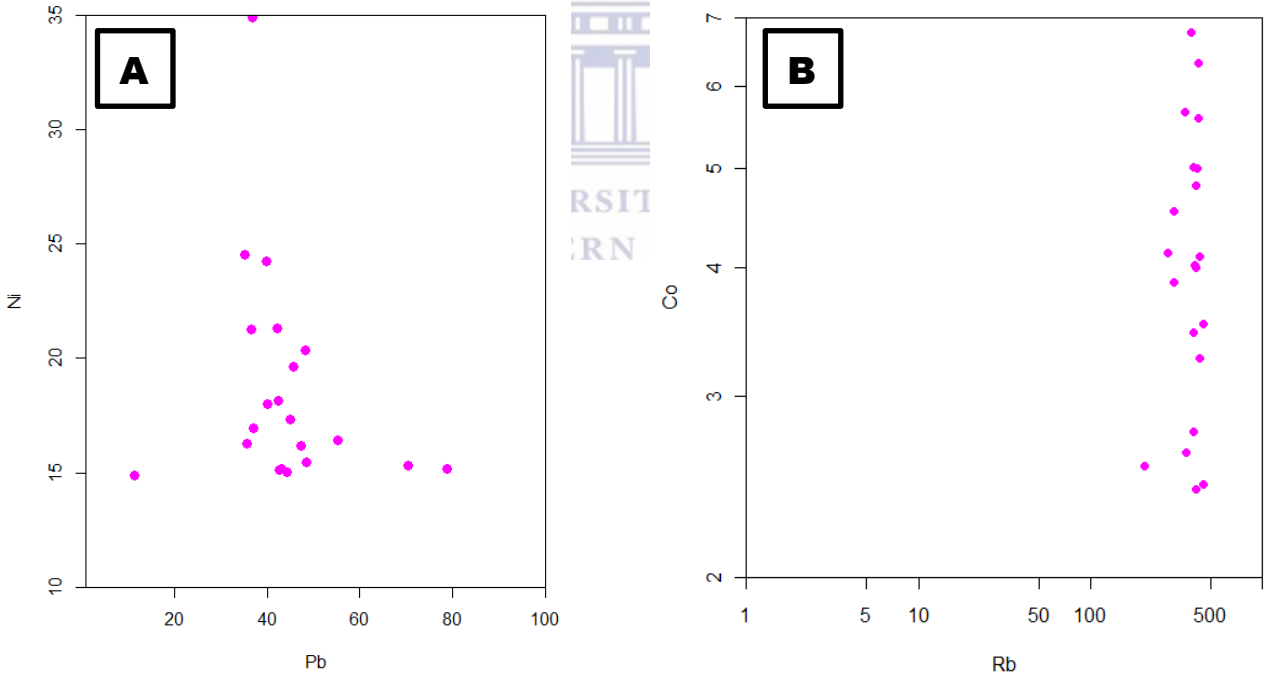

Figure 8-12. Bi-logarithmic compatible element vs. incompatible element diagrams of a) Rb vs. Co and b) Pb vs. Ni (after Cocherie, 1986).

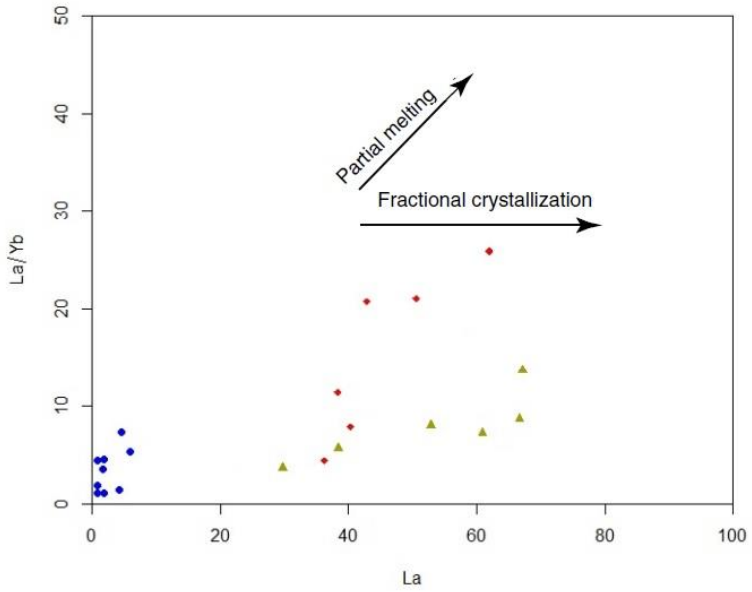

Figure 8-13.A La vs. La/Yb plot displaying whether these rocks have been subjected to partial melting, fractional crystallization or a combination of both. The symbols are the same as that used in the previous figures.

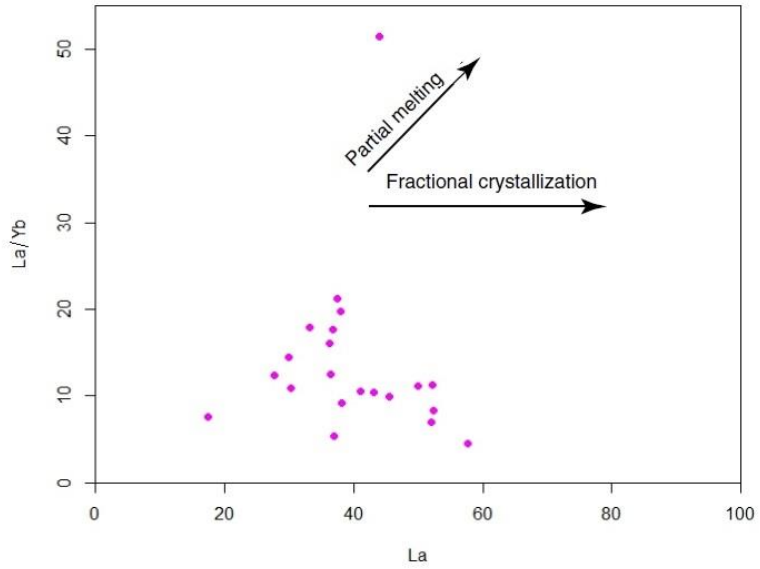

Figure 8-14. A La/Yb vs. La plot displaying whether pink gneiss have been subjected to partial melting, fractional crystallization or a combination of both.

The augen gneiss, pink gneiss and charnockite are all characterised as being high-K, calc-alkaline, peraluminous granites with pronounced negative Ba, Sr, Nb and Ti anomalies, and prominent positive Rb, Th, K and La anomalies, which all strongly indicate derivation from a crustal source. The strongly enriched LILE and LREE-enriched trace element contents, suggests partial melting of continental crust. However, the epsilon Nd value $\varepsilon_{Nd(t)}$ (-0.14) value for the streaky augen gneiss is

not that negative, at least not as negative as might be expected for crustally derived rocks. So there is a depleted component to these rocks, potentially a mantle-derived component. This is corroborated by the enrichments in U and Th, and depletions of Ta and Nb relative to La. Pearce (1983) suggests that Nb is contributed by the lithosphere in subduction related melt processes, this may suggest (this applies to basalts but could just as easily apply to any melting of the subcontinental lithospheric mantle) that melting of subcontinental lithospheric mantle may have contributed Nb to the melts that generated or influenced the charnockite. Furthermore, the Nb–Ce–Y and Nb–Y–Zr/4 discrimination diagrams of Eby (1992) reveal that the streaky augen gneiss and the Ibequas granites fall into the A2 subgroup of A-type granites (Figure 8-15, 8-16). This subgroup represents magmas derived from the lower continental crust, hence a mantle component to these melts.

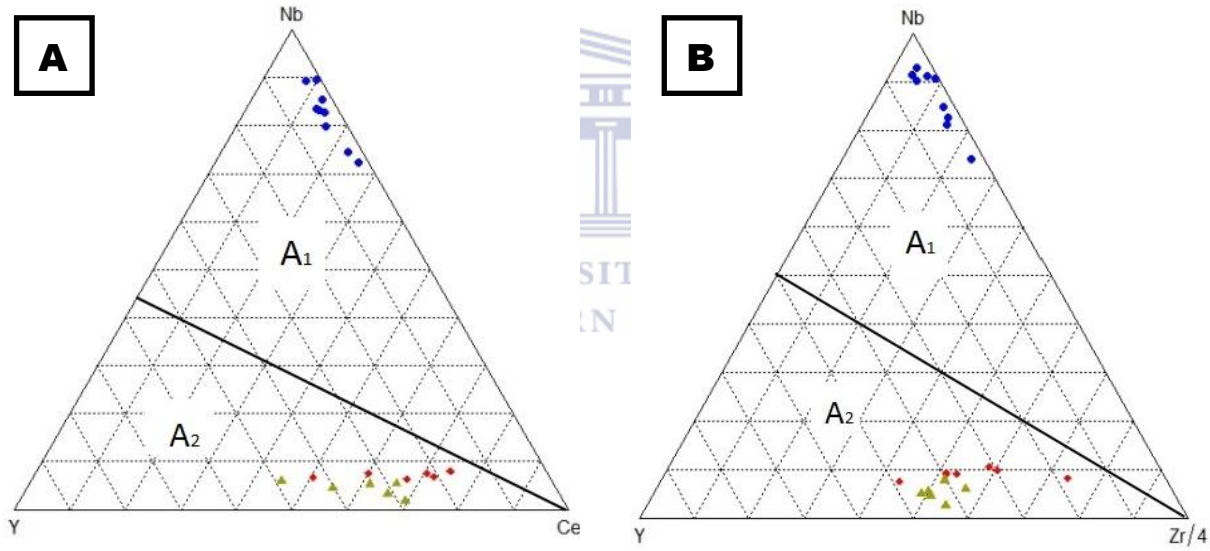

Figure 8-15. a) Nb–Y–Ce and b) Nb–Y–Zr/4triangular plot (after Eby, 1992). The A1 field refers to granitoids in anorogenic settings. The A2 field is for post-orogenic granites emplaced after a continental collision.

The geochemistry of the Ibequas granite suggests this is an A-type granite. If the Ibequas granite is, in fact, an A-type granite then it most likely formed as a result of partial melting of crustal material causing it to have the second youngest model age of 1.549 Ga. The relatively young model age is suggestive of a substantial Mesoproterozoic component to these melts, probably the mixing between a Paleoproterozoic and Mesoproterozoic source with, a greater Mesoproterozoic component. The Ibequas Granite is taken as the melt product of the metapelites in the region (Macey et al. 2011), but with a positive $\varepsilon_{Nd(t)}$ value (0.24) this source was depleted but fractionated.

The metapelites are likely derived from erosion of magmatic material originally derived from a depleted source, but are relatively fractionated because of erosion and reworking during transport and sedimentation. When these melted the melt product (the Ibequas Granite) carried these isotopic signatures.

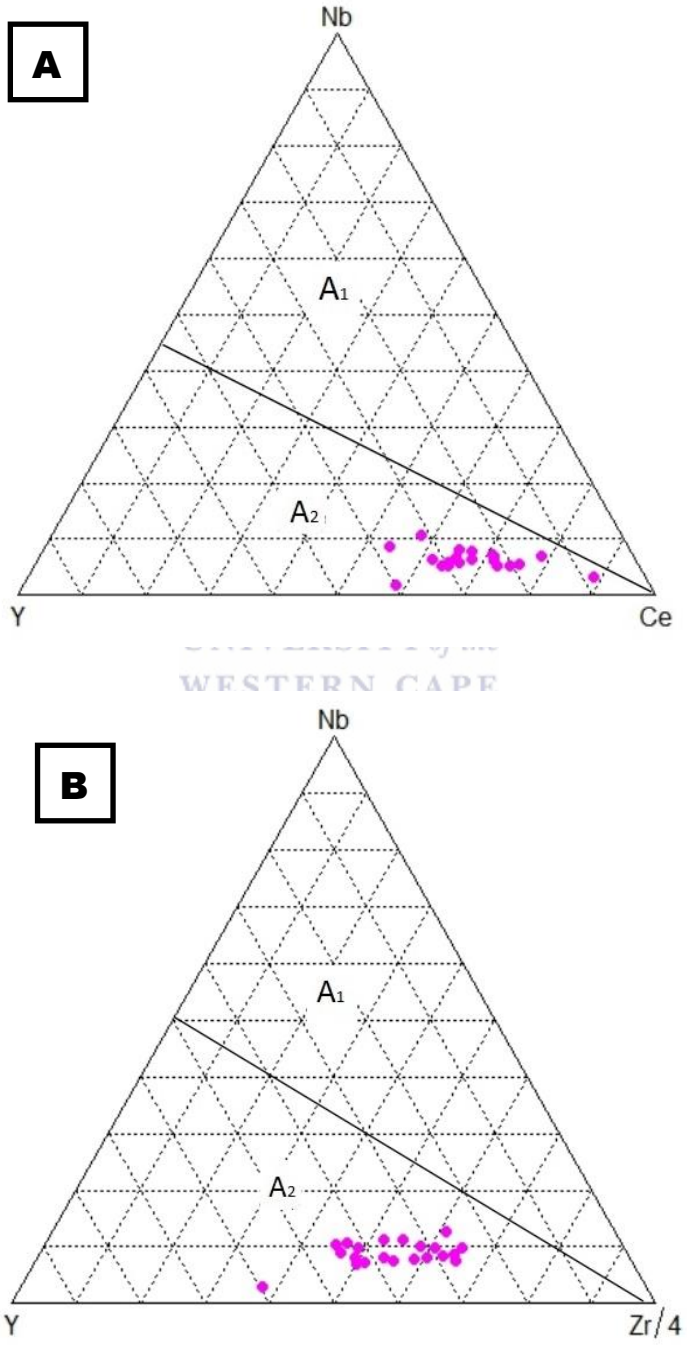

Figure 8-16. a) Nb–Y–Ce and b) Nb–Y–Zr/4triangular plot (after Eby, 1992). The A1 field refers to granitoids in anorogenic settings. The A2 field is for post-orogenic granites emplaced after a continental collision.

Table 19. A Comparison between the streaky augen gneiss, Ibequas granite and charnockites,with the major granitic types.

	M-type	I-type	S-type	A-type	Ibiquas granite	Augen gneiss	Charnockite
Major elements (wt%)							
SiO2	67.2	69.5	70.9	73.8	73.5	73.59	67.81
TiO2	0.5	0.4	0.4	0.3	0.44	0.4	0.74
Al2O3	15.2	14.2	14	12.4	12.43	12.64	14.04
FeOT	4.1	3.1	3	2.7	3.7	2.81	4.87
MnO	0.1	0.1	0.1	0.1	0.07	0.03	0.07
MgO	1.7	1.4	1.2	0.2	0.76	0.4	1.1
CaO	4.3	3.1	1.9	0.8	0.88	0.89	1.86
Na2O	4	3.2	2.5	4.1	2.03	2.46	2.59
K2O	1.3	3.5	4.1	4.7	4.4	5.51	5.1
P2O5	0.1	0.1	0.2	0	0.086	0.12	0.2
Trace elements (ppm)							
Ni	2	8	11	1	23.92	18.76	19.69
Co		10	10	3	6.74	6.04	10.02
Cr		20	30	2	443.25	314	303.49
Cu	42	9	9	2	29.41	23.21	20.68
Zn	56	48	59	120	52.85	39.15	82.64
V	72	57	49	6	85.73	63.93	97.67
La		31	27	55	52.64	45.08	71.14
Ce	16	66	61	137	112.51	103.37	148.13
Nd		30	28	67	45.55	43.47	63.68
Sm		6	6	16	8.85	9.11	11.95
Eu		1	1	2	1.55	0.97	1.79
Gd				14	8.29	8.1	10.15
Tb				2	1.43	1.3	1.58
Dy							
Yb		3	3	9	7.09	3.93	6.75
Lu		1	1	1	0.99	0.61	0.99
Rb	18	164	245	169	158.49	325.46	235.18
Ba	236	519	440	352	644.66	449.49	789.58
Sr	282	235	112	42	135.78	60.42	182.9
Pb	5	19	27	24	56.03	41.69	40.61
Zr	108	150	157	528	303.00	290.61	386.17
Th	1	20	19	23	26.52	27.62	28.53
Nb	1	11	13	37	7.77	11.26	11.52
U	0	5	5	5	2.57	4.03	2.51
Y	22	31	32	75	60.69	41.88	59.74
Rb/Sr	0.06	0.7	2.19	4.02	1.17	5.39	1.29
Rb/Ba	0.08	0.32	0.56	0.48	0.25	0.72	0.30
Th/U	1	4	3.8	4.6	10.31	6.85	11.37
K2O/Na2O	0.33	1.09	1.64	1.15	2.17	2.24	1.97
FeOT/MgO	2.41	2.21	2.5	13.5	4.87	7.03	4.43

Column 1- average of 17 M-type granitoids, New Britain arc (Whalen et al., 1987), Column 2 – average of 1074 I-type granitoids, Column 3 - average of 704 S-type granitoids and Column 4 – an average of 148 A-type granitoids (Whalen et al. 1987, REE from Collins et al., 1982).

9.2b Geotectonic evolution of the granites

Initially the tectonic diagram of Pearce et al. (1984) was constructed. This diagram is, however, rather outdated and largely ineffective in determining the tectonic settings of these felsic rocks, as the granites tend to plot in the same position, straddling the boundary between VAG (Volcanic Arc Granite), ORG (Ocean ridge granite) and syn-COLG (syn-collision granites) typical of A-type granites. Verma et al (2013) have devised an updated discriminant function based tectonic classification diagram. The Verma plots are useful in the sense that the probability of a certain tectonic setting can be calculated which helps when distinguishing between tectonic settings that are closely clustered. The equations for the various Verma diagrams used in this study are given by Verma et al. (2015), and therefore, shall not be reproduced in this study. The discrimination diagrams used for both felsic (Figures 8-17 and 8-18), and mafic rocks (Figure 8-23) make use of immobile trace elements.

With regards to the tectonic discrimination diagram of Verma et al. (2015), the streaky augen gneiss has the majority (39%) of its samples plotting in the collision field, whilst the remainder of the samples plot in the continental rift + ocean-island (31%) and continental arc (30%) fields (Figure 8-17; Appendix D, Table AG-1). The charnockite has the highest probability (56%) of samples plotting in the continental arc field with a smaller percentage (28%) plotting in the collision field, whilst the remainder of the samples plot in the island arc (10%) and continental rift + ocean-island field respectively (6%) (Figure 8-18; Appendix D, Table AG-2). Contrary to both the streaky augen gneiss and the charnockite, the ibequas granite has the highest probability (56%) of samples plotting in the continental rift + ocean-island field, with remainder of the samples plotting in the continental arc field (26%), island arc field (17%) and collision field (11%) (Figure 8-17, Appendix D, Table AG-3). Similarly to the streaky augen gneiss, the pink gneiss has a high abundance of samples plotting in the collision field (41%) and continental rift + ocean-island field (45.6%), with the remainder of the samples plotting in the continental arc (12.2%) and island arc field (1.2%) (Figure 8-18, Appendix D, Table AG-4). These immobile trace element diagrams points to a continental arc collisional continental rift tectonic setting, which is actually likely the case.

It has been acknowledged by numerous authors, including Julian Pearce himself, that tectonic setting diagrams really reflect the composition of the source material that is melting and may not be a true indicator of a particular tectonic setting. In the case of the charnockite the continental arc signature may reflect that material with a continental arc signature or composition, or simply an old continental arc, including portions of the subcontinental lithospheric mantle melted to give rise to these rocks and they were not likely emplaced in such a setting.

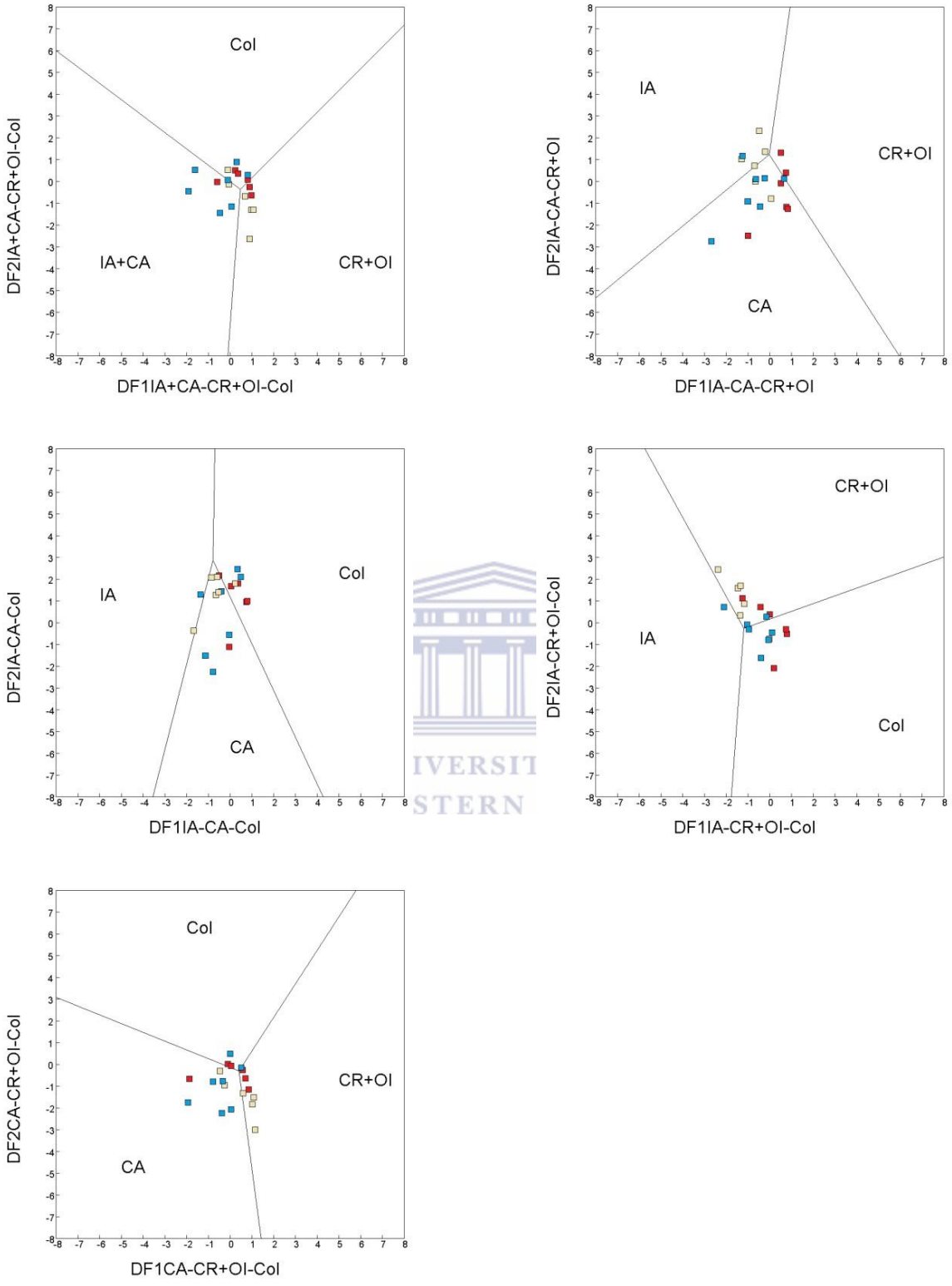

Figure 8-17. Application of the set of five multidimensional DF1 ‑DF2 diagrams based on log-ratios of immobile trace elements for felsic rock samples from the Kliprand study area (Verma et al., 2013). Three tectonic settings are shown on each diagram. (a) IA+CA ‑CR+OI ‑Col (b) IA ‑CA ‑CR+OI (c) IA ‑ CA ‑Col (d) IA ‑CR+OI ‑Col (e) CA ‑CR+OI ‑Col. The Streaky augen gneiss is represented by red squares, the Charnockite by Blue squares and the Ibequas granite by yellow squares.

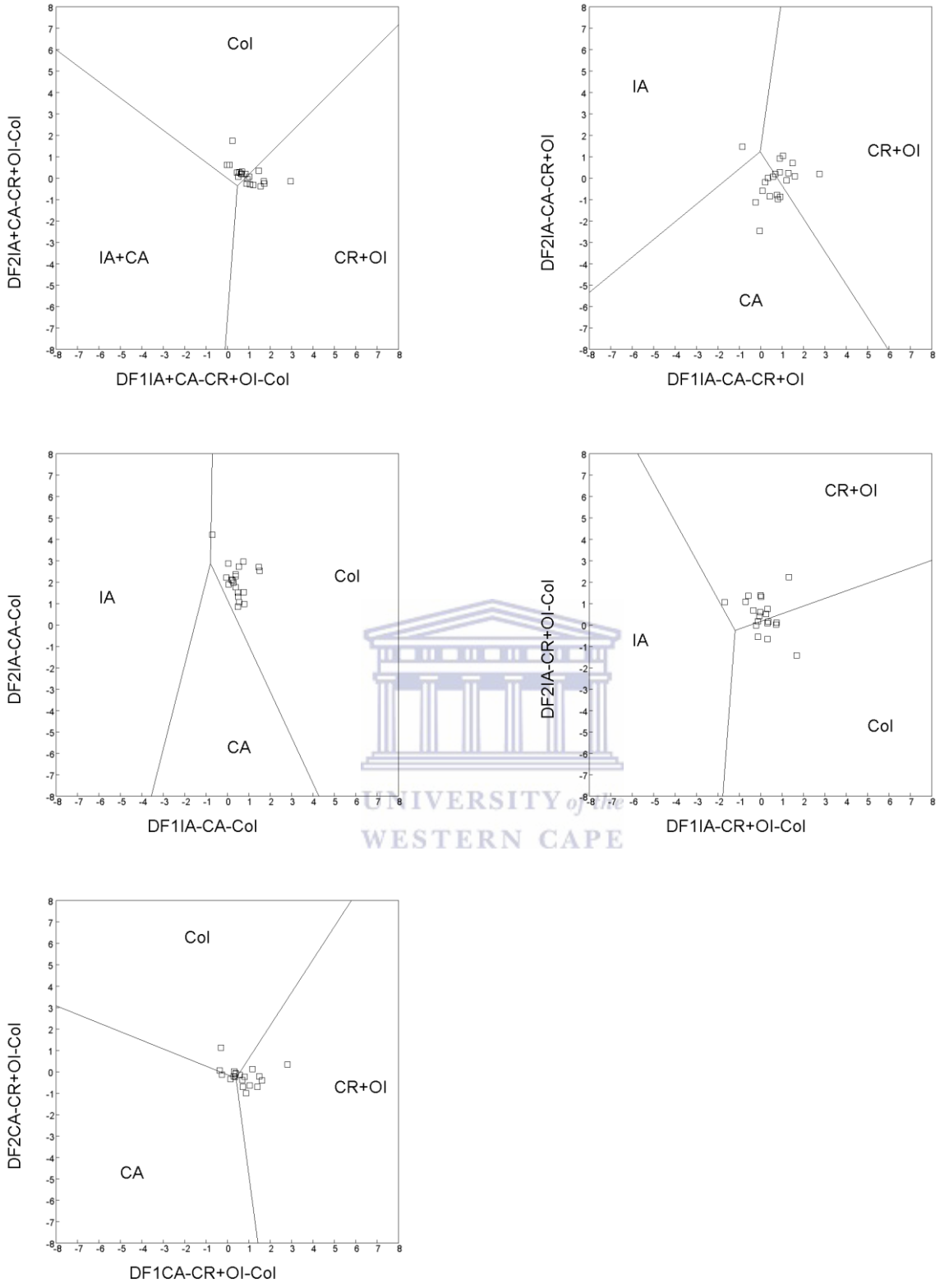

Figure 8-18. Application of the set of five multidimensional DF1 ‑DF2 diagrams based on log-ratios of immobile trace elements for the pink gneiss from the Kliprand study area (Verma et al., 2013). Three tectonic settings are shown on each diagram. (a) IA+CA ‑CR+OI ‑Col (b) IA ‑CA ‑CR+OI (c) IA ‑ CA ‑Col (d) IA ‑CR+OI ‑Col (e) CA ‑CR+OI ‑Col. These symbols are colourless as this software did not have the appropriates colouration. CR = Continental Rift, OI = Ocean-Island, IA = Island Arc, Col Collision and CA = Continental Arc.

The Ibequas Granite is a melt product of the metapelites. The metapelites were derived from sediments derived from a Paleoproterozoic-aged continental arc (hence that signature), with the sediments deposited in a rift-type basin (as shown above). Melting of that thus reflects these signatures. The Ibequas Granite wasn't likely emplaced in a rift setting (it was emplaced at a time of peak metamorphism and deformation).

On a similar note the augen gneiss carries a collisional setting. The 1.2 Ga tectonothermal event is largely believed to be a collisional event potentially between the Paleoproterozoic aged arc and some other (unidentified) continental block.

9.3a Source nature of the gabbro-norites

The gabbro-norite plots in the sub-alkaline basalt field (Figure 6-2) and exhibits Nb/Ta ratios of 12.66–23.08 (average = 14.5) and Zr/Hf ratios of 35.09–39.53 (average = 37.73) suggesting that they are mantle derived (Nb/Ta= and Zr/Hf= ratios of the mantle). The mantle sources can be recognized by the Th/Ta and Ta/Hf ratios, as shown in Figure 8-19. In the Th/ Ta vs. Ta/Hf plot (Figure 8-19), all the samples for the gabbro-norite plot mainly between the field of Depleted MORB Mantle (DMM) (the source of NMORB) and Upper Continental Crust (UCC). The plotting of the gabbro-norites between the DMM and UCC suggest that the gabbro-norites were derived from an enriched mantle source, most likely a subcontinental lithospheric mantle (Manya 2014).

The Th/Yb vs. Nb/Yb plot (Figure 8-20), displays the gabbro-norite lying above the MORB-OIB array, suggesting that either Th is enriched and/or Nb is depleted relative to the oceanic basalt array. This is a clear indication of a crustal influence. The enhanced Th concentration may have resulted due to the protoliths of these rocks experiencing crustal contamination, or they were formed in a subduction zone, thus Nb is depleted (Zhai et al. 2011). This interpretation is consistent with the straddle of the data points across the fields of MORB and VAB (volcanic arc basalt) as shown in Figure 8-21. The subcontinental lithospheric mantle can show a similar type of signature.

The rare earth elements (REE) of the meta- gabbro-norites have a strong negative REE slope [$(La/Sm)_N$ = 9.7] (Figure 6-19). This is not really typical of mafic rocks, particularly gabbro-norite which normally have flat REE patterns. These rocks are, therefore, relatively fractionated, as shown by their slight negative Eu anomalies, as well as the enrichment in the LREE relative to the HREE and enrichment in the LILE relative to the HFSE (figure 6-19). They are characterized by very low Nb/La ratios (0.14–0.61) and visible depletions in Nb, Ta, Zr, Hf and Ti (Figure 6-20). This indicates that their parental magmas were strongly influenced by assimilation and contamination of lithospheric components (Zhai et al. 2011). This is further confirmed by a low positive εNd(t) value (0.99; Table

18) suggesting the possibility of slight crustal assimilation. The $^{143}Nd/^{144}Nd$ initial ratio (0.512146) for the gabbro-norites are lower than MORB basalts suggesting an enriched component, and further suggests that these mantle derived magmas where subjected to minor degrees of crustal assimilation.

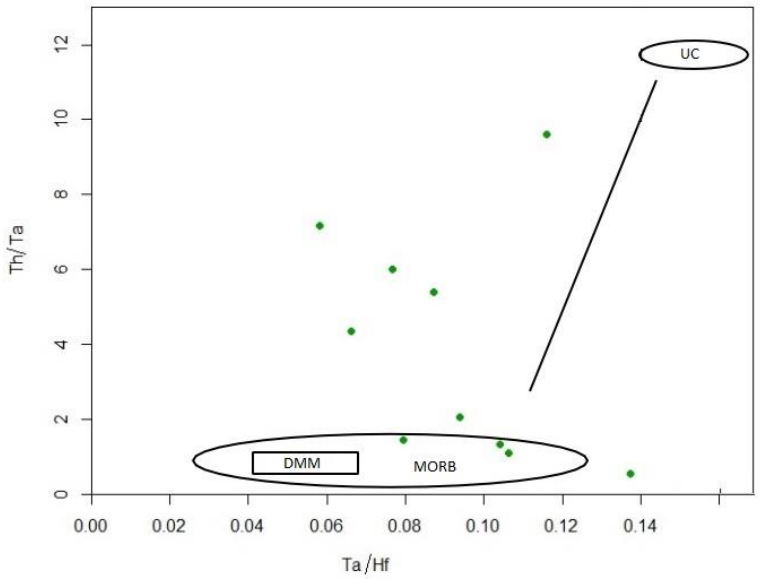

Figure 8-19. Ta/Hf vs. Th/Ta diagram for the gabbro-norites. DMM data is from Workman & Hart (2005), UC from Rudnick & Gao (2003) and NMORB data from Sun & McDonough (1989).

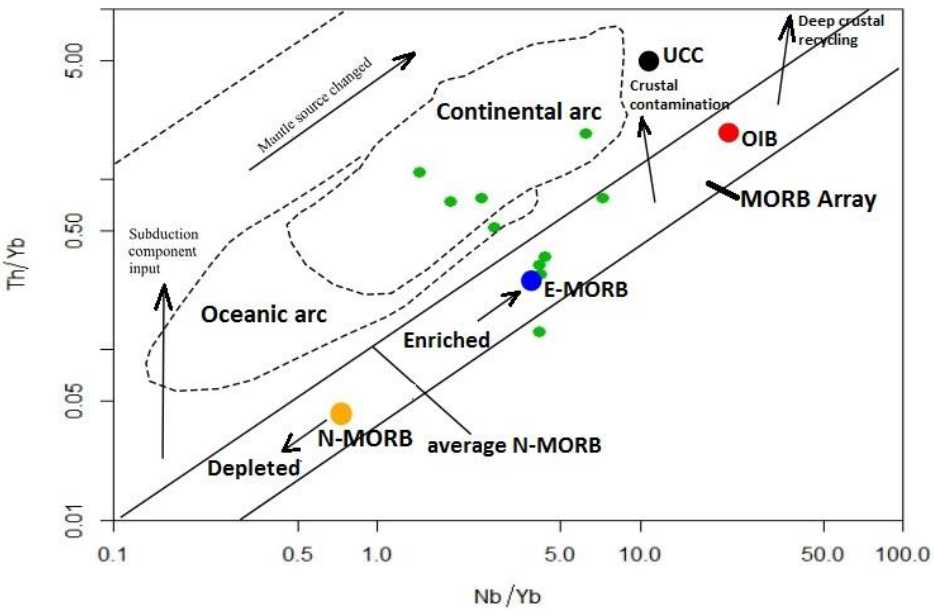

Figure 8-20. Th/Yb vs. Nb/Yb diagrams for the mafic rocks of this study, showing a continental arc affinity for the mafic rocks (after Pearce & Peate, 1995).

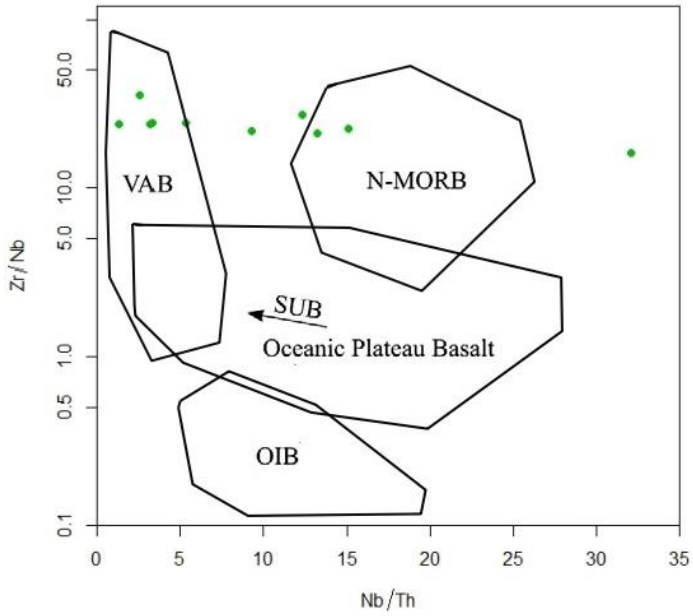

Figure 8-21. Zr/Nb-Nb/Th diagram of Condie (2005), SUB (subduction), VAB (volcanic arc basalt), OIB (Ocean island basalts), N-MORB (normal mid-ocean ridge basalt).

9.3b Tectonic setting of the gabbro-norites

Most gabbro-norites plot within the plate-margin basalt field (Figure 8-22), suggestive of a subduction-related setting. The fact that the gabbro-norite plots exclusively within the high K (calc-alkaline) series (Figure 6-18), together with the visible Nb depletion relative to La (Figure 6-20), as displayed by the low Nb/La ratios (avg. 0.31), the pronounced negative Nb–Ta trough (Figure 6-20), the dominantly negative to absent (average Eu/Eu* = 0.76) Eu anomaly and depletion of certain HFS elements relative to LIL elements all points to a typical arc environment.

Lin et al. (2015) state that within a subduction-related setting both the slab component and the mantle wedge contribute to the arc basalt composition. Thus the depletion in HFSE is related to the mantle–melt interaction during the percolation of mainly arc magmas through the overlying lithosphere (Lin et al. 2015). The presence of negative Nb and Ta anomalies can also be explained by the interaction of migrating melt and depleted mantle during the partial melting of subducted materials and/or relative immobility of Nb and Ta and other elements in aqueous fluids that are derived from the subducted slab (Lin et al. 2015). The low Nb/La ratio (avg. 0.31) of the analysed samples in this study suggests that the negative HFSE anomalies displayed by the gabbro-norite resulted from the interaction between depleted mantle and slab component sources (e.g. Lin et al. 2015).

The tectonic diagram described above is rather old, thus, in addition to this plot, the more updated diagrams of Agrawal et al. (2008) were used. The Kliprand domal structure is situated in a high grade metamorphic terrain, thus many elements are mobile under these conditions as previously discussed. The tectonic discrimination plots of Verma et al. (2006) and Verma and Agrawal (2011) for mafic rock types dominantly uses major elements, hence the immobile trace element plots of Agrawal et al. (2008) were used (Figure 8-23). Here most gabbro-norites plot within the OIB, IAB and CRB fields (Table 21; Figure 8-23). Figure 8-23 suggests some form of fractionation of these gabbro-norites seeing as how they define curvilinear trends.

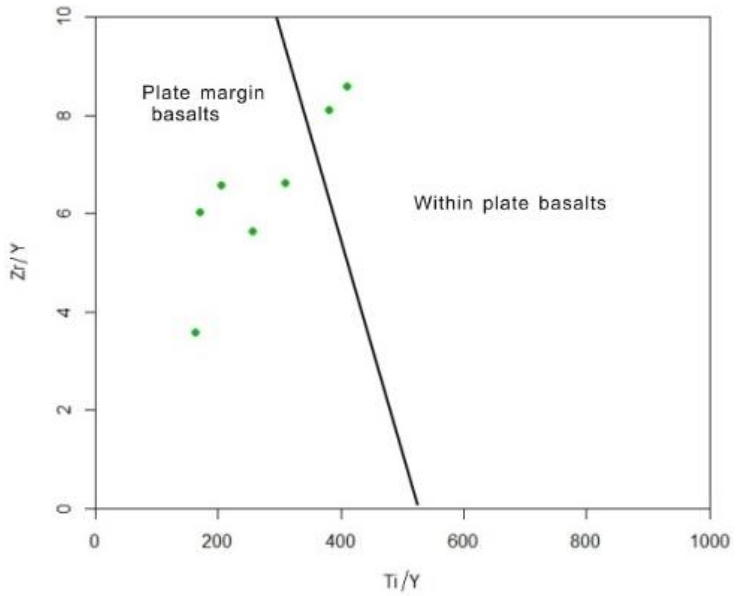

Figure 8-22. Zr/Y versus Ti/Y diagram after Rollinson (1993).

Table 20. Multidimensional diagrams for tectonic discrimination of the gabbro-norites

Reference, figure type	Discrimination diagram	Total no. of samples (%)	Number of discriminated samples				
			IAB	Within-plate			MORB
				CRB+OIB	CRB	OIB	
Agrawal et al. (2008); log-ratios of immobile trace elements	IAB-CRB+OIB-MORB	8 (100)	3 (37.5)	5 (62.5)	---	---	0 (0)
	IAB-CRB-OIB	8 (100)	3 (37.5)	---	1 (12.5)	4 (50)	---
	IAB-CRB+MORB	8 (100)	3 (37.5)	---	5 (62.5)	---	0 (0)
	IAB-OIB-MORB	8 (100)	3 (37.5)	---	---	5 (62.5)	0 (0)
	CRB-OIB-MORB	8 (100)	---	---	3 (37.5)	4 (50)	1 (12.5)
		40 (100)	12 (30)	5 (---)	11 (27.5)	16 (40)	1 (2.5)

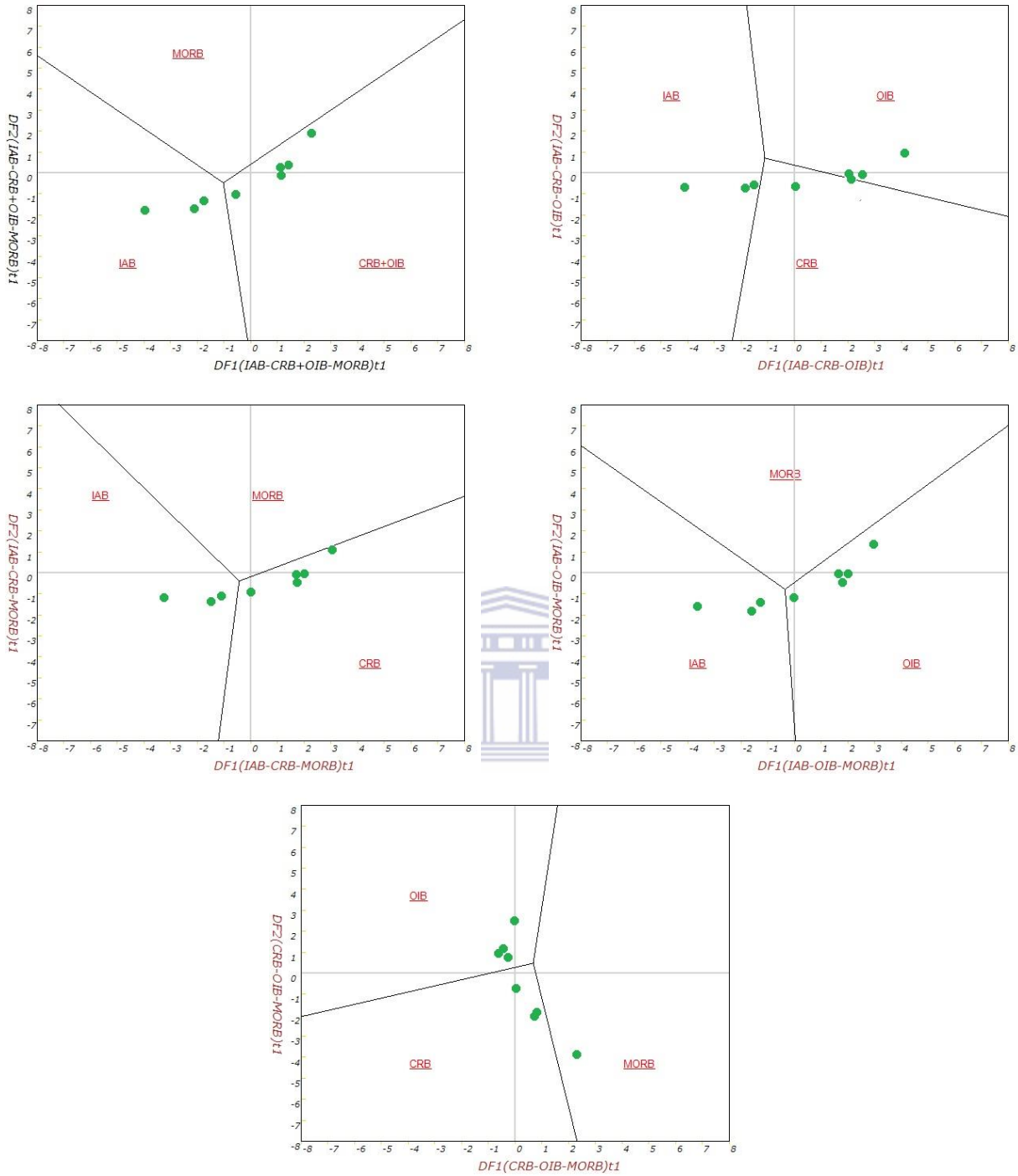

Figure 8-23. Statistical evaluation of the set of five discrimination diagrams based on natural logarithm transformation of trace-element ratios discriminant function DF1-DF2 (Agrawal et al. 2008) for island arc basalt (IAB), continental rift basalt (CRB), ocean island basalt (OIB) and mid-ocean ridge basalt (MORB), using basic and ultrabasic rocks from different tectonic settings. The subscript t1 refers to log-ratio transformation of trace-elements (subscript t1 instead of simply t was used, so this set of diagrams could be distinguished from the other set currently under preparation by Verma and Agrawal). (a) four-groups (IAB-CRB+OIB-MORB)$_{t1}$ diagram; (b) three-groups (IAB-CRB-OIB)$_{t1}$ diagram; (c) three-groups (IAB-CRB-MORB)$_{t1}$ diagram; (d) three-groups (IAB-OIB-MORB)$_{t1}$ diagram; and (e) three-groups (CRB-OIB- MORB)$_{t1}$ diagram.

Chapter 10 : Conclusion

Detailed field work combined with structural analysis, geochemistry and geochronology of highly deformed and metamorphosed Mesoproterozoic rock units of the central portion of the Garies Terrane, southwestern Namaqua Sector have been presented for the first time. The results and conclusions drawn from this work can be summarized as follows:

1. Six major lithological units (pink gneiss, Streaky augen gneiss, Ibequas granite, gabbro-norite, metaquartzite, and meta-pelite) were identified based on field investigation, petrography and geochemistry. The pink gneiss is the dominant lithological unit found throughout the Kliprand domal structure, based on field observations and the extent of this rock on the geologic map, the pink gneiss is more likely to be a volcanic rock, and possibly the volcanic, extrusive equivalent of the intrusive streaky augen gneiss (I may be wrong of course). The metasedimentary rocks occur more as thin little slivers within the sea of magmatic rocks, so the pink gneiss does not really fit with being a sedimentary rock despite its quartzofeldspathic nature compared to the predominantly more pelitic nature of the metasedimentary rocks.
2. The streaky augen gneiss and pink gneiss show characteristics resembling that of A-type granites (the high concentrations of K, LILE, HFSE and high Fe/Mg ratios for the felsic magmatic rocks (streaky augen gneiss, pink gneiss and Ibequas granite), but with some similarities to S- and I-type granites. The geochemical similarities between the pink gneiss and streaky augen gneiss make it seem as if the pink gneiss is simply the extrusive equivalent of the intrusive augen gneiss.

   The negative Ba, Sr, Nb and Ti anomalies, negative Nb-Ta (also suggestive of a subduction-related processes) trough low U and prominent positive Rb, Pb, Th, K and La anomalies, all strongly link to a crustal influence or derivation from a crustal source. The enrichments in Th and U, depletions of Nb and Ta relative to La and Nb–Y–Zr/4 and Nb–Ce–Y discrimination diagrams of Eby (1992) reveal that the streaky augen gneiss and pink gneiss were derived from the melting of subcontinental lithospheric mantle.

   The majority of the streaky augen gneiss and pink gneiss samples plotted in the collision field on the tectonic discrimination diagrams (Figure 8-17) indicating that they were generated from melting of a thickened crust or were emplaced during a continental collision event. The fact that the streaky augen gneiss and pink gneiss has both an arc and collisional tectonic signature on the tectonic discrimination plots, further likely reflects a collisional event.

3. The charnockite in the Kliprand area is a metasomatic product and not a direct magmatic fractionate as is also evident by the steeply negative slope for the HREE (Samples C133 $(Gd/Yb)_N$ = 2.75 and C106$(Gd/Yb)_N$ = 4.78, Figure 6-21) indicating that they are highly fractionated with the HREE more fractionation than the LREE. The geochemical similarities to thestreaky augen gneiss and pink gneiss all strongly points to a crustal influence or derivation from a crustal source. The enrichments in Th and U, and depletions of Nb and Ta relative to La for the charnockite suggest lower crustal metamorphism.

   The charnockite has the highest probability (56%) of samples plotting in the continental arc field the charnockite. The continental arc signature obtained, indicates that the material with a continental arc signature/ composition/ an old continental arc, including portions of the subcontinental lithospheric mantle melted to give rise to the metasomatic charnockite.
4. The strong negative REE slope [$(La/Sm)_N$ = 9.7] of the gabbro-norite is not typical of mafic rocks, particularly gabbro-norites which normally have flat REE patterns. The LREE enrichment relative to the HREE (La_N/Sm_N = 2.87) suggests derivation from a relatively enriched source. Crustal involvement is also seen in the strong Pb and Th enrichment (compared to UCC to LCC values) enrichment, negative Ti anomaly and a Nb-Ta "trough". The gabbro-norite is characterized by very low Nb/La ratios (0.14–0.61) and visible depletions Zr, Hf and Ti, this indicates that their parental magmas were strongly influenced by assimilation and contamination of lithospheric components.

   The immobile trace element plots of Agrawal et al. (2008), displays the majority of the gabbro-norites plotting within the OIB, IAB and CRB fields (Table 21; Figure 8-23). Based on this observation and the fact that the majority of the gabbro-norites plot within the plate-margin basalt field, is suggestive of a subduction-related setting (Figure 8-22). The fact that the gabbro-norite plots exclusively within the high K (calc-alkaline) series (Figure 6-18), together with the notable Nb depletion relative to La (Figure 6-20), as indicated by low Nb/La ratios (avg. 0.31), the pronounced negative Nb–Ta trough (Figure 6-20), the Eu anomalies that are mostly negative to absent (average Eu/Eu* = 0.76) and depletion of certain HFSE relative to LILE all points to a typical arc environment**.**
5. With regard to the provenance, the metasedimentary rocks were mainly derived by the erosion of felsic to intermediate igneous rocks (e.g. granodioritic in composition). The metapelites was derived from erosion of magmatic material originally derived from a depleted source

   The quartzites are very K and Rb-rich and hence feldspathic, but are quite mature, as evident in their low Ca, Ti, Mn, Fe and Co concentrations. The low Nb suggests a subduction-related

signature to the provenance to these rocks. The high Pb suggests a strong crustal signature to the provenance, as does the high Th and U. The mature nature is also expressed in slight fractionation of the LREE over the HREE.

The metasedimentary rocks (quartzite and metapelite) in the Kliprand area were derived from a Paleoproterozoic-aged continental arc provenance (as displayed by the tectonic discrimination diagrams in Chapter 9.1b), with the sediments deposited in a rift-type basin (as shown by the retention of the metapelite signature in the Ibequas granite (has the highest probability (56%) of samples plotting in the continental rift + ocean-island field, with remainder of the samples plotting in the continental arc field (26%)). Although no actual arc material is found or is evident in this region or the Garies terrane, the metasedimentary rocks carry the signature of an island arc and possibly were deposited on the margin, or within an extensive back-arc environment. A likely possibility is that the arc is represented by the Richtersveld Subprovince to the north.

6. Similarly to the Streaky augen gneiss and pink gneiss the Ibequas granite also has characteristics similar to A-type granites. Based on the presence of garnet in the granite, its common close association with the metapelite in the field, as well as the fact that the Ibequas granite displays S-type characteristics (strongly peraluminous and have some values similar to the S-type values of Whalen et al. 1987, REE from Collins et al., 1982), suggests that it was derived from melting of a sedimentary source.

   The Ibequas granite has the highest probability (56%) of samples plotting in the continental rift + ocean-island field. The Ibequas Granite is a melt product of the metapelites, melting of the metapelite (source rock) would reflect its signature in the Ibequas granite (newly formed rock). The Ibequas granite was thus not emplaced in a rift + ocean-island type setting (sediments of the sedimentary rock were deposited in a rift setting) but was rather emplaced at a time of peak metamorphism and deformation

7. Based on the new U-Pb geochronology data, both varieties of the pink gneiss were emplaced at around 1144-1135 Ma, with a major thermal event (peak metamorphism) at around 1077-1052 Ma. The emplacement of the pink gneiss (likely as volcanic extrusive) likely occurred toward the end of the peak magmatic episode related to the magmatic emplacement of the LNS (so ~1195-1135 Ma). The new U-Pb data of the Ibequas granite is unique in that it has two highly concordant age populations, with an older population and a younger highly concordant population of zircons. The older concordant age populations (1150-1165 Ma spot ages) has Th/U ratios of magmatic origin, whilst the 1067 Ma ages have low Th/U ratios (e.g. spot 30-5) suggesting metamorphic growth. Likewise, some are higher (e.g. 30-18), but

in general these are lower suggesting a greater thermal effect. The Ibequas granite thus represents melting of an older source with zircons of around 1153-1135 Ma (these are the magmatic ages seen in both varieties of the pink gneiss) and likely represents a major magmatic episode at that time. The quartzites were severely affected at around 1130/1120 Ma and possibly underwent anatectic melting during emplacement of the voluminous pink gneiss, and then experienced a subsequent high temperature event around 1050 Ma. With regard to the new U-Pb data of the quartzite Spot Q066-56 has an age of 1143 Ma and is 100% concordant corresponding to the ages (exactly) in the pink gneiss samples. The slightly younger ages of 1127 (sample Q066-59) and 1128 (sample Q066-72) may be due to the thermal state of the rock at that time. If it was partially melted at 1143 Ma, then it may have recrystallized at around 1128 Ma. Also the Th/U ratios are low suggesting a degree of metamorphism. The zircons extracted from the charnockite samples are very long and elongate and poorly zoned with a dull luminosity which is fairly typical of metamorphic zircon. The zircons in the charnockite reflect those found in the pink gneiss and there was renewed growth during the metasomatic event (not so much as emplacement as opposed to alteration). The most concordant ages obtained from the charnockite give ages around 1077-1084 Ma, these age are essentially the same as that of high-T metamorphism in the biotite-rich pink gneiss and is virtually the same as the one age obtained from the Ibequas Granite. The gabbro-norite has an emplacement age of 1059Ma indicating that it is the youngest rock in the area. The high U contents (average U content of > 1300 ppm) and Pb concentrations of 113-397ppm (Table 19) recorded for the gabbro-norites, resemble those trends that are characteristic of derivation from crustal areas subjected to high degrees of metamorphism (lower crustal is likely given the upper granulite facies conditions).

8. New isotopic findings of rock types in the Kliprand area indicates that the gabbro-norite has a small measure of an enriched (possibly crustal) component in the source, or it may reflect crustal contamination or a small degree of mixing with a more enriched source (positive εNd(t) value of 0.99 (Table 18), is close to 0). The streaky augen gneiss, pink gneiss and Ibequas granite has a crustal component influence (as displayed by their high initial 87Sr/86Sr ratio), the low εNd(t) value that is close to zero indicates that the source was mildly depleted but not strongly so. Its likely source, when taken with the negative $f^{Sm/Nd}$ value (streaky augen gneiss = -0 .319, biotite rich pink gneiss = -0.380, biotite poor pink gneiss = -0.337 and Ibequas granite = -0.5237) is of a crustal source carrying some depleted signature. The high initial Sr value of 0.76344 recorded for the quartzite, induicates that this rock has suffered anatectic events and had its isotopic ratios severely disturbed. This is

further corroborated by the low εNd(t) values (Table 18) recorded by the quartzite (-0.27) and metapelite (-0.03), these values aren't particularly strongly negative at all, so they were derived from a provenance that was itself having a fairly depleted source signature. The (143Nd/144Nd)i value of for charnockite (0.511309) is fairly high, approaching that of the gabbronorite suggesting some deleted source component. It may give indications as to the origin of the metasomatic fluids. The charnockite has a positive εNd(t) value of 0.91 (this is similar to that of the gabbronorite, so a depleted, even mantle-derived component is present. It may well be that the gabbronorite brought with it fluids that fluxed through the lower crust and metasomatised these upper crustal rocks such as the pink gneiss giving rise to this metasomatic charnockite).

9. Based on field observations four major deformational events were found. The first deformational event (D_1) was responsible for the tectonic banding in the gneisses (S_1 foliation) and in places by the first episode of folding, the F_1 intrafolial folds. This was followed by a major event, the D_2 deformational event (or Namaqua event), during which the first major structures were observed. The structures which formed during D_2, are large scale tight folds with a pervasively developed subparallel axial planar fabric (S_2) with a strong associated mineral lineation L_2 developed. The lineations in the Kliprand domal structure (L_2) have been rotated by the later D_3 and D_4 deformational events. The timing of D_2, within the Kliprand dome could be constrained by the fact that the S_2 foliation was observed in all of the lithologies (is most prominent in the Gabbro-norite), except the Ibequas granite and metasomatic charnockite. The D_3 deformational event is characterized by E-W trending open folds. On the aerial photos and google earth images (Figure 5-2), these folds could clearly be viewed as large scale fold closures. In addition to these large structures, D_3 also produced non-penetrative, sub-vertical (S_3) planar cleavages and parasitic F_3 folds (restricted to the F_3 fold closures). Rocks that have been subjected to melting, such as the metapelite, and its potential melt product, the Ibequas granite, were commonly found occupying the hinges of these large fold closures, indicating an intense pressure at those areas of the fold. The S_2 and S_3 fold closure are at an angle to one another in the hinge of the F_3 fold closure, and became aligned to one another away from the fold hinge. The fourth deformational event (D_4) produced no new deformational fabrics but rather caused the reorientation of the previous S_2 and S_3 fabrics.
10. With the exception of the abundant small scale joints, no major brittle structures were observed in the study area. Therefore, the only remaining possibilities of formation of the Kliprand domal structure according to Yin (2004) are multiple folding events and diapirism.

Field studies have revealed abundant boudins in the area, resulting in the possibility that the Kliprand domal structure may be a large scale boudin. Foliations in the Kliprand dome have a gradual dip both in the core and the rim of the dome, whereas domal structures formed as a result of diapirism usually have horizontal foliations in the core and steeper foliations along the rim. The Kliprand dome, hence, did not likely form as a result of diapirism. The Kliprand domal structure may in fact be a type 1 interference fold. The presence of the smaller dome within the larger Kliprand dome does not, however, strengthen this argument. The competency difference between the metapelite and the streaky augen gneiss is the main cause of boudins on a small scale. However, in order for the dome within a dome concept to be valid, an extremely high competency difference is required, which is not the case in Kliprand wherein the smaller dome comprises similar rock types to its larger equivalent. From the four mechanisms suggested above, the Kliprand domal structure closely resembles a sheath fold. The abundant boudins in the study area and the fact that the Kliprand area has been subjected to high grade metamorphism (upper granulite facies metamorphism), suggests that the ductility and strain value was high enough for sheath folding to have developed. This structure also best describes the dome within a dome concept, seeing that sheath folds commonly display eye structures. Which according to the data in this study, would classify the Kliprand domal structure as a cats eye sheath fold.

Reference list

Agrawal, S., Guevara, M. and Verma, S.P. 2008. Tectonic discrimination of basic and ultrabasic volcanic rocks through log-transformed ratios of immobile trace elements. International Geology Review, 50, 1057–1079.

Albat, H.M. 1979. The Kliprand area — a major charnockite province in Namaqualand. Annual Report, Precambrian Research Unit, University of Cape Town, 7, 49–64.

Albat, H.M. 1983. Garnet-cordierite thermometry/barometry and the temperature-pressure conditions of formation of granulite-facies metapelites in the Kliprand area. Annual Report, Precambrian Research Unit, University of Cape Town, 18–20, 105–115.

Albat, H.M. 1984. The Proterozoic granulite facies terrane around Kliprand, Namaqualand Metamorphic complex. Bulletin, Precambrian Research Unit, University of Cape Town, 33, 386.

Allen, P., Condie, K.C. and Narayana, B.L. 1985. The geochemistry of prograde and retrograde charnockite-gneiss reactions in southern India. Geochimica et Cosmochimica Acta, 49, 323–336.

Alsop, G.I. and Holdsworth, R.E. 2006. Sheath folds as discriminators of bulk strain type. Journal of Structural Geology, 28, 1588–1606.

Anderson, J.L. and Morrison, J. 2005. Ilmenite, magnetite, and peraluminous Mesoproterozoic anorogenic granites of Laurentia and Baltica. Lithos, 80, 45–60.

Andreoli, M.A.G., Moore, J.M. and Hambletonjones, B.B. 1991. Geology and mineralogy of the Hondekloof nickel prospect, Kliprand, Cape Province. Internal Report, Schonland Research Centre, University of Witwatersrand, 31 pp.

Andreoli, M.A.G., Hart, R.J., Ashwal, L.D., Coetzee, H. 2006. Correlations between U, Th content and metamorphic grade in the Western Namaqualand belt, South Africa, with Implications for radioactive heating of the crust. Journal of Petrology, 47, 1095–1118.

Armstrong-Altrin, J.S. and Verma, S.P. 2005. Critical evaluation of six tectonic setting discrimination diagrams using geochemical data of Neogene sediments from known tectonic settings. Sedimentary Geology, 177, 115–129.

Baars, F.J. 1990. Geologic and petrologic evidence for granulite-facies partial melting in the Garies–Platbakkies supra-crustal gneiss belt, Namaqualand Metamorphic Complex, South Africa. M.Sc. thesis (Unpublished), University of Cape Town, Cape Town, South Africa, 128 pp.

Bailie, R., Armstrong, R. and Reid, D. 2007. Composition and single zircon U-Pb emplacement and metamorphic ages of the Aggeneys Granite Suite, Bushmanland, South Africa: South African Journal of Geology, 110, 87–110.

Bailie, R.; Gutzmer, J.; Rajesh, H.M. 2010. Lithogeochemistry as a tracer of the tectonic setting, lateral integrity and mineralization of a highly metamorphosed Mesoproterozoic volcanic arc sequence on the eastern margin of the Namaqua Province, South Africa. Lithos, 119, 345–362.

Bailie, R., Gutzmer, J. and Rajesh, H.M. 2011. Petrography, geochemistry and geochronology of the metavolcanic rocks of the mesoproterozoic Leerkrans Formation, Wilgenhoutsdrif Group, South Africa - back-arc basin to the Areachap volcanic arc. South African Journal of Geology, 114, 167–194.

Bakkiaraj, D., Nagendra, R. and Nagarajan, R. 2010. Geochemistry of sandstones from the Upper Cretaceous Sillakkudi Formation, Cauvery Basin, southern India: Implication for provenance. Journal of the Geological Society of India, 76, 453–467.

Barton, E.S., Burger, A.J. 1983. Reconnaissance isotopic investigations in the Namaqua mobile belt and

implications for Proterozoic crustal evolution—Upington geotraverse. In: Botha, B.J.V. (Ed.), Namaqualand Metamorphic Complex: Special Publication of the Geological Society of South Africa, 10, 173–191.

Barton, M.D., and Young, S. 2002, Non-pegmatitic deposits of beryllium: Mineralogy, geology, phase equilibria and origin, in Grew, E.S., ed., Beryllium: Mineralogy, petrology and geochemistry: Reviews in Mineralogy and Geochemistry, 50, 591–691.

Bekker, P.G. 1980. The detailed geology and geochemistry of the Hondekloof prospect (Nuwefontein ptn. 3 block 3018AD, Kliprand). Internal Report, O'okiep Copper Company Limited, 10.

Ben Othman, D., Polve, M., Allerge, C.J. 1984. Nd-Sr isotopic composition of granulites and constraints on the evolution of the lower continental crust. Nature, 307, 510-515.

Bhatia, M.R. 1983. Plate Tectonics and Geochemical Composition of Sandstones. The Journal of Geology, 91, 611–627.

Bhatia, M.R. and Crook, K.A.W. 1986. Trace element characteristics of greywackes and tectonic setting discrimination of sedimentary basins. Contributions to Mineralogy and Petrology, 92, 181–193.

Bial, J., Büttner, S.H. and Frei, D. 2015. Formation and emplacement of two contrasting late-Mesoproterozoic magma types in the central Namaqua Metamorphic Complex (South Africa, Namibia): Evidence from geochemistry and geochronology. Lithos, 224-225, 272–294.

Blewett, R.S. 2002. Archaean tectonic processes: a case for horizontal shortening in the North Pilbara Granite-Greenstone Terrane, Western Australia. Precambrian Research, 36, 241-258.

Blignault, H.J., Van Aswegen, G., Van der Merwe, S.W. and Colliston, W.P. 1983. The Namaqualand Geotraverse and environs: part of the Proterozoic mobile belt. Special Publication of the Geological Society of South Africa, 10, 1-29.

Boynton, W.V. 1984. Geochemistry of the rare earth elements: meteorite studies. In: P. Henderson (Editor). Rare earth element geochemistry. Elsevier, Amsterdam, The Netherlands, 63-114.

Brun, J.P. and Van Den Driessche, J. 1994. Extensional gneiss domes and detachment faults- structure and kinematics. Bulletin de la Societé Geologique de France, 165,519-530.

Carmichae,l R.S. 1989. Practical handbook of physical properties of rocks and minerals. CRC Press, Boca Raton, 834.

Chappell, B.W. and White, A.J.R. 2001. Two contrasting granite types: 25 years later. Australian Journal of Earth Sciences, 48, 489–500.

Chaudhuri, S. and Cullers, R.L. 1979. The distribution of rare-earth elements in deeply buried Gulf Coast sediments. Chemical Geology, 24, 327–338.

Chen, M., Sun, M., Cai, K., Buslov, M.M., Zhao, G., Rubanova, E.S. 2014. Geochemical study of the Cambrian-Ordovician meta-sedimentary rocks from the northern altai-mongolian terrane, northwestern Central Asian Orogenic Belt: Implications on the provenance and tectonic setting. Journal of Asian Earth Sciences, 96, 69–83.

Clifford, T.N., Barton, E.A., Retief, E.A., Rex, D.C. and Fanning, C.A. 1995. A crustal progenitor for the intrusive anorthosite-charnockite kindred of the cupriferous Koperberg Suite, O'okiep district, Namaqualand, South Africa; New isotope data for the country rocks and intrusives. Journal of Petrology, 36, 231–258.

Clifford, T.N., Barton, E.S., Stern, R.A. and Duchesne, J-C. 2004. U-Pb calendar for Namaquan (Grenville) crustal events in the granulite-facies terrane of the O'okiep Copper District of South Africa. Journal of Petrology, 45, 669–691.

Clifford, T.N., Barton, E.A. 2012. The O'okiep Copper District, Namaqualand, South Africa: a review of the geology with emphasis on the petrogenesis of the cupriferous Koperberg Suite. Miner Deposita, 47, 837–857.

Cocherie, A. 1986. Systematic use of trace element distribution patterns in log-log diagrams for plutonic suites. Geochimica et Cosmochimica Acta, 50, 2517–2522.

Collins, W.J. Beams, S.D., White, A.J.R., and Chappell, B.W. 1982. Nature and orogin of A-type granites with particular reference to southeastern Australia. Contribution to Mineralogy and Petrology, 80, 189–200.

Colliston, W.P., Schoch, A.E. 2006. The distribution and diagnostic features of deformed plutonic rocks in two terranes of the Namaqua mobile belt along the Orange (Gariep) River, South Africa. S. African Journal of Geology, 109, 301–324.

Colliston, W.P., Schosh, A.E. 2013. Wrench-shearing during the Namaqua Orogenesis-Mesoproterozoic late stage deformation effects during Rodinia assembly. Precambrian Research, 233, 44– 58

Colliston, W.P., Schoch, A.E. and Cole, J. 2014. The Grenvillian Namaqua-Natal fold belt adjacent to the Kaapvaal Craton: 1. Distribution of Mesoproterozoic collisional terranes deduced from results of regional surveys and selected profiles in the western and southern parts of the fold belt. Journal of African Earth Sciences, 100, 7–19.

Condie, K.C. 2005. High field strength element ratios in Archean basalts: A window to evolving sources of mantle plumes? Lithos, 79, 491–504.

Cornell, D.H., Thomas, R.J., Bowring, S.A., Armstrong, R.A., Grantham, G.H. 1996. Protolith interpretation in metamorphic terranes: a back-arc environment with Besshi-type base metal potential for the Quha Formation, Natal Province, South Africa. Precambrian Research, 77, 243-271.

Cornell, D.H., Thomas, R.J., Moen, H.F.G., Reid, D.L., Moore, J.M., Gibson, R.L. 2006. The Namaqua-Natal Province In: Johnson, M.R., Anhaeusser, C.R., Thomas, R.J. (Eds.), The Geology of South Africa. Geological Society of South Africa, Johannesburg/Council for Geoscience, Pretoria, 325–379.

Cornell, D.H., Petterson, A., Whitehouse, M.J., and Schersten, A. 2009. A New Chronostratigraphic Paradigm for the Age and Tectonic history of the Mesoproterozoic Bushmanland Ore District, South Africa. Society of Economic Geologists. Inc. Economic Geology, 104, 385-404.

Cox, K.G, Bell, J.D. and Pankhurst, R.J. 1979. The Interpretation of Igneous Rocks. George, Allen and Unwin, London, 450.

Cullers, R.L. 1995. The controls on the major- and trace-element evolution of shales, siltstones and sandstones of Ordovician to tertiary age in the Wet Mountains region, Colorado, U.S.A. Chemical Geology, 123, 107–131.

Cullers, R.L. 2000. The geochemistry of shales, siltstones and sandstones of Pennsylvanian-Permian age, Colorado, USA: Implications for provenance and metamorphic studies. Lithos, 51, 181–203.

Cullers, R.L. 2002. Implications of elemental concentrations for provenance, redox conditions, and metamorphic studies of shales and limestones near Pueblo, CO, USA. Chemical Geology, 191, 305–327.

Davis, G.H. and Reynolds, S.J.; Kluth, C.F. 2011. The structural geology of rocks and regions (3rd ed.).

Davies, G.R., Gledhill, A. and Hawkesworth, C. 1985. Upper crustal recycling in southern Britain: evidence from Nd and Sr isotopes. Earth Planet. Sci. Lett., 75, 1-12.

De Beer, J.H. and Meyer, R. 1983. Geoelectrical and gravitational characteristics of the Namaqua-Natal mobile belt and its boundaries. Geologic Society of South Africa Special Publicie, 10, 91 -100.

De Beer, C.H. 2010. The geology of the Garies area. Explanation to Sheet 3017 Garies, Scale 1:250 000. Council

for Geoscience.

DePaolo, D.J., Wasserburg, G.J. 1976. Nd isotopic variations and petrogenetic models. Geophysical Research Letters, 3, 249–252.

Diergaardt, B.N. 2013. Rhyolitic volcanism in the Onverwacht Group, Barberton Greenstone Belt. M.Sc. thesis, Stellenbosch University, Cape Town, South Africa.

Dixon, J.M. 1975. Finite strain and progressive deformation in models of diapiric structures. Tectonophysics, 28, 89–124.

Duchesne, J.C., Auwera, J.V., Li´egeois, J.P., Barton, E.S., Clifford, T.N. 2007. Geochemical constraints of the petrogenesis of the O'okiep Koperberg Suite and granitic plutons in Namaqualand, South Africa: A crustal source in Namaquan (Grenville) times. Precambrian Research, 153, pp.116–142.

Eby, G.N. 1992. Chemical subdivision of the A-type granitoids:Petrogenetic and tectonic implications. Geology, 20, 641–644.

Eby, G.N. 1990. The A-type granitoids: A review of their occurence and chemical characteristics and speculatioins on their petrogenesis. Lihtos, 26, 115–134.

Eglington, B.M., Thomas, R.J., Armstrong, R.A., Walraven, F. 2003. Zircon geochronology of the Oribi Gorge Suite, KwaZulu-Natal, South Africa: constraints on the timing of trans-current shearing in the Namaqua-Natal Belt. Precambrian Research, 123, 29–46.

Eglington, B.M. 2006. Evolution of the Namaqua-Natal Belt, southern Africa - A geochronological and isotope geochemical review. Journal of African Earth Sciences, 46, 93–111.

Escuder-Viruete, J., Pérez-Estaún, A., Weis, D., Friedman, R. 2010. Geochemical characteristics of the Río Verde Complex, Central Hispaniola: Implications for the paleotectonic reconstruction of the Lower Cretaceous Caribbean island-arc. Lithos, 114, 168–185.

Eskola, P.E. 1948. The problem of mantled gneiss domes. Quarterly Journal of the Geological Society, 104, 461–476.

Elzein 2010 weathering of rocks

Feng, R. and Kerrich, R. 1990. Geochemistry of fine-grained clastic sediments in the Archean Abitibi greenstone belt, Canada: Implications for provenance and tectonic setting. Geochimica et Cosmochimica Acta, 54, 1061–1081.

Floyd, P.A. and Leveridge, B.E. 1987. Tectonic environment of the Devonian Gramscatho basin, south Cornwall: framework mode and geochemical evidence from turbiditic sandstones. Journal of the Geological Society, 144, 531–542.

Fossen, H. 2010. Structural geology, Cambridge. Cambridge University Press.

Fourie, D. 2010. An Isotope Study of the Felsic Units of the Bushveld Large Igneous Province, South Africa. M.Sc. thesis, University of Cape Town, Cape Town, South Africa.

Frei, D. and Gerdes, A., 2009. Precise and accurate in situ U-Pb dating of zircon with high sample throughput by automated LA-SF-ICP-MS. Chemical Geology, 261, 261–270.

Frost, B.R., Barnes, C.G., Collins, W.J., Arculus, R.J., Ellis, D.J., Frost, C.D. 2001. A geochemical classification for granitic rocks. Journal of Petrology, 42, 2033-2048.

Gerdes, A. and Zeh, A. 2006. Combined U-Pb and Hf isotope LA-(MC)-ICP-MS analysis of detrial zircons: comparison with SHRIMP and new constraints for the provenance and age of an Armorican metasediment in Central Germany. Earth and Planetary Science Letters, 249, 47–61.

Goldstein, S.L., O'Nions, R.K. and Hamilton, P.J. 1984. A SmNd isotopic study of atmospheric dusts and particulates from major river systems. Earth and Planetary Science Letters, 70, 221–236.

Grant, J.A. 2005. Isocon analysis: A brief review of the method and applications. Physics and Chemistry of the Earth, 30, 997–1004.

Grant, J.A. 1986. The isocon diagram-a simple solution to Gresens' equation for metasomatic alteration. Economic Geology, 81, 1976–1982.

Gresens, R.L. 1967. Composition-volume relationships of metasomatism. Chemical Geology, 2, 47–65.

Gromet, L.P.; Dymek, R.F.; Haskin, L.A. and Korotev, R.L. 1984. The "North American shale composite: its compilation, major and trace element chracteristics. Geochim. Cosmochim. Acta, 48, 2469-2482.

Gu, X.X., Liu, J.M., Zheng, M.H., Tang, J.X., Qi, L. 2002. Provenance and tectonic setting of the proterozoic turbidites in Hunan, South China: geochemical evidence. Journal of Sedimentary Research2, 72, 393–407.

Hamman, J.N., Rozendaal, A. and Jordaan, W. 1996. Gabbro-norite hosted Ni-Cu-(Co) sulphide mineralisation in southern Namaqualand and its relationship to the cuperiferous Koperberg Suite of the Okiep Copper District, South Africa. South African Journal of Geology, 99, 153–168.

Harris, N.B.W., Pearce, J.A. and Tindle, A.G. 1986. Geochemical characteristics of collision-zone magmatism. In: Coward M.P. and Reis A.C. (eds.), Collision tectonics. Special publication geological society. 19, 67-81.

Herron, M.M. 1988. Geochemical classification of terrigenous sands and shales from core or log data. Journal of Sedimentary Research, 58, 820–829.

Hoskin, P.W.O.; Black, L.P. 2000. Metamorphic zircon formation by solid state recrystallization of protolith igneous zircon. Journal Metamorphic Geology. 28: 423-439

Irvine, T.N. and Baragar, W.R.A. 1971. A guide to the chemical classification of the common volcanic rocks. Can. F. Earth Sci., 8, 523-548.

Holm, D.K., Snow, J.K, and Lux, D.R. 1992. Thermal and barometric constraints on the intrusive and unroofing history of the Black Mountains: implications for timing, dip and kinematics of detachment faulting in the Death Valley region, California. Tectonics, 11,507-522

Jacobs, J., Pisarevsky, S., Thomas, R.J., Becker, T. 2008. The Kalahari Craton during the assembly and dispersal of Rodinia. Precambrian Research, 160, 142–158.

Jiang, N. Zhang, S., Zhou, W., Liu, Y. 2009. Origin of a Mesozoic granite with A-type characteristics from the North China craton: Highly fractionated from I-type magmas? Contributions to Mineralogy and Petrology, 158, 113–130.

Johnson, S.D. 2005. Structural geology of the Usakos dome in in the Damara Belt, Namibia. M.Sc. thesis, Stellenbosch University, Cape Town, South Africa.

Joubert, P. 1971. The regional tectonism of the gneisses of part of Namaqualand Metamorphic Complex. Bulletin of the Precambrian Research Unit, University of Cape Town, 10, 220 .

Joubert, P. and Waters, D.J. 1980. The occurrence of kyanite at Zoutpan and metamorphism in western Namaqualand. Annual Report, Precambrian Research Unit, University of Cape Town, 17, 74–87.

Kisters, A.F.M., Gibson, R.L., Anhauesser, C.R. 1996. Steep structure formation in the Okiep Copper District, South Africa: bulk inhomogeneous shortening of a high-grade metamorphic granite-gneiss sequence. Journal of Structural Geology, 18, 735 to 751.

Kuno, H. 1968. Differentiation of basalt magmas. In: Hess H.H. and Poldervaart A. (eds.), Basalts: The Poldevaart treatise on rocks of basaltic composition, 2. Interscience, New York, 623-688.

Lambert, C.W. 2013. Granitic melt transport and emplacement along transcurrent shear zones: Case study of the Pofadder Shear Zone in South Africa and Namibia. M.Sc. thesis, Stellenbosch University, Cape Town, South Africa.Larrovere, M.A., De los Hoyos, C.R., Toselli, A.J., Rossi J.N., Basei, M.A.S., Belmar, M.E. 2011. High T/P evolution and metamorphic ages of the migmatitic basement of northern Sierras Pampeanas, Argentina: Characterization of a mid-crustal segment of the Famatinian belt. Journal of South American Earth Sciences, 31, 279-297.

Lee, J., Hacker, B. and Wang, Y. 2004. Evolution of North Himalayan gneiss domes: structural and metamorphic studies in Mabja Dome, southern Tibet. Journal of Structural Geology, 26, 2297-2316.

Le Maitre, R.W., Bateman, P., Dudek, A., Keller, J., Lameyre Le Bas, M.J., Sabine, P.A., Schmid, R.,Sorensen, H., Strekeisen, A., Wooley, A.R., and Zanettin, B. 1989. A classification of igneous rocks and glossary of terms, Blackwell, Oxford.

Leyshon, P.R., Lisle, R.J. 2004. Stereographic projection techniques in structural geology. Cambridge University Press, second edition.

Lin, M. et al., 2015. Geochemistry, petrogenesis and tectonic setting of Neoproterozoic mafic–ultramafic rocks from the western Jiangnan orogen, South China. Gondwana Research.

López-Moro, F.J. 2012. EASYGRESGRANT-A Microsoft Excel spreadsheet to quantify volume changes and to perform mass-balance modeling in metasomatic systems. Computers and Geosciences, 39, 191–196.

Ludwig, K.R. 2003. Isoplot/Ex version 3.00: A Geochronological Toolkit for Microsoft Excel. Berkeley Geochronology Center, Berkeley, CA.

Maier, W.D., Andreoli, M.A.G., Groves, D.L., Barnes, S.J. 2012. Petrogenesis of Cu-Ni sulphide ores from O'okiep and Kliprand, Namaqualand, South Africa: constraints from chalcophile metal contents. South African Journal of Geology, 115, 449-514.

Macey, P.H. 2001. The geology of the region between Garies and Kliprand, southern Namaqualand. 1:50 000 sheets 3018 CA (Buffelsfontein), 3018 CB (Suurdam), 3018 DA (Kliprand) and 3018 DB (Oubees). Council for Geoscience internal report. (Unpublished).

Macey, P.H., Siegfried, H.P., Minnaar, H., Almond, J. 2011. The Geology of The Loeriesfontein Area. Explanation to Sheet 3018, Scale: 1:250 000. Council for Geoscience.

Manya, S. 2014. Geochemistry of the Palaeoproterozoic gabbros and granodiorites of the Saza area in the Lupa Goldfield, southwestern Tanzania. Journal of African Earth Sciences, 100, 401–408.

Martin, H. 1987. Petrogenesis of archaean trondhjemites, tonalites, and granodiorites from Eastern Finland: Major and trace element geochemistry. Journal of Petrology, 28, 921–953.

Martin, H., Bonin, B., Capdevila, R., Jahn, M., Lameyre, J., Wang, Y. 1994. The Kuiqi peralkaline granitic complex (SE China): Petrology and geochemistry. Journal of Petrology, 35, 983–1015.

Matsumura, R. 2014. The petrogenesis of the Nelshoogte pluton: The youngest and most compositionally variable TTG pluton in the Barberton Granite-Greenstone Terrain. M.Sc. thesis, Stellenbosch University, Cape Town, South Africa.

McDonough, W.F., Stosch, H.G. and Warc, N. 1992. Distribution of titanium and the rare earth elements between peridotitic minerals. Contrib. Mineral. Petrol., 110, 321-328.

McDonough, W.F., Sun, S-S., Ringwood, A.E., Jagoutz, E. and Hofmann, A.W. 1992. Potassium, rubidium and cesium in the Earth and Moon and the evolution of the mantle of the Earth. Geochem. Cosmochim. Cosmochim Acta, 56: 1001-1012.

McDonough, W.F., Sun, S-S. 1995. The composition of the earth. Chemical geology, 120, 223-253.

McLennan S. M. 1989. Rare earth elements in sedimentary rocks: Influence of provenance and sedimentary processes. Rev. Mineral. 21, 169-200.

McLennan, S.M., Hemming, S., McDaniel, D.K. and Hanson, G.N. 1993. Geochemical approaches to sedimentation, provenance, and tectonics. Geological Society of America Special Paper, 284, 21–40.

McLennan, S.M. and Taylor, S.R. 1991. Sedimentary rocks and crustal evolution: Tectonic setting and secular trends. Journal of Geology, 99, 617–620.

McIver, J.R., McCarthy, T.S. and Packham, B. de V. 1983. The copper-bearing basic rocks of Namaqualand, South Africa. Mineralium Deposita, 18, 135-160.

Miková, J. and Denková, P. 2007. Modified chromatographic separation scheme for Sr and Nd isotope analysis in geological silicate samples. Journal of Geosciences, 52, 221 – 226.

Middelburg, J.J., Van Der Weijden, C.H. and Woittiez, J.R.W. 1988. Chemical processes affecting the mobility of major, minor and trace elements during weathering of granitic rocks. Chemical Geology, 68, 253–273.

Moen, H.F.G. 2007. The Geology of the Upington Area. Map Sheet Explanation, 2820. Scale 1:250 000. Council for Geoscience, Pretoria. 160.

Moghadam, H.S., Li, X-H., Ling, X-X., Stern, R.J., Santos, J.F., Meinhold, G., Ghorbani, M., Shahabi, S. 2015. Petrogenesis and tectonic implications of Late Carboniferous A-type granites and gabbronorites in NW Iran: Geochronological and geochemical constraints. Lithos, 212-215, 266–279.

Moore, J.M. 1983. Geochemical and genetic aspects of cordierite gneisses from south-central Namaqualand. Report, Precambrian Research Unit, University of Cape Town, 18–20, 116–131.

Moore, J.M. 1989. A comparative study of metamorphosed supracrustal rocks from Western Namaqualand Metamorphic Complex. Bulletin of the Precambrian Research Unit, University of Cape Town, 37, 370.

Mukherjee, P.K. and Gupta, P.K. 2008. Arbitrary scaling in ISOCON method of geochemical mass balance: An evaluation of the graphical approach. Geochemical Journal, 42, 247–253.

Nesbitt, H.W. and Young, G.M. 1982. Early Proterozoic climates and plate motions inferred from major element chemistry of lutites. Nature, 299, 715-717.

Nesbitt, H.W. and Young, G.M. 1984. Prediction of some weathering trends of plutonic and volcanic rocks based upon thermodynamic and kinetic considerations. Geochim. Cosmochim. Acta, 48, 1523-1534

Nesbitt, H.W. and Young, G.M. 1989. Formation and diagenesis of weathering profiles. Journal of Geology, 97, 129-147

Nesbitt, H. W. and Young, G. M. 1996. Petrogenesis of sediments in the absence of chemical weathering: effects of abrasion and sorting on bulk composition and mineralogy. Sedimentology, 43, 341–358.

Norwicki, T.E., Frimmel, H.E.F. and Waters, D.J. 1995. The occurrence of osumilite in pelitic granulites of the Namaqua Metamorphic Complex. South African Journal of Geology, 98, 191–201.

Nyakairu, G.W.A., Koeberl, C. 2001. Mineralogical and chemical composition and distribution of rare earth elements in clay-rich sediments from central Uganda. Geochemical Journal, 35, 13 to 28.

Pandey, S.N. 1973. Development of dome and basin structure due to interference of major folds on the southern margin of the Vindhyan basin, Ind. Nat. Sci. Acad., Vol. 39, Pt.A, No. 1, pp. 39-47.

Passchier, C.W., and Trouw, R.A.J. 2005. Microtectonics: New York, Springer, 366.

Peacock, M.A. 1931. Classification of igneous rock series. Journal of geology, 39, 54-67.

Pearce, J.A. 1983. Role of the sub-continental lithosphere in magma genesis at active continental margins. In: Hawkesworth, C.J. and Norry, M.J. eds. Continental basalts and mantle xenoliths, Nantwich, Cheshire: Shiva Publications, 230-249.

Pearce, J.A., Harris, N.B.W. and Tindle, A.G. 1984. Trace element discrimination diagrams for the tectonic interpretation of granitic rocks. Journal of Petrology, 25, 956–983.

Pearce, J.A. and Peate, D.W. 1995. Tectonic implications of the composition of volcanic arc magmas. Annual Review of Earth and Planetary Sciences, 23, 251–285.

Pearce, J.A. 1996. Sources and settings of granitic rocks. Episodes, 19, 120–125.

Peccerillo, R. and Taylor S.R. 1976. Geochemistry of Eoscene calc-alkaline volcanic rocks from the Kastamonu area, northern Turkey. Contrib. Mineral. Petrol., 58, 63-81.

Pettersson, A., Cornell, D.H., Yuhara, M. and Hirahara, Y. 2009. Sm-Nd data for granitoids across the Namaqua sector of the Namaqua-Natal Province, South Africa. Geological Society, London, Special Publications, 323, 219–230.

Plasma, I.C. 2007. Geochemistry of sandstones from Miocene Surma Group, Bengal Basin, Bangladesh: Implications for Provenance, tectonic setting and weathering. , 41, 1983.

Potdevin, J.L. 1993. Gresens 92: a simple Macintosh program of the Gresens method. pp.1229–1238.

Powell C.M., Jones D.L., Pisarevsky S. and Wingate M.T.D. 2001. Palaeomagnetic constraints on the position of the Kalahari craton in Rodinia. Precambrian Research 110, 33-46.

Price, N.J. and Cosgrove, J.W. 1990. Analysis of Geological Structures. Analysis of Geological Structures, 516.

Raith, J.G. 1995. Petrogenesis of the Concordia granite gneiss and its relation to W-Mo mineralisation in western Namaqualand, South Africa. Precambrian Research 70, 303-335.

Raith, J.G. and Harley, S.L. 1998. Low-P high-T metamorphism in the Okiep Copper District, western Namaqualand, South Africa. Journal of Metamorphic Geology, 16, 281–305.

Raith, J.G., Cornell, D.H., Frimmel, H.E.F. and De Beer, C.H. 2003. New Insights into the Geology of the Namaqua Tectonic Province, South Africa, from Ion Probe Dating of Detrital and Metamorphic Zircon. The Journal of Geology, 111, 347–366.

Ramsay, J.G. and Huber, M.I. 1988. The Techniques of Modern Structural Geology. Volume 2: Folds and Fractures.

Reid, D.L. 1982. Age relationships within the Vioolsdrif batholith, lower Orange River region. II. A two-stage emplacement history and the extent of Kibaran overprinting. Transactions of the Geological Society of South Africa, 85, 105-110.

Reid, D.L. and Barton, E.S. 1983. Geochemical characterization of granitoids in the Namaqualand geotraverse. Special publication geologic society of South Africa, 10, 67-82.

Robb, L.J. Armstrong, R. A. and Waters, D.J. 1999. The history of granulite-facies metamorphism and crustal growth from single zircon U-Pb geochronology: Namaqualand, South Africa. Journal of Petrology, 40, 1747–1770.

Roland, S.M., Duebendorfer, E.M. and Schiefelbein, I.M. 2007. Structural Analysis and Synthesis: A Laboratory Course in Structural Geology, 3rd edition. Blackwell publishing.

Rollinson, H.R. 1993. Using Geochemical Data: Evaluation, Presentation, Interpretation. Mineralogical Magazine, 58, 523–523.

Roser, B.P. and Korsch, R.J. 1986. Determination of tectonic setting of sandstone-mudstone suites using SiO_2-

content and K_2O/Na_2O ratio. The Journal of Geology, 94, 635–650.

Roser, B.P. and Korsch, R.J. 1988. Provenance signature of sandstone-mudstone suites determined using discriminant function analysis of major element data. Chemical Geology 67, 119-139.

Rudnick, R.L. and Gao, S. 2003. 3.01 - Composition of the Continental Crust.

Schmitz, M.D. and Bowring, S.A. 2004. Lower crustal granulite formation during Mesoproterozoic Namaqua-Natal collisional orogenesis, southern Africa. South African Journal of Geology, 107, 261–284.

Sendek, C. 2012. Using Structural Analysis to Assess Possible Formation Mechanisms of the Gneiss Domes of the Harvey Cardiff Domain, Eastern Ontario formation mechanisms of the gneiss domes of the Harvey Cardiff Domain, eastern Ontario. Msc thesis, Pomona College, Claremont California, United states, 84.

Shand, S. J. 1927. The Eruptive Rocks. John Wiley. New York.

Sheraton, J.W. and Black, L.P. 1988. Chemical evolution of granitic rocks in the East Antarctic Shield, with particular reference to post-orogenic granites. Lithos, 21, 37-52.

Sheratonl, J.W. and Sun, S-S. 1995. Geochemistry and origin of felsic igneous rocks of the western Musgrave Block. AGSO Journal of Australian Geology & Geophysics, 16, 107- 125

Solanki, A.M. 2011. A petrographic, geochemical and geochronological investigation of deformed granitoids from SW Rajasthan: Neoproterozoic age of formation and evidence of Pan-African imprint. Msc thesis (unpublished), University of Witwatersrand, Johannesburg, South Africa, 245.

Stumpfl, E.F., Clifford, T.N., Burger, A. J., Van Zy|, D. 1976. The Copper Deposits of the O ' Okiep District , South Africa : New Data and Concepts. Mineralium Deposita, 70, 46–70.

Sun. S-S. and McDonough, W.F. 1989. Chemical and isotopic systematics of oceanic basalts: Implications for mantle composition and processes. In: Saunders, AD. & Norry, M.J. (editors). Magmatism in ocean basins. Geological Society of London, Special Publication, 42, 313-345.

Tanaka, T., Togashi, S., Kamioka, H., Amakawa, H., Kagami, H., Hamamoto, T., Yuhara, M., Orihashi, Y., Yoneda, S., Shimizu, H., Kunimaru, T., Takahashi, K., Yanagi, T., Nakano, T., Fujimaki, H., Shinjo, R., Asahara, Y., Tanimizu, M. and Dragusanu, C. 2000. JNdi-1: a neodymium isotopic reference in consistency with LaJolla neodymium. Chemical Geology Short Communication., 168, 279 – 281.

Tarney, J., Wyborn, L.E.A, Sheraton, J.W. and Wyborn, D. 1987. Trace element differences between Archaean, Proterozoic and Phanerozoic crustal components-implications for crustal growth processes. In: Ashwal, L.D. (editor). Workshop on the growth of continental crust. Lunar and Planetary Institute, Technical Report, 88, 139-140.

Taylor, S. R., and McLennan, S. M. 1981. The Composition and Evolution of the Continental Crust: Rare Earth Element Evidence from Sedimentary Rocks. Philosophical Transactions of the Royal Society A: Mathematical, Physical and Engineering Sciences, 301, 381–399.

Taylor, S. R. and McLennan, S.M. 1985. The continental crust: its composition and evolution. Blackwell, Oxford.

Taylor, E. 1990. The geology and Ni-metallogenesis in the Namaqualand Mobile Belt, Kliprand, north-west Cape, South Africa. B.Sc. Honours project (Unpublished), University of the Witwatersrand, Johannesburg, South Africa, 69.

Taylor, J., Nicoli, G, Stevens, G., Frei, D. Moyen, J.F. 2014. The processes that control leucosome compositions in metasedimentary granulites: perspectives from the Southern Marginal Zone migmatites, Limpopo Belt, South Africa. Journal of metamorphic geology, 1111.

Teyssier, C. and Whitney, D.L. 2002. Gneiss domes and orogeny. Geological Society of America, 30, 1139-1142.

Twiss, R.J. and Moores, E.M. 2009. Structural Geology, 2nd edition, 735pp. New York: W.H. Freeman.

Van der Pluijm, B. and Marshak, S. 2004. Earth Structure: An Introduction to Earth Structure and Tectonics, 2nd edition: W.W. Norton and company, New York: 520. (geology majors' textbook).

Verma, S.P. and Agrawal, S. 2011. New tectonic discrimination diagrams for basic and ultrabasic volcanic rocks through log-transformed ratios of high field strength elements and implications for petrogenetic processes. Revista Mexicana de Ciencias Geologicas, 28, 24–44.

Verma, S.P., Guevara, M. and Agrawal, S. 2006. Discriminating four tectonic settings: Five new geochemical diagrams for basic and ultrabasic volcanic rocks based on log-ratio transformation of major-element data. Journal of Earth System Science, 115, 485–528.

Verma, S.P., Verma, S.K. and Oliveira, E.P. 2015. Application of 55 multi-dimensional tectonomagmatic discrimination diagrams to Precambrian belts. International Geology Review, 57, 1365–1388.

Waters, D.J. 1986a. Metamorphic history of sapphirine-bearing and related magnesian gneisses from Namaqualand, South Africa. Journal of Petrology, 27, 541– 565.

Waters, D.J. 1986b. Metamorphic zonation and thermal history of pelitic gneisses from western Namaqualand, South Africa. Transactions of the Geological Society of South Africa, 89, 97–102.

Waters, D.J. 1988. Partial melting and the formation of granulite facies assemblages in Namaqualand, South Africa. Journal of Metamorphic Geology, 6, 87–404.

Waters, D.J. 1989. Metamorphic evidence for the heating and cooling path of Namaqualand granulites. In: Evolution of Metamorphic Belts (J.S. Daly, R.A. Cliff and B.W.D. Yardley, Eds). Special Publication of the Geological Society, 43, 357–363.

Waters, D.J. 1990. Thermal history and tectonic setting of the Namaqualand granulites, southern Africa: clues to Proterozoic crustal development. In: (D. Vielzeuf and P. Vidal, Eds). Granulites and Crustal Evolution Kluwer Academic Publishers, Nederlands, 243–256.

Waters, D.J. and Whales, C.J. 1984. Dehydration melting and the granulite transition in metapelites from southern Namaqualand, South Africa. Contributions to Mineralogy and Petrology, 88, 269–275.

Waters, D.J. and Moore, J.M. 1985 Kornerupine in Mg- Al-rich gneisses from Namaqualand, South Africa: mineralogy and evidence for late metamorphic fluid activity. Contributions to Mineralogy and Petrology, 91, 369–382.

Weltje, G.J. and Von Eynatten, H. 2004. Quantitative provenance analysis of sediments: Review and outlook. Sedimentary Geology, 171, 1–11.

Whalen, J.B., Currie, K.L. and Chappell, B.W. 1987. A-type granites: geochemical characteristics, discriminations and petrogenesis. Contributions to Mineralogy and Petrology, 95, 407–419.

Winter, J.D. 2001. An introduction to igneous and metamorphic petrology. Prentice Hall, Upper Saddle River, New Jersey, United States of America, 697pp.

Winter, J.D. and Winter, J.D. 2010. Principles of igneous and metamorphic petrology. New York: Prentice Hall.

Will, T.M., Frimmel, H.E., Zeha, A., Le Roux, P., Schmadicke, E. 2010. Geochemical and isotopic constraints on the tectonic and crustal evolution of the Shackleton Range, East Antarctica, and correlation with other Gondwana crustal segments. Precambrian Research, 180, 85–112.

Willner, A., Schreyer, W. and Moore, J.M. 1990. Peraluminous metamorphic rocks from the Namaqualand Metamorphic Complex (South Africa): Geochemical evidence for an exhalation-related, sedimentary origin in a Mid-Proterozoic rift system. Chemical Geology, 81, 221–240.

Winchester, J.A. and Max, M.D. 1982. The geochemistry and origins of the Precambrian rocks of the Rosslare Complex, SE Ireland . Journal of the Geological Society , 139, 309–319.

Workman, R.K. and Hart, S.R. 2005. Major and trace element composition of the depleted MORB mantle (DMM). Earth and Planetary Science Letters, 231, 53–72.

Wronkiewicz, D.J. and Condie, K.C. 1990. Geochemistry and mineralogy of sediments from the Ventersdorp and Transvaal Supergroups, South Africa: Cratonic evolution during the early Proterozoic. Geochimica et Cosmochimica Acta, 54, 343–354.

Yakovlev, F. L. 2009. Reconstruction of Linear Folding Structures with the Use of Volume Balancing. Physics of the Solid Earth, 45, 1025–1036.

Yakovlev, F. L. 2012. Methods for detecting formation mechanisms and determining a final strain value for different scales of folded structures. Tectonophysics, 344, 125–137

Yardley, B. W. D., McKenzie, W. S. and Guilford, C. 1990. Atlas of Metamorphic Rocks and their Textures. Longmans. Essex.

Yin, A. 2004. Gneiss domes and gneiss dome systems. Geological Society of America, Special paper, 1–14.

Yuhara, M. 2002. Rb-Sr and Sm-Nd Mineral Isochron Ages. Gondwana Research, 5, 771–779.

Zelt, G.A.D. 1980. Granulite facies metamorphism in Namaqualand, South Africa. Precambrian Research, 13, 253–274.

Zhai, Q.G., Jahn, B-M., Zhang, R-Y., Wang, J., Su, L. 2011. Triassic Subduction of the Paleo-Tethys in northern Tibet, China: Evidence from the geochemical and isotopic characteristics of eclogites and blueschists of the Qiangtang Block. Journal of Asian Earth Sciences, 42, 1356–1370.

Zharikov, V.A., Pertsev, N.N., Rusinov, V.L., Callegari, E. and Fettes, D.J. 2007. Metasomatism and metasomatic rocks, Nauchnyi Mir, Recommendations by the IUGS Subcommission on the Systematics of Metamorphic Rocks: Web version 01.02.07

Zindler, A. and Hart, S.R. 1986. Chemical Geodynamics. Annual Review of Earth and Planetary Sciences, 14, 493–571.

APPENDICES

Appendix A

Structural measurements

Table A-1. Subarea 1 foliation data.

Coordinates			Orientation	
X(East)	Y(North)	Z	dip	azimuth
18.63963	-30.56086	977	62	355
18.63966	-30.56287	983	72	350
18.63987	-30.56502	978	72	9
18.63919	-30.56688	980	77	25
18.63883	-30.56906	986	76	334
18.63912	-30.57087	988	69	326
18.63852	-30.57435	965	84	230
18.63884	-30.57650	956	77	212
18.63438	-30.57864	954	52	24
18.63088	-30.57813	962	65	21
18.62995	-30.57397	986	70	215
18.63084	-30.57170	995	77	262
18.63182	-30.56928	998	54	285
18.63231	-30.56668	1001	65	330
18.63449	-30.56436	1001	60	319
18.63717	-30.56285	995	59	346
18.63629	-30.57528	964	83	226
18.63151	-30.57407	977	73	225

Table A-2. Subarea 1 lineation data.

Coordinates			Orientation	
X(East)	Y(North)	Z	plunge	trend
18.63966	-30.56287	983	17	259
18.63883	-30.56906	986	26	257
18.63912	-30.57087	988	19	246
18.63088	-30.57813	962	15	241
18.63449	-30.56436	1001	10	230
18.63629	-30.57528	964	23	317
18.63151	-30.57407	977	13	316
18.62995	-30.57397	986	30	302
18.63852	-30.57435	965	9	310
18.64210	-30.57971	987	19	307
18.64850	-30.57008	1011	16	311
18.65023	-30.56756	1017	11	303
18.63884	-30.57650	956	31	283

Table A-3. Subarea 2a foliation data.

Coordinates			Orientation	
X(East)	Y(North)	Z	dip	azimuth
18.67789	-30.56899	920	70	34
18.67412	-30.56737	926	58	30
18.67524	-30.57864	909	55	117
18.67307	-30.58206	905	83	128
18.66792	-30.57956	916	72	172
18.66674	-30.58262	916	68	170
18.66352	-30.58233	925	73	176
18.67577	-30.56639	962	77	36
18.67555	-30.57022	948	67	29
18.67543	-30.57074	949	65	40
18.67515	-30.57209	945	79	41
18.67516	-30.57226	949	83	334
18.66531	-30.57098	977	65	59
18.66432	-30.57620	959	77	357
18.66378	-30.57856	964	81	207
18.66348	-30.58497	958	83	197
18.67367	-30.58059	905	70	135
18.66886	-30.57812	918	68	142
18.66979	-30.58042	912	73	144

Table A-4. Subarea 2b foliation data.

Coordinates			Orientation		Coordinates			Orientation	
X(East)	Y(North)	Z	dip	azimuth	X(East)	Y(North)	Z	dip	azimuth
18.70056	-30.58377	916	81	37	18.684209	-30.57693	948	43	72.9
18.69692	-30.58489	906	69	166	18.69335	-30.58305	913	66	179
18.70009	-30.57738	923	80	55	18.69284	-30.58410	906	60	178
18.69166	-30.57686	958	72	51	18.69274	-30.58560	892	84	173
18.68979	-30.58192	942	65	102	18.69529	-30.58184	916	63	186
18.68836	-30.58558	928	75	166	18.68449	-30.58570	895	74	147
18.68640	-30.59127	909	68	143	18.68474	-30.58509	898	56	150
18.69388	-30.57039	964	71	64	18.68069	-30.58934	906	52	156
18.69388	-30.57039	964	78	60	18.68015	-30.59038	903	66	160
18.69395	-30.57041	950	67	51	18.67793	-30.59224	902	67	173
18.69397	-30.57043	956	82	181	18.69431	-30.58028	925	56	63
18.69326	-30.56929	958	80	31	18.69467	-30.58077	923	63	70
18.68393	-30.57014	934	83	45	18.68542	-30.57114	932	65	37
18.68701	-30.57408	926	78	50	18.69346	-30.57730	929	72	32
18.68477	-30.58464	900	81	113	18.69331	-30.57644	927	73	26
18.68150	-30.58774	907	53	121	18.69471	-30.57789	926	55	54
18.68371	-30.58664	896	74	119	18.68459	-30.58580	892	76	154
18.68901	-30.57372	929	85	50	18.68464	-30.58579	890	71	150
18.68517	-30.57594	956	55	42	18.68558	-30.58733	908	81	149
					18.68558	-30.58765	911	69	151

Table A-5. Entire Subarea 2 foliation data.

Coordinates			Orientation	
X(East)	Y(North)	Z	dip	azimuth
18.70056	-30.58377	916	81	37
18.69692	-30.58489	906	69	166
18.70009	-30.57738	923	80	55
18.69166	-30.57686	958	72	51
18.68979	-30.58192	942	65	102
18.68836	-30.58558	928	75	166
18.68640	-30.59127	909	68	143
18.69388	-30.57039	964	71	64
18.69388	-30.57039	964	78	60
18.69395	-30.57041	950	67	51
18.69397	-30.57043	956	82	181
18.69326	-30.56929	958	80	31
18.68393	-30.57014	934	83	45
18.68701	-30.57408	926	78	50
18.68477	-30.58464	900	81	113
18.68150	-30.58774	907	53	121
18.68371	-30.58664	896	74	119
18.68901	-30.57372	929	85	50
18.68517	-30.57594	956	55	42
18.68421	-30.57693	948	43	73
18.69335	-30.58305	913	66	179
18.69284	-30.58410	906	60	178
18.69274	-30.58560	892	84	173
18.69529	-30.58184	916	63	186
18.68449	-30.58570	895	74	147
18.68474	-30.58509	898	56	150
18.68069	-30.58934	906	52	156
18.68015	-30.59038	903	66	160
18.67793	-30.59224	902	67	173
18.69431	-30.58028	925	56	63
18.69467	-30.58077	923	63	70
18.68542	-30.57114	932	65	37
18.69346	-30.57730	929	72	32
18.69331	-30.57644	927	73	26
18.69471	-30.57789	926	55	54
18.67789	-30.56899	920	70	34
18.67412	-30.56737	926	58	30
18.67524	-30.57864	909	55	117
18.67307	-30.58206	905	83	128
18.66792	-30.57956	916	72	172
18.66674	-30.58262	916	68	170
18.66352	-30.58233	925	73	176
18.67577	-30.56639	962	77	36
18.67555	-30.57022	948	67	29
18.67543	-30.57074	949	65	40
18.67515	-30.57209	945	79	41
18.67516	-30.57226	949	83	334
18.66531	-30.57098	977	65	59
18.66432	-30.57620	959	77	357
18.66378	-30.57856	964	81	207
18.66348	-30.58497	958	83	197
18.67367	-30.58059	905	70	135
18.66886	-30.57812	918	68	142
18.66979	-30.58042	912	73	144

Table A-6. Entire Subarea 2 lineation data.

Coordinates			Orientation	
X(East)	Y(North)	Z	plunge	trend
18.66341	-30.57651	952	12	297
18.66444	-30.57037	966	17	337
18.65791	-30.57915	976	12	296
18.67417	-30.58901	951	19	294
18.68827	-30.57284	970	30	329
18.69148	-30.57686	957	29	309
18.69085	-30.57900	947	17	320
18.67981	-30.57020	921	31	290
18.68023	-30.57175	918	42	287
18.68680	-30.57615	919	29	300
18.67445	-30.57989	907	43	225
18.67212	-30.57914	910	35	232
18.67813	-30.58210	900	38	212
18.66880	-30.57992	916	30	230
18.69346	-30.57730	929	19	282
18.69331	-30.57644	927	23	310
18.69467	-30.58077	923	31	289
18.69284	-30.58410	905	28	267
18.69274	-30.58560	894	13	279
18.66674	-30.58262	916	13	126
18.66352	-30.58233	925	12	117
18.67307	-30.58206	905	17	228
18.66886	-30.57812	918	14	210
18.68069	-30.58934	906	15	253
18.68015	-30.59038	903	20	246
18.67793	-30.59224	902	8	232
18.68150	-30.58774	907	12	212
18.69274	-30.58560	892	13	340
18.69284	-30.58410	906	27	260
18.66432	-30.57620	959	18	196

Table A-7. Subarea 3 lineation data.

Coordinates			Orientation	
X(East)	Y(North)	Z	plunge	trend
18.66444	-30.57037	966	17	337
18.66433	-30.57617	956	5	279
18.63743	-30.60207	931	8	299
18.63521	-30.59250	1044	7	291
18.65791	-30.57915	976	12	296
18.66341	-30.57651	952	12	297
18.66341	-30.57650	955	6	294
18.61050	-30.59929	924	33	321
18.61047	-30.59928	927	33	322
18.60775	-30.59076	947	4	308
18.60705	-30.58431	1010	10	304
18.61437	-30.57594	1048	14	306
18.62627	-30.59273	989	20	309
18.65490	-30.55660	997	2	275
18.65634	-30.55728	992	25	296
18.66579	-30.55916	982	10	304
18.67260	-30.56202	968	17	287
18.68707	-30.56827	967	6	281
18.67828	-30.56353	962	14	276
18.69500	-30.56585	949	4	315
18.64937	-30.60001	982	15	272
18.65609	-30.59932	975	8	179
18.67642	-30.59557	946	6	249
18.64603	-30.60197	986	4	291
18.69166	-30.57688	957	3	347
18.69116	-30.57773	951	8	312
18.69085	-30.57900	947	7	320
18.69148	-30.57686	957	9	309
18.69325	-30.56926	958	9	306
18.69318	-30.56929	954	9	312
18.69318	-30.56929	954	9	308
18.69318	-30.56929	954	5	313
18.65490	-30.55660	997	2	275
18.65492	-30.55658	997	5	263
18.65492	-30.55658	997	5	276
18.62472	-30.60451	939	22	266
18.62473	-30.60452	940	22	244
18.62473	-30.60452	940	24	238
18.62506	-30.60314	916	41	263
18.62510	-30.60316	915	57	260

Table A-8. Subarea 3 lineation data.

Coordinates			Orientation	
X(East)	Y(North)	Z	plunge	trend
18.64528	-30.60023	966	9	212
18.64528	-30.60023	966	8	258
18.64528	-30.60023	966	4	266
18.64472	-30.59825	987	1	314
18.64472	-30.59825	987	1	314
18.64473	-30.59828	982	9	209
18.64473	-30.59827	978	8	198
18.64473	-30.59826	977	8	216
18.64469	-30.59841	982	14	300
18.64471	-30.59840	981	4	285
18.64472	-30.59840	982	13	295
18.66009	-30.59781	968	4	235
18.66008	-30.59781	968	6	232
18.66008	-30.59781	968	8	237
18.66591	-30.59625	957	19	215
18.66591	-30.59625	957	19	210
18.66591	-30.59625	957	24	22
18.65490	-30.55660	997	18	275
18.65492	-30.55658	997	5	263
18.65492	-30.55658	997	5	276
18.65492	-30.55658	997	4	260
18.67639	-30.59556	947	4	254
18.67642	-30.59557	946	6	249
18.67642	-30.59557	946	8	254
18.64937	-30.60001	982	15	266
18.64937	-30.60001	982	15	272
18.64937	-30.60001	982	17	266
18.64937	-30.60001	982	17	264
18.68934	-30.58295	942	9	240
18.68935	-30.58295	942	5	232
18.64640	-30.57323	997	4	138
18.64214	-30.57970	988	2	143
18.64672	-30.56859	1010	13	320
18.65180	-30.56313	983	24	290
18.65074	-30.56596	1004	7	118
18.65427	-30.59167	998	9	123

Table A-9. Subarea 4 foliation data

Coordinates			Orientation	
X(East)	Y(North)	Z	dip	azimuth
-30.59975	18.61175	900	86	205
-30.59966	18.61160	910	75	216
-30.59956	18.61139	910	64	213
-30.59973	18.61566	908	59	230
			68	206
			74	197
			79	225
			60	210
			62	208
			71	170
			75	149
			66	168
			69	174
			68	171
			60	166
			64	161
			71	169
			67	178
			71	169
			57	175

Table A-10. Joint set 1

Coordinates			Orientation	
X(East)	Y(North)	Z	dip	azimuth
18.64523	-30.59998	963	66	343
18.64524	-30.59998	964	76	358
18.69136	-30.57713	962	78	343
18.65351	-30.59870	976	69	330
18.69036	-30.58048	942	85	333
18.69035	-30.58048	941	87	350
18.69149	-30.57726	957	79	334
18.64820	-30.57054	1009	87	347
18.67557	-30.56638	966	77	346
18.67557	-30.56638	966	81	343
18.67517	-30.57225	950	90	354
18.67356	-30.57368	953	67	352
18.65555	-30.58501	974	88	331
18.67262	-30.56203	974	30	164
18.68700	-30.56824	970	84	181
18.69305	-30.56923	962	84	166
18.69305	-30.56923	962	84	167
18.69311	-30.56943	959	74	178
18.64636	-30.57303	1001	79	161
18.66518	-30.57306	974	89	181

Table A-11. Joint set 2

Coordinates			Orientation	
X(East)	Y(North)	Z	dip	azimuth
18.64532	-30.60021	961	75	73
18.67262	-30.56203	974	90	79
18.65187	-30.55344	1010	90	72
18.69402	-30.56865	956	81	75
18.65595	-30.55867	991	73	232
18.65595	-30.55867	991	70	223
18.65594	-30.55867	992	64	229
18.64837	-30.60139	989	87	240
18.64837	-30.60139	989	83	239
18.65181	-30.56316	987	86	228
18.66518	-30.57308	975	84	248
18.67621	-30.56403	963	90	231
18.67557	-30.56637	966	84	221
18.63583	-30.60256	928	76	238
18.65639	-30.55725	995	83	250
18.64837	-30.60140	989	86	245
18.64631	-30.57308	1000	83	246
18.62123	-30.57849	1041	65	250

Table A-12. Joint set 3

Coordinates			Orientation	
X(East)	Y(North)	Z	dip	azimuth
18.63549	-30.60478	976	122	74
18.67655	-30.59586	943	106	80
18.65477	-30.55657	993	116	78
18.65476	-30.55656	992	121	69
18.65474	-30.55656	992	116	79
18.65488	-30.55655	996	116	71
18.65487	-30.55655	996	106	81
18.65492	-30.55656	995	121	63
18.65492	-30.55656	995	113	65
18.65492	-30.55656	995	109	68
18.65598	-30.55865	997	102	88
18.66589	-30.55918	981	113	75
18.67261	-30.56204	975	122	81
18.69518	-30.56544	953	107	81
18.69518	-30.56544	953	102	81
18.69518	-30.56544	953	102	83
18.63742	-30.59948	1012	107	76
18.65681	-30.58327	970	125	74
18.64818	-30.57058	1010	103	80
18.69310	-30.56931	960	119	79
18.64511	-30.60001	956	88	85
18.67655	-30.59586	942	98	77
18.65598	-30.55865	997	88	90
18.65598	-30.55865	997	94	90
18.66226	-30.55837	986	93	80
18.66589	-30.55919	980	84	85

Table A-13. Joint set 3

Coordinates			Orientation	
X(East)	Y(North)	Z	dip	azimuth
18.69402	-30.56865	955	94	87
18.64839	-30.60139	984	92	64
18.69083	-30.57900	946	91	78
18.69083	-30.57900	946	90	79
18.69311	-30.56943	959	92	85
18.63877	-30.60397	970	289	78
18.63878	-30.60395	970	286	81
18.64509	-30.59996	967	271	77
18.64511	-30.59997	963	276	79
18.64510	-30.59997	963	281	87
18.64525	-30.59996	966	279	72
18.69514	-30.56548	951	271	74
18.68267	-30.56590	958	279	77
18.65187	-30.55345	1010	290	79
18.69514	-30.56548	951	272	73
18.67619	-30.59566	944	277	61
18.67620	-30.59566	944	273	63
18.67619	-30.59566	943	271	62
18.69035	-30.58048	942	279	68
18.69150	-30.57688	959	290	81
18.66444	-30.57036	967	290	75
18.66444	-30.57037	970	286	76
18.67356	-30.57370	953	286	89
18.62122	-30.57850	1040	282	68

Table A-14. Joint set 4

Coordinates			Orientation	
X(East)	Y(North)	Z	dip	azimuth
18.65351	-30.59870	976	329	72
18.65351	-30.59870	976	329	75
18.69117	-30.57774	952	326	83
18.69117	-30.57774	952	320	84
18.69116	-30.57773	951	312	82
18.68981	-30.58185	939	308	86
18.68976	-30.58189	938	308	76
18.68976	-30.58189	938	307	79
18.69150	-30.57725	956	329	79
18.65181	-30.56317	985	330	86
18.65073	-30.56597	1004	316	89
18.66348	-30.58497	959	322	84
18.66347	-30.58498	960	302	81
18.63585	-30.60256	929	302	80
18.65793	-30.57918	976	313	68
18.60805	-30.58753	974	304	86
18.60705	-30.58430	1010	311	77
18.69502	-30.56533	954	316	89
18.69502	-30.56533	954	320	88
18.69502	-30.56533	954	315	86
18.69401	-30.56864	956	309	85
18.69401	-30.56864	956	304	82
18.69401	-30.56864	956	306	84
18.68912	-30.58757	915	132	81
18.65524	-30.55848	993	136	83
18.66237	-30.55841	984	136	72
18.68700	-30.56824	970	130	73
18.67621	-30.59565	943	136	64

Table A-14 cont. Joint set 4

Coordinates			Orientation	
X(East)	Y(North)	Z	dip	azimuth
18.67621	-30.59565	943	134	64
18.67621	-30.59565	943	138	64
18.69167	-30.57687	959	140	90
18.69167	-30.57687	959	141	89
18.69084	-30.57903	948	139	72
18.69084	-30.57903	948	141	68
18.69148	-30.57684	958	151	60
18.69147	-30.57685	958	156	76
18.69305	-30.56923	962	157	85
18.69282	-30.56877	958	144	82
18.69282	-30.56877	958	138	83
18.69282	-30.56877	958	155	82
18.65181	-30.56317	984	146	75
18.66444	-30.57036	965	155	84
18.67620	-30.56402	966	150	70
18.67620	-30.56402	966	149	80
18.68708	-30.57433	966	159	79
18.65558	-30.58499	968	133	87
18.69498	-30.56582	947	157	86
18.69498	-30.56582	947	160	85
18.69498	-30.56582	947	157	88

Appendix B

Kliprand Geologic map

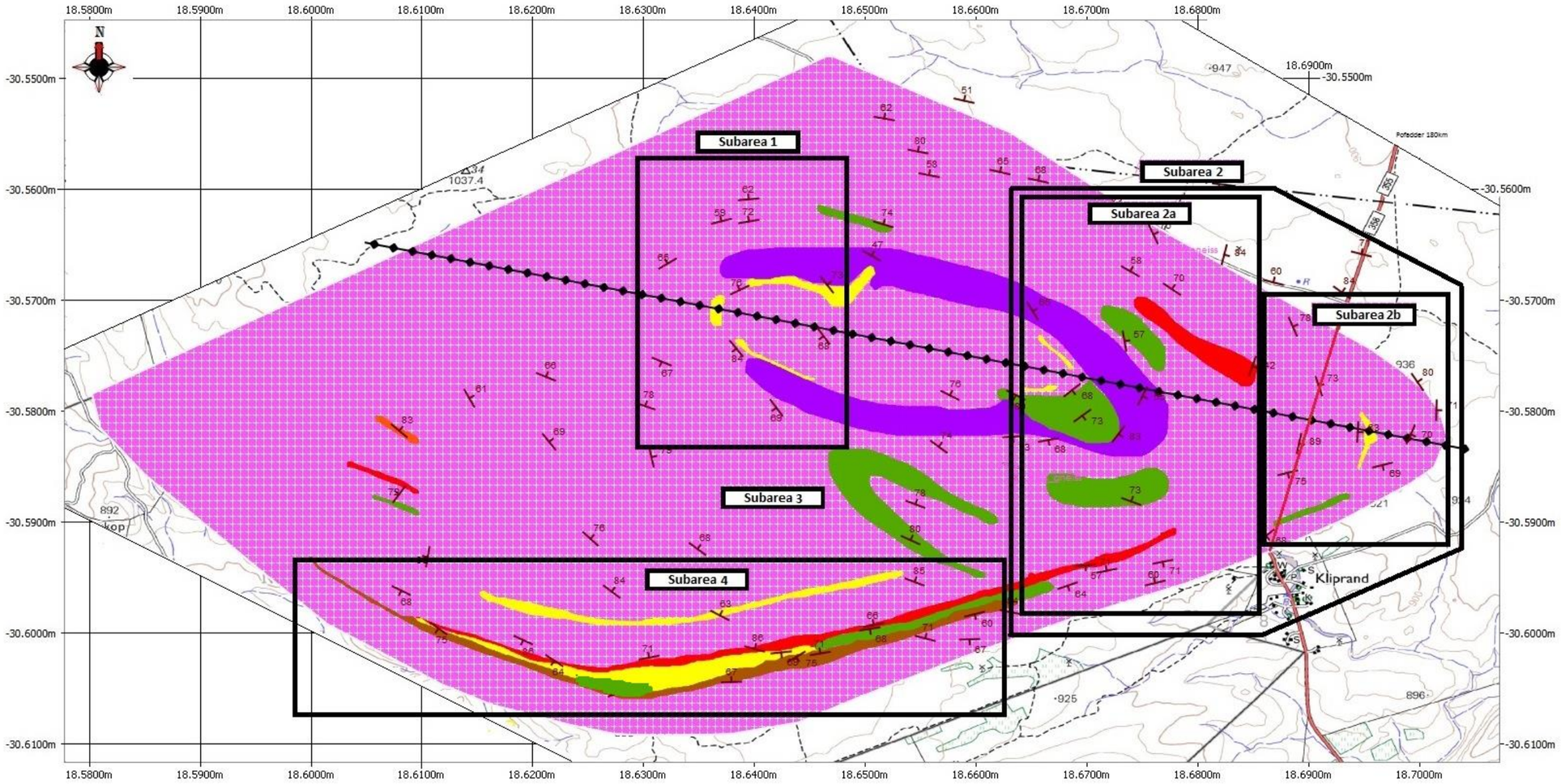

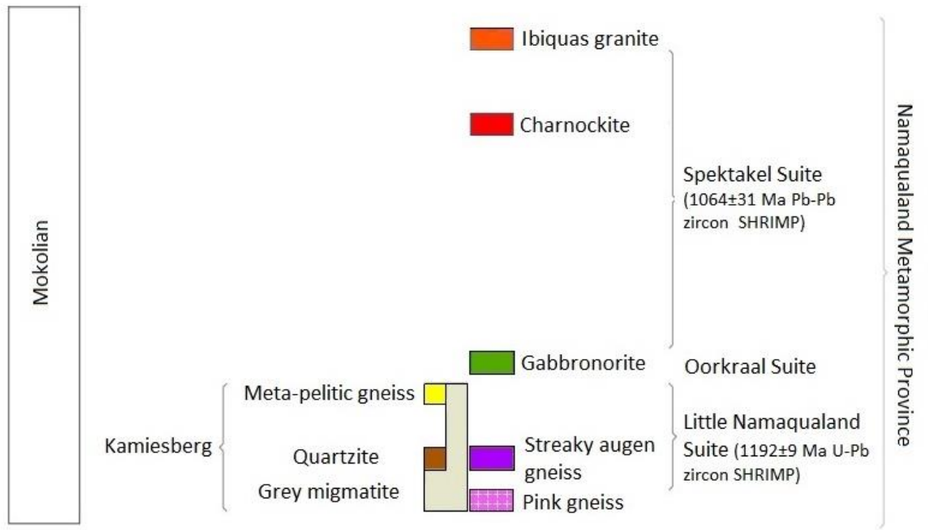

Appendix C

Geochemical Sample lists

Table C-1. Location of whole rock samples collected.

Station number	Coordinates			Short description of the lithology	Station number	Coordinates			Short description of the lithology
	X	Y	Z			X	Y	Z	
Q066	18.627808	-30.605462	944	Quartzite	C035	18.656099	-30.599315	975	Charnockite
Q068	18.634087	-30.60196	899	Quartzite	C063	18.691371	-30.577142	959	Charnockite
Q134	18.684204	-30.576929	949	Quartzite	C106	18.646716	-30.568586	1010	Charnockite
Q145	18.63806	-30.60044	984	Quartzite	C125.1	18.675155	-30.572092	945	Charnockite
Q164	18.654981	-30.596414	977	Quartzite	C133	18.685169	-30.575942	956	Charnockite
Q190	18.610497	-30.599291	924	Quartzite	C141	18.635075	-30.604816	964	Charnockite
					C144	18.637425	-30.602065	931	Charnockite
M010	18.687003	-30.568239	970	Metapelitic gneiss	C171	18.65682	-30.583231	969	Charnockite
M022	18.69502	-30.565329	954	Metapelitic gneiss	C188	18.607551	-30.586378	976	Charnockite
M102	18.650226	-30.567526	1012	Metapelitic gneiss					
M103	18.64807	-30.570375	1002	Metapelitic gneiss	G033	18.65095	-30.599339	983	Gabbro
M105	18.642101	-30.579714	987	Metapelitic gneiss	G036	18.665562	-30.596349	950	Gabbro
M205	18.614361	-30.575945	1049	Metapelitic gneiss	G115	18.663781	-30.578557	964	Gabbro
					G124	18.675434	-30.57074	949	Gabbro
I30	18.646113	-30.601913	986	Ibequas granite	G125.2	18.675161	-30.572255	949	Gabbro
I31	18.648372	-30.601391	989	Ibequas granite	G162	18.655368	-30.598887	972	Gabbro
I61	18.624722	-30.604512	939	Ibequas granite	G169.1	18.654843	-30.586173	984	Gabbro
I73	18.700085	-30.57738	923	Ibequas granite	G196	18.608262	-30.588664	952	Gabbro
I142	18.635848	-30.602559	929	Ibequas granite	G182	18.672043	-30.582763	940	Gabbro
I201	18.608045	-30.581787	1026	Ibequas granite	G216	18.628043	-30.597698	1015	Gabbro

Table C-2. Location of whole rock samples collected.

Station number	Coordinates			Short description of the lithology	Station number	Coordinates			Short description of the lithology
	X	Y	Z			X	Y	Z	
AG112	18.665182	-30.573058	974	Augen gneiss	PG65	18.624786	-30.604722	948	Pink gneiss
AG113	18.66432	-30.576196	959	Augen gneiss	PG70	18.698957	-30.585897	917	Pink gneiss
AG114	18.663781	-30.578557	964	Augen gneiss	PG71	18.702928	-30.579952	927	Pink gneiss
AG148	18.63501	-30.592473	1025	Augen gneiss	PG100	18.651804	-30.563128	983	Pink gneiss
AG170	18.655579	-30.584987	968	Augen gneiss	PG110	18.664437	-30.570359	967	Pink gneiss
AG212	18.626313	-30.592675	990	Augen gneiss	PG122	18.67577	-30.566392	962	Pink gneiss
					PG128	18.672647	-30.57428	956	Pink gneiss
PG1	18.65493	-30.556543	998	Pink gneiss	PG131	18.688267	-30.572842	970	Pink gneiss
PG4	18.655242	-30.558481	993	Pink gneiss	PG140	18.635075	-30.604816	964	Pink gneiss
PG6	18.662273	-30.558367	984	Pink gneiss	PG145	18.637471	-30.599415	1003	Pink gneiss
PG7	18.665886	-30.559182	981	Pink gneiss	PG150	18.630847	-30.584166	1008	Pink gneiss
PG20	18.651868	-30.553443	1009	Pink gneiss	PG165	18.654627	-30.595454	997	Pink gneiss
PG21	18.695136	-30.565483	951	Pink gneiss	PG169.2	18.654844	-30.586173	984	Pink gneiss
PG24	18.659337	-30.551982	962	Pink gneiss	PG186	18.674171	-30.589014	951	Pink gneiss
PG38	18.646253	-30.602697	988	Pink gneiss	PG194	18.607767	-30.590714	947	Pink gneiss
PG40	18.691665	-30.576865	959	Pink gneiss					
PG41	18.691172	-30.577744	952	Pink gneiss					
PG50	18.693252	-30.569258	958	Pink gneiss					

Table C-3. List of samples sent for isotope analysis

SAMPLE ID	rock name	LITHOLOGY	SUBPROVINCE/ TERRANE	Co-ordinates in UTM			Rb (ppm)	Sr (ppm)	Sm (ppm)	Nd (ppm)
				X	Y	Z				
PBG131	streaky gneiss	Medium grained quartz-feldspar-biotite gneiss	Bushmanland/ Garies	18.688267	-30.572842	970	303.7	57.04	7.3	36.18
PG169.2	pink gneiss	Medium to fine grained quartz-feldpsar gneiss	Bushmanland/ Garies	18.654844	-30.586173	984	429.73	52.9	5.31	24.64
AG212	streaky augen gneiss	medium grained quartz-feldspar-biotite gneiss with well defined feldspar augens	Bushmanland/ Garies	18.626313	-30.592675	990	292.78	70.56	8.07	36.44
G182	gabbro-norite	Coarse grained mafic granulite	Bushmanalnd/ Garies	18.672043	-30.582763	940	102.79	483.07	12.82	65.38
C133	charnockite	medium to coarse grained granite	Bushmanland/ Garies	18.685169	-30.575942	956	190.86	168.16	6.77	41.5
IG142	Ibiquas granite	Coarse grained Granite	Bushmanland/ Garies	18.635848	-30.602559	929	177.4	294.83	7.69	49.65
Q134	quartzite	Medium grained equigranular quartz rich rock with minute crystals of garnet	Bushmanland/ Garies	18.684204	-30.576929	949	35.62	85.16	3.47	22.19
M102	metapelite	Medium grained displaying well defined gneissic fabric	Bushmanland/ Garies	18.650226	-30.567526	1012	256.63	106.22	13.85	67.07

Table C-4. List of samples sent for U-Pb zircon dating

SAMPLE ID	rock name	LITHOLOGY	SUBPROVINCE/ TERRANE	ZIRCON ABUNDANCE (ppm)	Co-ordinates in UTM		
					X	Y	Z
PBG001	streaky gneiss	Medium grained quartz-feldspar-biotite gneiss	Bushmanland/ Garies	184.57	18.65493	-30.556543	998
PG006	pink gneiss	Medium to fine grained quartz-feldpsar gneiss	Bushmanland/ Garies	165	18.662273	-30.558367	984
G162	gabbro-norite	Coarse grained mafic granulite	Bushmanalnd/ Garies	17.069	18.655368	-30.598887	972
C144	charnockite	medium to coarse grained granite	Bushmanland/ Garies	351.33	18.637425	-30.602065	931
IG30	Ibiquas granite	Coarse grained Granite	Bushmanland/ Garies	348	18.646113	-30.601913	986
Q066	quartzite	Medium grained equigranular quartz rich metasediment with minute crystals of garnet	Bushmanland/ Garies	222.03	18.627808	-30.605462	944
M103	metapelite	Medium grained displaying well defined gneissic fabric	Bushmanland/ Garies	439.51	18.64807	-30.570375	1002

Appendix D

Petrographic Descriptions

1. Pink gneiss

***Hand specimen*:** The Pink gneiss consists of alternating 1-2mm biotite streaks and 1.5cm quartzo-feldspathic bands. In the more biotite-poor variety of the pink gneiss the 1mm biotite bands are non-existent and the rock is distinctly pinker in colour.

Table AD-1: Mineral abundances of various Pink gneiss samples

Sample no.	*1*		*4*		*165*		*169*		
Mineral	*Modal* %	*Grain size* (mm)	*Modal* %	*Grain size* (mm)	*Modal* %	*Grain size* (mm)	*Modal* %	*Grain size* (mm)	*Description*
Quartz	37		41		37		38	0.1-1.0	strained grains displaying undulose extinction
K-feldspar	30	0.3-1.0	33	0.3-1.0	32	0.1-1.1	33	0.4-2.1	sericitised; perthitic grains with quartz inclusions
Plagioclase	15	0.1-0.4	12	0.1-0.4	17		14		Minor myrmekite, An_{17}
Biotite	13		12		10	0.3-1.0	11		Prismatic laths with red brown pleochroism; aligned
Oxides	trace		Trace		trace		0.5		
Zircon	trace		Trace		trace		trace		
garnet	4	0.4-0.8	2		3		3		

***Texture*:** This rock is medium grained and has a granoblastic texture. The K-spar is perthitic and the quartz grains strained with serrated boundaries, except for quartz inclusions which have well rounded grain boundaries.

Table AD-2: The CIPW norm calculated by using gcdkit for the Pink gneiss

Mineral	*Sample*									
	PG1	PG4	PG7	PG20	PG41	PG50	PG100	PG122	PG165	PG169.2
Quartz	38	43	38	41	40	43	40	42	37	37
Orthoclase	36	35	33	25	35	32	33	34	32	40
plagioclase	22	19	25	31	21	22	22	21	26	19
Biotite	3	2	3	2	3	2	4	2	4	3

2. Streaky augen gneiss

***Hand specimen*:** The streaky augen gneiss has similar characteristics to that of the biotite-rich pink gneiss, in the sence that this rock is also pinkish cream consisting of alternating bands of biotite (±1.5mm thick) and quartz-feldspar (±2cm thick), with large white augen feldspar being the only exception (10-50% of the rock).

Table AD-3: Mineral abundances of various streaky augen gneiss samples

Sample no.	*113*		*212*		
Mineral	*Modal* %	*Grain size* (mm)	*Modal* %	*Grain size* (mm)	*Description*
Quartz	37	0.3-1.4	36	0.3-1.4	strained grains displaying undulose extinction
K-feldspar	39	0.3-1.0	40	0.3-1.0	sericitised; perthitic grains with quartz inclusions
Plagioclase	8	0.2-0.6	7	0.2-0.6	An_{16}
Biotite	15	0.2-0.5	16	0.2-0.5	Prismatic laths with red brown pleochroism; aligned
Oxides	trace	0.3	trace	0.3	
Zircon	trace	0.2	trace	0.2	

***Texture*:** This rock has a porphyrtic texture, in the sence that there are large orthoclase feldspar grains surrounded by fine to medium grained matrix of quarts and feldspar. Sub-parallel grains of biotite, forming a well defined regional fabric is a major characterstic of the both the pink and streaky augen gneiss.

Table AD-4: The CIPW norm calculated by using gcdkit for the streaky augen gneiss

Mineral	*Sample number*					
	AG212	AG148	AG112	AG113	AG114	AG170
Quartz	39	33	33	41	39	32
Orthoclase	32	36	34	33	35	29
plagioclase	23	26	28	21	21	33
Biotite	5	4	5	4	4	5

3. Quartzite

***Hand specimen*:** This equigranular fine grained leucocratic rock consists of quartz (50%), white feldspar (25%) and 25% of dispersed garnet (±5-10mm), bioite and plagioclase.

Table AD-5: Mineral abundances of various quartzite samples

Sample no.	68		190		67		
Mineral	*Modal* %	*Grain size* (mm)	*Modal* %	*Grain size* (mm)	*Modal* %	*Grain size* (mm)	*Description*
Quartz	55	0.3-1.4	48	0.3-1.4	47	0.1-1.6	strained grains: undulose extinction, and has serrated grain boundaries
K-spar	29	0.3-1.7	34	0.3-1.7	32	0.3-1.9	Perthitic, contains Qtz inclusions and are sericitized
Biotite	9	0.2-0.7	5	0.3-0.9	7	0.2-0.6	Majority are dark red brown, strongly pleochroic, interstitial grains
Plagioclase	4	0.3-1.0	10	0.2-0.8	8	0.3-0.7	anhedral, An_{14}
Garnet	2	N/A	2	N/A	5	0.7-1.2	Subhedral to anhedral, quartz inclusions
oxides	trace	N/A	trace	N/A	trace	N/A	irregular shaped interstitial grains
chlorite	trace	0.2-0.7	trace	0.2-0.7	trace		

***Texture*:** This rock is fine grained and has a granoblastic texture. Similarly to the pink gneiss the K-spar in this rock is perthitic and the quartz grains strained with serrated boundaries, except for quartz inclusions which have well rounded grain boundaries. .

Table AD-6: The CIPW norm calculated by using gcdkit for the quartzite

Mineral	*Sample number*					
	Q68	Q66	Q134	Q190	Q145	Q164
Quartz	61	50	63	44	41	34
Orthoclase	15	32	7	35	35	31
plagioclase	18	15	26	16	19	28
Biotite	5	2	3	4	4	6

5. Gabbro-norite

***Hand specimen*:** This dark red to black mafic rock has an equigranular texture, with the abundant biotite forming a moderate gneissic fabric.

Table AD-7: Mineral abundances of various gabbro-norite samples

sample	167		184		33		
Mineral	*Modal* %	*Grain size* (mm)	*Modal* %	*Grain size* (mm)	*Modal* %	*Grain size* (mm)	*Description*
Quartz	9	0.2-0.5	4	0.1-0.5	17	0.1-1.1	
K-feldspar	18	0.4-1.1	17	0.3-1.1	19	0.2-1.1	
Plagioclase	28	0.2-1.0	26	0.2-0.7	25	0.1-0.7	tabular, polysynthetic twinning, serrated grain boundaries; An_{42}
Olivine	4		5		3		colourless; unaltered, rounded equant grains with fractures
Clinopyroxene	7	0.2-0.9	8		8	0.2-0.5	Weak pleochroism, small xenoblastic grains
Orthopyroxene	12	0.3-1.7	14	0.2-0.5	10	0.3-0.7	pink-pale green pleochroic
Hornblende	5		8		6		Brown and yellow pleochroism
Biotite	16	0.3-0.8	17	0.2-0.6	11	0.3-0.6	Aligned laths, reddish brown pleochroic
Opaques	trace	0.1-0.4	trace	0.2-0.1	accessory		

***Texture*:** This rock is medium to coarse grained with an equigranular texture with a hyp-hbl-plag assemblage. Biotite grains are occasionally observed replacing mafic minerals (particularly the pyroxenes). Rounded stubby grains of pyroxene and olivine where found together with randomly oriented tabular crystals of plagioclase.

Table AD-8: The CIPW norm calculated by using gcdkit for the Gabbro-norite

Mineral	*Sample*									
	G33	G36	G125.2	G182	G115	G196	G169.1	G162	G216	G124
Quartz	20	21	14	10	11	8	7	18	5	6
Orthoclase	13	19	15	13	10	19	10	10	11	14
plagioclase	46	44	48	49	51	57	51	40	53	46
Hypersthene	9	7	10	12	13	10	16	17	14	14
Biotite	12	8	12	15	14	15	15	14	16	19

6. Charnockite

***Hand specimen*:** This medium grained equigranular rock has a dark green to olive-brown colour which weathers to a dark red/brown colour

Table AD-9: Mineral abundances of various charnockite samples

sample no.	*63*		*133*		*188*		
Mineral	*Modal* %	*Grain size* (mm)	*Modal* %	*Grain size* (mm)	*Modal* %	*Grain size* (mm)	*Description*
Quartz	24	0.2-0.8	28	0.2-1.2	27	0.2-1.4	strained grains: undulose extinction; sutured grain boundaries, fluid inclusion
K-feldspar	30	0.5-1.3	36	0.3-2.0	33	0.3-1.0	Subhedral-anhedral, perthitic
Plagioclase	18	0.3-0.8	16	0.3-0.6	15	0.3-0.6	Subhedral-anhedral; An_{17}; myrmekite
Hypersthene	2	0.3-0.6	5	0.3-0.7	7	0.2-0.5	Colourless weakly pleochroic; altered to chlorite
Hornblende	9		5		6	0.4-0.9	
Biotite	16	0.2-0.6	9	0.3-0.8	11	0.3-0.9	Dark red-brown pleochroism; weakly aligned laths
Oxides	trace		trace		trace		
Zircon	trace		trace		trace		

***Texture*:** This rock has an equigranular granitic texture consisting of intergrown quartz and abundant green feldspar (responsible for the green Hugh of the rock).

Table AD-10: The CIPW norm calculated by using gcdkit for the charnockite

Mineral	*Sample number*								
	C35	C63	C106	C188	C133	C141	C125.1	C171	C144
Quartz	35	39	29	31	33	19	29	27	38
Orthoclase	29	32	30	27	32	25	37	41	4
plagioclase	27	23	28	32	27	43	28	22	44
Hypersthene	4	2	6	4	3	6	2	4	6
Biotite	5	3	6	5	4	6	3	5	7

7. Ibiquas granite

***Hand specimen*:** This magmatic leucosome has an equigranular medium to coarse grained texture and consists mainly of quartz and K-feldspar, with spotted red garnet (±4mm) porphyroblasts.

Table AD-11: Mineral abundances of various Ibiquas granite samples

Sample no.	IG30		IG61		IG142		
Mineral	*Modal* %	*Grain size* (mm)	*Modal* %	*Grain size* (mm)	*Modal* %	*Grain size* (mm)	*Description*
Quartz	42	0.4-1.7	46	0.5-1	40	0.1-1.8	strained grains: undulose extinction; fluid inclusions
K-feldspar	36	0.6-1.6	38	1-4	37	0.5-2.0	embayed grain boundaries; perthitic; myrmekite
Plagioclase	4	0.5-1.0	4	1-2	6	0.6-1	twinning: $An_{12,}$; sericitized
Garnet	8	2	7	2	9	2-4	Subhedral to anhedral, poikiloblastic; quartz inclusions
Biotite	9	0.5-1.0	4	0.4-0.9	7	0.5-l.0	red-brown strongly pleochroic; randomly oriented laths
Oxides	trace	0.2-0.4	trace		trace		
Zircon	trace	0.1-0.2	trace		trace		

***Texture*:** This rock has a predominantly granoblastic texture and is medium to coarse grained, with roughly equigranular, quartz, feldspar and garnet porphyroblasts.

Table AD-12: The CIPW norm calculated by using gcdkit for the charnockite

Mineral	*Sample number*					
	IG30	IG30	IG61	IG73	IG201	IG142
Quartz	41	47	43	39	44	35
Calcite	3	3	3	2	3	2
Orthoclase	28	19	27	34	21	27
plagioclase	19	21	18	15	24	26
Biotite	2	3	2	1	2	3
Garnet	6	7	6	8	5	6

Appendix E

Additional images of axial planar cleavages viewed in the field

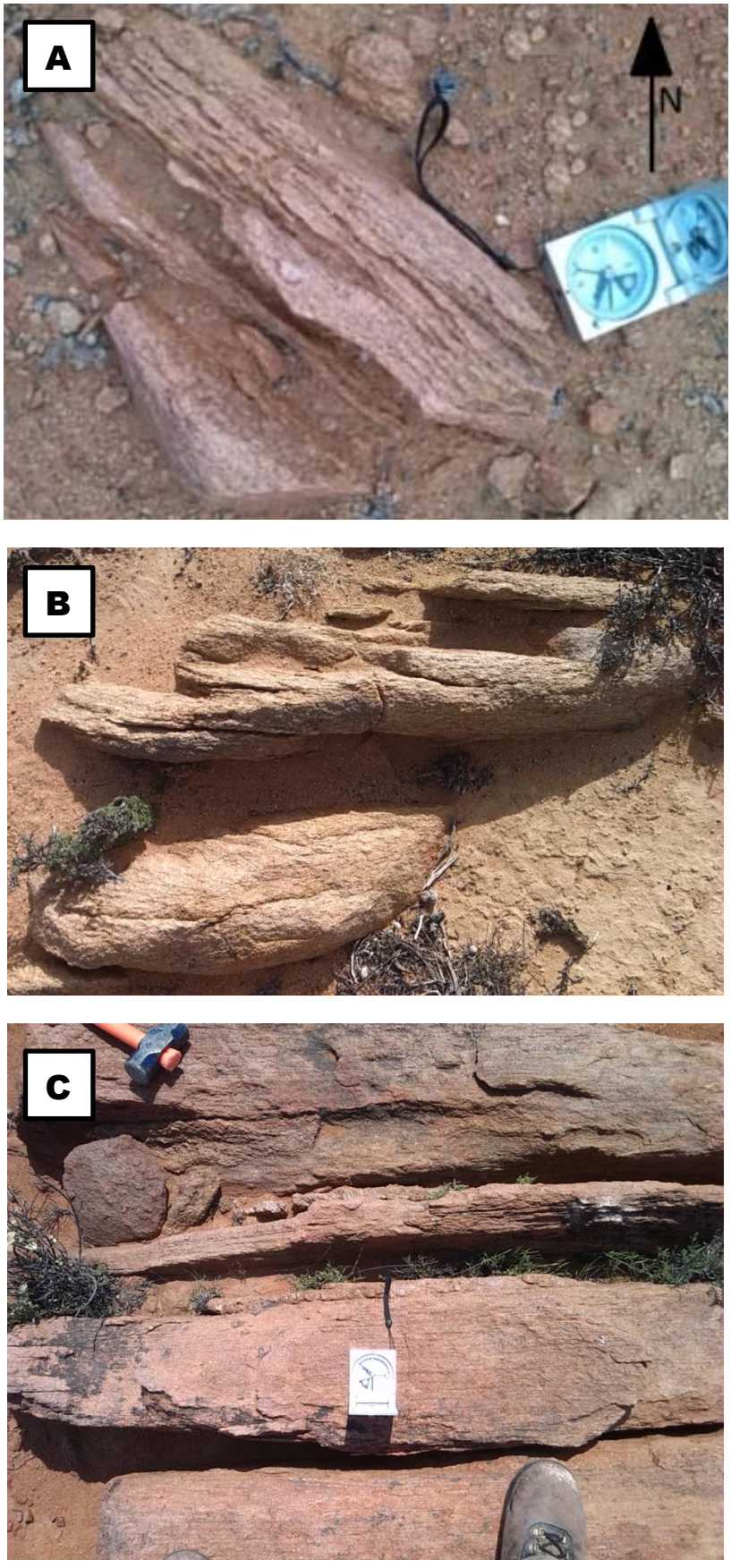

Figure AE. A, B, C) Various outcrop of Pink gneiss and streaky augen gneiss displaying axial planar cleavage.

Appendix F

Bar graphs of mass balance table

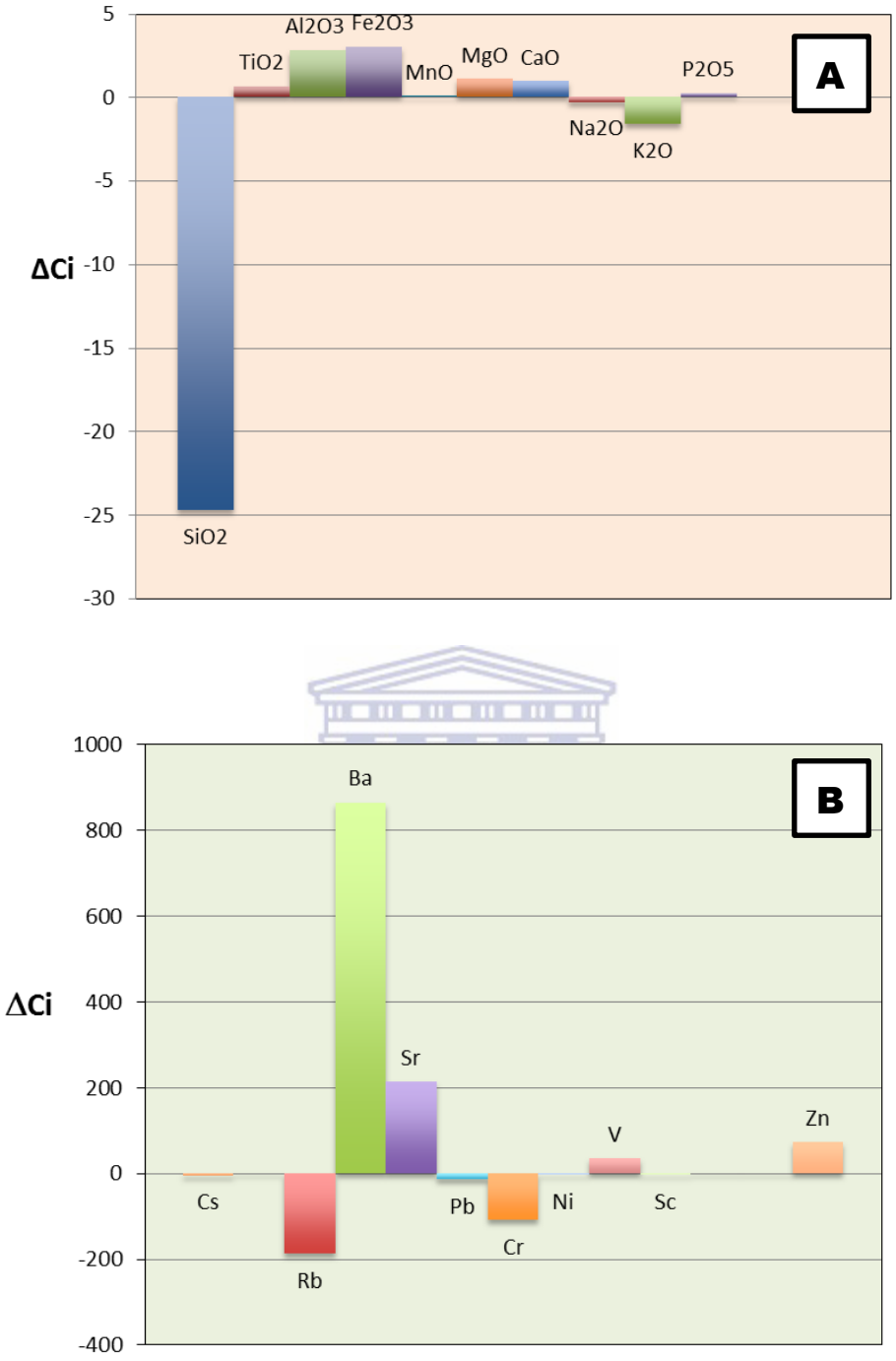

Figure AF-1. Median gains and losses pattern for the selected oxides in wt% (a) and selected trace elements in ppm. (b) for the charnockite relative to the streaky augen gneiss

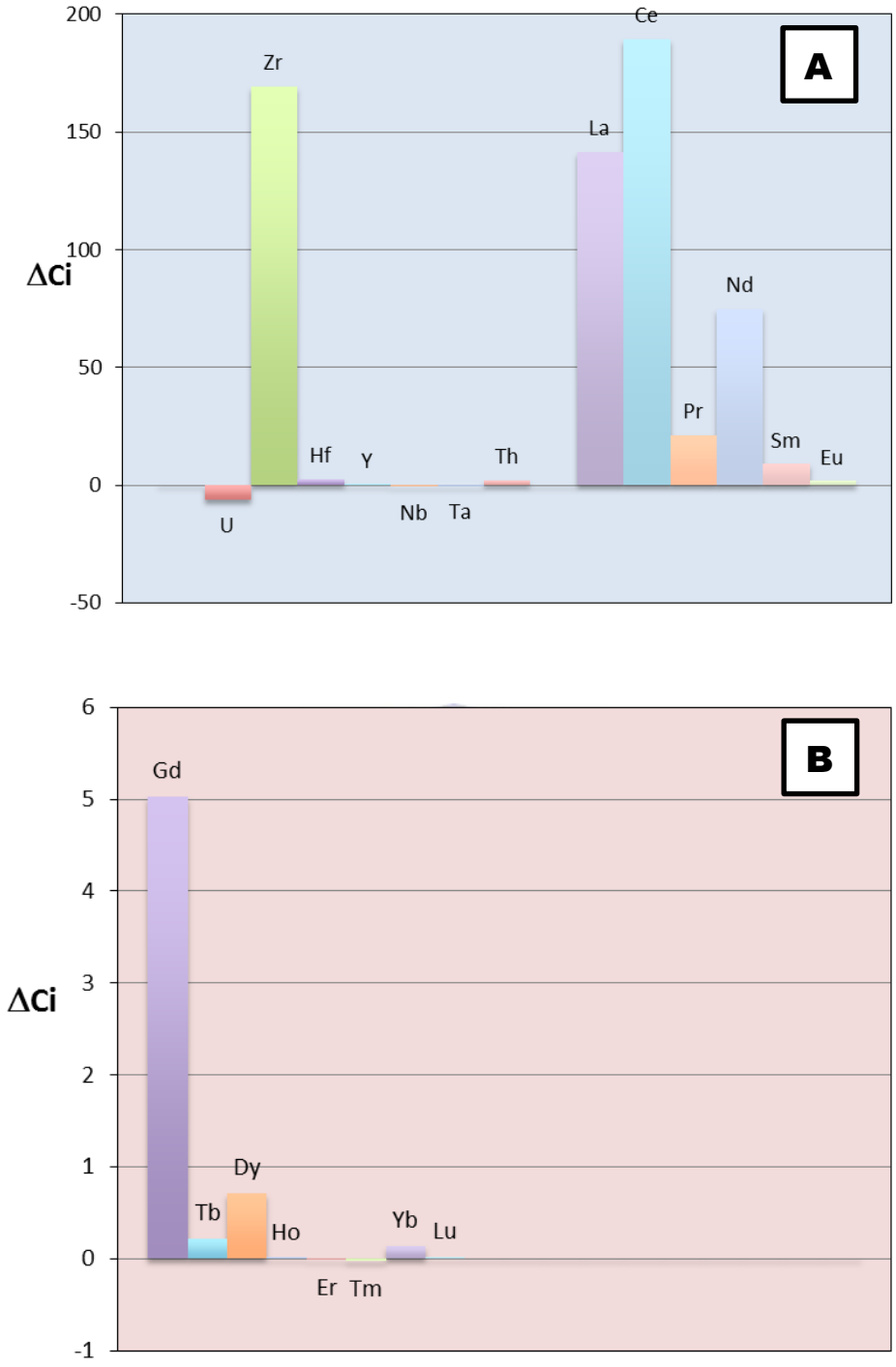

Figure AF-2. Median gains and losses pattern for the selected oxides in wt% (a, b) for the charnockite relative to the streaky augen gneiss

Table AF-1: Losses or gain of the chemical composition for the altered charnockite relative to the unaltered Streaky augen gneiss

			Overall volume change (%)	-17.64
			Overall mass change (%)	-20.58
			Slope	1.26
Sample	Unaltered AG114	Altered C106	Gain/Loss relative to C_i^0 $\Delta C_i/C_i^0$	Gain/Loss in wt.% or ppm ΔC_i
SiO_2	74.84	63.05	-0.33	-24.77
TiO_2	0.34	1.28	1.99	0.68
Al_2O_3	12.09	14.92	-0.02	-0.24
Fe_2O_3	2.37	6.78	1.27	3.01
MnO	0.01	0.06	3.76	0.04
MgO	0.32	1.77	3.39	1.09
CaO	0.62	1.98	1.54	0.95
Na_2O	2.14	2.33	-0.14	-0.29
K_2O	5.88	5.37	-0.27	-1.62
P_2O_5	0.14	0.51	1.89	0.27
Cs	6.23	2.11	-0.73	-4.55
Rb	373.02	234.31	-0.50	-186.94
Ba	263.02	1417.70	3.28	862.86
Sr	39.42	318.00	5.41	213.12
Pb	42.38	35.72	-0.33	-14.01
Cr	346.98	238.93	-0.45	-157.23
Ni	23.43	20.78	-0.30	-6.93
V	62.53	122.68	0.56	34.90
Sc	15.78	16.54	-0.17	-2.64
Zn	45.34	118.02	1.07	48.39
U	7.02	0.88	-0.90	-6.32
Zr	237.53	511.96	0.71	169.05
Hf	8.66	14.10	0.29	2.53
Y	31.23	39.30	0.00	-0.02
Nb	10.69	12.72	-0.05	-0.58
Ta	0.63	0.47	-0.41	-0.26
Th	31.83	42.58	0.06	1.99
La	42.89	184.31	2.41	103.48
Ce	101.24	365.77	1.87	189.24
Pr	10.85	40.33	1.95	21.18
Nd	40.17	144.53	1.86	74.61
Sm	8.44	21.79	1.05	8.86
Eu	0.65	2.93	2.58	1.67
Gd	7.18	15.37	0.70	5.02
Tb	1.18	1.75	0.18	0.21
Dy	6.16	8.65	0.11	0.71
Ho	1.25	1.59	0.00	0.01
Er	3.01	3.78	0.00	-0.01
Tm	0.40	0.47	-0.06	-0.02
Yb	2.07	2.78	0.07	0.14
Lu	0.30	0.40	0.06	0.02

Appendix G

Tables with tectonic probability calculations

Table AG-1. Probability calculations of the streaky augen gneiss for certain tectonic discrimination diagrams.

Tectonic diagram	Total number of samples	Number of discriminated samples [x ± s of probability values] (range of probability values for samples)				
		IA+CA	IA	CA	CR+OI	Col
IA+CA-CR+OI-Col	6	1 (0.7284)	---	---	2 [0.600±0.105] (0.5255, 0.6746)	3 [0.586±0.107] (0.4660-0.6706)
IA-CA-CR+OI	6	---	0 (0)	4 [0.860±0.127] (0.6910-0.9986)	2 [0.696±0.086] (0.6347, 0.7564)	---
IA-CA-Col	6	---	0 (0)	2 [0.637±0.260] (0.4530, 0.8211)	---	4 [0.684±0.064] (0.5886-0.7278)
IA-CR+OI-Col	6	---	0 (0)	---	3 [0.806±0.147] (0.6409-0.9210)	3 [0.932±0.062] (0.8734-0.9973)
CA-CR+OI-Col	6	---	---	1 (0.8943)	3 [0.538±0.118] (0.4177-0.6528)	2 [0.4662±0.0274] (0.4468, 0.4856)
{Σn} {Σprob} [%prob]	**30**	**{1} {0.7284} [---]**	**{0} {0} [0%]**	**{7} {5.6068} [30%]**	**{10} {6.6233} [31%]**	**{12} {8.2239} [39%]**

Table AG-2. Probability calculations of the charnockite for certain tectonic discrimination diagrams.

Tectonic diagram	Total number of samples	Number of discriminated samples [x ± s of probability values] (range of probability values for samples)				
		IA+CA	IA	CA	CR+OI	Col
IA+CA-CR+OI-Col	7	4 [0.776±0.152] (0.6464-0.9443)	---	---	0 (0)	3 [0.602±0.171] (0.4614-0.7925)
IA-CA-CR+OI	7	---	1 (0.8946)	6 [0.840±0.182] (0.5110-0.9844)	0 (0)	---
IA-CA-Col	7	---	1 (0.5898)	4 [0.784±0.168] (0.5585-0.9438)	---	2 [0.78293±0.00149] (0.7819, 0.7840)
IA-CR+OI-Col	7	---	1 (0.8209)	---	2 [0.5878±0.0108] (0.5802, 0.5955)	4 [0.808±0.219] (0.4894-0.9763)
CA-CR+OI-Col	7	---	---	5 [0.851±0.102] (0.7236-0.9814)	1 (0.3709)	1 (0.6631)
{Σn} {Σprob} [%prob]	**35**	**{4} {3.1044} [---]**	**{3} {2.3053} [10%]**	**{15} {12.4324} [56%]**	**{3} {1.5466} [6%]**	**{10} {7.2696} [28%]**

Table AG-3. Probability calculations of the ibiquas granite for certain tectonic discrimination diagrams.

Tectonic diagram	Total number of samples	Number of discriminated samples [x ± s of probability values] (range of probability values for samples)				
		IA+CA	IA	CA	CR+OI	Col
IA+CA-CR+OI-Col	6	1 (0.5084)	---	---	4 [0.743±0.148] (0.5240-0.8413)	1 (0.6368)
IA-CA-CR+OI	6	---	4 [0.699±0.219] (0.5040-0.9087)	2 [0.885±0.090] (0.8220, 0.9488)	0 (0)	---
IA-CA-Col	6	---	1 (0.5421)	4 [0.524±0.082] (0.4410-0.6076)	---	1 (0.6714)
IA-CR+OI-Col	6	---	0 (0)	---	5 [0.805±0.209] (0.4622-0.9733)	1 (0.9147)
CA-CR+OI-Col	6	---	---	2 [0.679±0.090] (0.6147, 0.7427)	4 [0.680±0.131] (0.4852-0.7670)	0 (0)
{Σn} {Σprob} [%prob]	**30**	**{1} {0.5084} [---]**	**{5} {3.3390} [17%]**	**{8} {5.2256} [26%]**	**{13} {9.7170} [46%]**	**{3} {2.2230} [11%]**